NASA Contractor Report 159518
PSU TURBO R 80-4

NASA-CR-159518
19800018789

THREE DIMENSIONAL MEAN FLOW AND TURBULENCE CHARACTERISTICS OF THE NEAR WAKE OF A COMPRESSOR ROTOR BLADE

A. Ravindranath and B. Lakshminarayana

The Pennsylvania State University
University Park, Pennsylvania 16802

June 1980

Prepared for

NATIONAL AERONAUTICS AND SPACE ADMINISTRATION
Lewis Research Center
Under Grant NSG-3012

TABLE OF CONTENTS

Page

Chapter 3: EXPERIMENTAL RESULTS AND INTERPRETATION (cont'd)

Page

SUMMARY

Three-dimensional characteristics of the mean velocity and turbulence structure in the near-wake of a moderately loaded compressor rotor is reported in this thesis. The experimental investigation was carried out using the rotating hot-wire technique. To discern the effect of annulus- and hub-wall boundary layer, secondary flow and tip-leakage on the wake structure, measurements were also taken inside the end-wall boundary layer. Static pressure gradients across the wake were measured using a static-stagnation pressure probe insensitive to flow direction changes.

The set of wake data presented in this thesis is probably the first set of comprehensive measurements taken in the trailing-edge and near-wake regions and reflects the highly complex and three-dimensional nature of the rotor-wake. The axial and the tangential velocity defects, the radial component of velocity and turbulence intensities were found to be very large as compared to the near- and far-wake regions. The radial velocities in the trailing-edge region exhibited characteristics prevalent in a trailing-vortex system. Flow near the blade tips was found to be highly complex due to interaction of the end-wall boundary layers, secondary flows, and tip-leakage-flow with the wake. The streamwise curvature was found to be appreciable near the blade trailing-edge. This investigation did reveal that flow properties in the trailing-edge region are quite different compared to that in the near- and far-wake regions with respect to their decay characteristics, similarity, etc. Fourier decomposition of the rotor-wake revealed that for a normalized wake only the first three coefficients are dominant. The derived results of the measurements indicated the inability of the cascade analysis to accurately

predict the deviation angles for the rotor. Many useful correlations are attempted and reported in this investigation.

ACKNOWLEDGMENTS

The authors wish to thank J. Rishell and G. Kane for their aid in the experimental set up and instrumentation and S. Kovacic for his help in data processing.

The work was supported by the National Aeronautics and Space Administration through Grant NSG 3012, with M. F. Heidmann as the project monitor.

NOMENCLATURE

A_n	Fourier cosine coefficient
a	constant (Equation 1)
B	intercept of the calibration curve
B_n	Fourier sine coefficient
b	constant (Equation 1)
c	blade chord length
C_d	section drag coefficient
c_P	stagnation-pressure rise coefficient = $(P - P_1)/(\frac{1}{2} \rho U_T^2)$
c_p	static-pressure rise coefficient = $(p - p_1)/(\frac{1}{2} \rho U_T^2)$
C_{Lo}	camber expressed as design lift coefficient of isolated airfoil
E	mean voltage
E_o	hot-wire voltage at zero velocity
e	fluctuating voltage
G	percentage of annulus from hub
H	wake shape factor = δ^*/θ^*
i	incidence of inlet-flow with rotor-blade in relative (rotating) frame of reference
K	constant, probe factor (Equation 2)
L	$2(L_s + L_p)/S$ = sum of the characteristic length on the pressure and suction surfaces normalized by semi-blade spacing (interval of integration, Equations 36 and 37)
L_s, L_p	wake width at half the depth on rotor blade suction- and pressure-surface of the wake, respectively
L_o	value of L at the trailing-edge
ℓ_s, ℓ_p	wake width at half the depth of turbulence intensity on the rotor-blade suction- and pressure-surface of the wake, respectively
n	exponent, slope, and number of coefficients in the Fourier series

P	stagnation-pressure
p	static-pressure
R	radius ratio = (r/r_T)
R_c	radius of curvature
R_e	Reynolds number
r	local radius, radial direction
(r,θ,z)	rotating cylindrical coordinate system (radial, tangential, and axial coordinate directions) (Figure 1)
S	blade spacing
(s,n,r)	natural coordinate system (streamwise, normal, and radial coordinate directions) (Figure 1)
U	peripheral speed
u_{dn}	normalized velocity defect = $(u_d/u_{dc}) = (u_{max} - u)/(u_{max} - u_{min})$
U_{max}	maximum velocity in the wake
U_{min}	minimum velocity in the wake
U	velocity at any point in the wake
V	local absolute velocity
v	defect in absolute velocity $(V_{max} - V)$
W	total relative velocity
w	defect in relative velocity
w'	fluctuating component of relative velocity
y	tangential distance
$(2y/S)$	tangential distance normalized by half the blade spacing (y = 0 at wake center)
Z	axial distance from blade trailing-edge normalized by rotor blade chord
$\overline{\phi}$	mass averaged flow coefficient $(\overline{W}/U_T)$
$\overline{\psi}$	mass averaged stagnation pressure rise coefficient (normalized by $\frac{1}{2} U_T^2 \rho$)

Ω	speed of rotation of rotor blade
η_s, η_p	wake traverse distance normalized by L_s and L_s, respectively
$\bar{\eta}$	rotor efficiency (Euler) = $\bar{\psi}/\bar{\psi}_{Euler}$
σ	solidity = c/S
β_o	blade outlet angle
β	air outlet angle
β_1	streamline angle (Equation 3)
δ	deviation angle (Equation 11), boundary layer thickness
δ^*	displacement thickness = $\frac{1}{s}\int_o^s (1 - \frac{W}{W_o})rd\theta$
θ_L	angular distance between wake centerline and the location where $U_d = U_{d_c}/2$
θ^*	momentum thickness, Equation 9
$\tau_z, \tau_r, \tau_\theta$	normalized turbulence intensities in the axial, radial, and tangential direction, respectively ($\sqrt{\overline{w_z'^2}}/W$, $\sqrt{\overline{w_r'^2}}/W$ $\sqrt{\overline{w_\theta'^2}}/W$)
$\tau_{sn}, \tau_{rn}, \tau_{sr}$	normalized streamwise, radial Reynolds stress, and stress correlation, respectively ($\overline{w_s'w_n'}/W_s^2$, $\overline{w_r'w_n'}/W_s^2$, $\overline{w_s'w_r'}/W_s^2$
ε_n	Neumann's factor
α	angle of attack

Subscripts

c	value at wake center
d	defect (difference between free-stream and wake value)
m,max	maximum value in the wake
o	value at wake edge/free-stream value/stagnation property
p	pressure side
(r,θ,z)	values in the radial, tangential, and axial coordinate directions, respectively
(s,n,r)	values in the streamwise, normal, and radial coordinate directions, respectively
s	suction side, blade spacing

T	value at the rotor tip, stagnation condition
TE	values at the trailing-edge
1	value at inlet (passage averaged), wire number one
2,3	wire number two and three

Superscript

$\bar{}$	average value
'	flucutating quantity

Chapter 1

INTRODUCTION

1.1 Problem Relevance and Objectives

The flow through a compressor rotor blade row is very complex and deviates considerably from a two-dimensional flow-field because of a number of phenomena including vortex shedding, variation in spanwise circulation, radial flows in boundary layers, and hub- and annulus-wall boundary layer growth. These are in addition to inviscid and compressibility effects. The boundary layers on the blades are shed out from the pressure and suction surfaces, and they combine at the trailing-edge to form the viscous wake referred to as the rotor-wake. Study of the rotor-wake should yield a comprehensive understanding of the flow and the acoustic fields induced by this phenomena, which is essential to the progress in reducing the noise, aerodynamic losses, and in improving the mechanical, aerodynamic and acoustic performance of rotors. The wake has considerable influence on the noise generated, aerodynamic losses, as well as vibration, flutter, and stress characteristics of the rotor-blade.

Rotor-wakes, which influence the flow-field downstream of the rotor, are not only dependent on the upstream flow-field conditions but are also controlled by such parameters as blade spacing, distance from the blade trailing-edge, curvature and rotation. Complexity brought about by these and other effects makes both the analytical and experimental investigations extremely complicated.

The characteristics of the rotor-wakes change rapidly in the trailing-edge region. The flow-field at these locations is shown schematically in Figure 1. The three-dimensional nature of the flow-field exists in

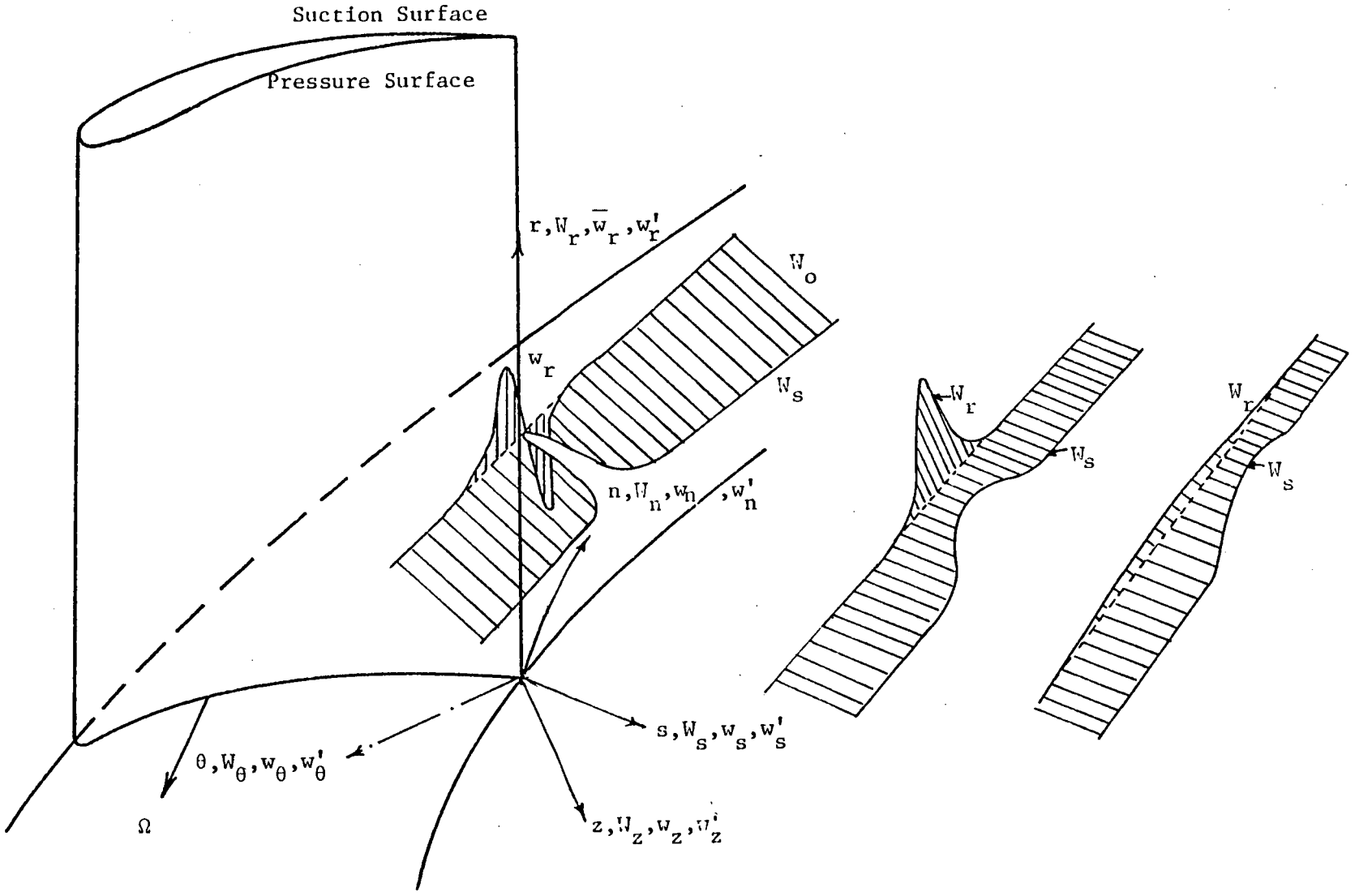

Figure 1. Nature of the Rotor-Wake and Coordinate System

both the mean velocity as well as in the turbulent structure of the wake.

Lack of knowledge of the flow-field downstream of compressor-rotor-blade has hampered the progress in many areas of compressor development, particularly in the fields of acoustics and performance prediction. It is known that the rotation-induced centrifugal and Coriolis forces generate spanwise flows inside the boundary layers, the magnitude of which depends on rotor-blade geometry, angular velocity of the blade, flow coefficient, etc. This spanwise migration of the flow results in a decrease of the boundary layer near the hub and an increase near the tip. In addition, near the tip, very complex flow interactions take place between the blade boundary layer, secondary flow, tip-leakage flow, and the wake. The resulting flow is extremely difficult to model analytically as well as to evaluate it experimentally.

It is thus essential to carry out a systematic study of the compressor-rotor-wake and the exit flow for the prediction of the aerodynamic, acoustic and mechanical performance of compressors. Previous investigations have given an insight into the flow far downstream of the rotor-blade. The present study was conducted in the trailing-edge and near-wake regions of a moderately loaded compressor blade using a tri-axial hot-wire-probe in a non-inertial frame of reference. The flow-field was surveyed very close to the trailing-edge as well as inside the annulus- and hub-wall boundary layers.

The scope and objectives of this investigation are as follows:

1. To study experimentally the three-dimensional wake characteristics in the vicinity of the blade trailing-edge. The primary interest is in the three-dimensional mean velocity and turbulence flow-field.

2. To study the wake characteristics in the near- and far-wake regions and to calculate the decay and profile characteristics.

3. To study experimentally the effects of annulus- and hub-wall boundary layers on the blade wake.

4. To evaluate the static-pressure gradients in the wake.

5. Correlate the data from this study with earlier measurements and theory.

This study was conducted in a low speed (low subsonic Mach numbers) single stage compressor using rotating hot-wire and conventional probes. Many parameters relevant to design were derived out of these measurements.

1.2 Previous Investigations

A comprehensive survey of isolated airfoil wakes and rotor-wakes are given by Raj and Lakshminarayana (1975) and Reynolds (1978), respectively. In order to compliment the earlier reviews only the investigation of cascade, stator, and inlet-guide-vane wakes are reviewed in this sections. Interested readers are referred to earlier reviews.

The interest in laminar wakes which started around 1920 soon gave way to the analytical and experimental study of turbulent wakes as it was realized that many of the flows in practical applications were usually highly turbulent. Excellent reviews of the laminar wake of bodies are given by Goldstein (1953), Eagleson, et al. (1961), and Berger (1971).

The work on turbulent wakes in subsonic flow received much attention due to its practical application in many aerodynamic problems, both internal and external aerodynamics. A review of all the work done on two-dimensional turbulent wakes has been reported by Raj and Lakshminarayana (1975). Lieblein (1956) and Reynolds (1978) have summarized much

of the work done related to isolated airfoil wakes. The isolated airfoil wake study received great acclaim from turbomachinery aerodynamicists as these wakes represented the rotor-wakes to a first approximation.

The effect of adjoining blades in a cascade would greatly influence the wake behavior downstream of a cascade of blades. The first measurements that have been reported on cascade wakes are by Lieblein and Roudebush (1956). They reported extensive measurements at one downstream station of a cascade of blades. They covered a wide range of blades and flow parameters. Their correlations, based on semi-empirical formulations, seem to envelop a large portion of the existing data. Since these measurements were carried out with pressure probes they were able to provide information on only the gross properties, such as semi-wake width and the decay of the total mean velocity with downstream distance. No turbulence measurements have been reported. This set of measurements has inadequate data to derive the decay characteristics. But it is interesting to note that their decay law as given by

$$\frac{V_c}{V_o} = 1 - a\left(\frac{z}{c} + b\right)^{-1/2} - d\left(\frac{z}{c} + b\right)^{-1} \qquad (1)$$

is of the same nature as the one employed by Reynolds, et al. (1978) in predicting the decay of lightly loaded rotor-blade wakes.

Detailed measurements of the cascade wake using an "x" configuration hot-wire probe were reported by Raj and Lakshminarayana (1973). This is probably the first and most complete set of measurements where turbulence data as well as mean velocity was measured at various downstream locations and incidences. These measurements show that the wake is asymmetrical and that its structure is different from that of a flat plate, cylinder, or even isolated airfoil (symmetrical) wakes. It was also

realized that the turbulence intensities are higher than those of a flat plate or isolated airfoil wake while the decay rates are about the same. Lakshminarayana (1976) has shown semi-analytically that the wakes become self-similar when proper characteristic lengths and velocity scales are employed. Raj and Lakshminarayana (1975) have also provided semi-analytical expressions for the decay of wake-centerline velocity with downstream distance. Gustafson, et al. (1977) have obtained an analytical solution to the equations of motion and have predicted the wake shape using local as well as global similarity solutions. The agreement between their theory and the experimental data of Raj and Lakshminarayana (1973) is good, particularly for wakes beyond a tenth of a chord downstream. The similarity solution was tried because Raj and Lakshminarayana (1973) have shown that the wake edge velocity and the wake centerline velocity vary as a power law in downstream distance. It is of interest to note that the similarity solution required a power law variation of the eddy-viscosity downstream of the trailing edge, the exponent taking different values for each incidence angle.

Pollard and Gastelow (1967) have also reported the wake measurements downstream of a cascade of blades. Unfortunately, not enough information is available on these meaurements. However, the significant result from this investigation was to show that high free-stream turbulence tends to promote early boundary layer transition and to delay the increase in loss normally associated with a reduction of Reynolds number.

All the wake data discussed above seems to follow the similarity rule given by Lakshminarayana (1976). The similarity plots will be given at a later section in this thesis. Even the decay of the cascade wakes can be collapsed onto a single curve when $c_D^{-0.5}$ was used as the norma-

lizing factor. This seems to indicate that the wake decay depends mainly on the section drag coefficient of the blades.

In present day compressors the stage is invariably preceded by an inlet-guide-vane assembly and the rotors are separated by a stator assembly. It is necessary to understand the flow downstream of these inlet-guide-vanes and stators accurately to predict the pure tone noise, blade row vibration and aerodynamic losses in axial-flow compressors arising due to the interaction of these wakes with the downstream or upstream rotor.

Very little literature is available on the inlet-guide-vane and stator-wakes. The earliest data available on stator-wakes is due to Bitterlich and Rubner (1972). They have made a very extensive radial survey downstream of the stator. Probably this is the first set of data on stator-wakes where the effect of interaction of the secondary flow with the wakes is given. Lakshminarayana and Davino (1978) have measured the stator- and inlet-guide-vane wakes using a single sensor hot-wire and rotating the wire about its axis to obtain the three components of the mean velocity and turbulence intensities. This was the first comprehensive set of measurements reported where turbulence as well as mean velocity data for the inlet-guide-vane wakes are available as a function of radius and downstream distance. Correlations of these data in terms of profile and decay are reported in a later section. One of the striking features of the boundary layer development on the stator blades was reported by Evans (1975) who measured the boundary layer on the stator blades using the ensemble average technique. The results of Evans indicate that the boundary layer development on the stator blades is much greater compared to the two-dimensional cascade case. Further, the

stator blade boundary layer is found to be highly unsteady, which implies that the stator-wake is unsteady. This is due to the rotor-wake interaction with stator blade boundary layer.

Rotor-wakes are probably the most complex of all the wakes considered so far. This is because of the complexity introduced by the centrifugal and the Coriolis forces arising from the rotation. A comprehensive survey of literature has been given by Reynolds (1978).

It should be realized that the flow situation and wake properties in each component of a compressor stage (for example, the inlet-guide-vanes, stator, rotor) are very different, it is essential to study each component individually and arrive at correlations which are unique to each one of them. When the flow phenomena in each of these components have been properly understood it is possible to combine these effects and arrive at an analytical formulation that could be employed to predict the combined effect.

Chapter 2

TEST FACILITY, DATA ACQUISITION, AND PROCEDURE

All the measurements reported in this investigation were performed using the axial-flow compressor facility located in the Turbomachinery Laboratory of The Pennsylvania State University. All the data were acquired with a tri-axial hot-wire probe and a direction insensitive spherical headed pitot probe rotating with the rotor. The study included the measurements of the mean velocities, turbulence intensities, Reynolds stresses and their decay characteristics downstream of the blade trailing-edge region. This experimental information is needed not only for the understanding of the wake but is also essential in predicting the aerodynamic and acoustic properties of the turbomachines.

2.1 The Axial-Flow Compressor Facility

The axial-flow compressor facility, shown in Figure 2 consists of a rotor which is located between an inlet-guide-vane assembly and a stator assembly. The design features of this single-stage compressor are given by Smith (1956). A 37.29 KW (50 HP) variable speed motor drives the rotor through a belt and pulley system. An aerodynamically designed throttle, placed downstream of an auxiliary fan can vary the flow rate through the machine to enable operation at varying flow coefficients (Figure 3). Table 1 lists some of the relevant data of the compressor stage. The rotating hub of the machine has slots cut in it to traverse the probe across the blade passage. The traverse mechanism, described later, is located inside the rotating hub and the slots on the hub facilitate a comprehensive flow survey to be undertaken downstream of the rotor blade.

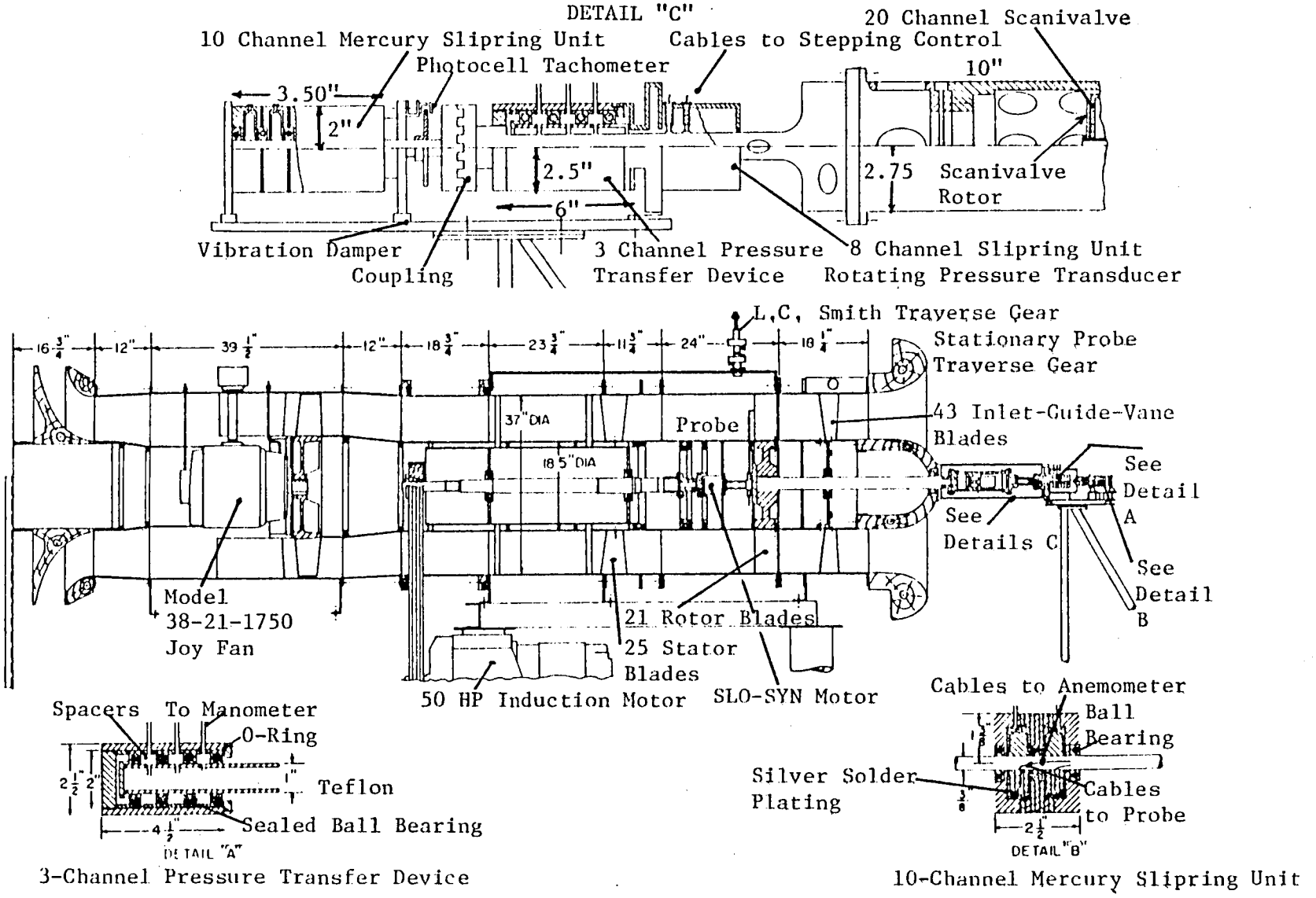

Figure 2. PSU Axial-Flow Compressor Facility and Data Transmission Systems

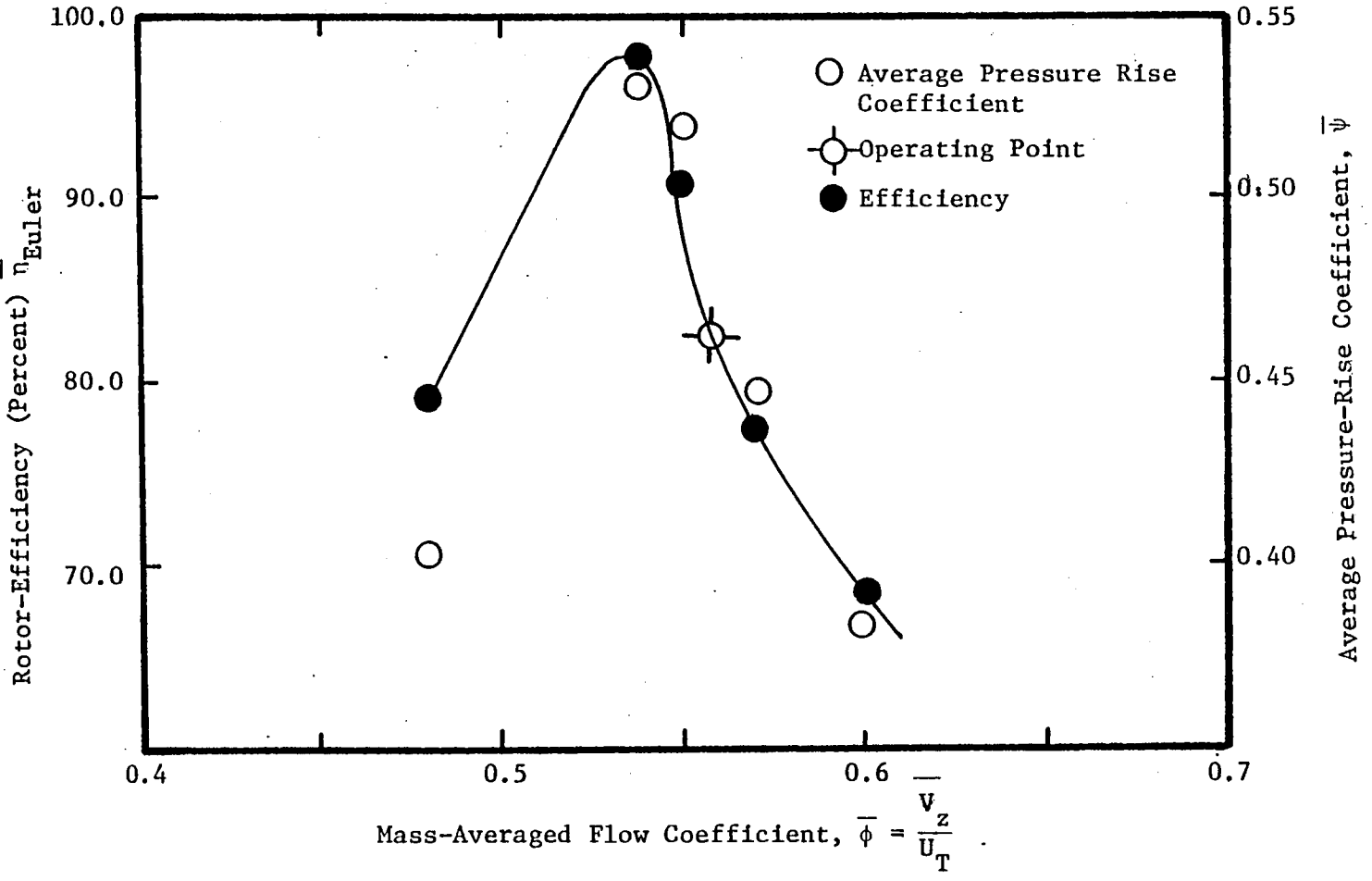

Figure 3. Performance Curve of the Penn State Axial-Flow Compressor

Table 1

Axial-Flow Compressor Facility Specifications

	Particulars	IGV	Rotor	Stator
1.	Number of Blades	43	21	25
2.	Rotor Speed (Operating)	-	1050 (rpm)	-
3.	Outer Diameter of Rotor		0.9322m (36.7 inch)	
4.	Hub/Tip Ratio		0.5	
5.	Blade Element	NACA 65-010	Modified NACA 65 Series (see Table 2)	
6.	Tip Clearance		0.089" at L.E. (0.0024 m) 0.091" at T.E. (0.0025 m)	
7.	Electric Power		37.29 KW (50 HP)	
8.	Spacing between Elements (at Tip)	18 1/4"		-
9.	Inlet-Static-Pressure (Wall)		-1.758" of H_2O (88.44 ft/sec)	
10.	Auxiliary Fan		Series 1000 Joy Axivane Fan #0 to #16 Blade Setting Fan Dia. 96.52 cm (38")	
11.	Fan Drive Power		37.29 KW (50 HP)	

2.2 The Compressor Rotor

The rotor consists of 21 cambered and twisted blades and has a tip diameter of 0.9322 m (36.7 inch). The hub-tip ratio is 0.5. The blade elements are of modified NACA 65-010 basic profile on a circular arc camber. The blades have varying stagger angles and blade chords along the radius and relevant details are tabulated in Table 2. Reference is made to Smith (1956) for detailed design. The blades are made out of aluminum with cast tee-shaped roots and are attached to the hub at the design pitch angle.

To evaluate the blade element properties and to find out the blade static pressure, one of the blades is instrumented by pressure taps. The pressure leads from the rotating blade are taken to a stationary data acquisition system through a 20-channel scanivalue and a three-channel pressure transfer device. These are illustrated in Figure 2.

All measurements reported here have been carried out at a rotor speed of 1066 rpm, at the operating flow coefficient (ϕ) of 0.56. The speed of the rotor is monitored by a photocell circuit with a 60 slot calibrated disk mounted on the rotor shaft and displayed on an electronic counter.

2.3 Rotating Probe Traverse Gear

One unique feature of this facility is the traverse gear unit for the rotating probe measurements. Figure 4 shows the traverse gear, which is a modified version of the one used by Anand (1976). This gear achieves the objectives of the gear used by Reynolds (1978) in a much simpler fashion.

Referring to Figure 4 the traverse gear consists of a SLO-SYN motor of 1.589 Nm (225 in-oz) torque driving a 3.81×10^{-2} m (1.5") diameter

Table 2

Blade Element Details

Particulars	Radius Ratio																	
	Inlet-Guide-Vane						Rotor						Stator					
Radius Ratio	0.5	0.6	0.7	0.8	0.9	1.0	0.5	0.6	0.7	0.8	0.9	1.0	0.5	0.6	0.7	0.8	0.9	1.0
Chord, cm (in)	5.19 (2.04)		7.64 (3.01)		9.80 (3.86)		12.39 (4.88)		13.25 (5.22)		14.41 (5.67)		8.83 (3.48)		10.37 (4.08)		12.39 (4.88)	
		6.63 (2.61)		8.64 (3.40)		10.95 (4.31)		12.68 (4.99)		13.68 (5.39)		15.41 (6.07)		9.80 (3.86)		10.95 (4.31)		13.97 (5.50)
Spacing, cm (in)	3.46 (1.36)		4.90 (1.93)		6.05 (2.38)		6.91 (2.72)		9.80 (3.86)		12.68 (4.99)		5.76 (2.27)		8.35 (3.29)		10.66 (4.20)	
		4.61 (1.82)		5.47 (2.16)		6.91 (2.72)		8.35 (3.29)		11.24 (4.42)		14.12 (5.56)		6.91 (2.72)		9.51 (3.74)		11.67 (4.59)
Camber (c_{Lo} for Rotor & Stator)	-5.0 (deg)		16.0 (deg)		32.0 (deg)		1.35		1.5		1.48		1.7		1.05		0.5	
		6.0 (deg)		24.0 (deg)		45.0 (deg)		1.45		1.5		1.32		1.4		0.8		0.4
Thickness (t/c x 100)	13.0		10.5		8.5		9.50		7.6		5.9		-		-		-	
		12.0		9.5		8.0		9.1		6.5		5.1		-		-		-
Chord Angle, ° (Stagger)	-		-		-		22.5		28.5		39.0		16.5		31.0		42.0	
		-		-		-		26.0		34.0		45.0		24.0		37.0		50.0
Blade Outlet Angle, °							19.5		16.0		26.0							
								13.5		19.5		33.5						

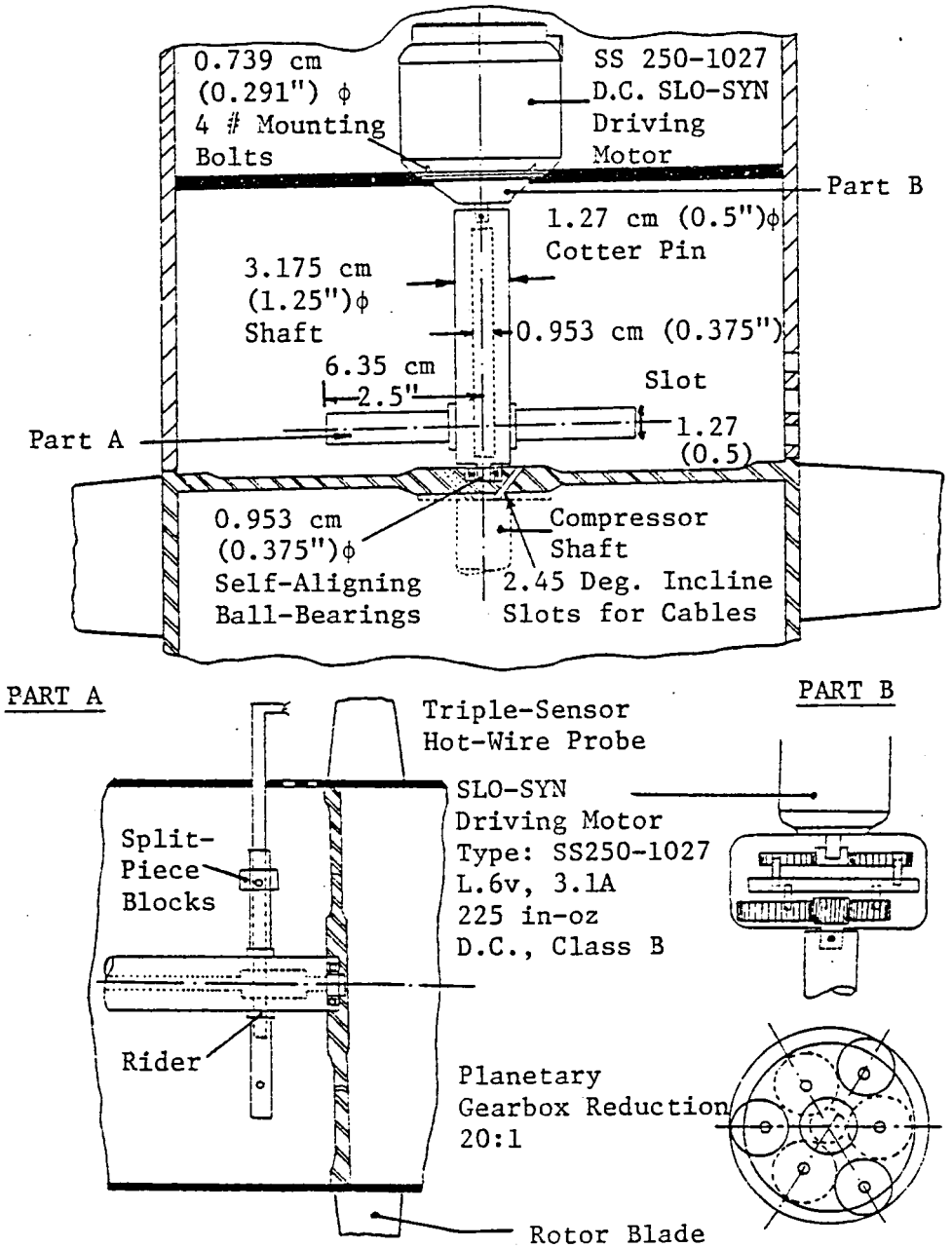

Figure 4. Rotating Probe Traverse Gear

shaft through a planetary reduction gear train. The gear train steps down (1.8°/step) the circumferential stepping to (0.09°/step). The shaft carries a rider which can be traversed axially. The rider in turn carries a pair of mounting blocks which can be used to hold the probe. The mounting blocks give the probe two degrees of freedom; (a) rotation about the probe axis, which is used to align the hot-wire sensors in any desired direction and (b) movement in the radial direction; the probe can be traversed from hub to tip of the machine.

The probe holder, the stepping motor, and the probe are mounted inside the rotating hub of the machine (Figure 2). The probe which is located behind the blade row traverses a slot in the hub. The motor is powered and controlled by a stationary traverse indexing device (SLO-SYN preset indexer) through a eight-channel brush slip-ring unit. The traverse gear and probe are locked except when indexed. Though the circumferential traverse can be accomplished when the rotor is rotating, the radial and axial motions have to be accomplished manually when the rotor is stationary.

2.4 Data Transmission System

2.4.1 Pressure transfer device

To transfer the pressure from the rotating frame to the stationary data acquisition system, a three-channel pressure transfer device (PTD) was employed. Referring to Figure 2, each channel of the PTD was made air tight by using double sealed ball bearings. Pressure leakage along the shaft was prevented by the use of o-rings and plastic sealers. Pressure from the rotating system was transferred to the PTD through a hollow shaft and the pressure was measured by a micro-manometer. The pressure transfer device, which is located in front of the nose cone, is housed

inside a streamlined cowling to avoid interference with the incoming flow.

2.4.2 Brush slip-ring unit

A commercial eight-channel slip-ring unit was used to conduct electrical signals from the stationary indexing unit to the rotating traverse gear motor. Carbon brushes in contact with rotating commutator provided electrical continuity from the stationary frame to the rotating frame. The brush slip-ring unit was mounted next to pressure transfer device and the hollow shaft that carried the pressure tubings also carried the electrical connections.

2.4.3 Mercury slip-ring unit

A ten-channel mercury slip-ring unit made by Rotocon was used to transmit the hot-wire signals from the rotating, tri-axial hot-wire probe to the stationary hot-wire anemometer and data acquisition system. This interface component was chosen, as the triple distilled mercury in the unit provided the greatest conductivity and the lowest noise level distortions possible. The slip-ring unit was connected to the rotor assembly through a flexible coupling. To eliminate spurious electrical signals from the rotor assembly and vibrations to its electrical contacts, the entire unit was mounted on a four-arm vibration damper.

2.5 Probes and Instrumentation

2.5.1 Three-sensor hot-wire probe

In order to evaluate the properties of the rotor-wake both hot-wire and pressure measurements were undertaken. Described below are the probes and instrumentation employed during the experimentation,

The special three-sensor boundary layer hot-wire probe shown in Figure 5 was used for all rotating hot-wire measurements. The probe sensors were built out of tungsten wire and had a length-to-diameter ratio of 270. The sensor resistances were around 5.0 ohms. The probe calibrations were corrected from the variation of temperature and aging of the wire. The effect of rotation on heat transfer properties of the wire was found to be negligible (Hah and Lakshminarayana, 1978). Figure 5 also shows the orientation of the wires; during measurements they are placed in the media to be measured such that the velocity vector falls inside the cone formed by the three sensors. In order to eliminate the influence of prongs only the middle third was etched to give a sensor length of 1.25 mm (0.0492 in). (The distance between the prongs is 3.2 mm (0.126 in).) The prongs were imbedded in ceramic tubing. The spatial resolution was such that the active positions of the wires were inside a sphere of 3 mm (0.1181 in) diameter.

2.5.2 The spherical-head static-stagnation pressure probe

One of the main problems in the measurement of static pressure in the wake is that the direction of the velocity vector will be varying continuously across the wake and it is impossible to obtain an accurate measurement of the static pressure using conventional probe. To overcome this difficulty a spherical-headed static-stagnation probe, insensitive to direction, was built at The Pennsylvania State University.

Main features of the probe are illustrated in Figure 6. It consists of an 3.175 mm (0.125 in) brass sphere with trips around it to stabilize the wake region. The sphere has a total pressure port at its center and the stem at the back carries four static pressure ports which actually measure the pressure behind the sphere (p_w). Knowing the total pressure

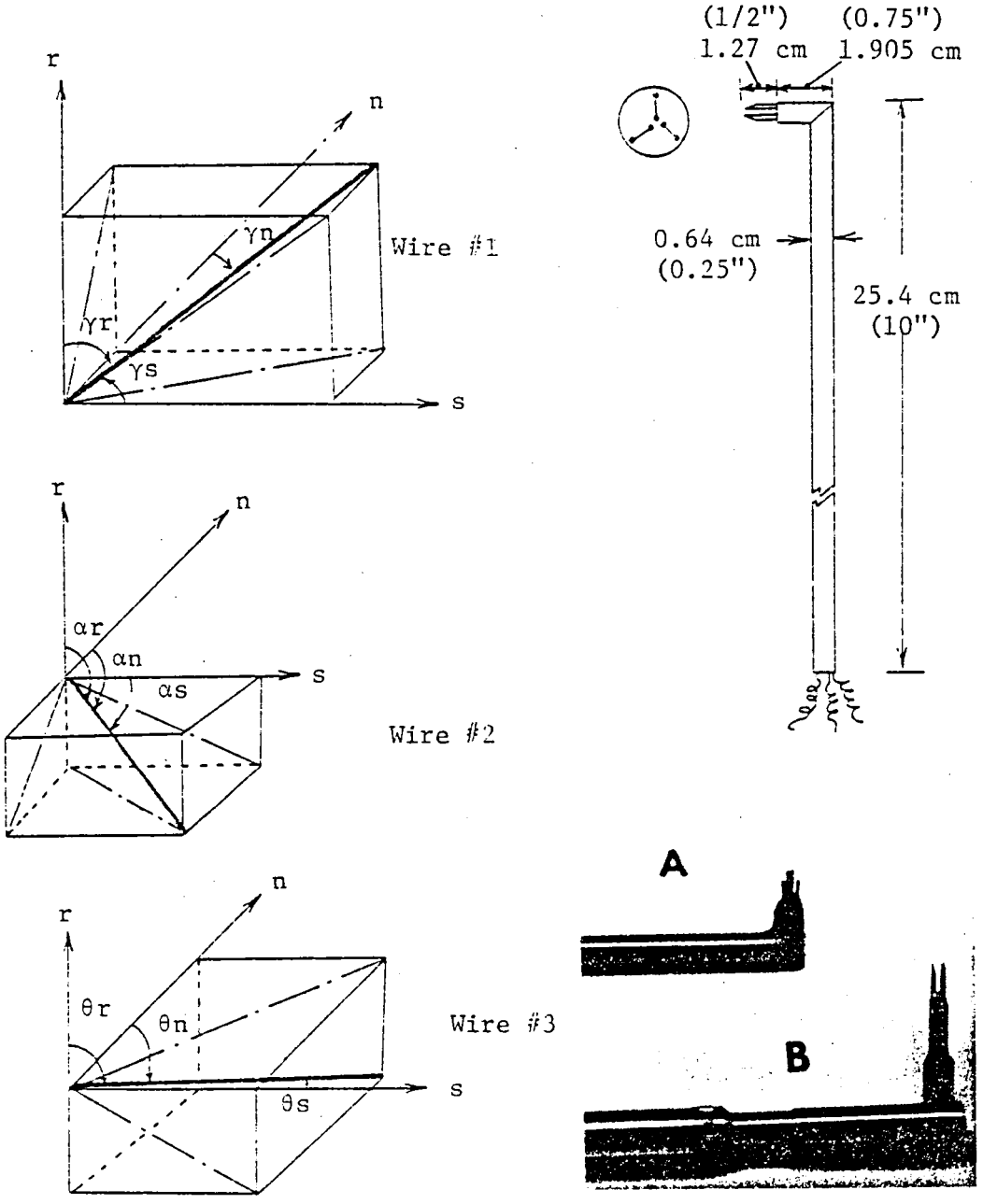

(For Details of Probe B, Refer to Reynolds (1978))

Figure 5. Three-Sensor Hot-Wire Probe for Axial-Flow Compressor Rotor-Wake Measurements

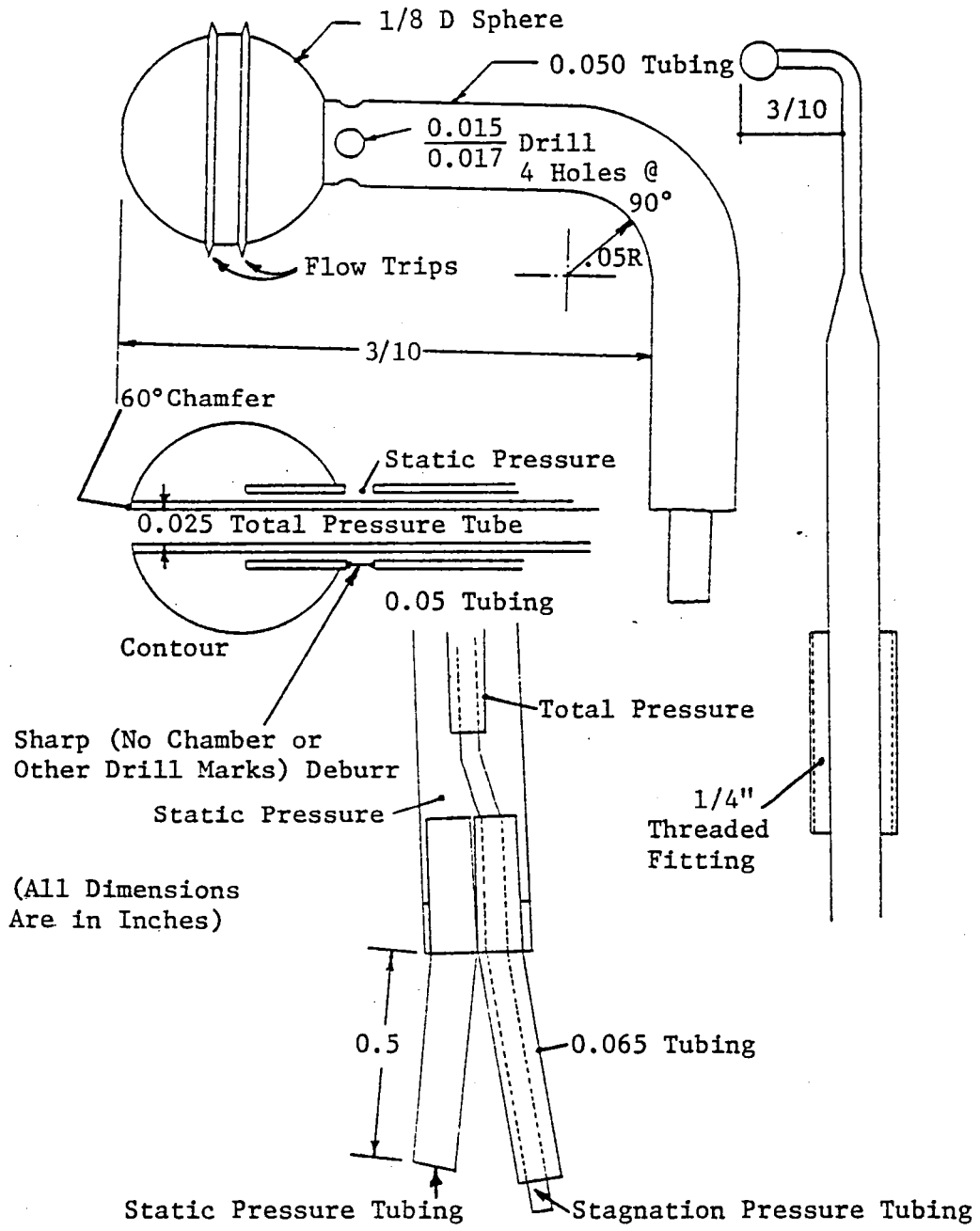

Figure 6. Spherical-Head Static-Stagnation Pressure Probe

(P) and the pressure p_w, it is possible to get the static pressure in the wake, which is given by:

$$p = \frac{p_w + kP}{1 + k} \quad . \tag{2}$$

The sphere-static-stagnation probe has been designed so that the k, which is known as the probe factor, is substantially constant at a value near 0.305 over the entire range of yaw and pitch angles.

The sphere-static-stagnation probe gives a time average pressure reading, as long as the characteristic velocity of the flow is such that their product is large compared to the sphere diameter. It should be realized that even though time averages of p and P may be obtained from the probe, the corresponding velocity magnitude may not be a correct time average of the velocity magnitude, since the velocity does not depend linearly on the pressure.

Wall vicinity effects might adversely affect the data from these probes. Experimental evidence has shown that a distance of at least three-sphere diameters should be maintained between the center of the sphere and the walls, and no obstacle should be placed in the wake of the sphere closer than seven sphere diameters from the probe to insure accuracy of the probe reading. The probe is calibrated in a known uniform flow and, therefore, the calibration shown in Figure 7, includes the aerodynamic interference effects. However, errors due to the probe immersed in shear gradients are not included.

2.5.3 Measurement stations

Rotating hot-wire data was taken at seven radial stations and at several axial stations at each of these radii. The measurement locations are tabulated in Table 3 (see Figure 2).

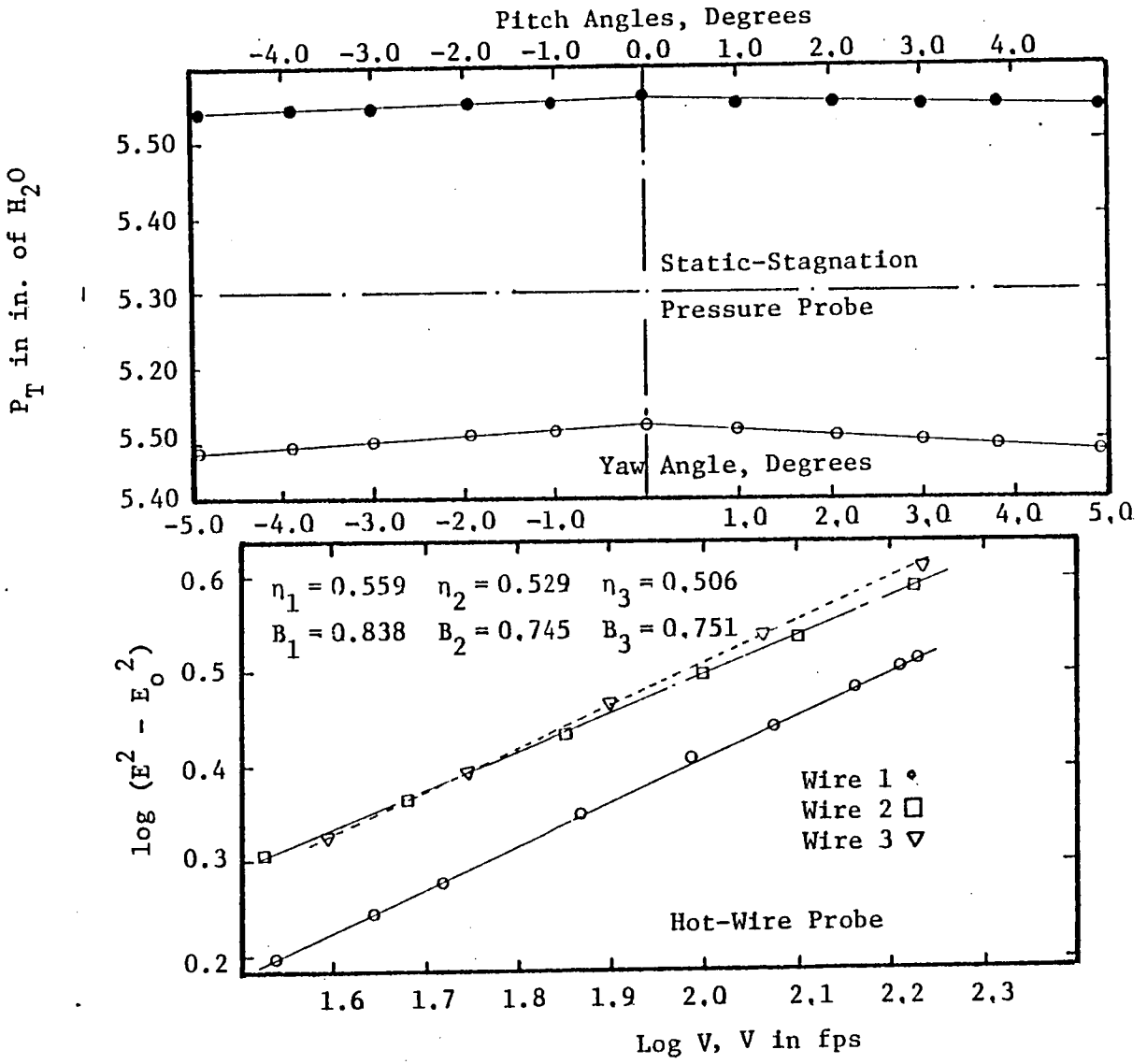

Figure 7. Pressure Probe and Hot-Wire Calibration

Table 3

Wake Measuring Stations

R	Chord m(inch)	Axial Location From Trailing Edge 2						Inlet Turbulence
0.9595	0.150(5.90)	0.0104	0.0417	0.124	0.240	0.458		0.5% (Axial Intensity/ Axial Vel.)
0.9324	0.147(5.80)	0.0104	0.0412	0.125	0.250	0.458		
0.8615	0.141(5.56)	0.0104	0.0417	0.125	0.208	0.417	0.625	
0.7973	0.137(5.40)		0.03125	0.146	0.229	0.375	0.563	
0.7297	0.134(5.26)	0.0104	0.0208	0.1354	0.219	0.354	0.5313	
0.6581	0.130(5.12)			0.1146	0.240	0.458	0.6875	
0.5676	0.128(5.02)			0.125	0.208	0.458	0.656	

Static pressure measurements were carried out at mid-radius and at other representative radial locations.

2.6 Signal Processing Equipment

Figure 8 illustrates the instrumentation used for processing the tri-axial hot-wire probe signals. The choice of the instrumentation was made so that the raw data from the experiment could be used directly in the data processing program developed by Gorton and Lakshminarayana (1976).

The output from the anemometer consists of three d.c. signals (a measure of mean velocity) and three fluctuating a.c. signals (a measure of turbulence). The d.c. signals were measured with a 5327B timer counter digital voltmeter up to an accuracy of 1 millivolt while the a.c. signals corresponding to intensity were read on a TSI 1060 RMS meter with a 100 second integration time. A model AD530 analog device sum and difference unit was used to evaluate the Reynolds stress component in the flow. The three sums and three differences were channeled through a DISA 52A35 channel selector switch and were read on a DISA D35 RMS meter with a 100 second integration time.

The turbulence spectral measurements were done using a UA-500 ubiquitous spectrum analyzer in conjunction with a HP 7044A x-y recorder.

A four-channel 3A74 type Tektronix storage oscilloscope was used in all the hot-wire measurements to visualize the magnitude of all three turbulent signals. The scope was also used in measuring the d.c. levels in the flow, which information was needed to set the tape speed and d.c. attenuation while taping the signals. A photograph of the instrumentation used is shown in Figure 9.

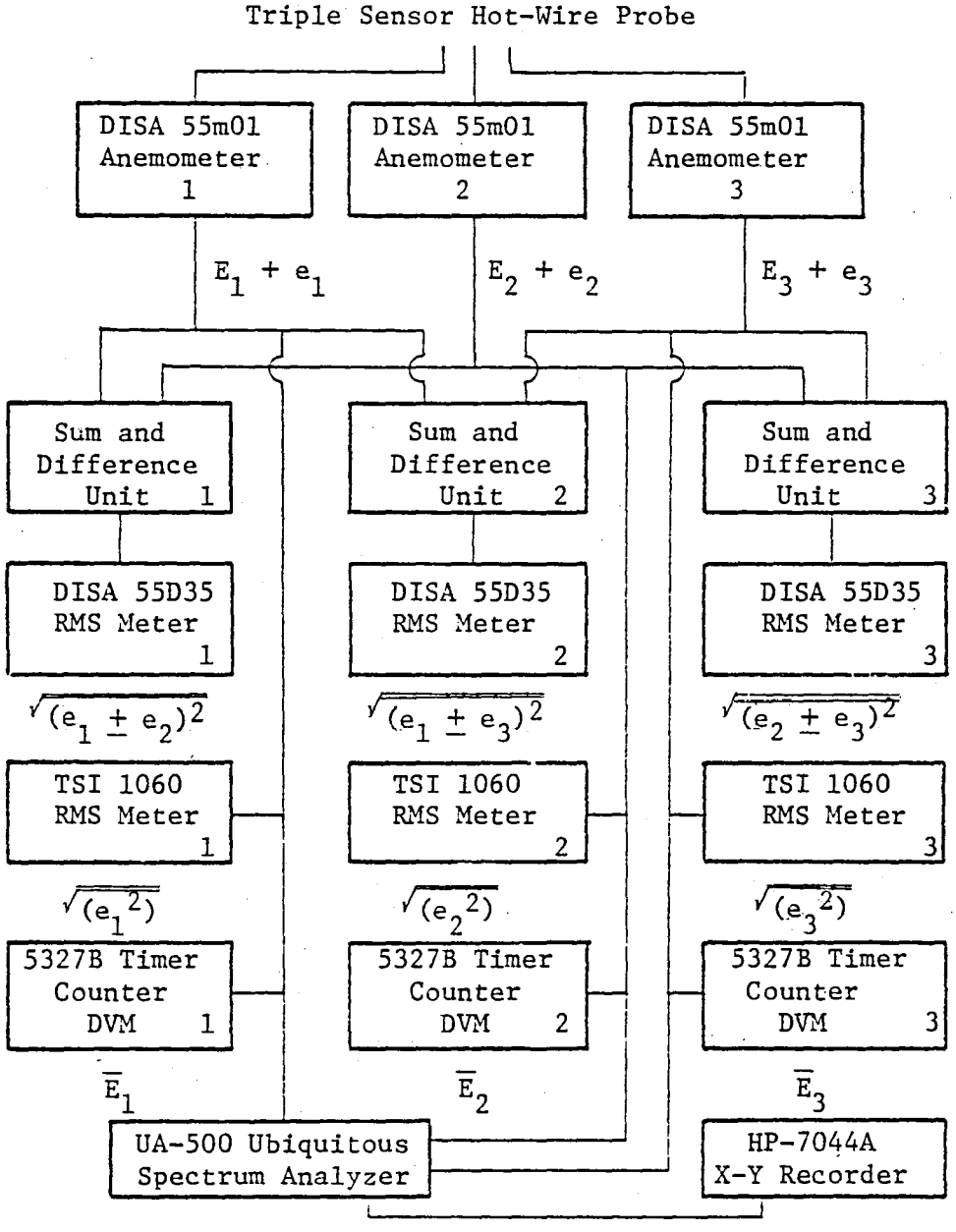

Figure 8. Schematic of Instrumentation for Rotating Hot-Wire Measurement

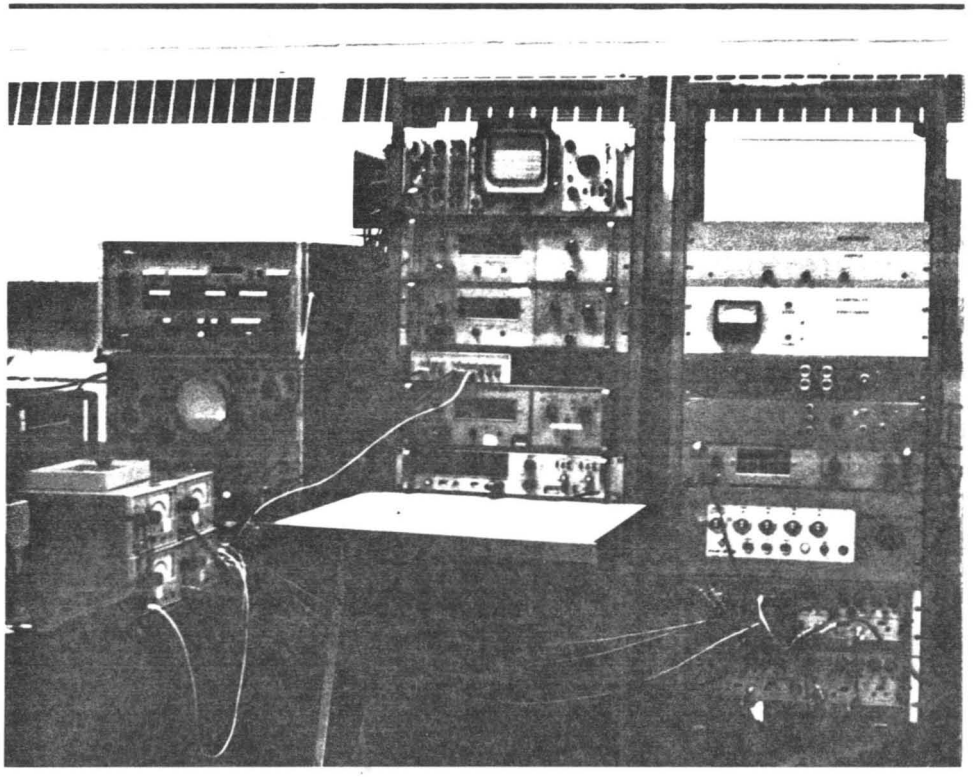

Figure 9. Instrumentation Set-Up for Rotating Hot-Wire Measurements

The data from the hot-wire E_1, E_2, E_3, $\sqrt{e_1^2}$, $\sqrt{e_2^2}$, $\sqrt{e_3^2}$, $\sqrt{(e_1 \pm e_2)^2}$, $\sqrt{(e_2 \pm e_3)^2}$, $\sqrt{(e_3 \pm e_1)^2}$ are used in the computer program developed by Gorton and Lakshminarayana (1976) to derive the values of the three components of mean velocity, turbulence intensities and shear stresses. Consistent with the assumptions made in the program (Appendix A1), the output yield velocities and turbulence quantities in the streamline coordinate system. These quantities were then transformed, using a subsequent coordinate transformation program, into the r-θ-z coordinate system where r was in the radial outward direction and z in the axial direction.

Hot-wire measurements are found to be very sensitive to the ambient conditions as well as to the physical constraints imposed on the probe. The type of anemometer employed dictates that correct cable lengths should be employed. The cable compensation unit served the purpose of compensating for the bridge unbalance caused by the differences in cable parameters. Procedures for adjusting these controls are given in the DISA 55M service and instruction manual.

Integration times for the rms meters and digital voltmeters were set at 100 sec. All spectra were taken at 10 KHZ on a 0 db scale (that is no attenuation). There was no gain on any of the instruments employed.

2.7 Peripheral Equipment

A low-turbulence calibration tunnel was used for the hot-wire and static-pressure probe calibration. The horizontal open jet tunnel had a square cross section and operated in the range of air velocities of 0 to 54 m/s (0 to 175 f/s). A spherical probe attachment built at The Pennsylvania State University was used to align the probe in the direc-

tion of the flow. It could also be used to traverse the probe across the jet or to be set at different pitch and yaw angles.

Available hot-wire-making techniques at the Department of Aerospace Engineering were used for all sensor replacements. The hot-wire elements were of 12μ copper plated tungsten wire. After the wire was made, dilute nitric acid was used to etch the wire (approximately middle one-third was etched to the desired resistance, 4 to 5 ohms). The over-heat ratio was calculated based on the "actual" resistance of the wire and dialed on the anemometer.

The sensor angles and the probe geometry were measured using a Bausch and Lomb stereo zoom microscope in conjunction with length and angle measuring eyepiece disks, with a least count of 0.002" at 3X power-pod magnification.

Chapter 3

EXPERIMENTAL RESULTS AND INTERPRETATION

3.1 Rotor In-Flow Conditions

The rotor-wake development and decay is strongly influenced by the rotor inlet-flow conditions. It is essential that an accurate knowledge of the flow-field ahead of the rotor be known before any attempt is made to study the flow-field downstream of the rotor. Both the mean velocity and turbulence structure ahead of the rotor and the pressure field upstream of the rotor are of importance.

In The Pennsylvania State University axial-flow compressor facility, the rotor is preceeded by an inlet-guide-vane assembly. Some typical pressure and velocity surveys were done upstream and downstream of the guide-vane to evaluate the effects of inlet-guide-vane on the mean velocity and turbulence structure.

3.1.1 Measurements upstream of the inlet-guide-vanes

Mean velocity and turbulence intensity profiles ahead of the inlet-guide-vanes were measured using a hot-wire and a spherical-headed static-stagnation pressure probe. Figure 10 shows the velocity that exists in the annulus just ahead of the inlet-guide-vanes. Also plotted in Figure 10 is the velocity derived from wall-static measurements. It is evident that the velocity variation across the annulus is less than two percent from hub-to-tip, indicating nearly uniform entry flow.

Figure 11 shows the spectrum of the wall-static pressure taken just ahead of the inlet-guide-vanes. It is seen that pressure fluctuations exists ahead of the guide-vanes and that most of the fluctuations are concentrated in the lower energy range (0 to 100 HZ). The reasons for

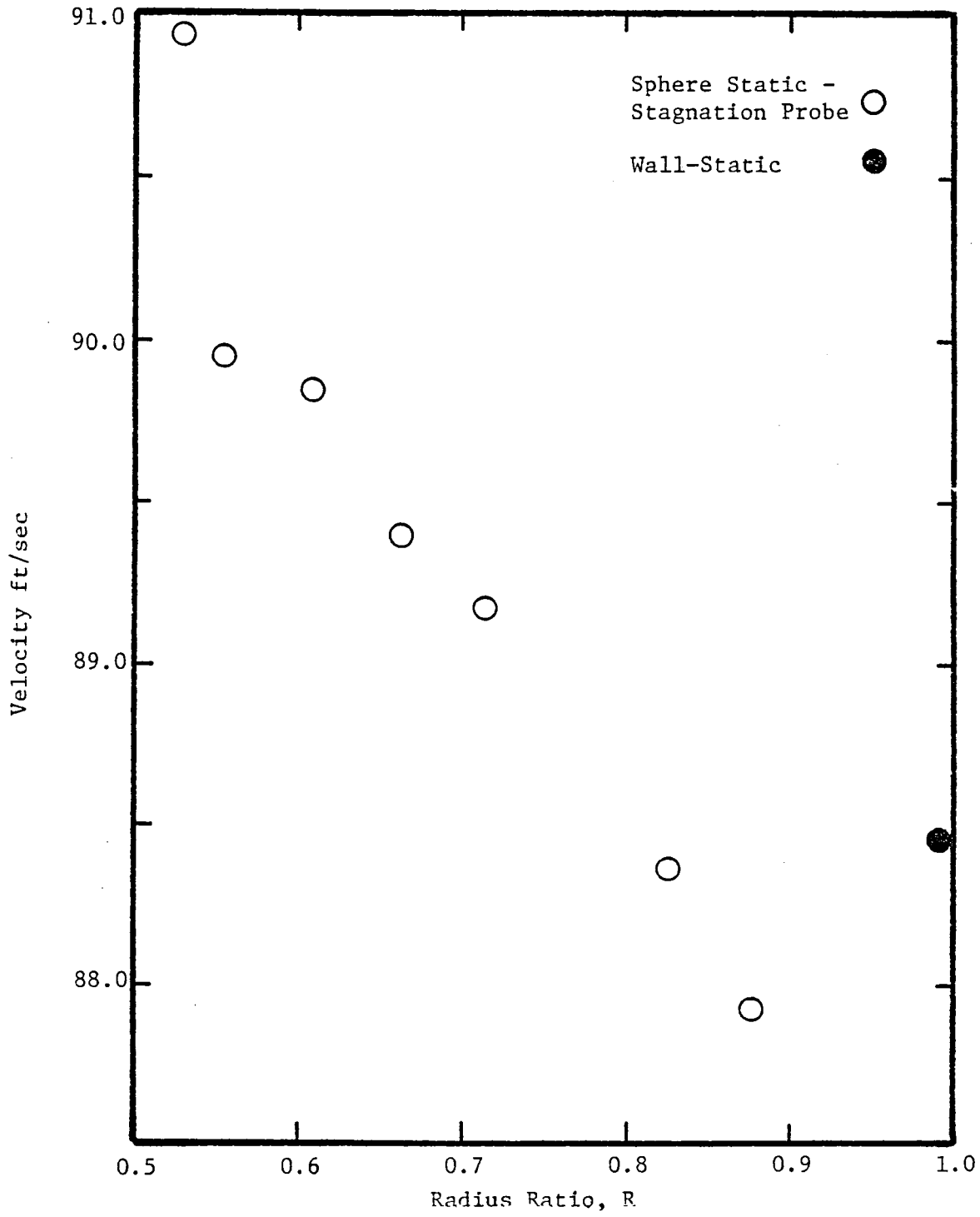

Figure 10. Velocity across the Annulus Upstream of the Inlet-Guide-Vanes

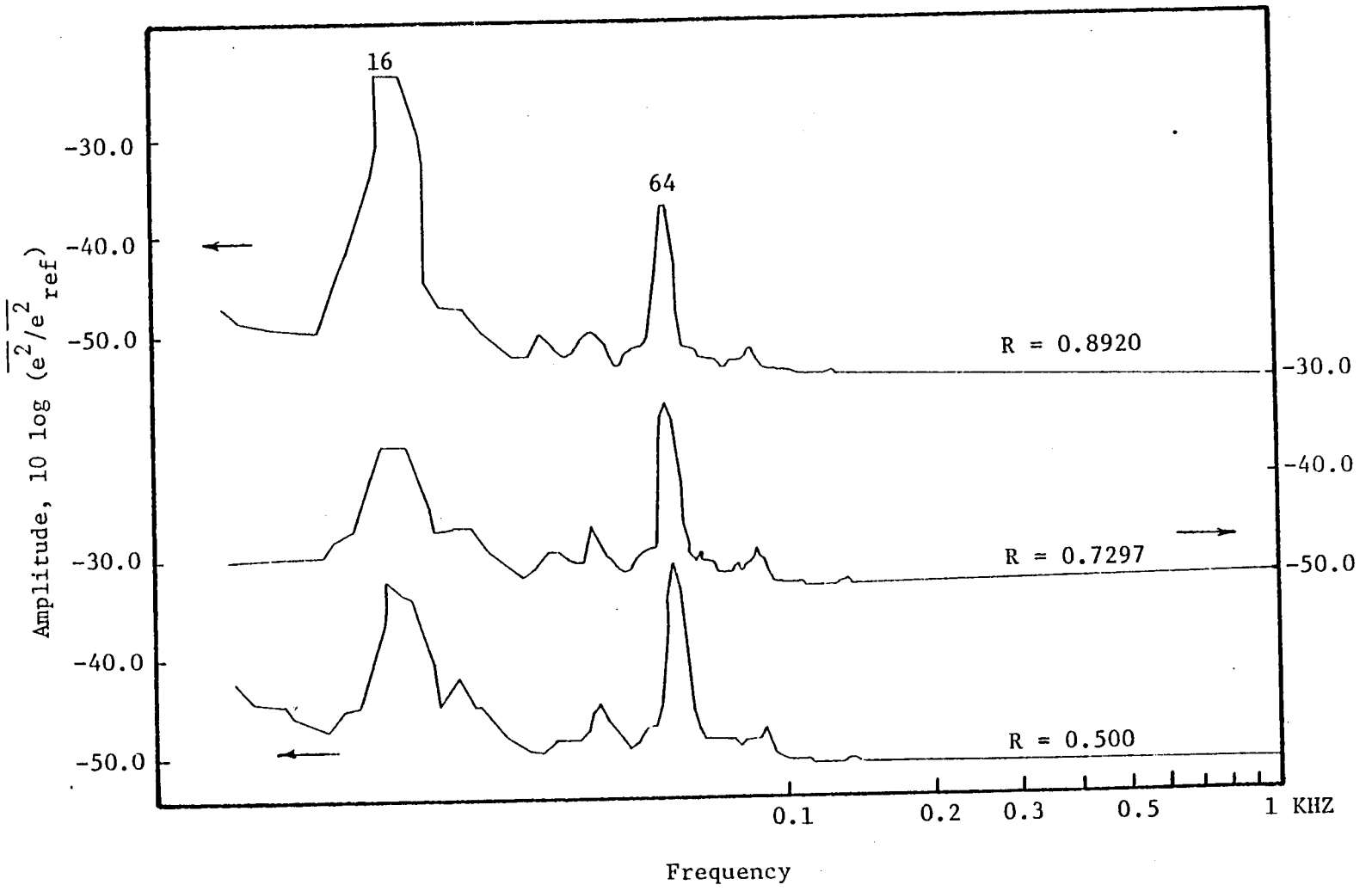

Figure 11. Spectrum of Static Pressure Fluctuations Upstream of Inlet-Guide-Vanes

the existance of such peaks are not known. They occur at the rotor frequency and its harmonics, and may be caused by vibration or the interaction of one of the strut wakes with the rotor.

3.1.2 Measurements downstream of the inlet-guide-vanes

An "X" hot-wire was employed for the inlet-guide-vane wake survey. An axial velocity defect (which is defined as the ratio of the defect of axial velocity to the free-stream axial velocity, v_z/V_{zo}) of 0.16 at 0.158 chords downstream becomes 0.03 at two chords downstream and an axial turbulent intensity of 30 percent at 0.158 chords reduces to less than two percent at two chords downstream. It is thus seen that the inlet-guide-vane wakes have decayed considerably before reaching the rotor. There is a three percent defect in velocity near the rotor inlet and as will be seen later, this will be picked up by the rotating hot-wire downstream of the rotor. Figures 12 and 13 show the plots of velocity and turbulence intensity downstream of the inlet-guide-vane. Detailed measurements of the inlet-guide-vane wakes have been reported by Lakshminarayana and Davino (1979).

The spectra of the wall static taken ahead of and downstream of the inlet-guide-vanes, Figure 14, do not show significant differences. So it can be assumed that the inlet-guide-vanes do not affect the pressure fluctuations.

It can thus be said that the position of the inlet-guide-vanes with respect to the rotor (1.5 rotor chords at tip and 2.03 rotor chords at hub) is such that no appreciable distortion in mean velocity is introduced because of the inlet-guide-vanes. A turbulence level of two percent before the inlet-guide-vane gets amplified to about three to four

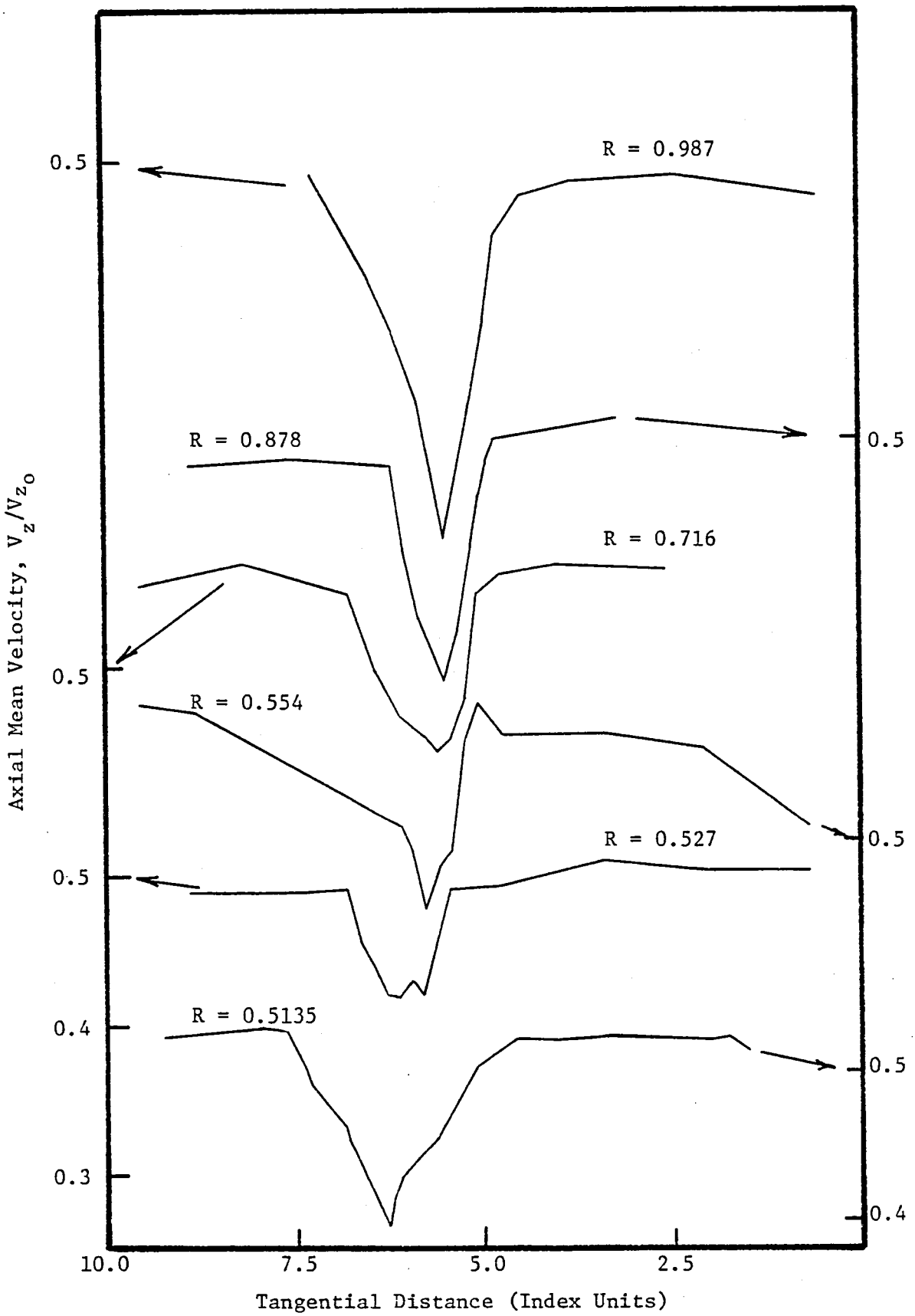

Figure 12. Tangential Variation of Axial Velocity behind Inlet-Guide-Vanes, Z = 0.0417, ϕ = 0.56

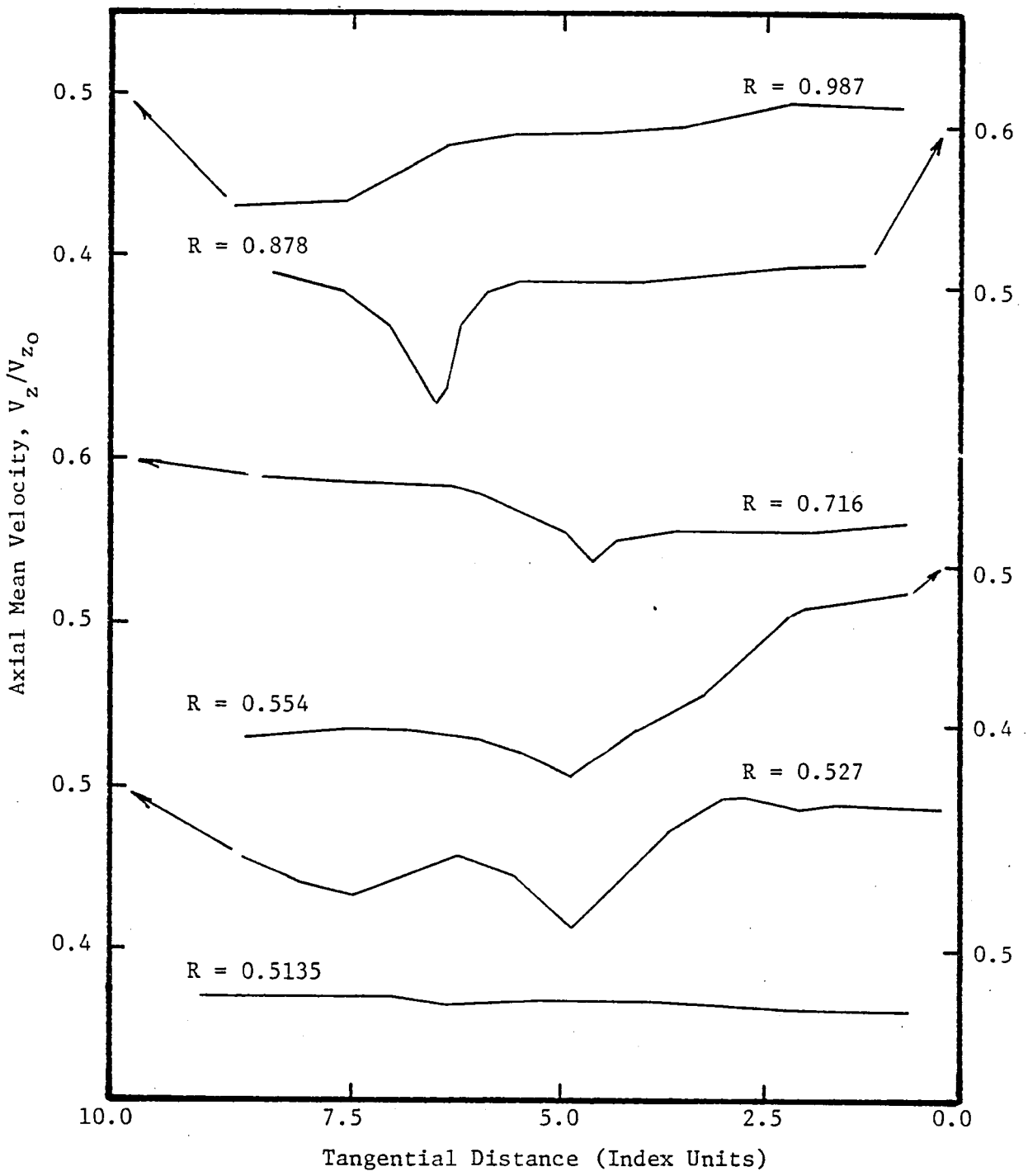

Figure 13. Tangential Variation of Axial Velocity behind Inlet-Guide-Vanes, Z = 1.00, ϕ = 0.56

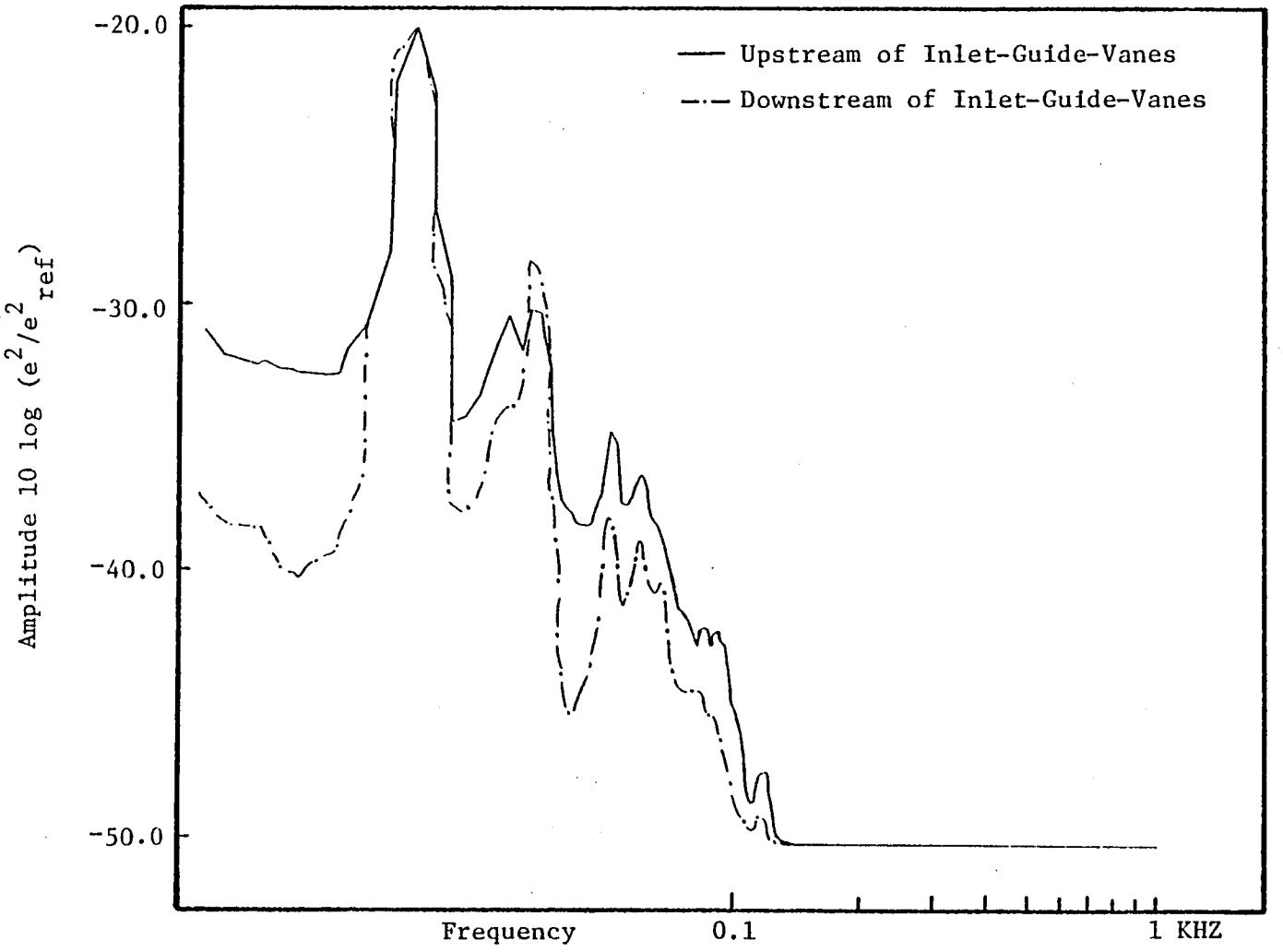

Figure 14. Spectrum of Wall-Static Pressure Fluctuations Upstream and Downstream of Inlet-Guide-Vanes

percent after the vanes and this might add up to the overall turbulence level of the rotor-wake.

3.2 Rotor-Wake Velocity Profiles

Rotating tri-axial hot-wire probe measurements were used to study the properties of the rotor-wake of a moderately loaded compressor-rotor in the trailing edge, near-wake and far-wake regions. The trailing-edge region is defined as the region very close to the blade trailing-edge where the radial velocities show trends similar to that of a trailing vortex system; a near-wake region is defined as the region where the velocity defects are of the same order of magnitude as the free-stream velocity. The far-wake region is defined as the region where the velocity defects are very small. Mean velocity, turbulence intensity and Reynolds stress profiles are studied in this section. The effect of loading, blade incidence, annulus- and hub-wall boundary layer effects on the profile was also studied. To compliment the hot-wire measurements, static-stagnation pressure surveys were also taken and velocity from pressure measurements was compared with those obtained from hot-wire measurements.

All velocities discussed in this section are relative velocities and are normalized to the corresponding free-stream axial-velocity, unless otherwise specified.

3.2.1 Axial mean velocity

The variation of the axial velocity across the wake at various downstream and radial locations is shown plotted in Figures 15 through 20. The tangential distance is normalized by the semi-blade spacing $(\frac{2y}{s})$. It is clear that the wake profiles are asymmetrical about the wake center

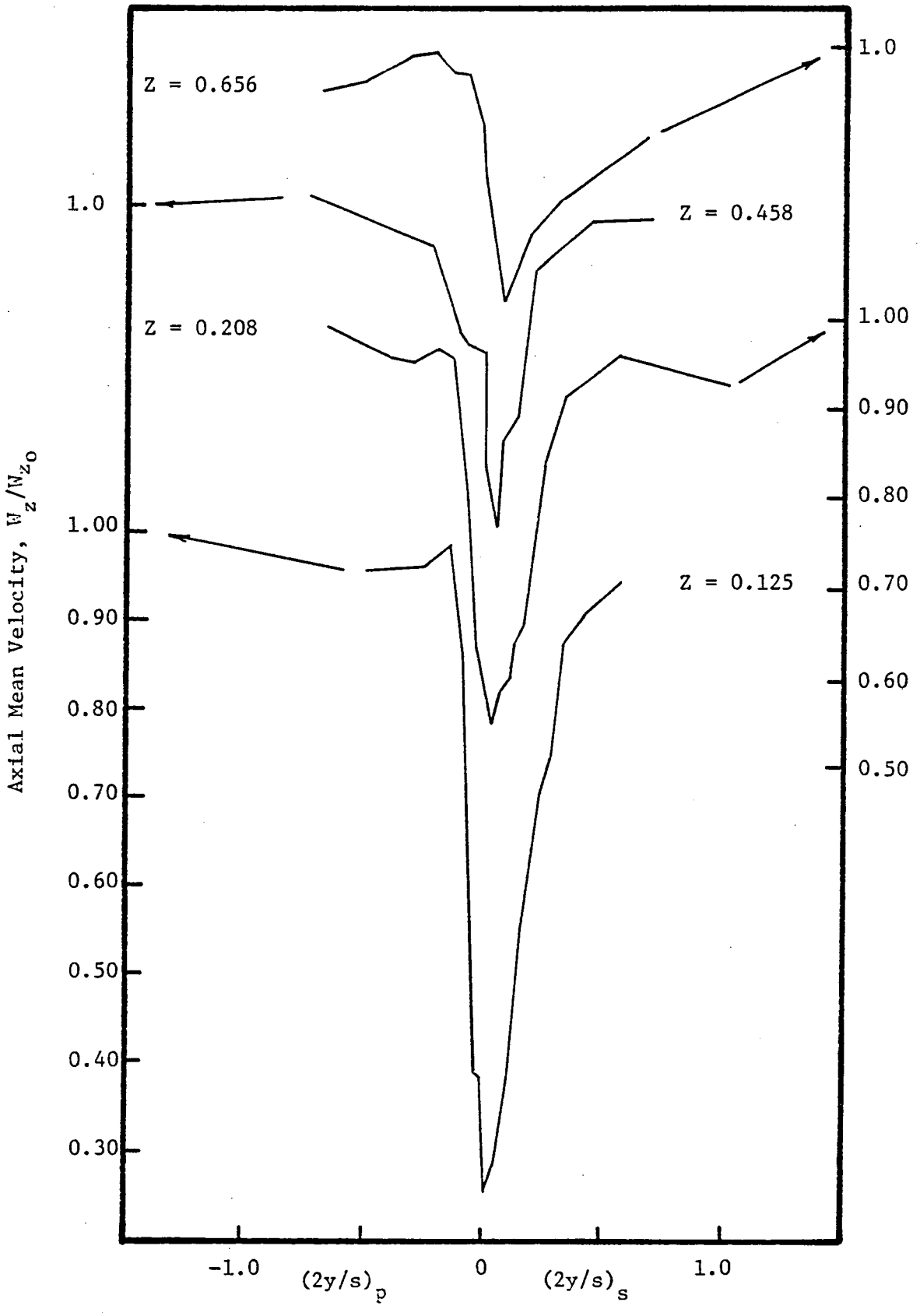

Figure 15. Axial Mean Velocity Profiles, R = 0.5676, ϕ = 0.56

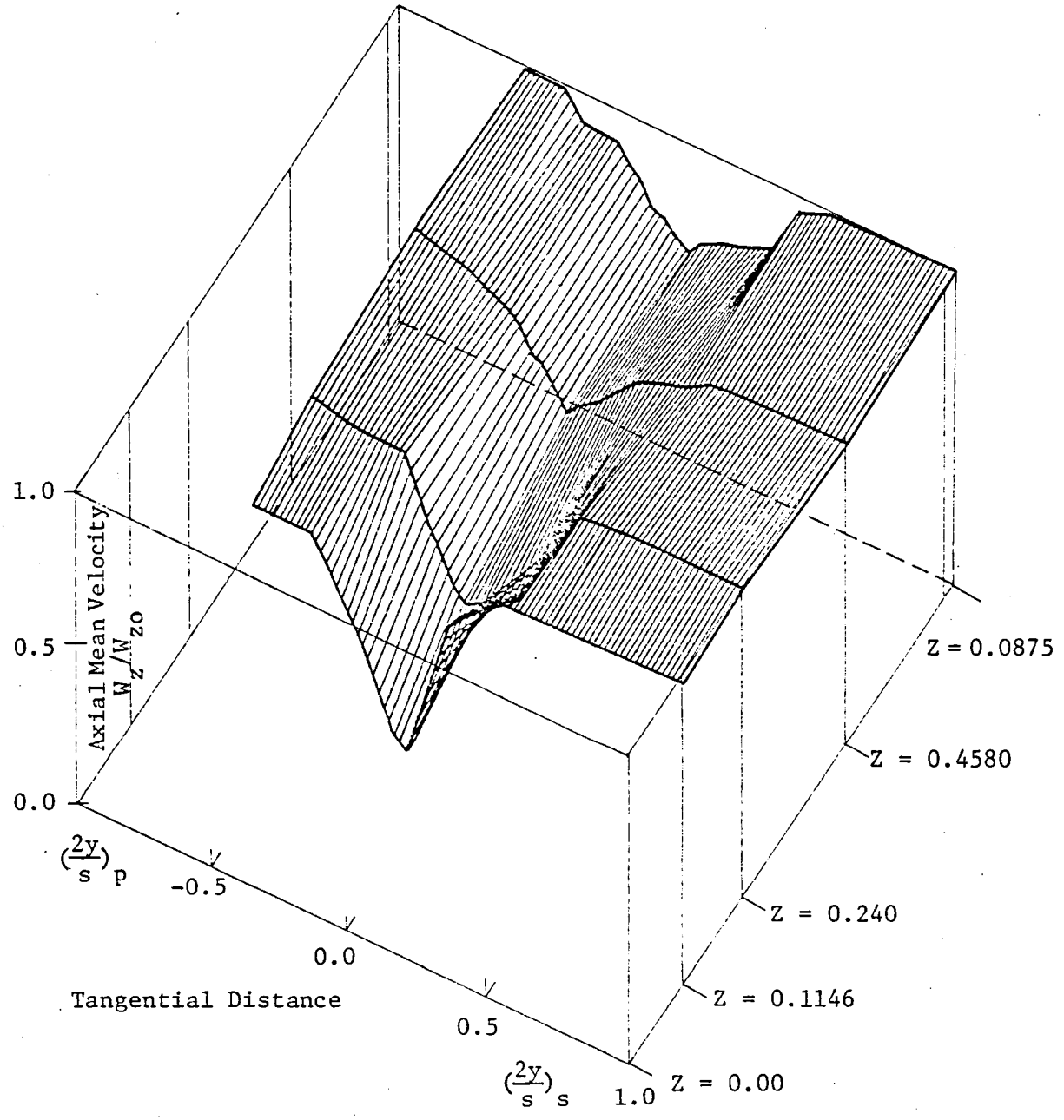

Figure 16. Three-Dimensional Plot of Axial Velocity Profiles, R = 0.6581, ϕ = 0.56

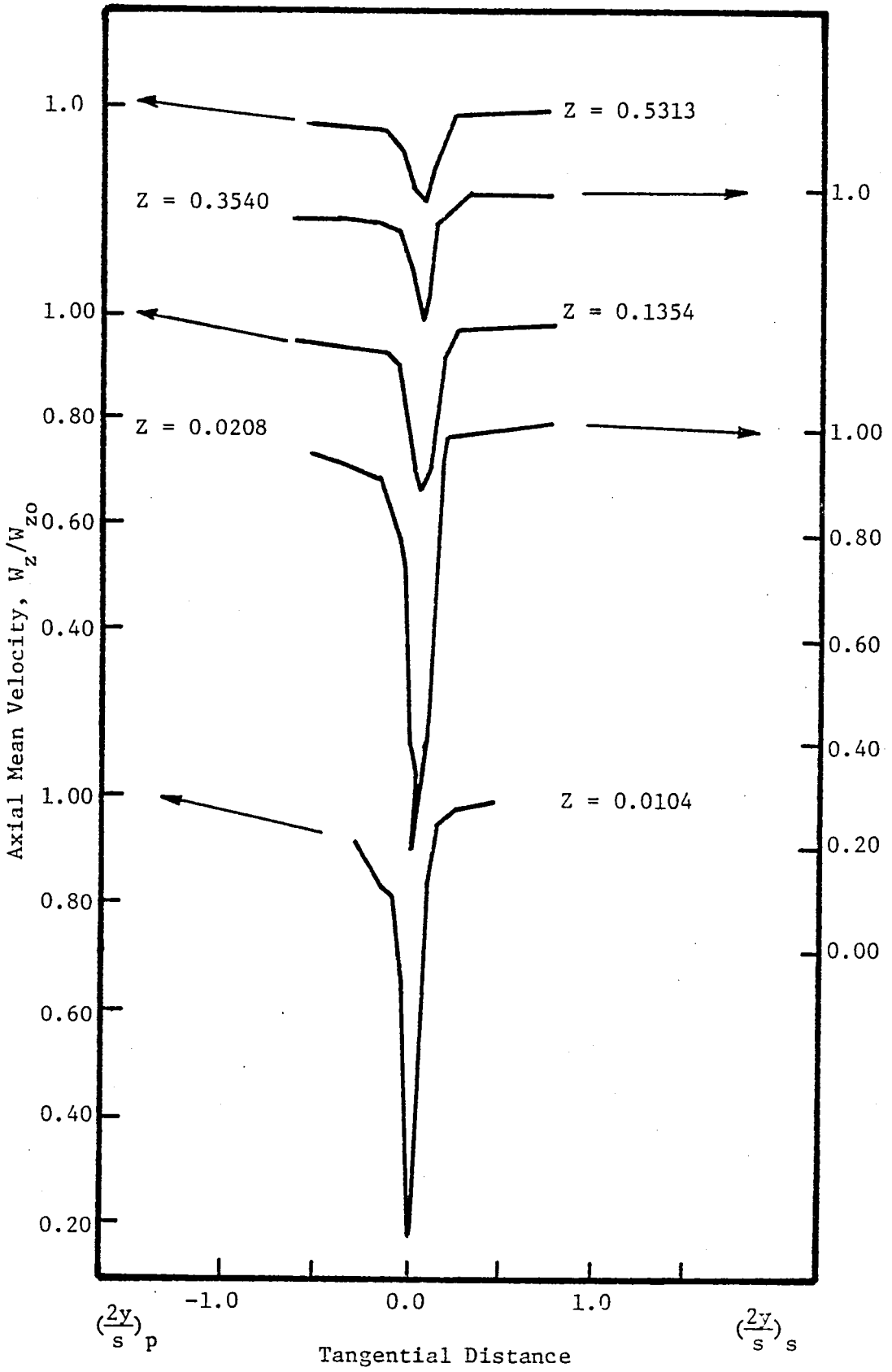

Figure 17. Axial Velocity Profiles, R = 0.7297, ϕ = 0.56

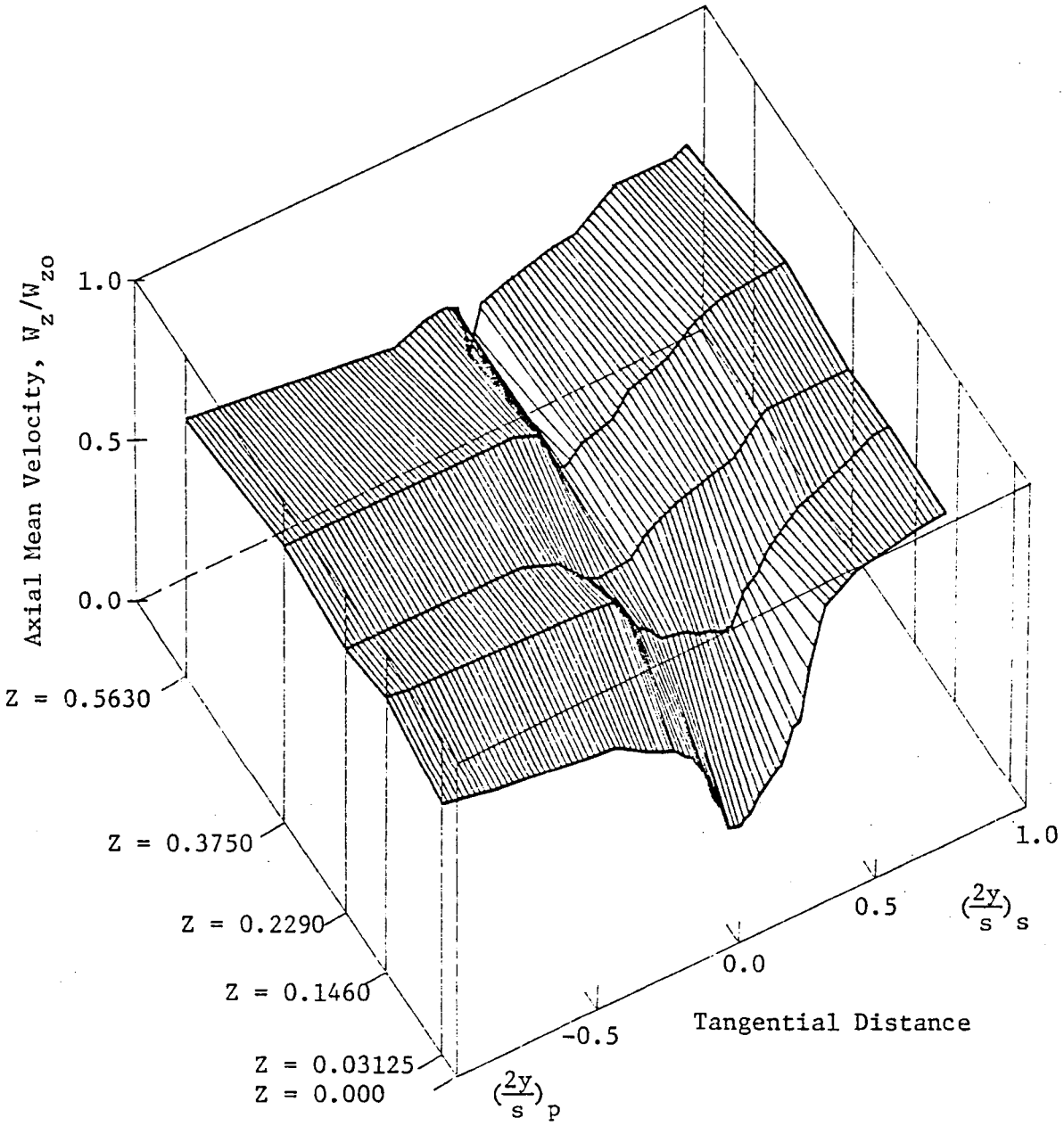

Figure 18. Three-Dimensional Plot of Axial Velocity Profiles, R = 0.7973, ϕ = 0.56

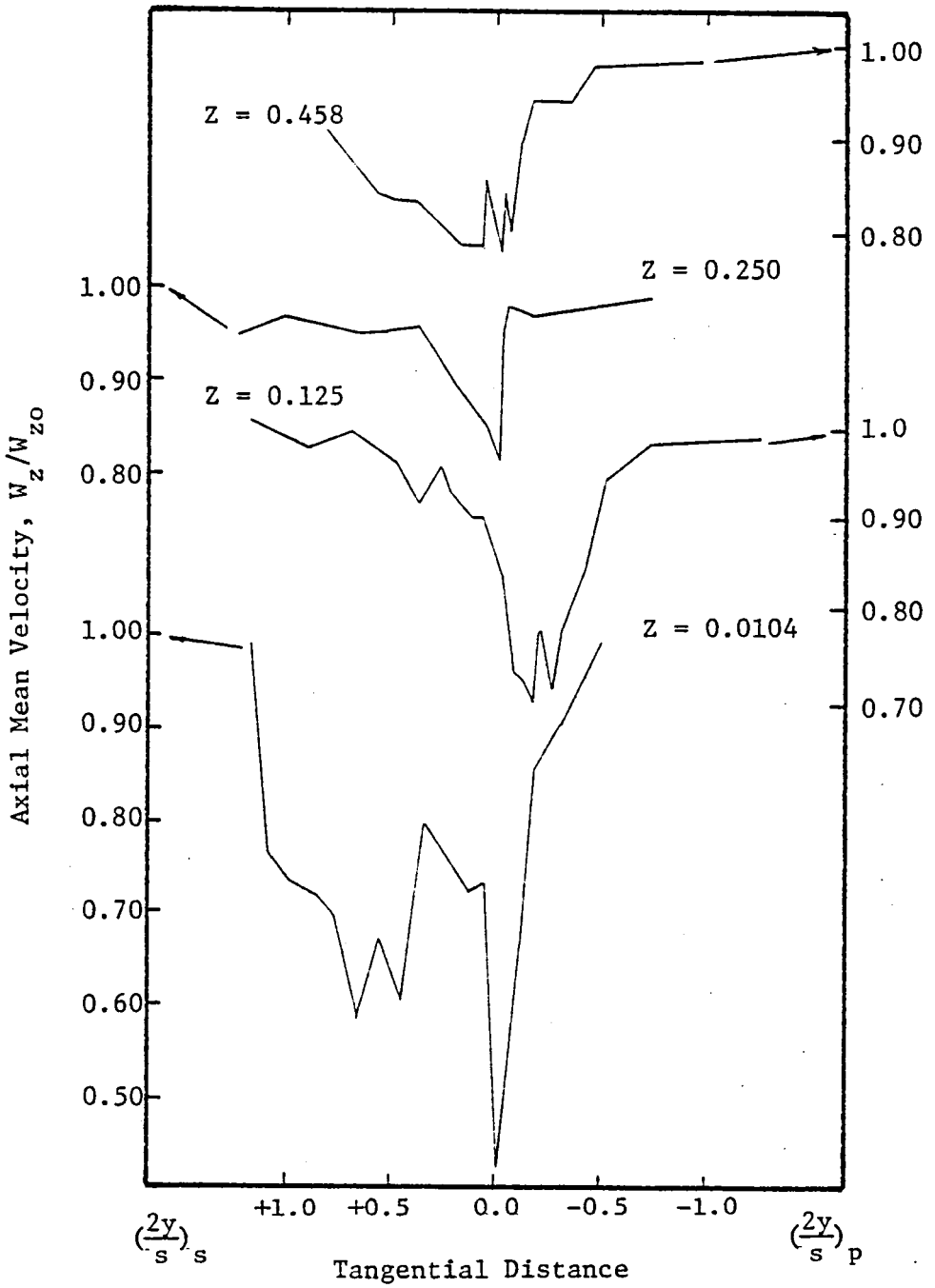

Figure 19. Axial Velocity Profiles, R = 0.9324, ϕ = 0.56

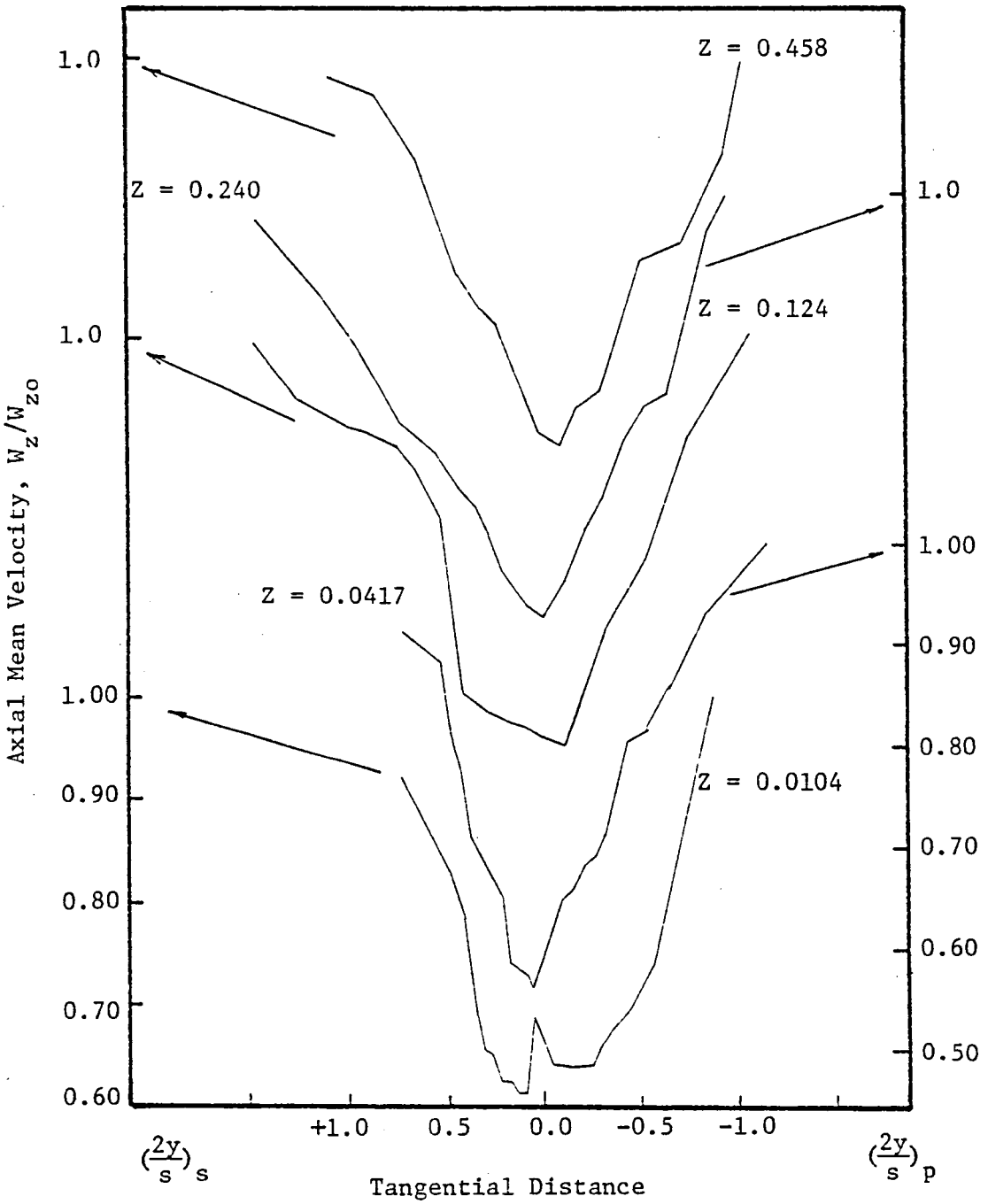

Figure 20. Axial Velocity Profiles, R = 0.9595, ϕ = 0.56

indicating the differential growth of boundary layers on the two surfaces of the blade. This is to be expected as the suction-surface boundary layers are thicker than the pressure-surface boundary layers. This asymmetry is maintained even at half-a-chord downstream of the blade trailing-edge. The existance of pressure gradients (inviscid effects) across the passage immediately downstream of the blade trailing-edge is reflected in the free-stream velocity distributions, where the suction-surface velocity is higher than the pressure-surface velocity (Figure 17). This effect persists to about 0.3 chords downstram. Velocity profiles outside and inside of the annulus- and hub-wall boundary layers exhibit characteristics which are quite different. Not only the velocity profiles but also the decay rates are different.

Variations of axial velocity across the wake and at various downstream locations for the radii R = 0.6581 and 0.7973 are shown as three-dimensional plots in Figures 16 and 18. Figures 15, 17, 19, and 20 shows the variations of the axial velocity profiles for R = 0.5676, 0.7297, 0.9324 and 0.9595, respectively. The wake profiles at R = 0.6581, 0.7297, and 0.7973 are outside annulus- and hub-wall boundary layer regions. Wake profiles and decay are fairly well behaved in these regions. Because of wake spreading and mixing with free-stream as well as interchange of momentum and energy on either side of the wake, the wake shows a tendency to become symmetrical at far downstream locations.

In the trailing-edge region, for the radius R = 0.7297 (Figure 17), the wake defect (w_z/W_{zo}) is 0.88 which reduces to 0.2 at Z = 0.5313. For the wake at R = 0.7973, a defect of 0.71 at Z = 0.03125 reduces to 0.24 at Z = 0.5625. As the hub-wall is approached the decay rate decreases as shown at the radius R = 0.6581 (Figure 16), where a defect of 0.66 at

Z = 0.1146 reduces to 0.33 at a Z-location of 0.6880. The same trend is observed even when the annulus-wall boundary layer is approached. So the wakes decay differentially in the radial direction.

Because of the radially outward transport of mass, momentum, and energy in the boundary layer, the wakes at the hub are expected to be thinner, gradually increasing towards the tip. But in the present case the wakes at the lower radius are as thick as those at the higher radii. The probable reason for this is that the drag coefficient at the root is higher than that at tip due to larger turning and consequently offset the effect discussed earlier. One other possible reason is the existance of inward radial velocity discussed later in this section.

For the wake in the trailing-edge region the gradients in the tangential direction are very large as can be clearly seen in Figure 17. This characteristic for the wake results from the development of the boundary layer flow as it moves over the rotor-blade and transforms into the wake at the trailing-edge. In the far-wake region the gradient becomes considerably smaller because of the wake spreading and mixing with the free-stream. The steep gradient in the trailing-edge region represents highly unstable and developing flow conditions. There is another interesting feature that can be observed in the trailing-edge region. Here the pressure-side wake is thicker than the suction-side wake. One probable cause of this is that the radial inward velocities on the pressure-surface, observed experimentally, will cause a larger accumulation of boundary layer on the pressure-surface compared to that on the suction-surface. As the wake travels downstream, the radially inward velocities decrease, and beyond 0.15 chord downstream, only

radially outward flow exists. In such a situation the suction-side of the wake is thicker and follows the usual trend.

The effect of blade loading can be observed in the near-wake plots shown in Figure 17, for R = 0.7297. The wakes are highly asymmetrical because of loading and it is noted by comparing Figure 17 with Figures 4 and 5 of Reynolds, et al. (1978). From the Figures 4 and 5 of Reynolds, et al. (1978) we note that the wakes become approximately symmetrical at 0.271 chords downstream, where as in the present case the wakes still tend to be asymmetrical at half-a-chord downstream. Thus the effect of blade loading is to sustain the asymmetry to much larger extent downstream of the blade trailing-edge.

Blade loading not only makes the velocity profiles asymmetrical, but it also increases the velocity defect and slows down the decay rate. Thus at mid-radius (comparing Figure 17 with Figures 4 and 5 of Reynolds, et al., 1978) we note that at about the same Z-location (say Z = 0.028) a heavily-loaded-blade gives a much deeper wake compared to that of a lightly-loaded-blade. The decay of the heavily-loaded-rotor-wake is also slower. A velocity defect (w_z/W_{zo}) of 0.16 exists at half-a-chord downstream of the present rotor compared to that of a lightly-loaded-fan wake of Reynolds, et al. (1978) where the defect is 0.2 at Z = 0.271.

The wake in the annulus-wall region exhibits complex behavior. At Z = 0.0104 and R = 0.9595, Figure 20, the velocity defect is 0.34 which initially increases to 0.40 at Z = 0.0417 beyond which it decreases very slowly. This may be attributed to the tip vortices and secondary flow as well as annulus-wall boundary layer in this region. As the vortex grows in strength immediately behind the trailing-edge it adds to the overall defect in the wake. Beyond Z = 0.0417, the strength of the

vortex decreases and consequently the usual wake behavior is seen. Not only the decay of mean velocity defect is different but also the profile is different. As seen from Figure 20 we note that the wake covers the entire blade passage and hence reflects the effect of leakage and secondary flow on the wake. The secondary flow not only distorts the wake profile but also has the effect of slowing down the decay.

The existence of large wake-width in the tip region which is attributed to the leakage and secondary flows can be explained as follows: The effect of secondary and leakage-flow is to increase the blade boundary layer thickness on the suction-side. This effect can be seen at Z = 0.0104 and R = 0.9595 (Figure 20). The profile becomes nearly symmetrical beyond Z = 0.124. The presence of an additional dip in the profile at Z = 0.0104 and R = 0.9324 (Figure 19) seems to indicate the presence of vortices. Since this vortex is located closer to the pressure-surface, it may be either the scraping vortex or the secondary flow vortex. This radial location is at the edge of the annulus-wall boundary layer.

For the wake inside the hub-wall boundary-layer, Figure 15, the wake decay is comparatively slow. This might be due to the complex interaction of the wake with the hub-wall boundary layer. It is also seen that the wake spread is not appreciable, indicating that the spread of the wake is greatly altered by the hub-wall boundary layer.

3.2.2 Tangential mean velocity

Variations of the tangential mean velocity across the wake at various downstream and radial locations are shown plotted in Figures 21 through 26. As in the case of axial velocity, the tangential distance is noramlized by the semi-blade spacing.

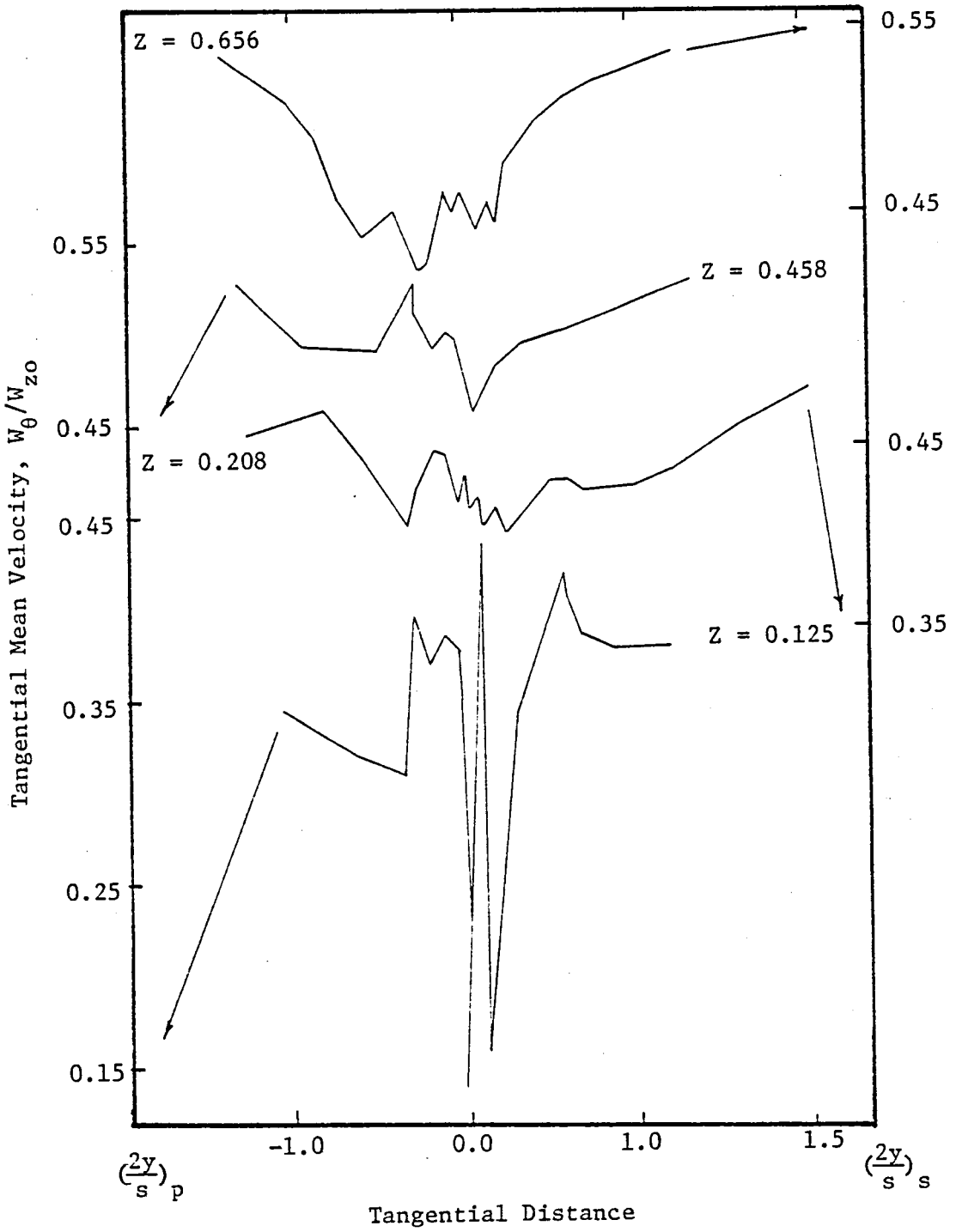

Figure 21. Tangential Velocity Profiles, R = 0.5676, ϕ = 0.56

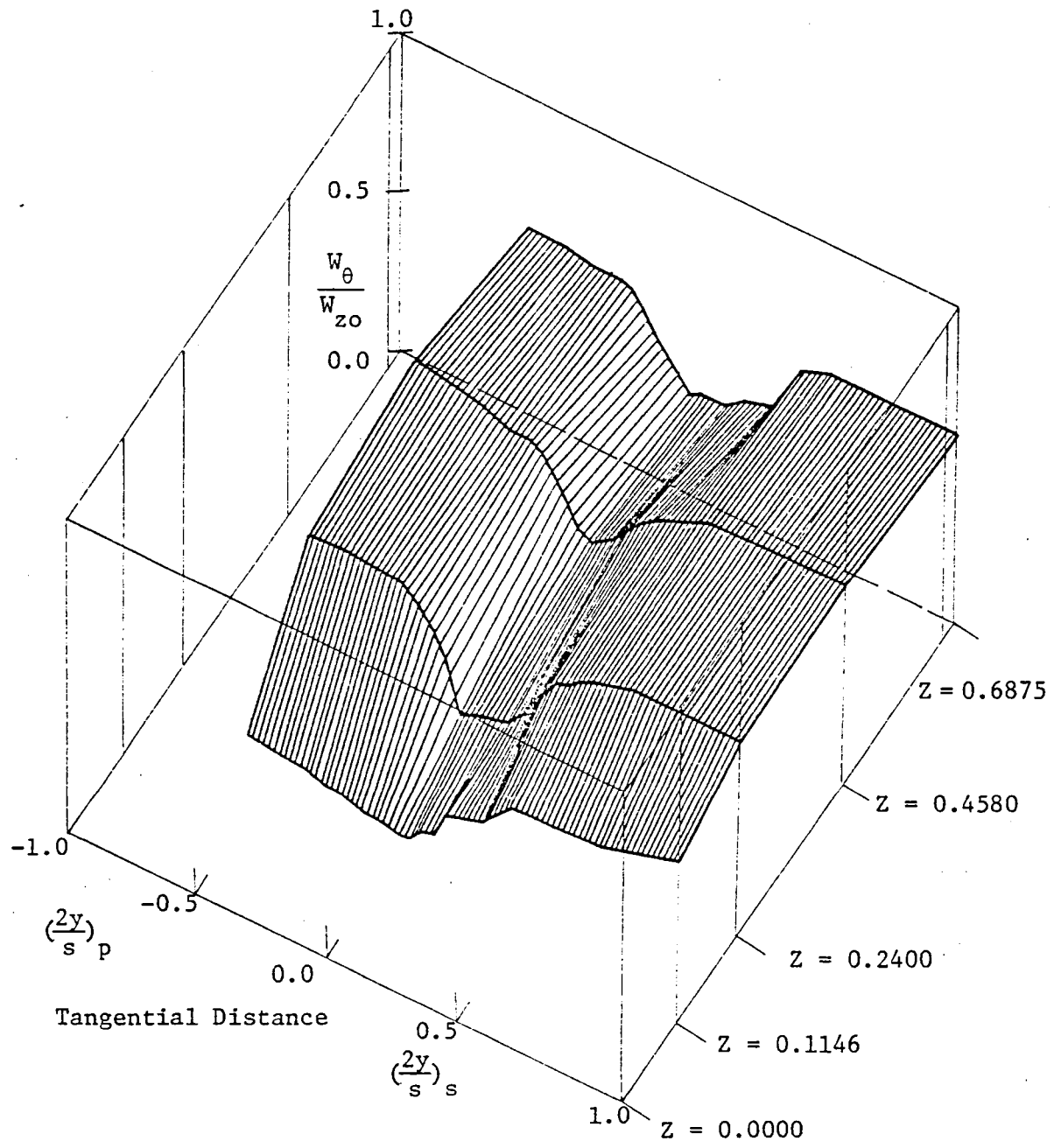

Figure 22. Three-Dimensional Plot of Tangential Velocity Profiles, R = 0.6581, ϕ = 0.56

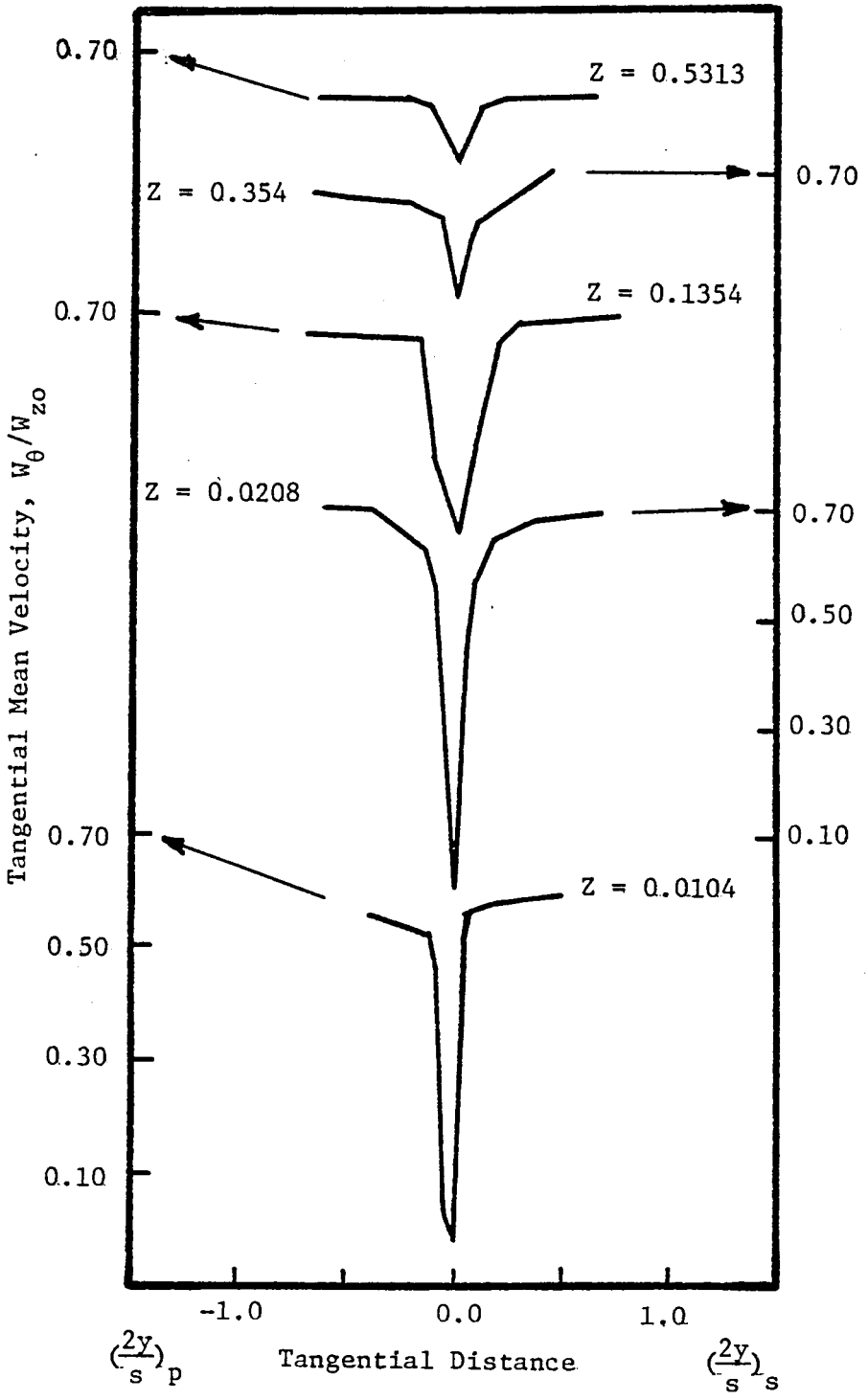

Figure 23. Tangential Velocity Profiles, R = 0.7297, ϕ = 0.56

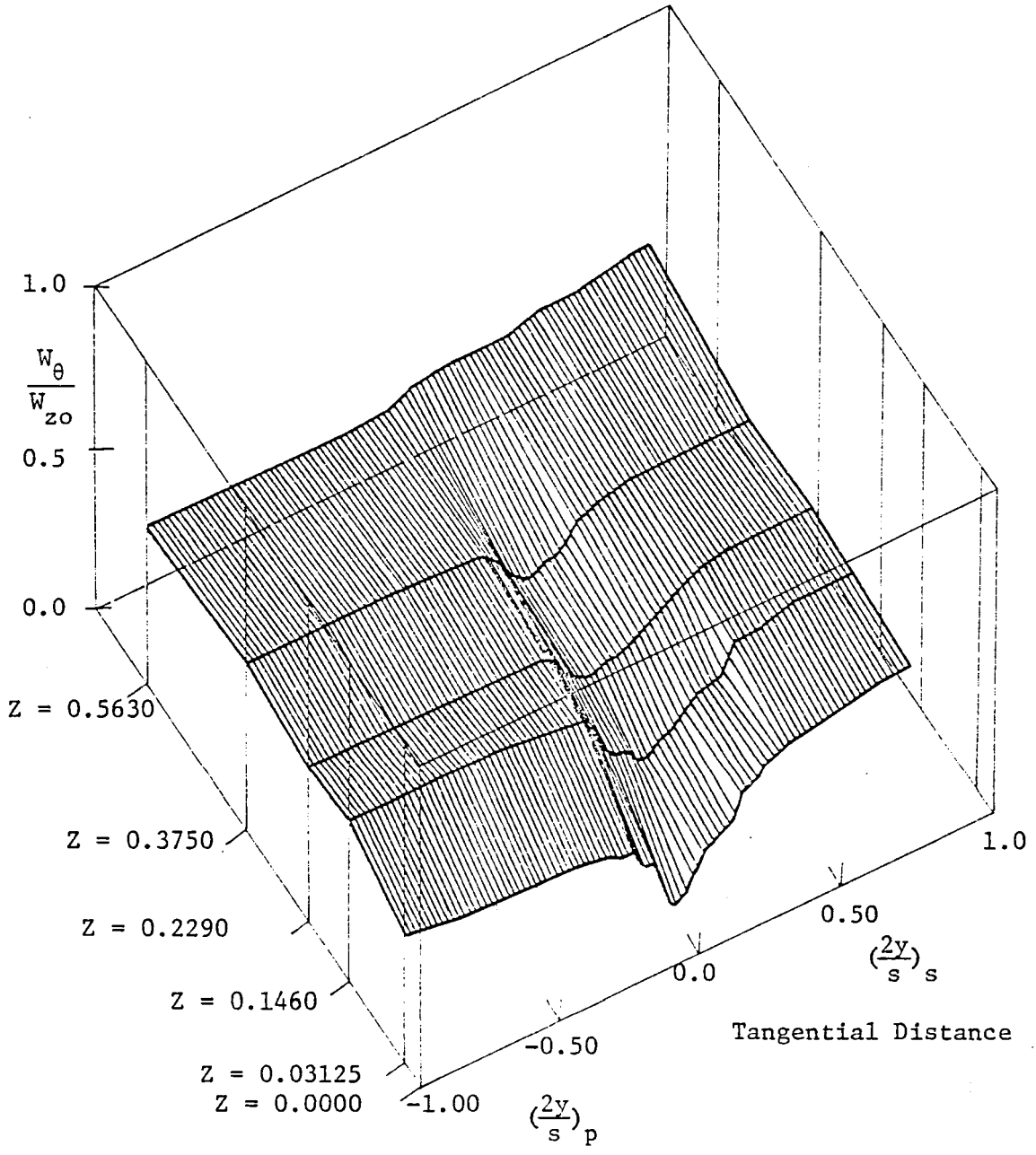

Figure 24. Three-Dimensional Plot of Tangential Velocity Profiles, R = 0.7973, ϕ = 0.56

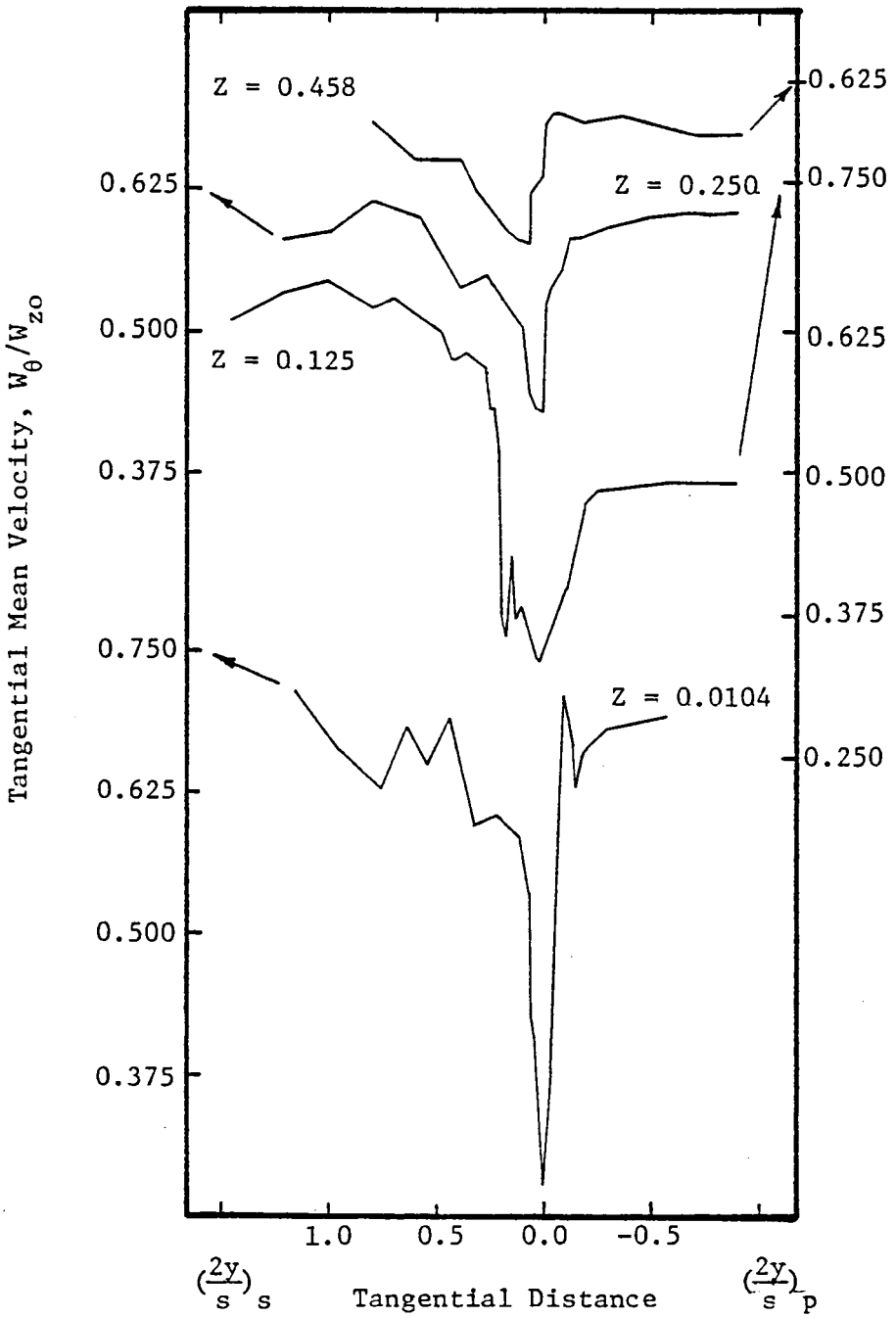

Figure 25. Tangential Velocity Profiles, R = 0.9324, ϕ = 0.56

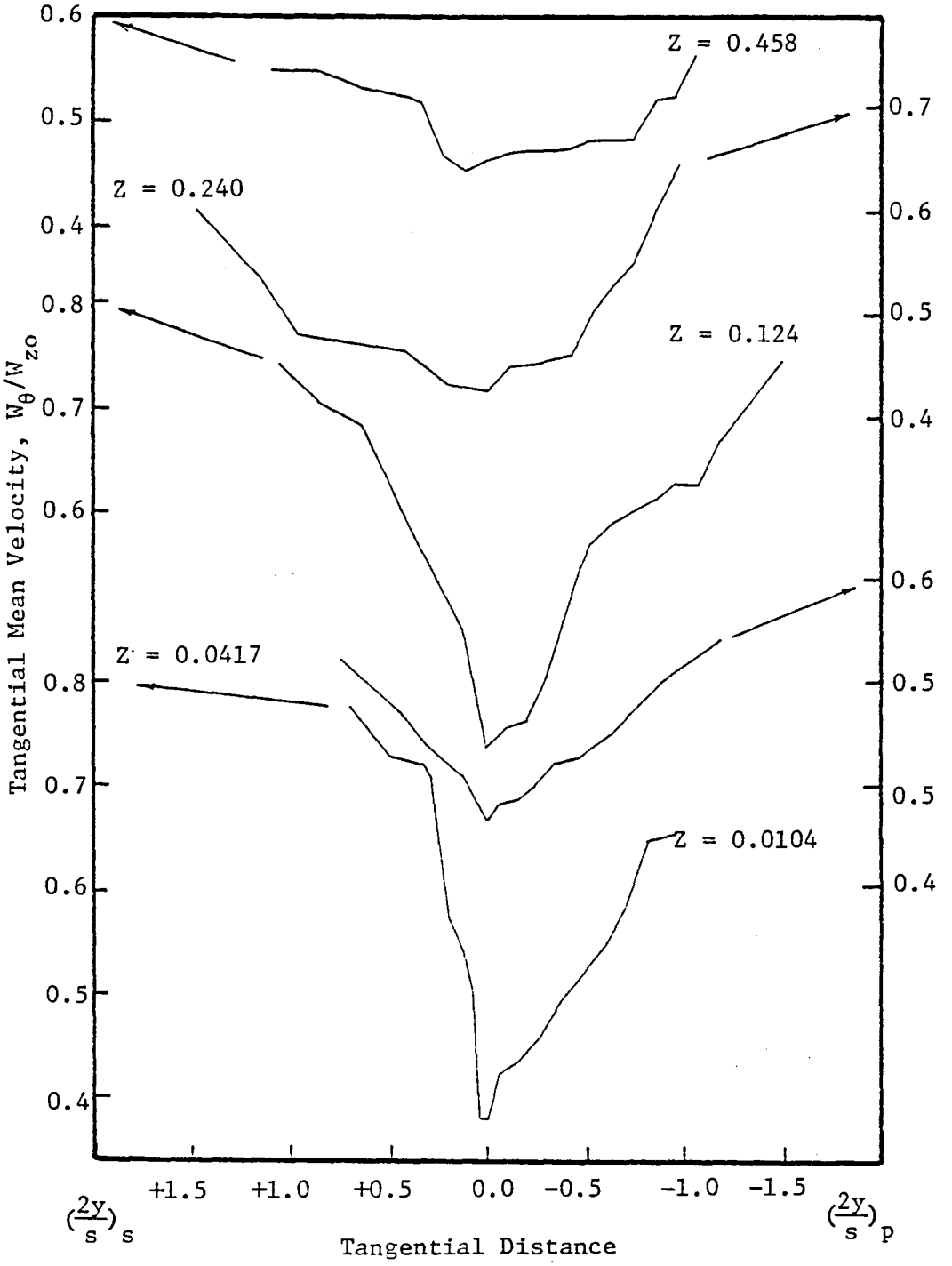

Figure 26. Tangential Velocity Profiles, R = 0.9595, ϕ = 0.56

For the wakes outside the annulus- and hub-wall boundary layers represented by the radii R = 0.6581, 0.7297, and 0.7978 it is found that the tangential velocity defects are greater than axial velocity defects. At R = 0.7297 (Figure 23) and at Z = 0.0104 the defect is almost 0.9 dropping off to about 0.2 in half-a-chord downstream. The same type of trend is observed for the other radii, R = 0.7973 and 0.6581. The tangential velocity profiles are also asymmetrical because of differential growth of boundary layers on the two surfaces. The decay of the defect in tangential velocity varies radially and is clearly seen by comparing Figures 22, 23, and 24. The tangential velocity defects are much larger near the hub and tends to decay much more slowly. But compared to axial velocity, the tangential velocity defect decays much more rapidly.

For the wakes inside the annulus-wall boundary layer, R = 0.9324 and R = 0.9595 (Figures 25 and 26) tangential velocities do not show any marked change in behavior except that the defects are much smaller compared to those at other radii found outside the boundary layer. The tangential velocity profiles in these regions show the effect of interaction between the wake and the annulus-wall boundary layer. As discussed in the case of axial velocities the leakage-flow, secondary flow and the annulus-wall boundary layer contribute significantly to the overall shape of the velocity profile and its decay in this region.

The tangential velocity behavior in the hub-wall boundary layer region represented by the radius R = 0.5676, Figure 21, shows marked changes. A defect of 0.4 at Z = 0.125 drops off to 0.15 at 0.2 chords downstream and the defect increases beyond 0.3 chords and this values is maintained even at 0.65 chords downstream of the blade. This strange behavior can be attributed to the radial velocity which is radially

inward at this location. Also the "dips" that are observed on either side of the viscous wake are attributed to the secondary flow that exists at the hub-wall. It can thus be said that the wake behavior, as to its decay and profile, are greatly altered by the hub- and annulus-wall boundary layer, secondary flow at these locations and the tip-vortex in the annulus-wall region.

The effect of loading is not only to increase the defect and asymmetry, but also to reduce the decay rate. Comparison of Figures 22, 23, and 24 with that of Figures 6 and 7 of Reynolds, et al. (1978) confirm this argument. Tangential velocities also show considerable asymmetry in the trailing-edge and near-wake regions. Blade loading does make a significant contribution to the asymmetry and its effect persists up to half-a-chord downstream.

Tangential velocities are influenced by the radial component of velocities through the radial equilibrium equation. In the trailing-edge and the near-wake regions for R = 0.7297, it is observed that there are very large radial velocities and a small component of negative relative tangential velocities. This implies that the absolute and relative velocities are in the same direction and that there is a very large change in angle inside the wake in these regions.

3.2.3 Radial mean velocity

Radial velocity profiles for the various radial locations are shown plotted in Figures 27 through 32. It is clear that radial velocities show trends which are quite unique in the trailing-edge region compared to that at far downstream locations.

Radial velocities are caused by an imbalance in the radial pressure gradients and the centrifugal forces. Physically, at either surface of

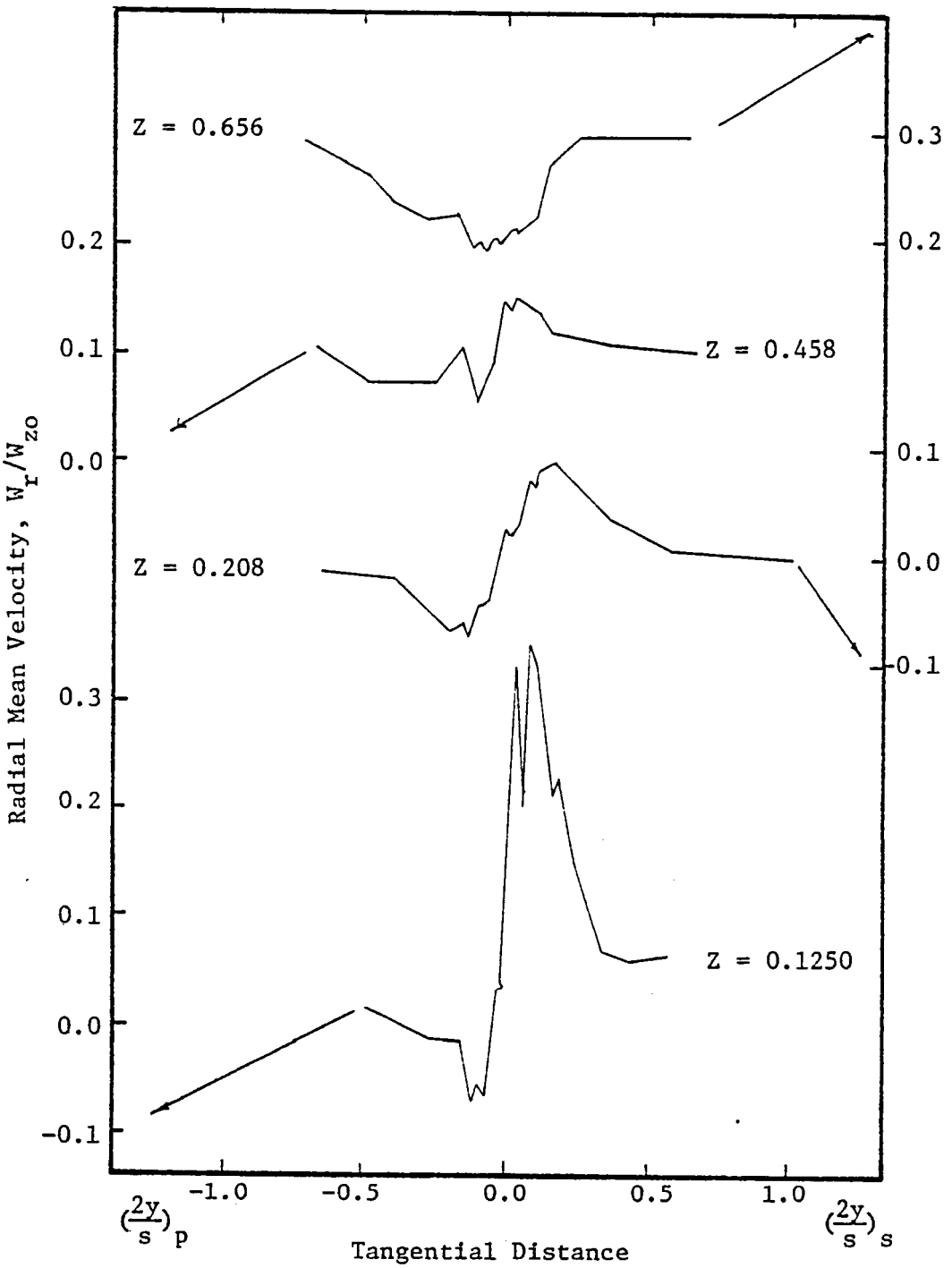

Figure 27. Radial Velocity Profiles, R = 0.5676, ϕ = 0.56

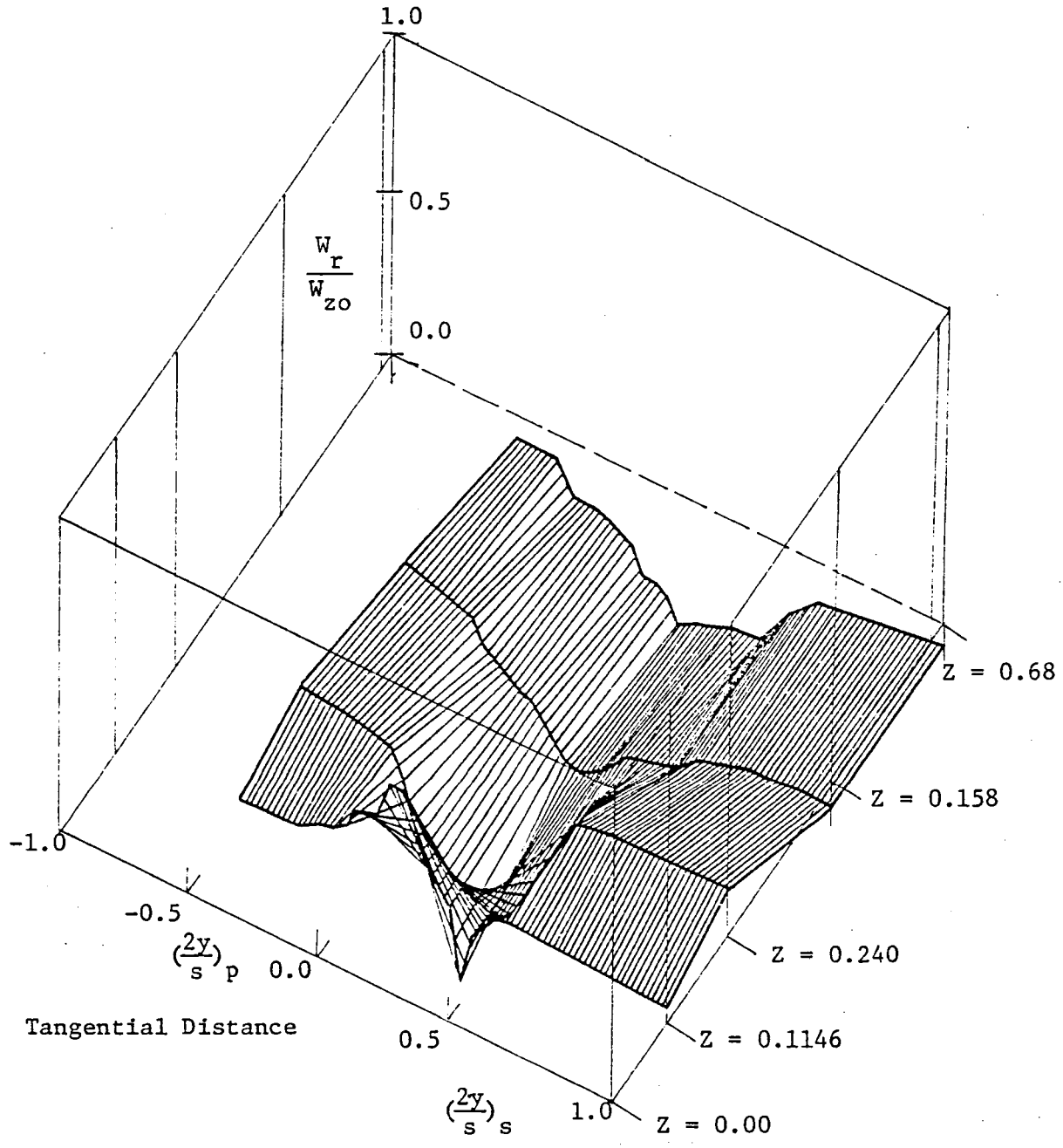

Figure 28. Three-Dimensional Plot of Radial Velocity Profiles
R = 0.6581, ϕ = 0.56

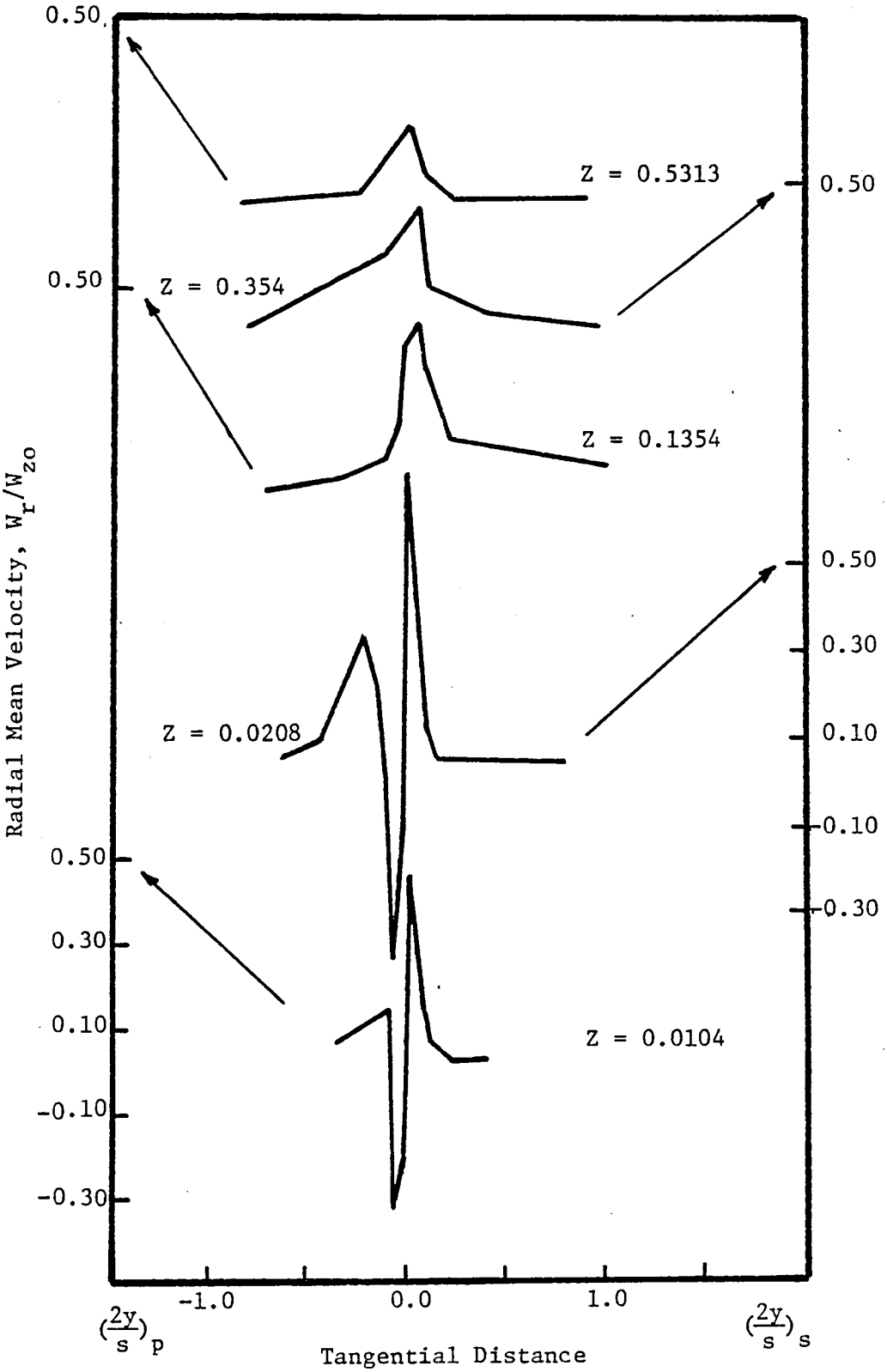

Figure 29. Radial Velocity Profiles, R = 0.7297, ϕ = 0.56

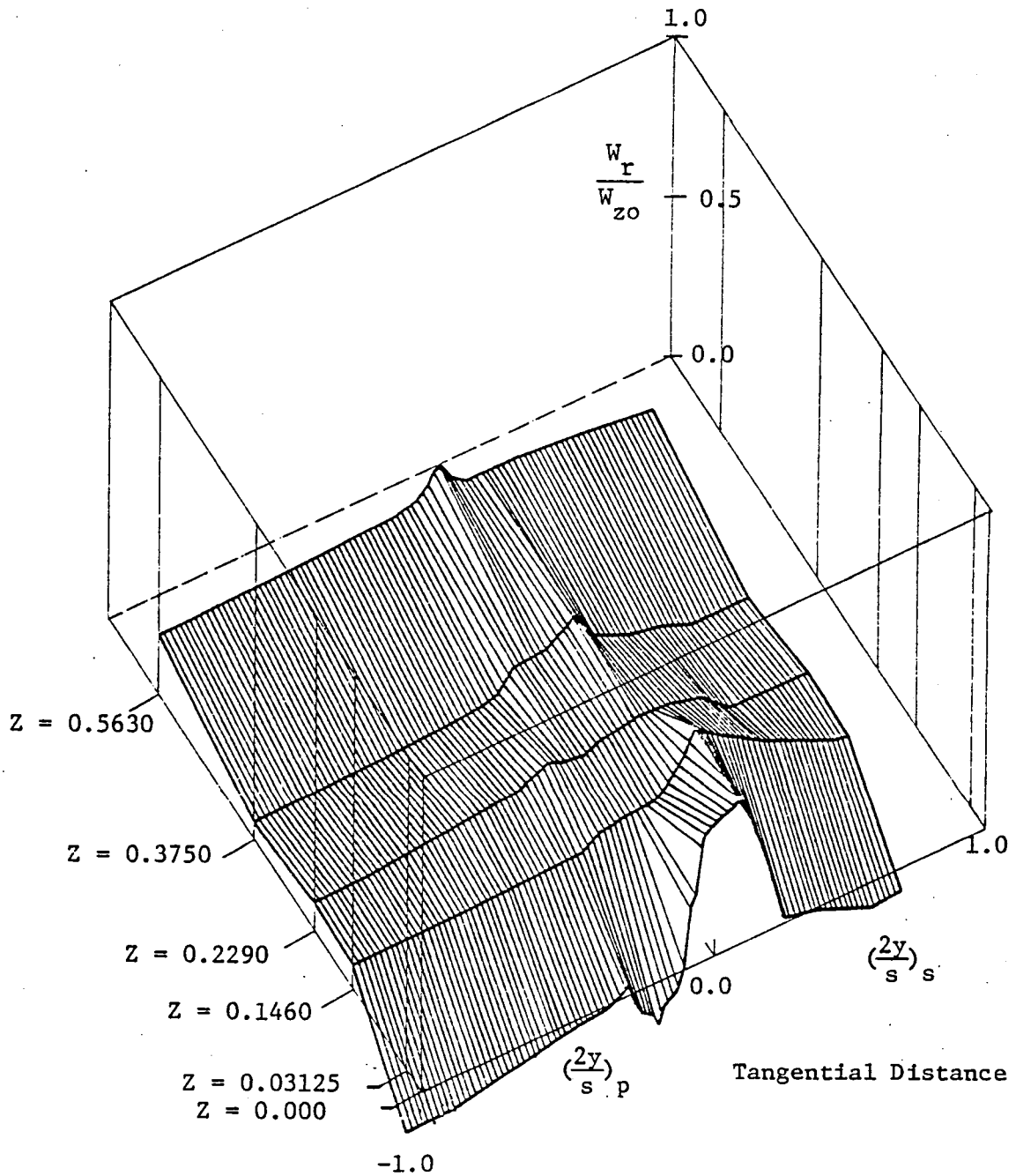

Figure 30. Three-Dimensional Plot of Radial Velocity Profiles, R = 0.7973, ϕ = 0.56

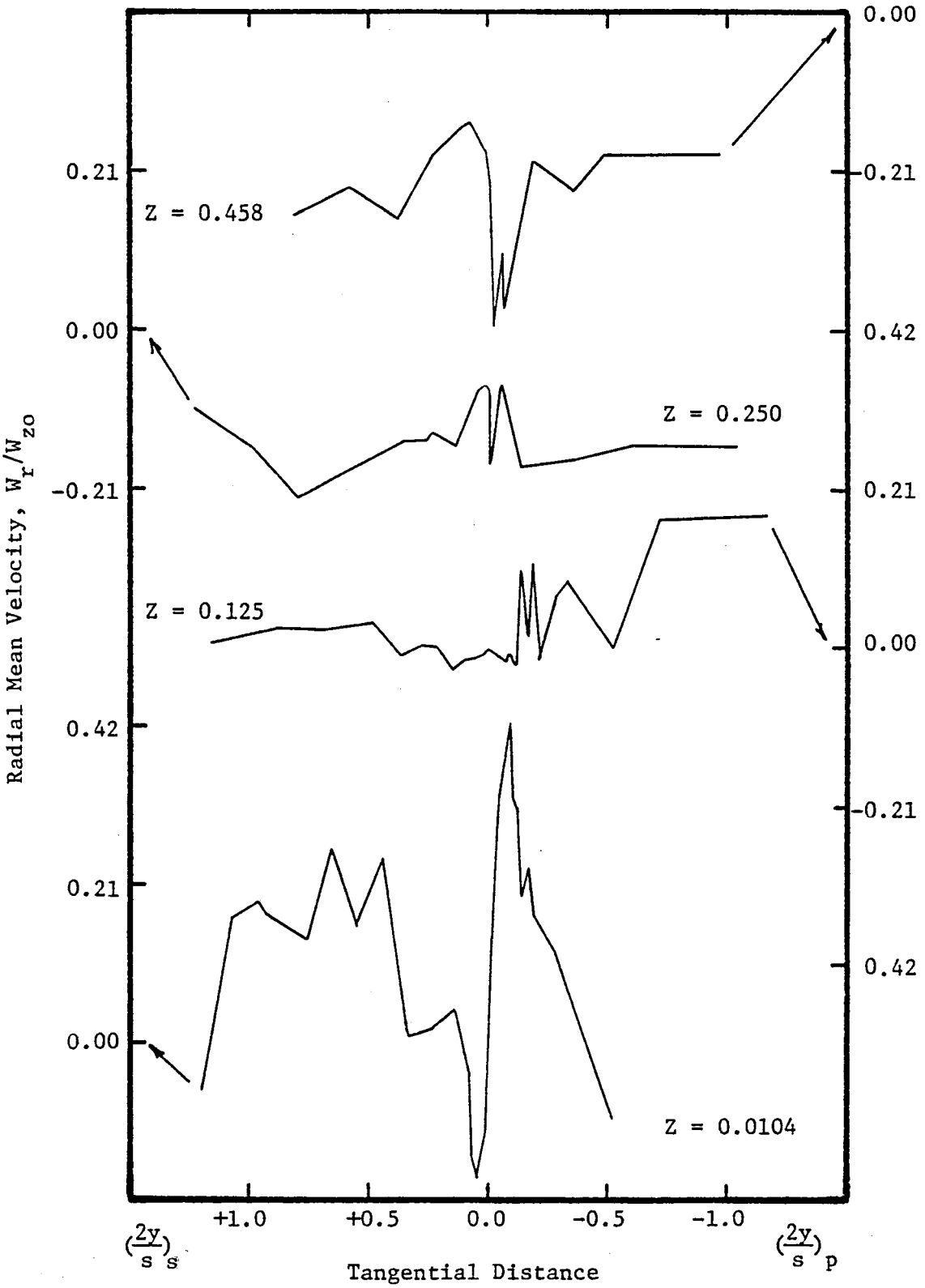

Figure 31. Radial Velocity Profiles, R = 0.9324, ϕ = 0.56

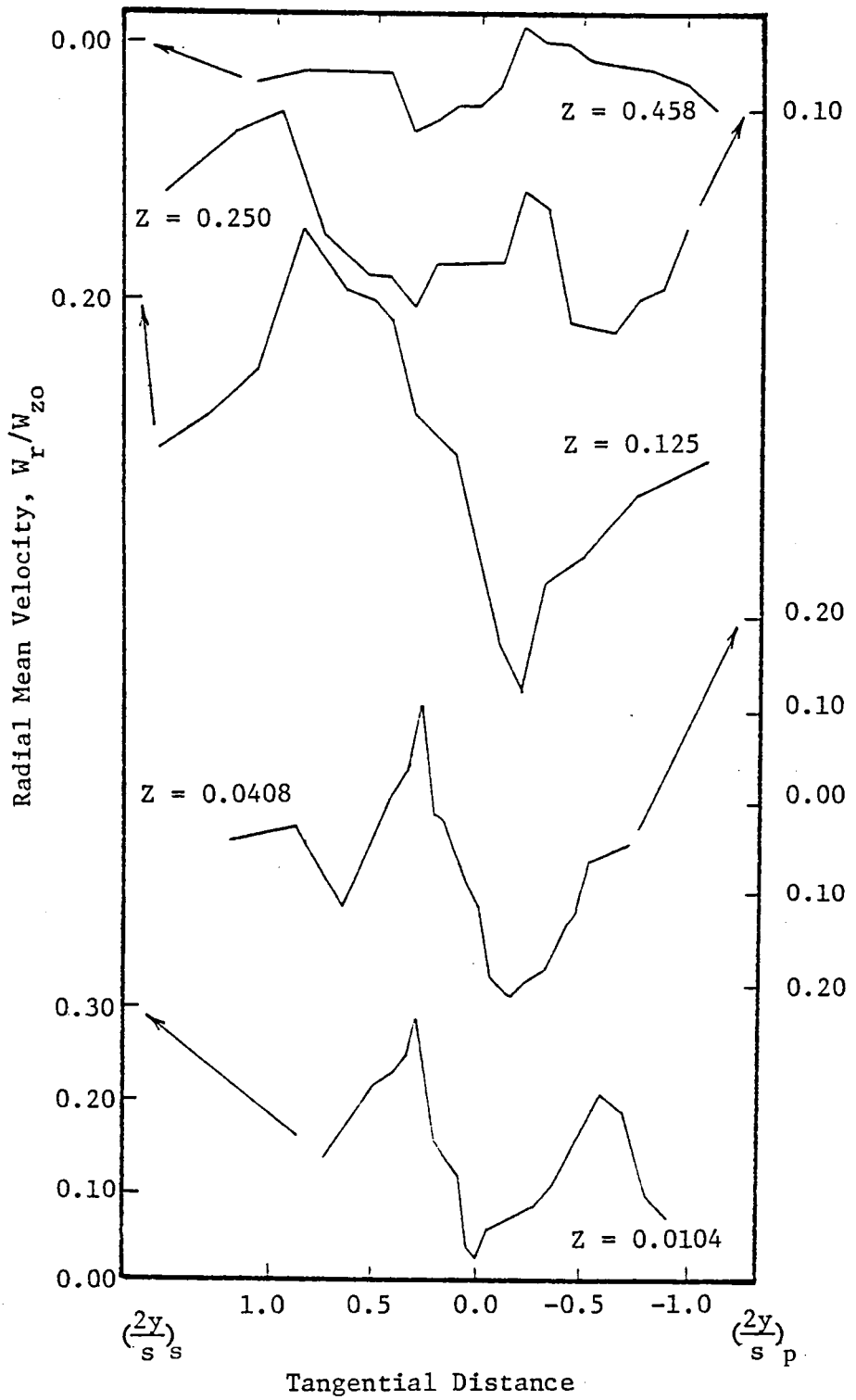

Figure 32. Radial Velocity Profiles, R = 0.9595, ϕ = 0.56

the trailing-edge of a compressor rotor-blade, the radial velocities must be zero, while the maximum radial velocities occur slightly away from the blade surface. This was confirmed by measurements on an inducer blade by Lakshminarayana, et al. (1972). Raj and Lakshminarayana (1976) and Reynolds, et al. (1978) measured the radial velocity profiles in the wake of a lightly loaded rotor. The behavior of the radial velocities were different from those anticipated on the basis of the investigation by Lakshminarayana, et al. (1972). On the other hand, a trailing vortex system associated with the shed circulation might give a radially inward-flow on one side and radially outward-flow on the other side of the blade. Referring to Figure 29 it is seen that at the wake center as well as in the free-stream there is nearly zero radial velocity while there is radially inward-flow near the pressure-surface and radially outward-flow near the suction-surface. This situation is possible if a trailing vortex system dominates the flow in the trailing-edge region while the boundary layer type of flow dominates the flow in the near- and far-wake regions. This complex flow phenomenon is not fully understood and a knowledge of the flow on the blades (for eg., near the blade boundary layer) could assist in explaining the nature of the flow. Further experiments in this region along with the flow visualization studies could assist in a better understanding of this data.

As the shed circulation and the centrifugal and Coriolis forces vary with radius, there will be a variation in the magnitude and nature of radial velocities in the radial direction. This can be seen by comparing the Figures 28, 29, and 30. The radial velocities are also influenced by the constraints imposed on the flow by the existance of annulus- and hub-walls, end-wall boundary layers, secondary and tip vortices.

The nature of the radial velocities inside the annulus-wall boundary layer, Figures 31 and 32, shows trends similar to those observed in the trailing-edge region at lower radii, except the spread of the wake is considerable. This is believed to be caused by the secondary flow and the tip-vortex. Referring to Figure 33 it is noted that at the pressure-surface the tip leakage- and secondary-vortices assist each other and that they oppose one another at the suction-surface. Hence the radial velocities get amplified at the pressure-surface and attenuated on the suction-surface. This is seen clearly in Figure 32 for R = 0.9595. The tip-vortex initially grows in strength as it travels downstream before it starts to dissipate and this phenomenon is seen in Figure 32 for R = 0.9595 and Z = 0.125. Very complex flow phenomena exist at the edge of the annulus-wall boundary layer where the secondary flow, tip-leakage flow and the annulus-wall boundary layer interact. Figure 31, R = 0.9324 represents this region where highly complex flow conditions exist.

For the wake inside the hub-wall boundary layer, R = 0.5676, Figure 27, the radial velocities in the near-wake region show trends similar to those that exist in the trailing-edge region at other radii; but in the far-wake region only radially inward velocities exist. The effect of secondary vorticity is very clearly seen in the near-wake plots of Figure 27. Here the radial velocities are radilly inward at the pressure-surface and radially outward at the suction-surface. This nature of the radial velocity pattern is opposite to what is observed in the annulus-wall region. The large radial component of the velocities indicate the highly three-dimensional nature of the rotor-wake. The radially inward or outward flow in the wake will result in an increased dissipation of energy.

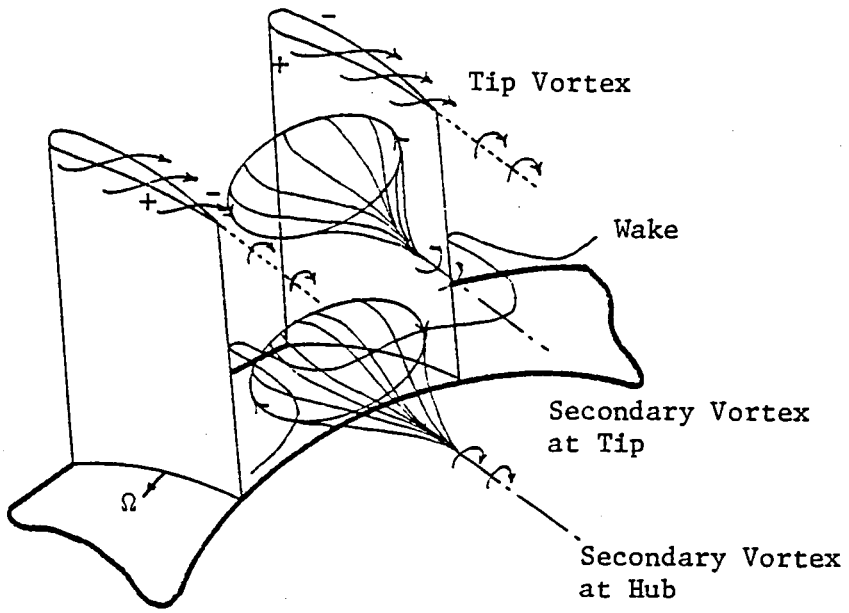

Figure 33. Trailing Vortex, Tip Vortex, Secondary Flow, and Resultant Radial Velocity Profile

The spread of the radial velocity profile downstream of the blade is not as marked as in the case of the axial or the tangential component of velocity.

Because very near the trailing-edge both the wake and the vortices are decaying it is to be expected that the decay of radial velocity be much more rapid than the axial and tangential components. In the far-wake region the decay rates of all the three components of velocity are the same.

The effect of blade loading on the radial velocities can be discerned by comparing Figure 29 with Figures 8 and 9 of Reynolds, et al. (1978). The radial velocities are dependent on the pressure gradient, centrifugal forces and Coriolis forces arising due to rotation and the strength of the trailing-vortex. All these effects increase with increased blade loading. Referring to Figure 29, it is noted for this rotor at R = 0.7297 and at Z = 0.5313 the magnitude of the maximum radial velocity is nearly 0.2, while for a lightly loaded fan used by Reynolds, et al. (1978), the radial velocities have dropped to a value of around 0.1 even at 0.2 chords downstream. So the effect of loading is to induce higher radial velocities, and these decay at a slow rate.

3.2.4 Total mean relative velocity

The total mean relative velocity, which is the resultant of the axial, tangential, and radial velocities, is shown plotted in Figures 34 through 39. The velocities are normalized to the corresponding free-stream velocity and the abscissa represents the tangential distance as a fraction of blade spacing, with $(\frac{2y}{s})$ being equal to zero at the wake centerline. A maximum wake defect of 0.8 at Z = 0.0104, for R = 0.7297 (Figure 36) reduces to about 0.2 at Z = 0.5313. The data seem to confirm

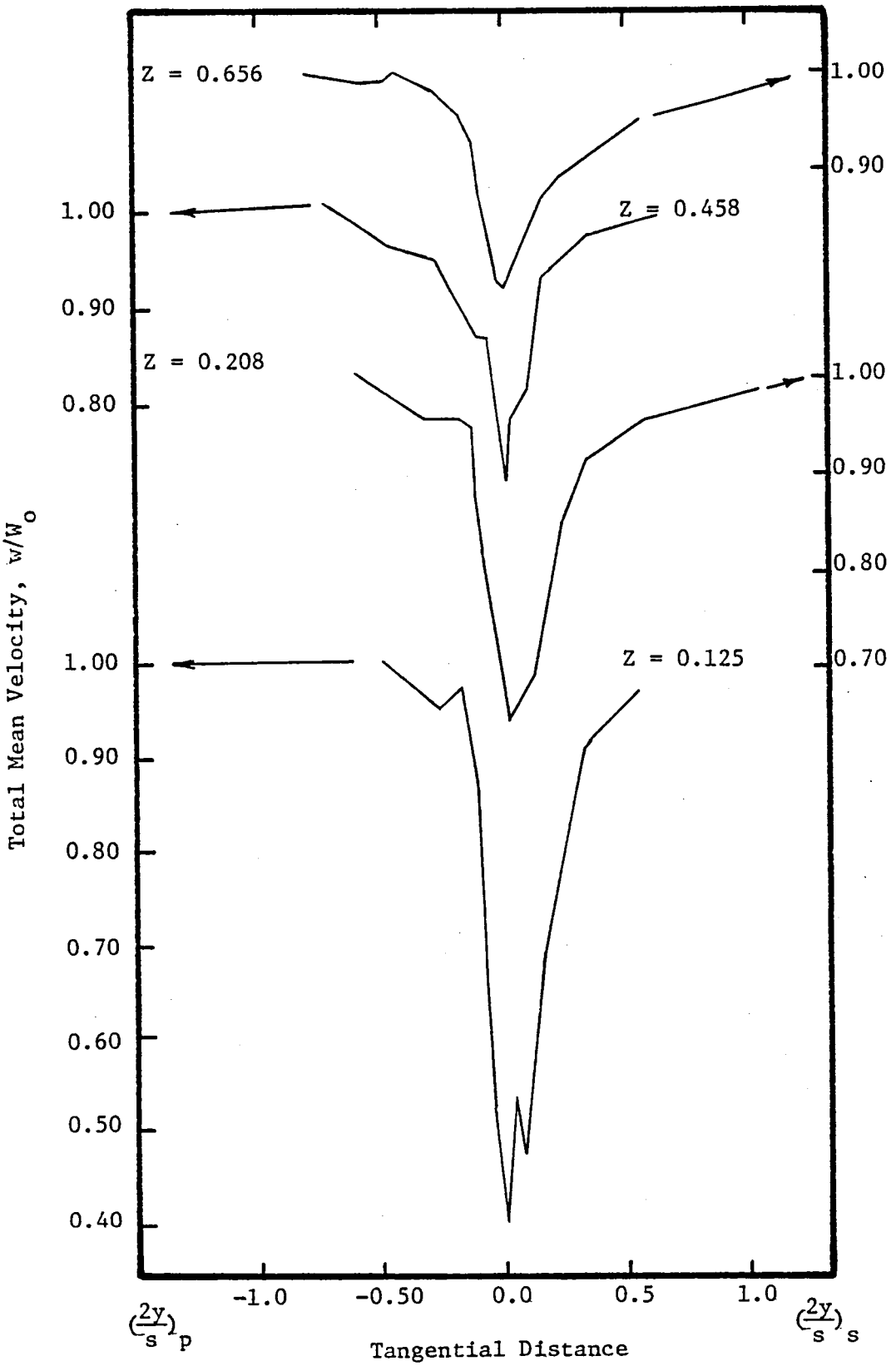

Figure 34. Total Mean Velocity Profiles, R = 0.5676, ϕ = 0.56

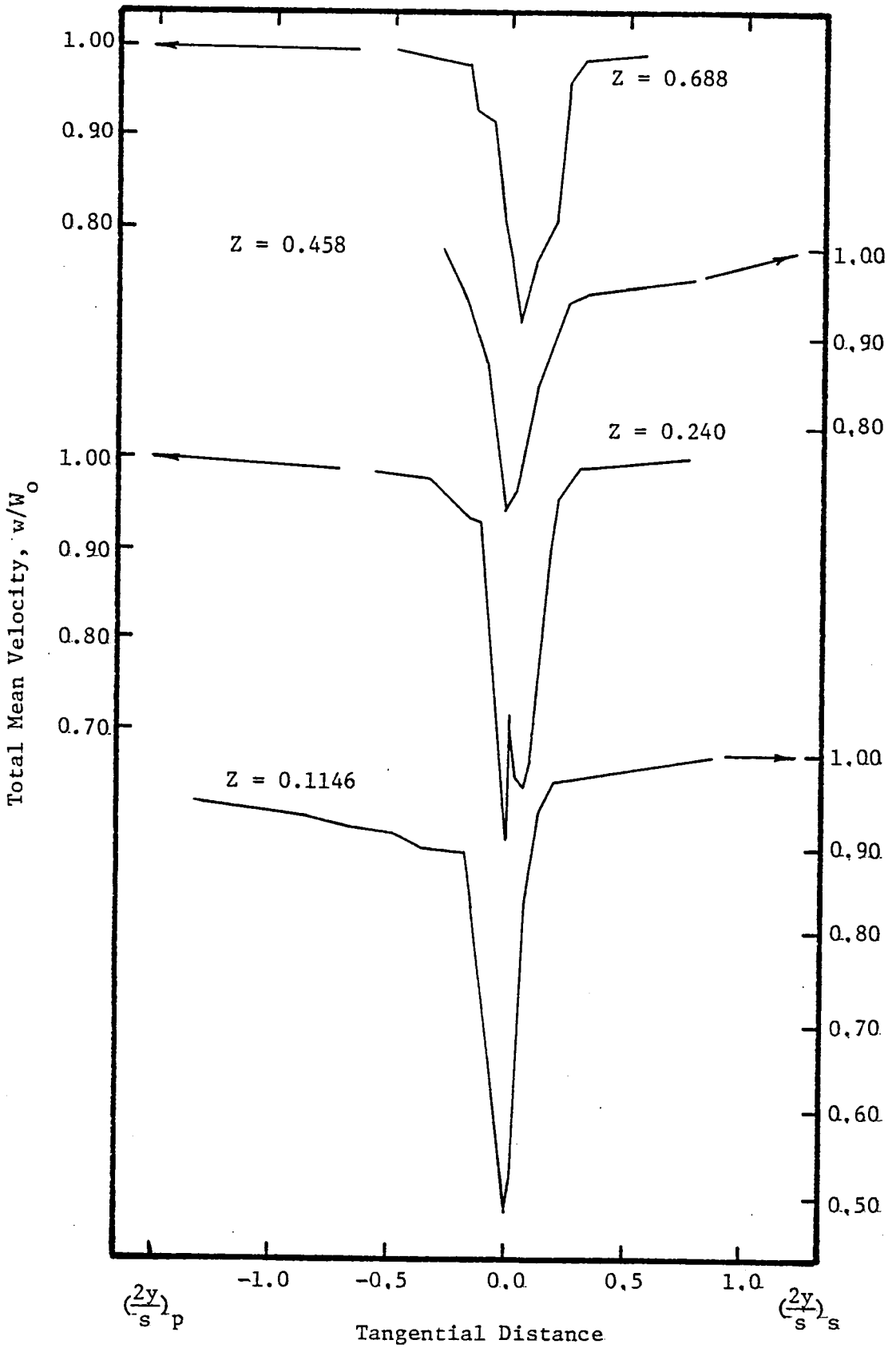

Figure 35. Total Mean Velocity Profiles, R = 0.6581, ϕ = 0.56

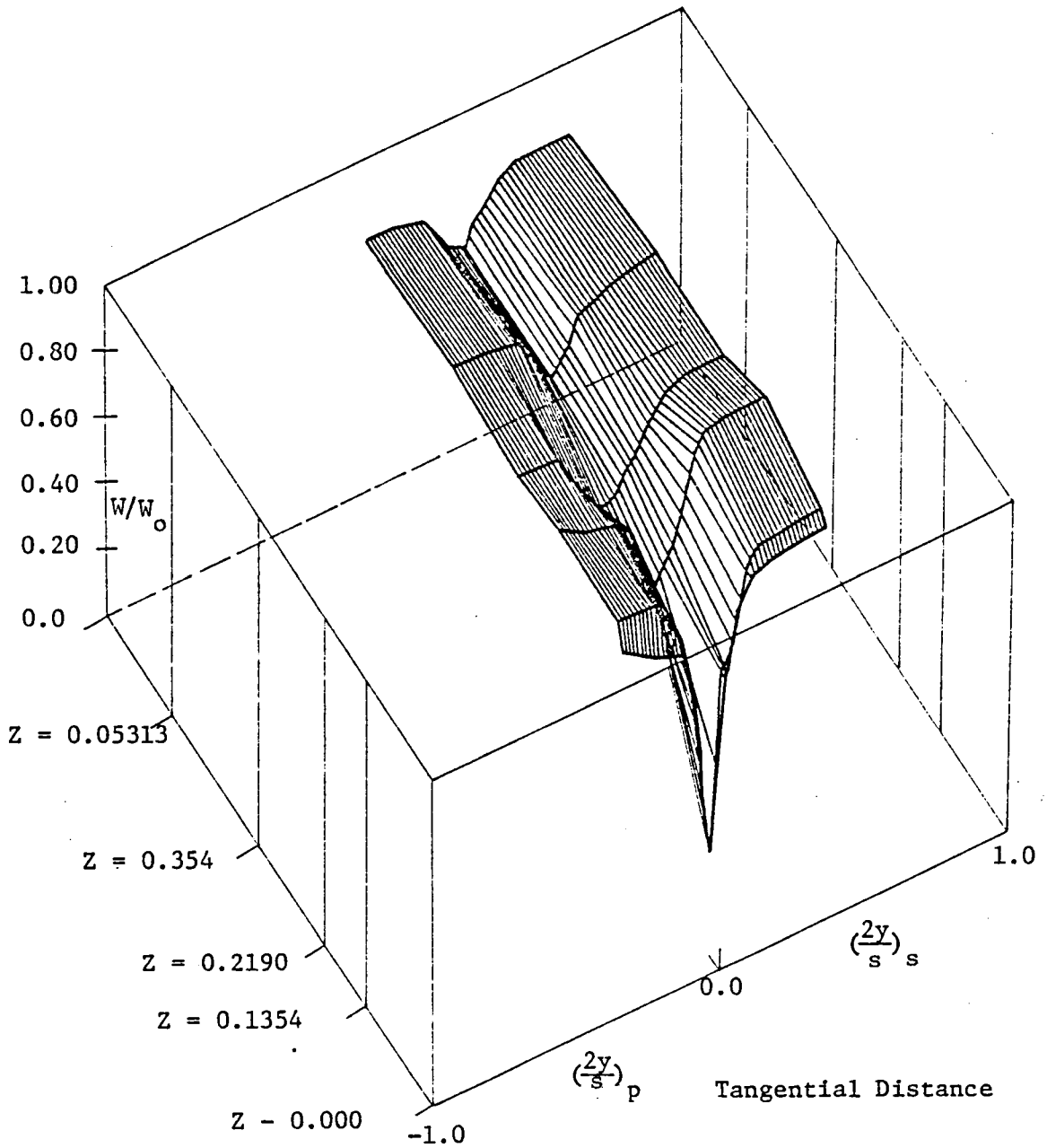

Figure 36. Three-Dimensional Plot of Total Mean Velocity, R = 0.7297, ϕ = 0.56

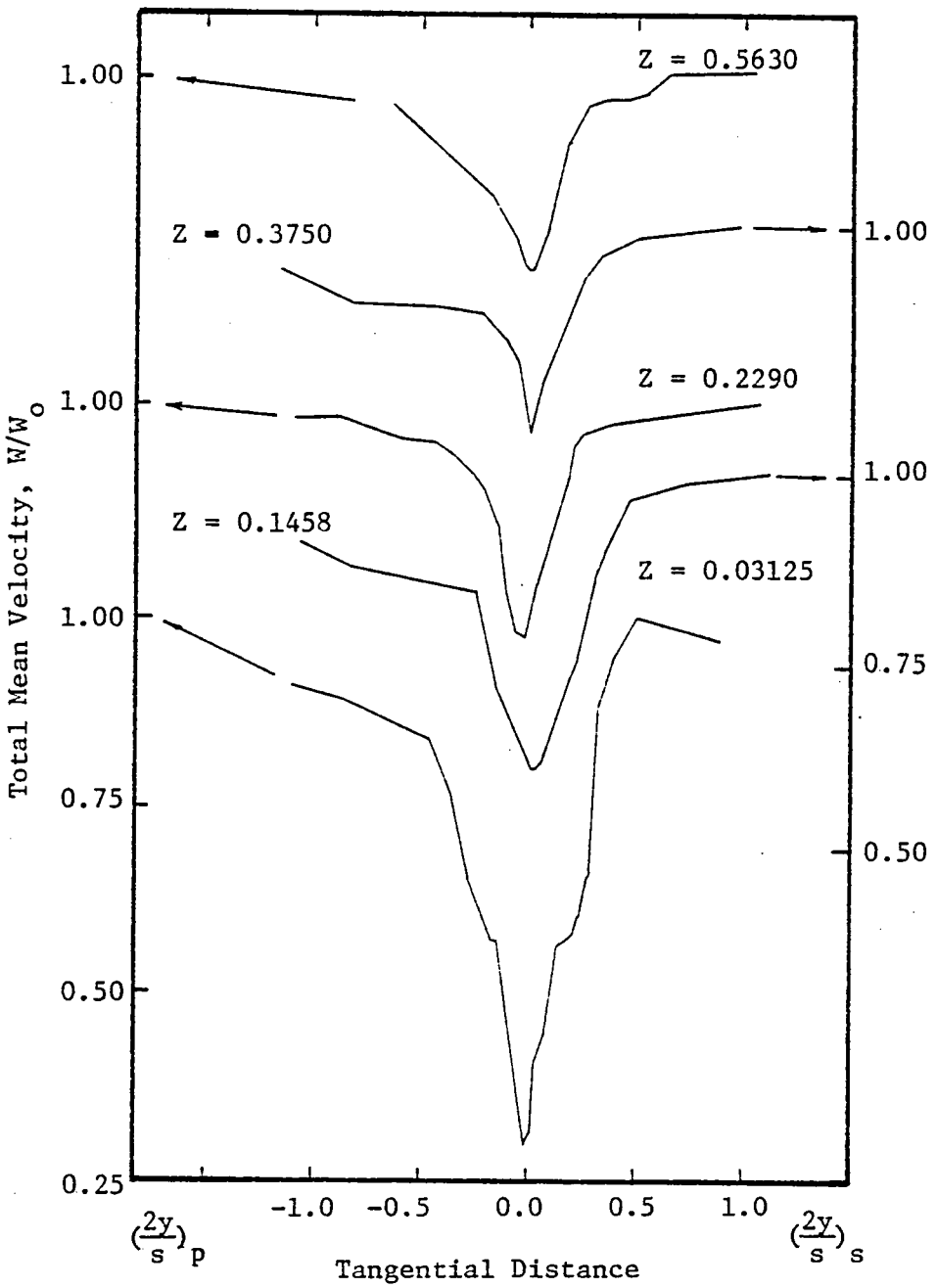

Figure 37. Total Mean Velocity Profiles, R = 0.7973, ϕ = 0.56

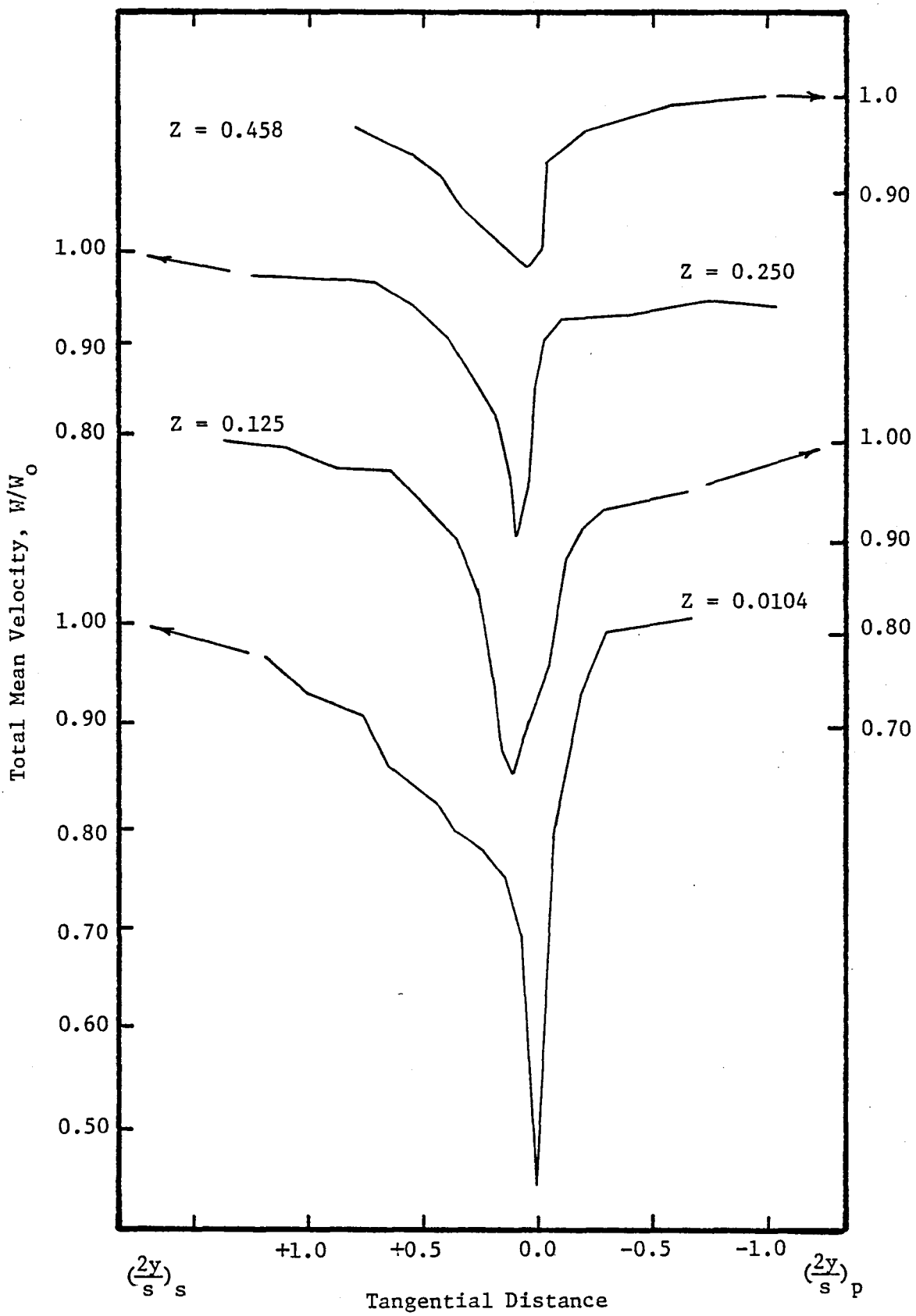

Figure 38. Total Mean Velocity Profiles, R = 0.9324, ϕ = 0.56

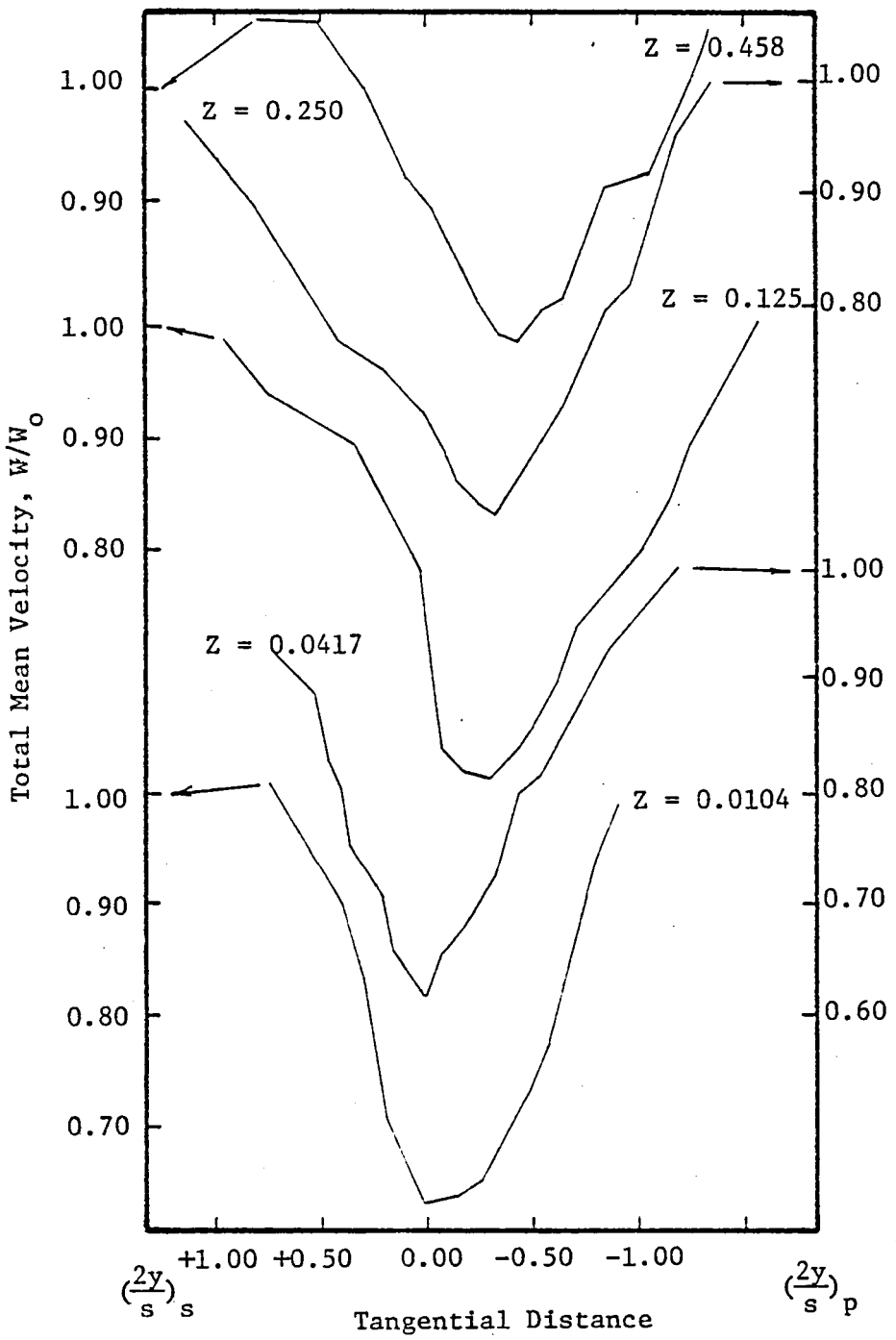

Figure 39. Total Mean Velocity Profiles, R = 0.9595, ϕ = 0.56

that the velocities are very low at the blade trailing-edge and the defect decays very rapidly in this region ($0 < Z < 0.13$). In the case of rotor-wakes this is probably the closest station to the trailing-edge ($Z = 1.588 \times 10^{-1}$ cm or 6.25×10^{-2} in) where measurements are available. Furthermore, the defects measured are larger than any reported so far. The asymmetry in the velocity profiles, which arises due to differential growth of boundary layers, and the effect of loading in sustaining the asymmetry to beyond half-a-chord downstream can also be observed in Figure 36.

The nature of total relative mean velocity in the hub- and annulus-wall boundary layers, Figures 34, 38, and 39 shows the same type of trend as that of axial velocity. The wakes are relatively thick because of the effect of secondary flows at hub and tip (and at tip there is the added effect of the tip clearance flow). The decay rates are very slow in these regions. This can be attributed to the secondary flow, leakage-flow and the annulus- and hub-wall boundary layers.

Velocity derived from the hot-wire and pressure measurements are shown plotted in Figure 40 for the radius $R = 0.7297$. The agreement beyond $Z = 0.1354$ is very good indicating pressure measurements are as accurate as hot-wire measurements. In the trailing-edge and near-wake measurements there is slight discrepancy between the two measurements. The pressure measurements do show the inviscid effects which are not reflected in the hot-wire measurements. A point of concern is that the velocity measured by hot-wire is greater than that measured by the pressure-probe and the difference between the two is as much as ten per-cent. Although the spatial resolution of the hot-wire is better than that of the pressure probe, it is not possible to assume that the hot-

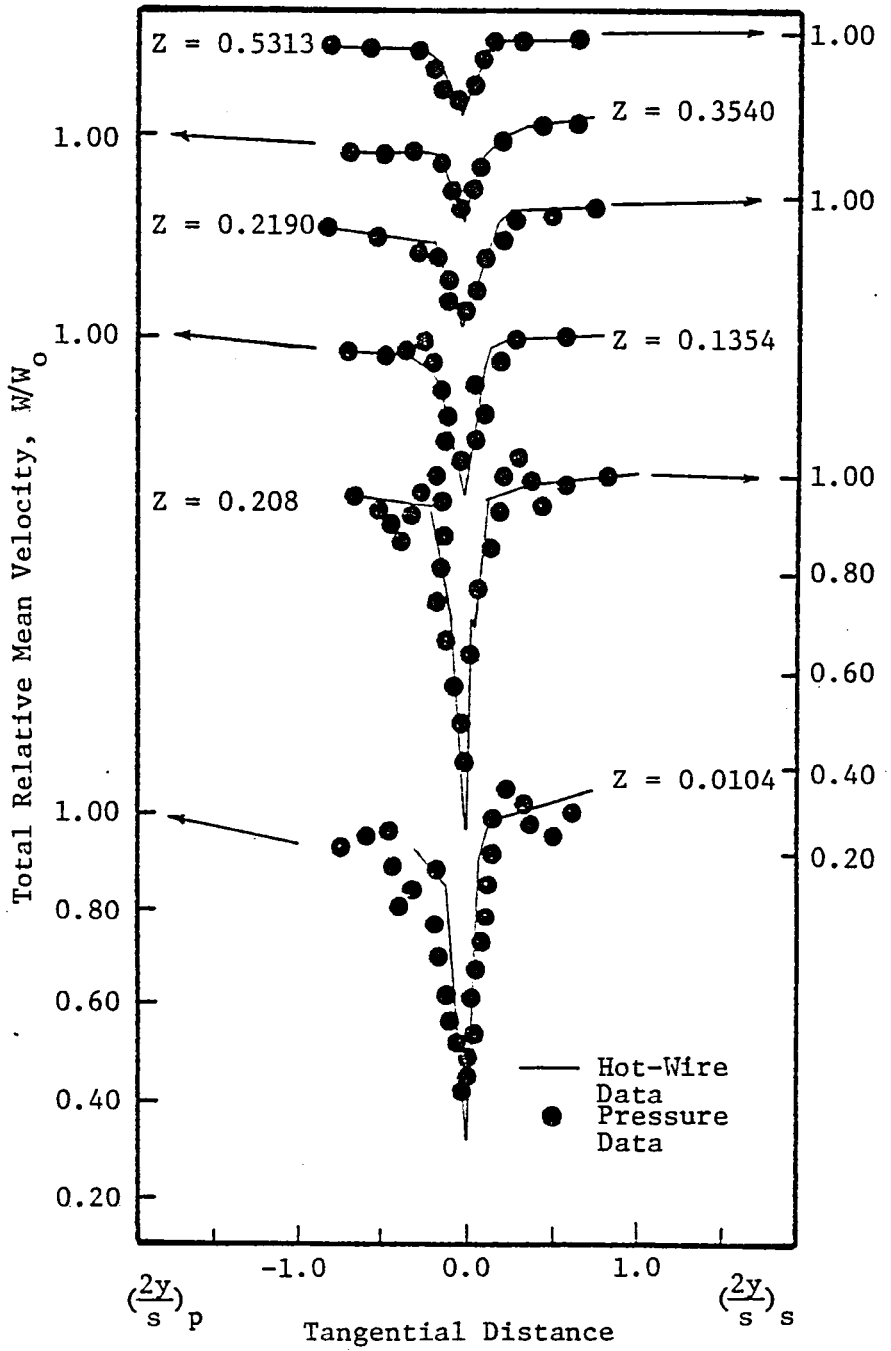

Figure 40. Total Relative Mean Velocity Profiles, R = 0.7297, ϕ = 0.56

wire has better accuracy than the pressure-probe. Two most probable errors at the trailing-edge locations are (a) wall vicinity effects in the case of pressure-probe and (b) distortion of cooling characteristics of the wire because of vicinity of the wall. No attempt is made in this investigation to evaluate the relative merits of the two systems in the near-wake and trailing-edge region as the source of error is not properly understood. The probe is calibrated in a known uniform flow, and, therefore, the calibration would include the aerodynamic interference effects. But the errors due to the probe immersed in shear gradients are not included.

3.3 Pressure Variation across the Wake

In order to get a complete understanding of the flow in the wake, time averaged static-stagnation-pressure surveys were done in a relative frame of reference. A spherical head static-stagnation pressure probe, built at The Pennsylvania State University and described earlier, was employed for all pressure surveys reported in this section. Variation of the static-pressure rise coeffcient (c_p) across the wake of the rotor is shown plotted in Figure 41. Some of the traditional models of an inviscid core flow plus a viscous wake appear in these plots. The static-pressure not only varies across the wake, but also at the wake-edge near trailing-edge due to inviscid effects, which are not reflected in the stagnation-pressure plots. In the trailing-edge region the static-pressure variation across the wake is as large as 40 percent, which drops off to about five percent at half-a-chord downstram. The measurement seems to confirm the trend observed by Thompkins and Kerrebrock (1975) who have reported a 25 percent variation in static-pressure across the wake at ten percent of an axial chord downstream of a transonic rotor. In the present

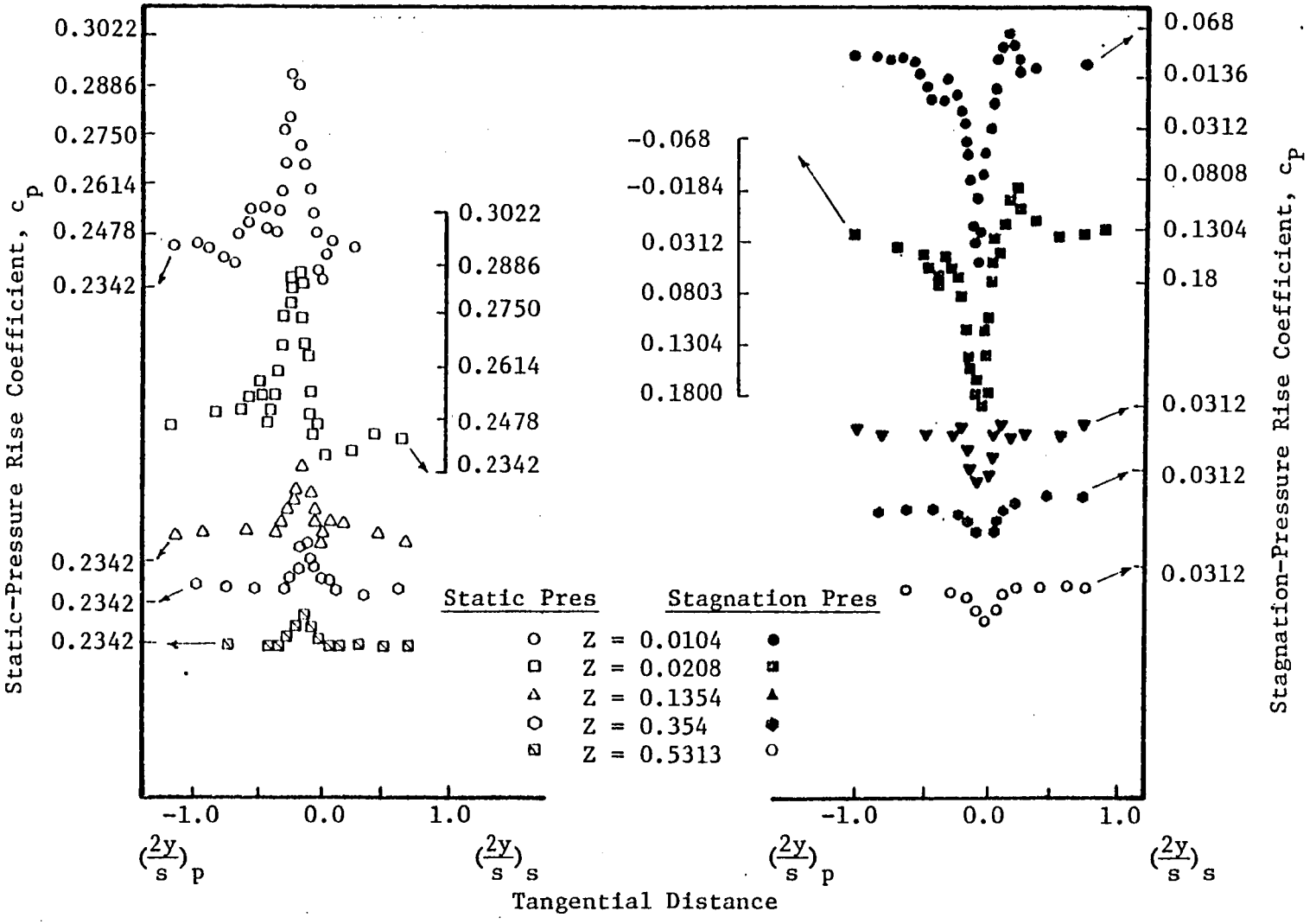

Figure 41. Static-and Stagnation-Pressure Variation across the Wake

case the first measurement station is very close to the trailing-edge and consequently very large static-pressure gradients were measured. However, the data must be viewed with some caution. As reported earlier, the pressure probes are subject to wall vicinity effects and also the large angle variations reported earlier would adversely affect the values in the trailing-edge region.

Experimental evidence indicates that static-pressure increases at the wake center and as the wake travels downstream this difference decreases. For the data presented for R = 0.7297, the ratio of the static-pressure at the wake center to the corresponding static-pressure in the free-stream decays rather rapidly in the trailing-edge region and the decay is markedly slower in the near- and far-wake regions. This very rapid decay at the trailing-edge region is attributed to the very rapid decay in velocity defect and turbulence intensity.

The existence of pressure gradients across the wake can be understood by examining the equation of motion in rotating coordinate system in a direction normal (n) to the streamlines (s). The equation can be approximately written as (neglecting the viscous terms as well as some of the inertial terms)

$$-\frac{1}{\rho}\frac{\partial p}{\partial n} \simeq 2\Omega W_r \cos\beta_1 - \frac{W_s^2}{R_c} - \frac{\partial}{\partial n}(\overline{w_n'^2}) \qquad (3)$$

where n is the direction normal to streamlines, W_s is the streamwise velocity, R_c is the radius of curvature of the streamline and $\overline{w_n'^2}$ is the turbulent fluctuation in the n-direction. It is evident from the above equation that, in addition to Coriolis and centrifugal forces, the gradients of turbulent intensity in the n-direction have an appreciable influence on the pressure gradient $\partial p/\partial n$. At the wake center, near the trailing-edge region, the turbulence intensity terms dominate and hence

the static-pressure gradients can exist even in the absence of curvature (R_c). Qualitative analysis of this effect is given by Reynolds (1978).

3.4 Turbulence Intensity Profiles

3.4.1 Axial turbulence intensity

Axial turbulence intensity profiles for the rotor-wake at various radii from hub-to-tip are shown in Figures 42 through 47. The turbulence intensity has been non-dimensionalized by the local mean velocity, since turbulence is dependent on local flow conditions. The abscissa in the figures represents the tangential distance normalized to half the blade spacing.

The axial intensity profiles show very high values in the trailing-edge region. In the near- and far-wake regions the magnitude reduces considerably. The very high values in the trailing-edge region are attributed to the hot-wire's sensing the trailing vortices as an unsteady signal which shows up as turbulence.

The axial turbulence intensity profiles are asymmetrical in the trailing-edge region and tend to become symmetrical beyond 0.2 chords downstream. The asymmetry in the profile results from the differential growth of turbulence on the suction- and pressure-surfaces of the blade. In the near-wake plots of Figures 43, 44, and 45, the turbulence intensity profiles show a dip (a lower intensity value) in that the peak value occurs on either side of the centerline. This type of trend is to be expected as the turbulence intensity must be zero on the blade surface and the maximum value occur slightly away from the surfaces. Further the centrifugal force increases the intensity on the suction-surface and diminishes the intensity on the pressure-surface. This is very clearly seen in the Figures 43 and 45. The profiles for R = 0.7297,

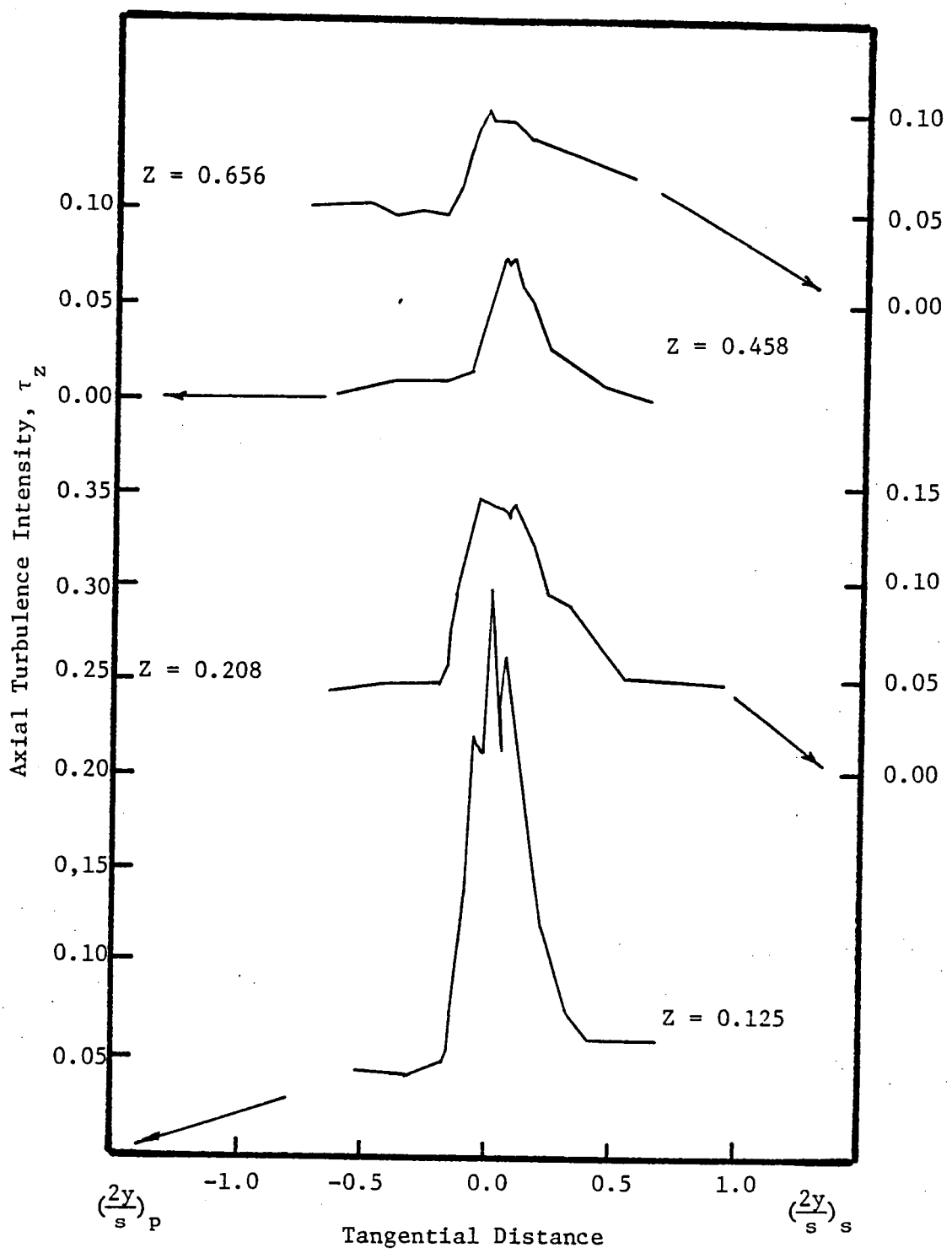

Figure 42. Axial Turbulence Intensity Profiles, R = 0.5676, ϕ = 0.56

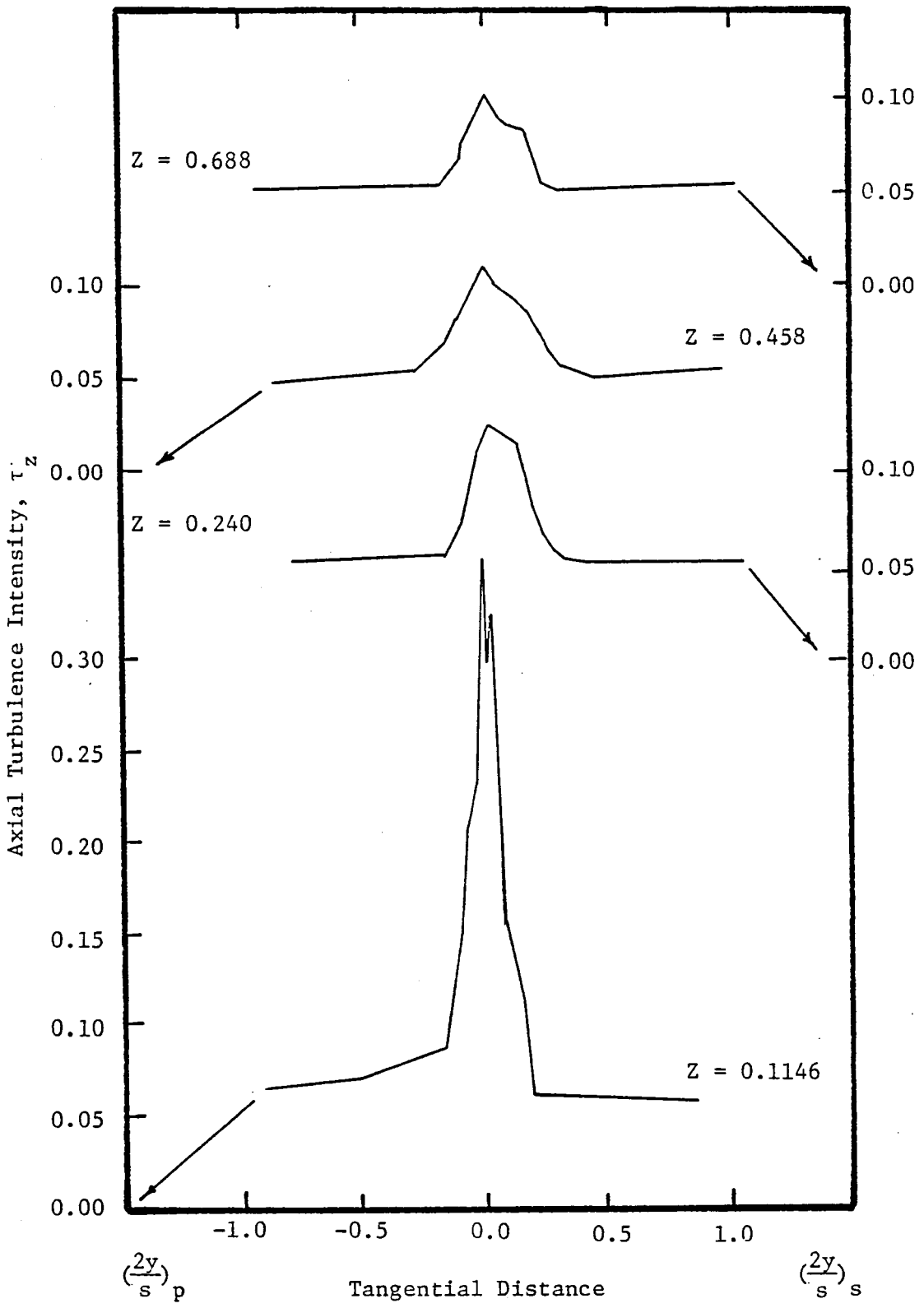

Figure 43. Axial Turbulence Intensity Profiles, R = 0.6581, ϕ = 0.56

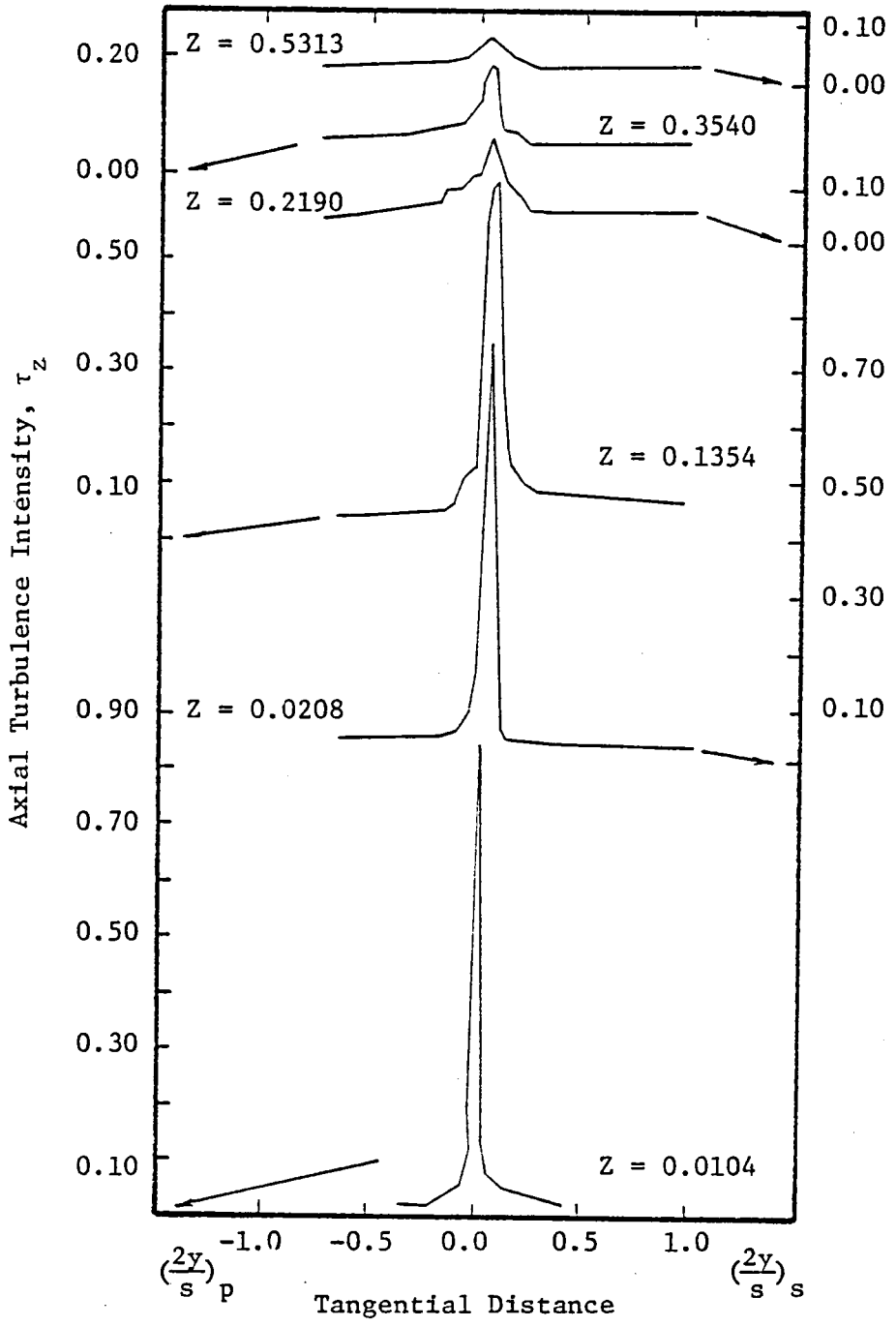

Figure 44. Axial Turbulence Intensity Profiles, R = 0.7297, ϕ = 0.56

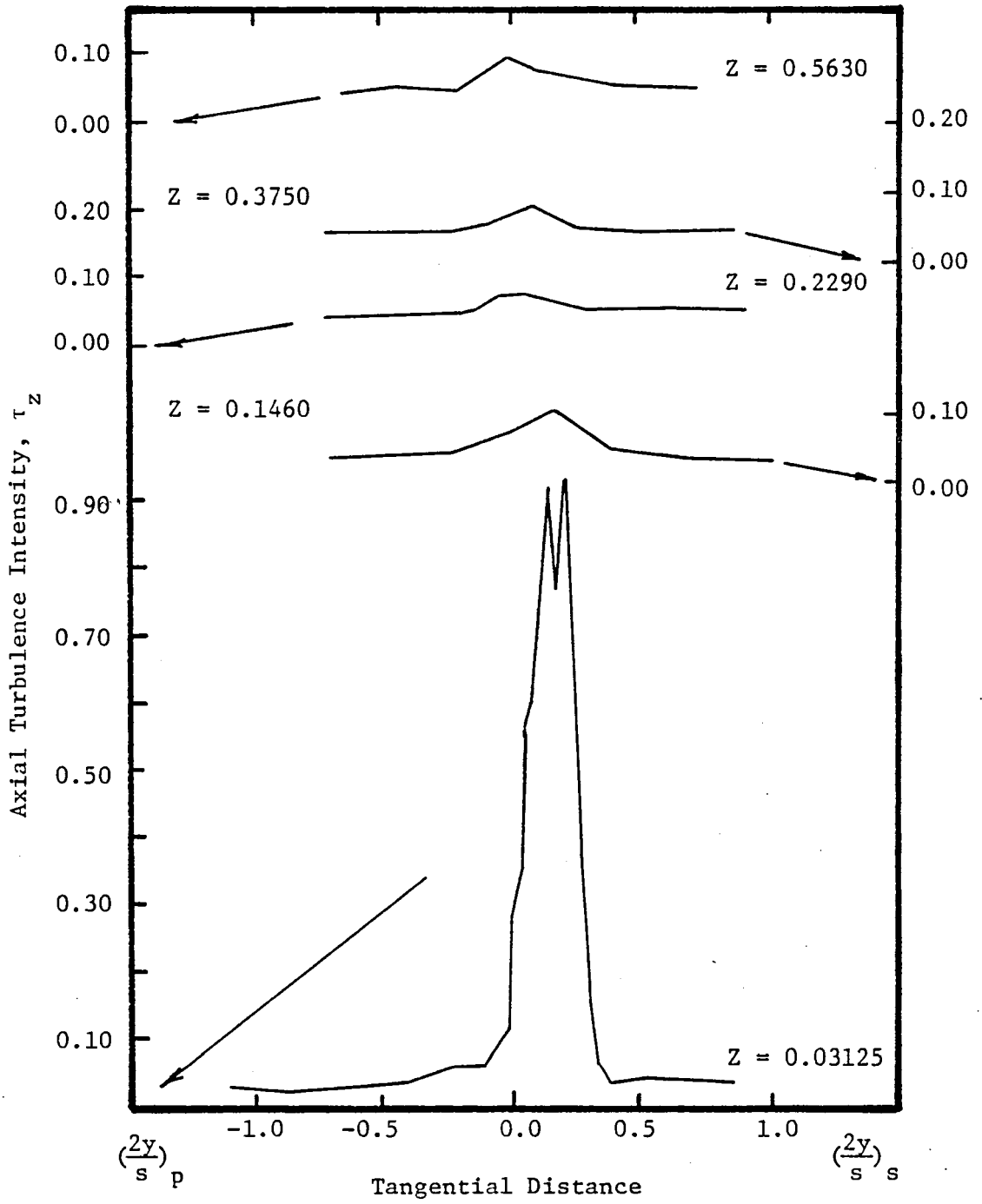

Figure 45. Axial Turbulence Intensity Profiles, R = 0.7973, ϕ = 0.56

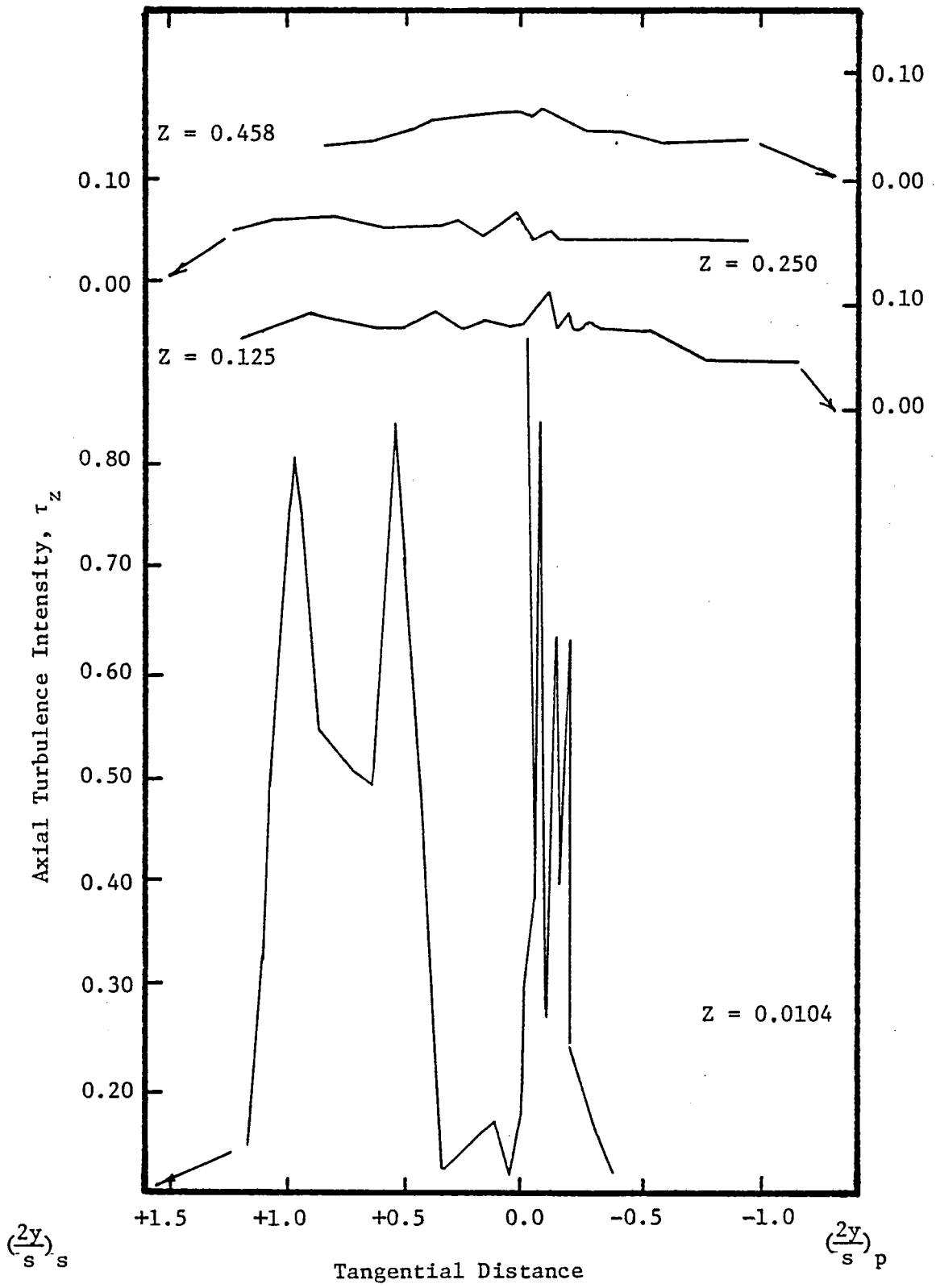

Figure 46. Axial Turbulence Intensity Profiles, R = 0.9324, ϕ = 0.56

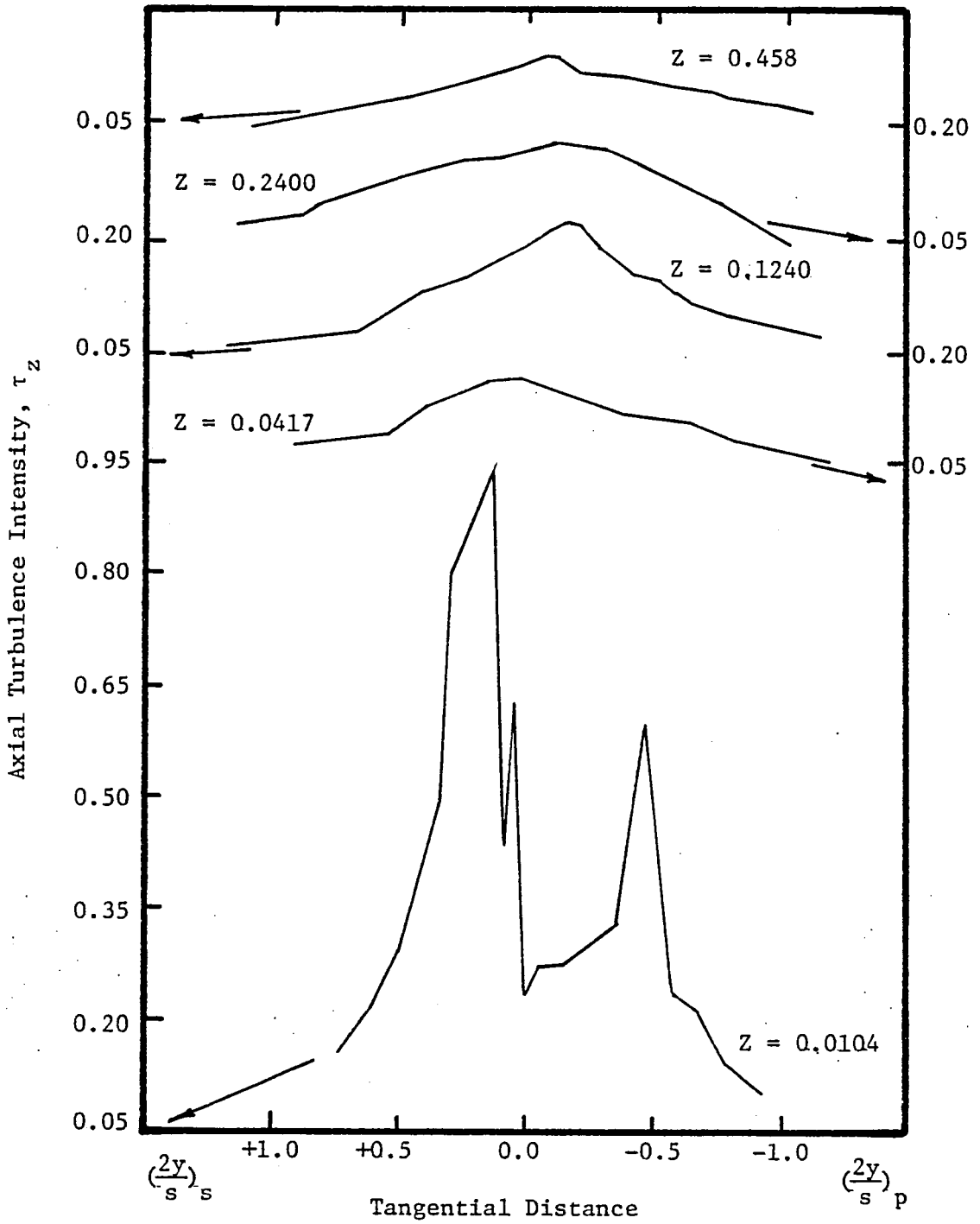

Figure 47. Axial Turbulence Intensity Profiles, R = 0.9595, ϕ = 0.56

Figure 44 do not depict this trend very clearly. This might be due to the region's being too narrow and the large spatial resolution of the probe may not have detected this feature.

The magnitude of axial turbulence intensity is about 0.85 at Z = 0.0104 (and R = 0.7297) which reduces to less than 0.15 at Z = 0.5313. This implies that the decay of intensities is very rapid in the trailing-edge region and it slows down considerably beyond 0.2 chords downstream. The same trend is observed for the other radii R = 0.7973 and 0.6581. The rapid decay of turbulence intensities indicates that there is a very rapid redistribution of energy and momentum in these regions.

The axial intensity profiles for the wakes inside the annulus-wall boundary layer are shown plotted in Figures 46 and 47 and they depict very complex turbulence structure in the trailing-edge region. The effect of interaction of the secondary flow, tip-leakage flow and the wake is very clearly seen in these plots. Free-stream turbulence intensity is far higher than those that exist outside this region (seven to ten percent as compared to three to five percent outside the annulus-wall boundary layer). There are also two very distinct peaks in the turbulent intensity profiles. One of these peaks is believed to have been caused by the tip-clearance flow and the associated tip-vortex. The other peak is due to the wake. Peak intensity reaches nearly 90 percent at the trailing-edge locations. As the tip-vortex travels downstream it dissipates very rapidly and consequently the turbulence intensity contributed by it to the overall rotor-wake also decays rapidly. A 90 percent intensity at Z = 0.0104 drops off to 15 percent at Z = 0.0417. The decay beyond this is rather gradual and the free-stream intensity remains

fairly high at a value of above five percent even at the far downstream location of Z = 0.458.

For the wake inside the hub-wall boundary layer, R = 0.5676, Figure 42, the decay of axial turbulence intensity is rather slow compared to the one in the annulus-wall boundary layer region. The interaction of the hub-wall boundary layer, the secondary flow and the wake make the intensities decay at a much slower rate. For the wakes inside the hub-wall boundary layer, even though the free-stream axial turbulence intensities are below five percent, the maximum intensity at the wake center remains as high as ten percent even at 0.656 chords downstream. It can thus be said that the decay of intensities are slowed down to a greater extent inside the hub-wall boundary layer besides sustaining higher values of free-stream intensity.

The axial intensity measured before the inlet-guide-vanes was about 0.5 percent and this does not show any appreciable amplification after moving through the rotor blade row. Free-stream axial turbulence intensity downstream of the rotor was found to be around the same order of magnitude in the region outside the wake boundary layer.

The effect of blade loading on the axial turbulence intensity can be seen by comparing Figure 44 with Figure 3 of Lakshminarayana and Reynolds (1979). The free-stream axial turbulence intensity for both the rotors were of the same order, but very near the blade trailing-edge the turbulence intensities are nearly 80 percent for the heavily loaded rotor. On the other hand, the intensities are about 30 percent for the lightly loaded fan blade. Thus the effect of loading is to increase the turbulence level in the wake. Increase in blade loading not only increases the turbulence levels, but also increases the decay rate.

3.4.2 Tangential turbulence intensity

Tangential turbulence intensity profiles are shown plotted in Figures 48 through 53 for various radii and varying axial distances. In these plots the ordinate represents the tangential turbulence intensity normalized to the local mean velocity and the abcissa represents the tangential distance normalized to half the blade spacing.

Asymmetry in the tangential intensity profiles is clearly seen in these plots. In the trailing-edge region it is not very clear because of the scales. This asymmetry, as in axial intensity profiles, is attributed to differential turbulence growth on the two sides of the blade. The symmetry in these profiles was not obtained until 0.6 chords downstream, the last measuring station using a rotating probe. This seems to confirm the arguments put forth by Raj and Lumley (1976) and Lakshminarayana and Reynolds (1978), that symmetry will be obtained only beyond one chord downstream.

Unlike the axial component of turbulence intensity, no dip in the turbulence profiles was found at the wake centerline for the tangential intensity profiles for all the radii. This indicates that in the inner layer of the wake a larger redistribution of energy and momentum occurs for the tangential intensities near the rotor-blade trailing-edge than does in the axial component of intensity. The magnitude for both axial and tangential intensities is the same in the trailing-edge region but in the far-wake region the tangential intensities are far smaller than the axial intensities indicating that the tangential component of intensity decays faster than the axial component.

The turbulence intensity profiles for the wake inside the annulus-wall boundary layer region, Figures 52 and 53, show distinctly different

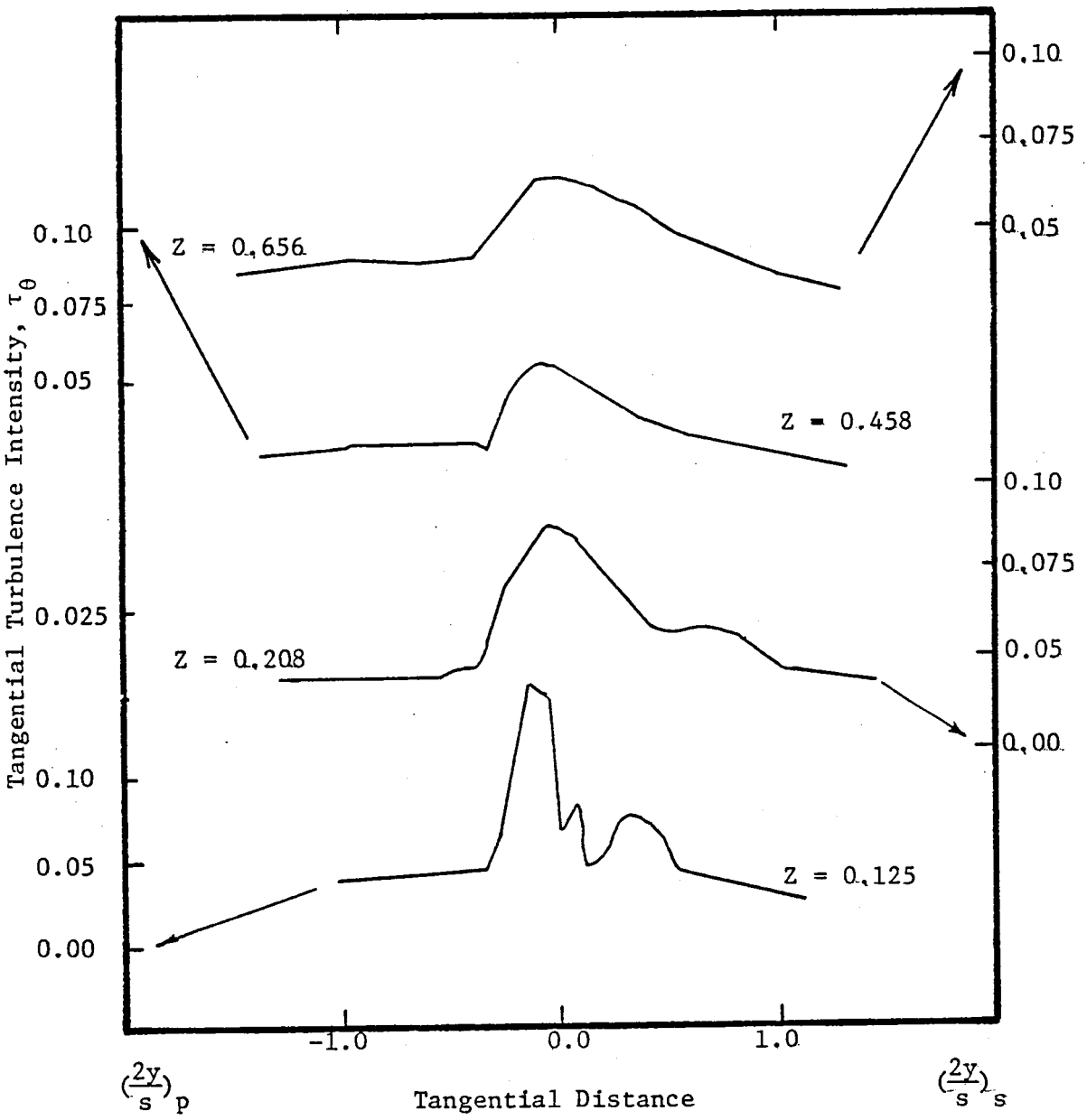

Figure 48. Tangential Turbulence Intensity Profiles, R = 0.5676, ϕ = 0.56

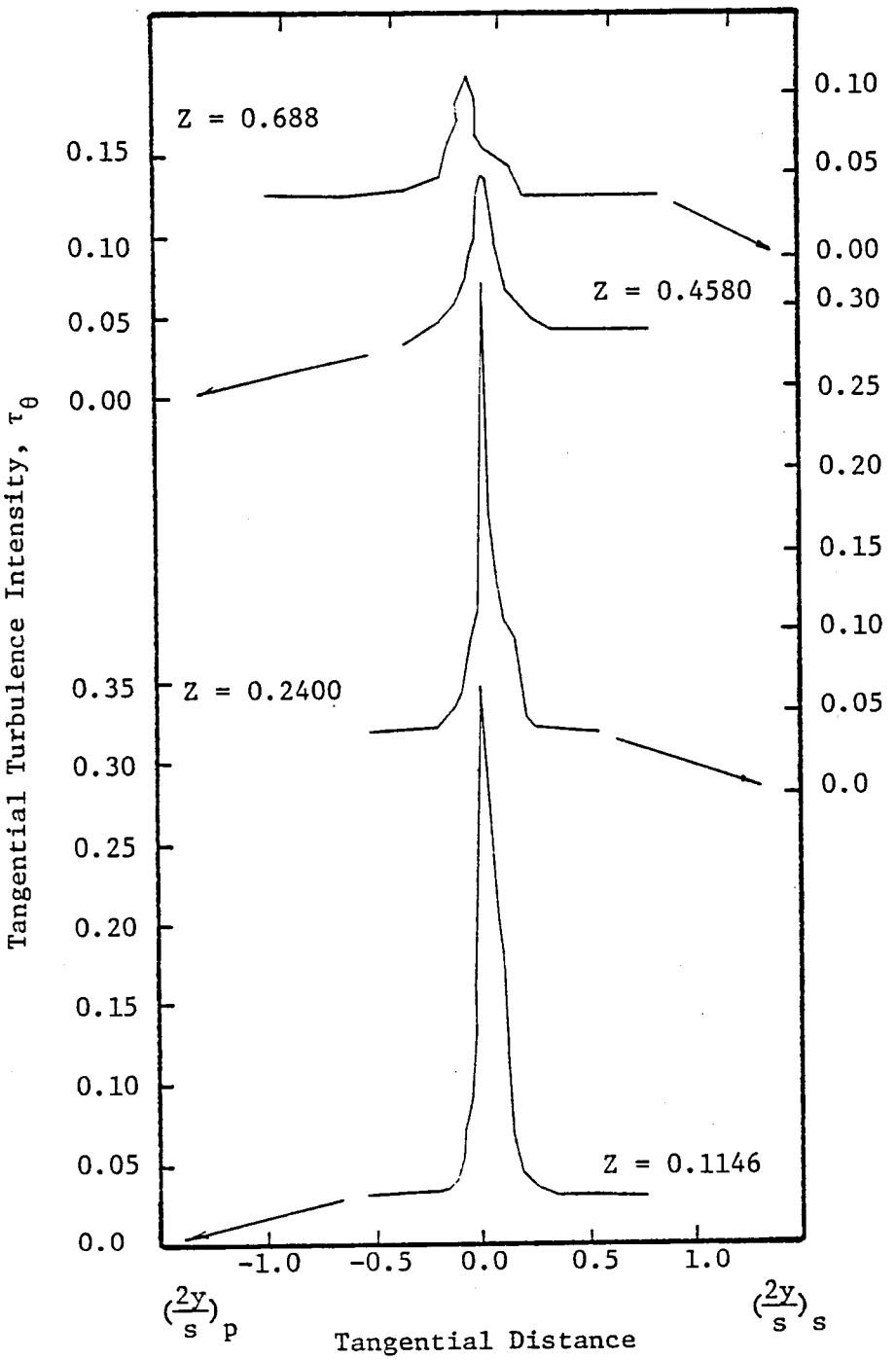

Figure 49. Tangential Turbulence Intensity Profiles, R = 0.6581, ϕ = 0.56

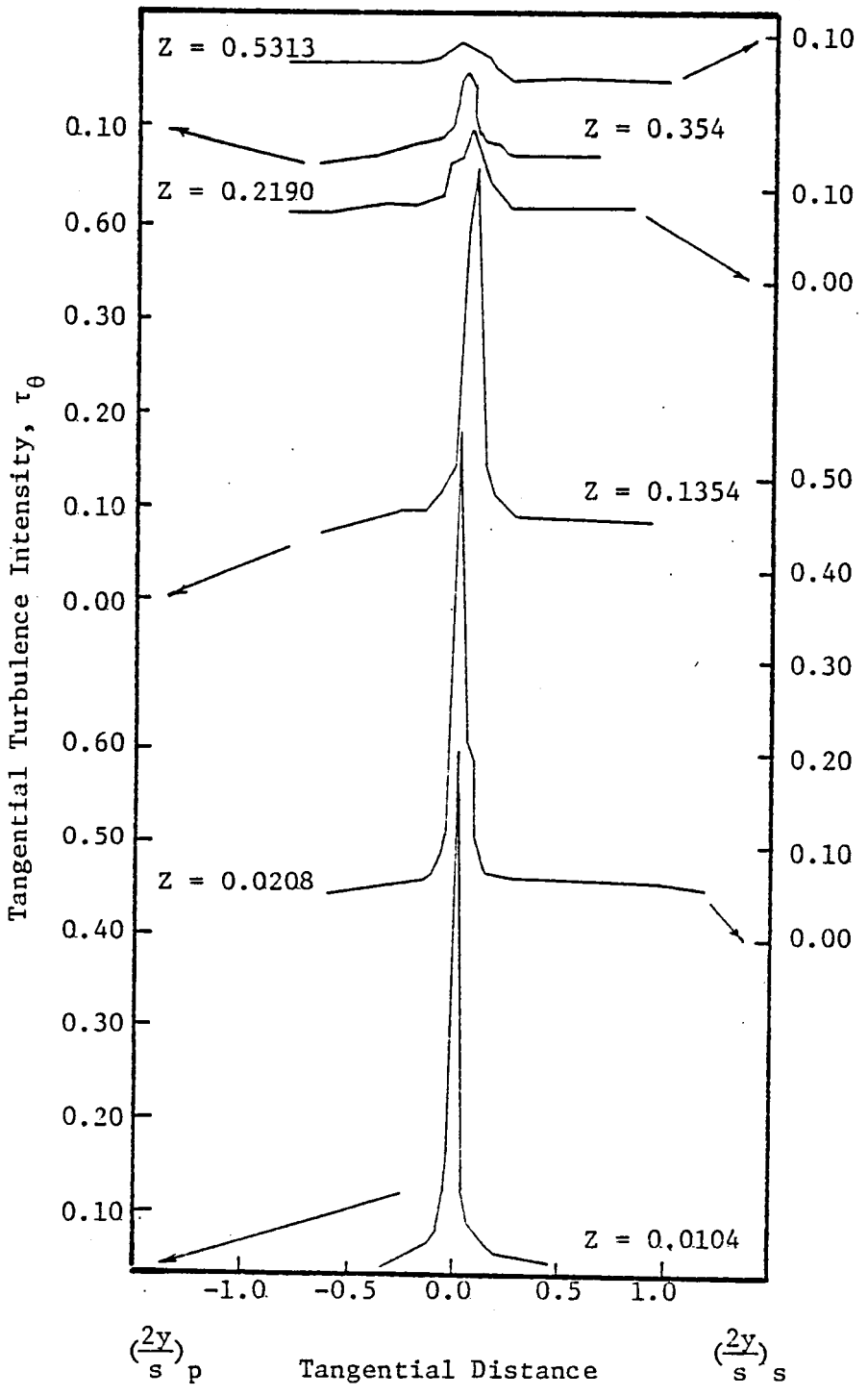

Figure 50. Tangential Turbulence Intensity Profiles, R = 0.7297, ϕ = 0.56

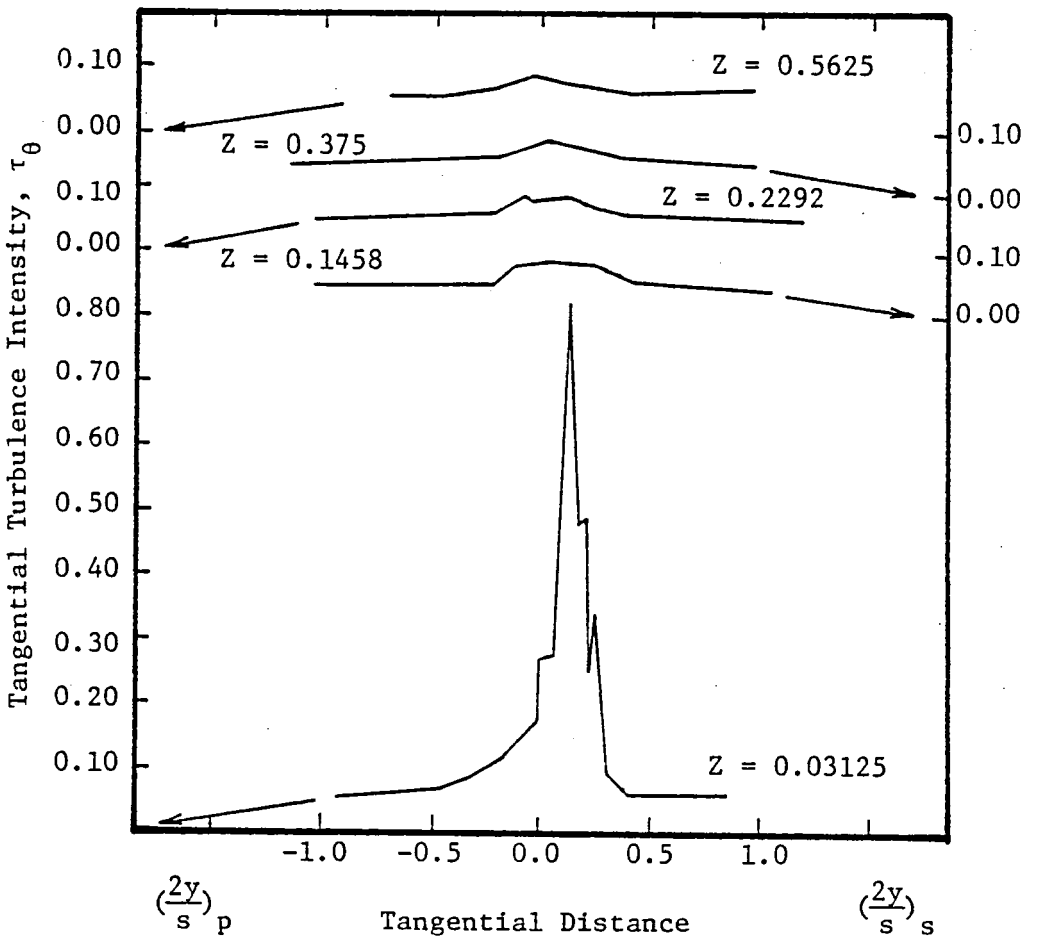

Figure 51. Tangential Turbulence Intensity Profiles, R = 0.7973, ϕ = 0.56

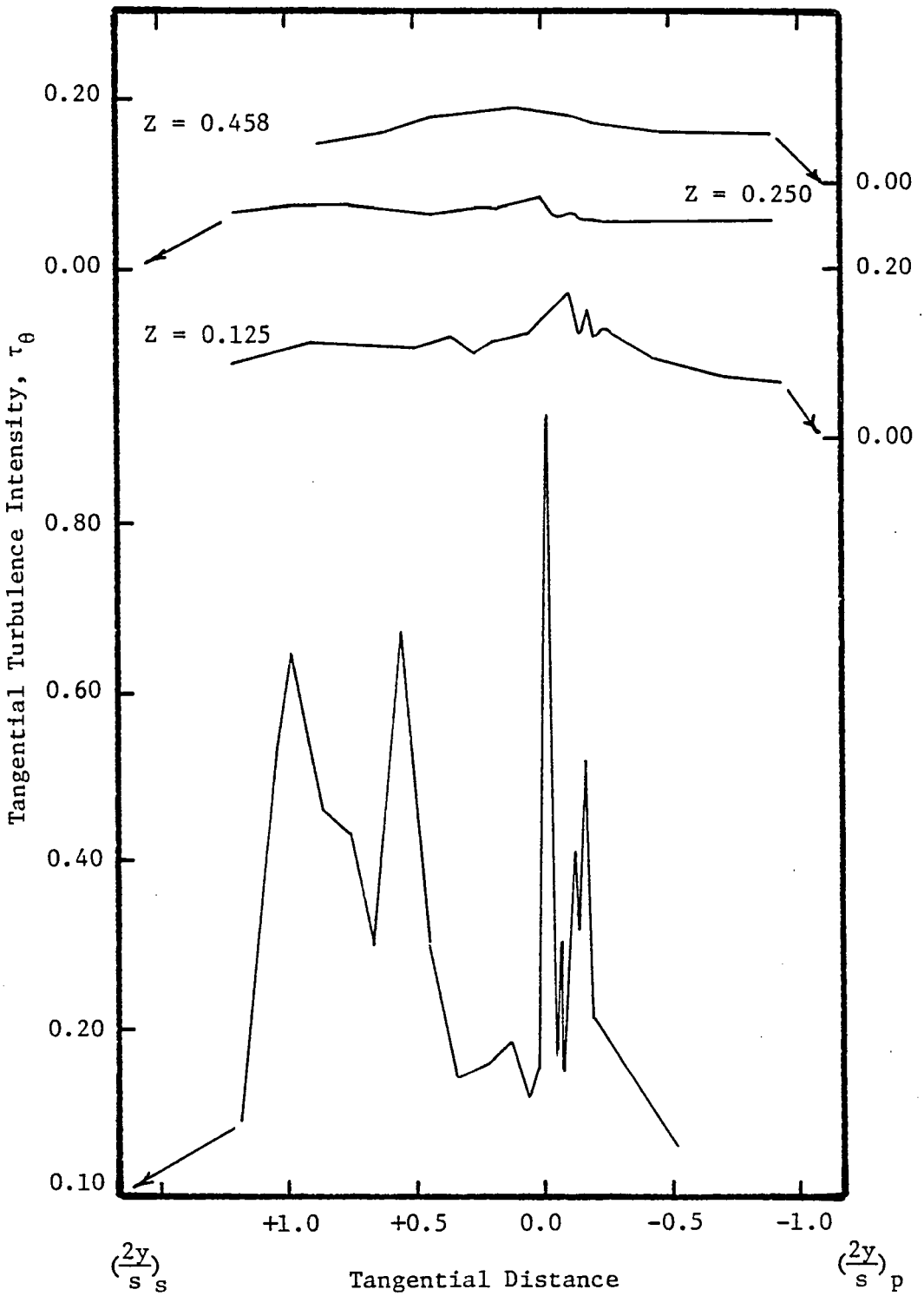

Figure 52. Tangential Turbulence Intensity Profiles, R = 0.9324, ϕ = 0.56

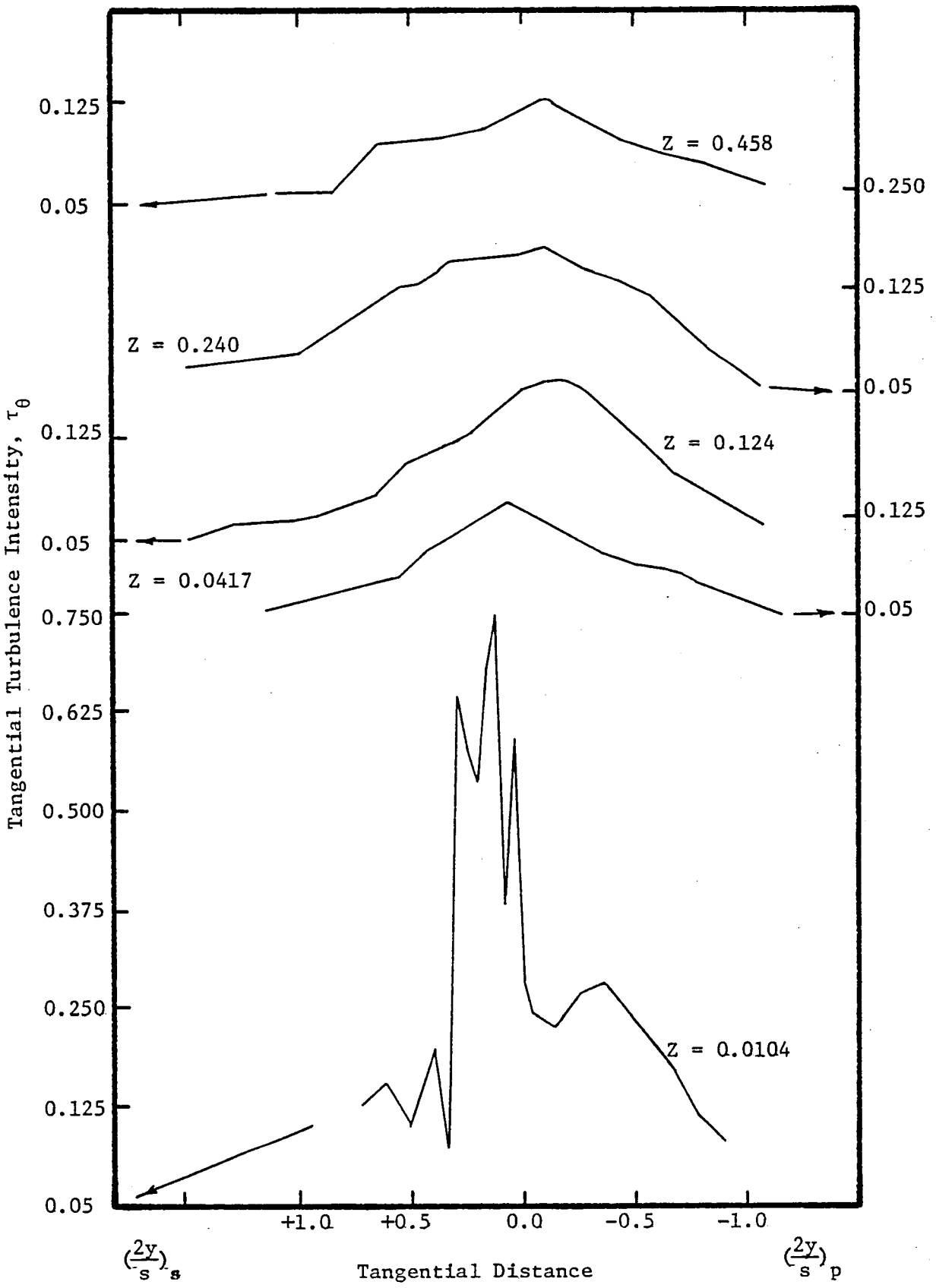

Figure 53. Tangential Turbulence Intensity Profiles, R = 0.9595, ϕ = 0.56

trends. The dominant effect of the tip-clearance vortex is seen in these plots. Not only is the turbulence intensity high, but it also extends to most of the passage which is attributed to the tip vortex arising due to the clearance flow. It is also interesting to note that the turbulence profile is highly unsymmetrical in the trailing-edge region which also reflects the effect of the tip vortex and the secondary flow on the turbulence intensity. The decay of the turbulence intensity in this region has to be viewed with some caution as we are not only dealing with the decay of the turbulence but also the decay of the vortex. In the trailing-edge region the decay is extremely rapid and becomes very gradual in the far-wake region with the free-stream tangential turbulence intensity remaining as high as six percent even at 0.458 chords downstream of the blade trailing-edge.

For the wake inside the hub-wall boundary layer the magnitude of the tangential turbulence intensity is very small, as can be seen in Figure 48. Not only is the magnitude of the intensities smaller, the decay is also slow compared to those outside the boundary layer. The effect of secondary flow that exists at the hub region can be seen in these plots.

The effect of blade loading on the turbulence intensity can be seen by comparing Figure 50 with Figure 4 of Lakshminarayana and Reynolds (1979). For a heavily loaded rotor the turbulence intensities are nearly 60 percent while for a lightly loaded fan blade the maximum value is less than 30 percent. Increase in blade loading not only increases the turbulence levels, but also increases the decay rate. Tangential and axial turbulence intensities are of the same order with similar profiles and decay characteristics.

3.4.3 Radial turbulence intensity

Radial turbulence intensity profiles for various radii from hub-to-tip are shown plotted in Figure 54 through 59. Figure 54, R = 0.5676, represents the region inside the hub-wall boundary layer, Figures 55, 56, and 57 for the radii R = 0.6581, 0.7297, and 0.7973 outside the end-wall boundary layers while Figures 58 and 59 for R = 0.9324 and 0.9595 inside the annulus-wall boundary layer. The abscissa in these figures represents the tangential distance normalized to half-the-blade spacing while the ordinate represents the radial turbulence intensity normalized by the local mean velocity.

Radial turbulence intensity profiles are asymmetric in the trailing-edge and near-wake regions. Not only do the profiles show marked changes from one radius to the other; so do the decay rates.

Radial intensities in the free-stream are found to be approximately two to four percent for all the radii. These intensities are larger than the axial and tangential components. At the wake center the radial velocities are very high and reach nearly the same value as axial velocity in the trailing-edge region. The existance of these large radial components of intensities demonstrates the three-dimensional nature of the rotor-wake. Large radial intensities result from centrifugal and Coriolis force effects on the rotor-blade boundary layers and on the wake flow. Anand and Lakshminarayana (1978) have reported dominant radial component in their measurement on helical inducer blades.

It is noted for comparison that the radial turbulence intensity decay is by far the slowest compared to the axial and tangential turbulence intensity decays. This indicates that the rotation effects are significant in the turbulence intensity structure of the rotor-wake.

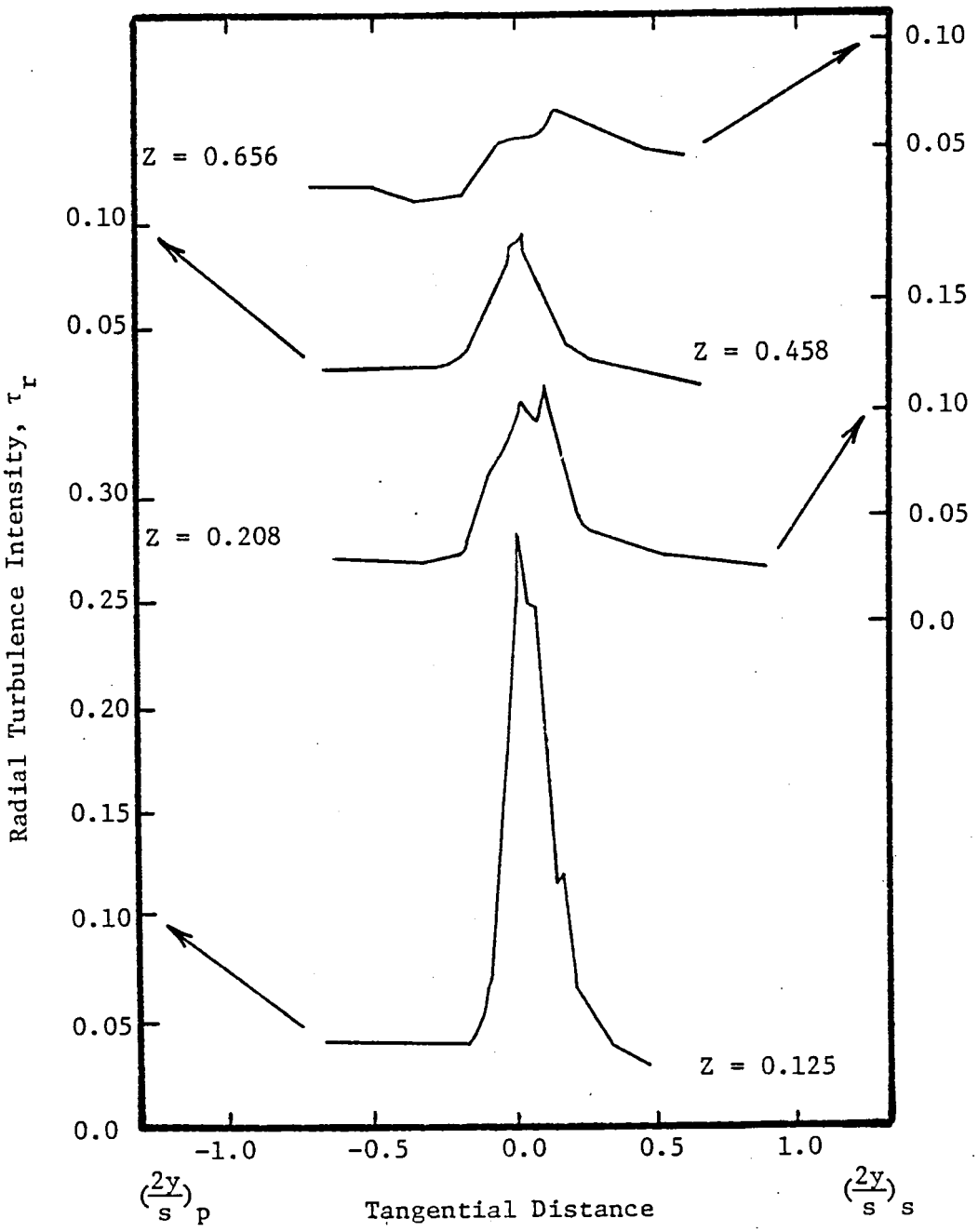

Figure 54. Radial Turbulence Intensity Profiles, R = 0.5676, ϕ = 0.56

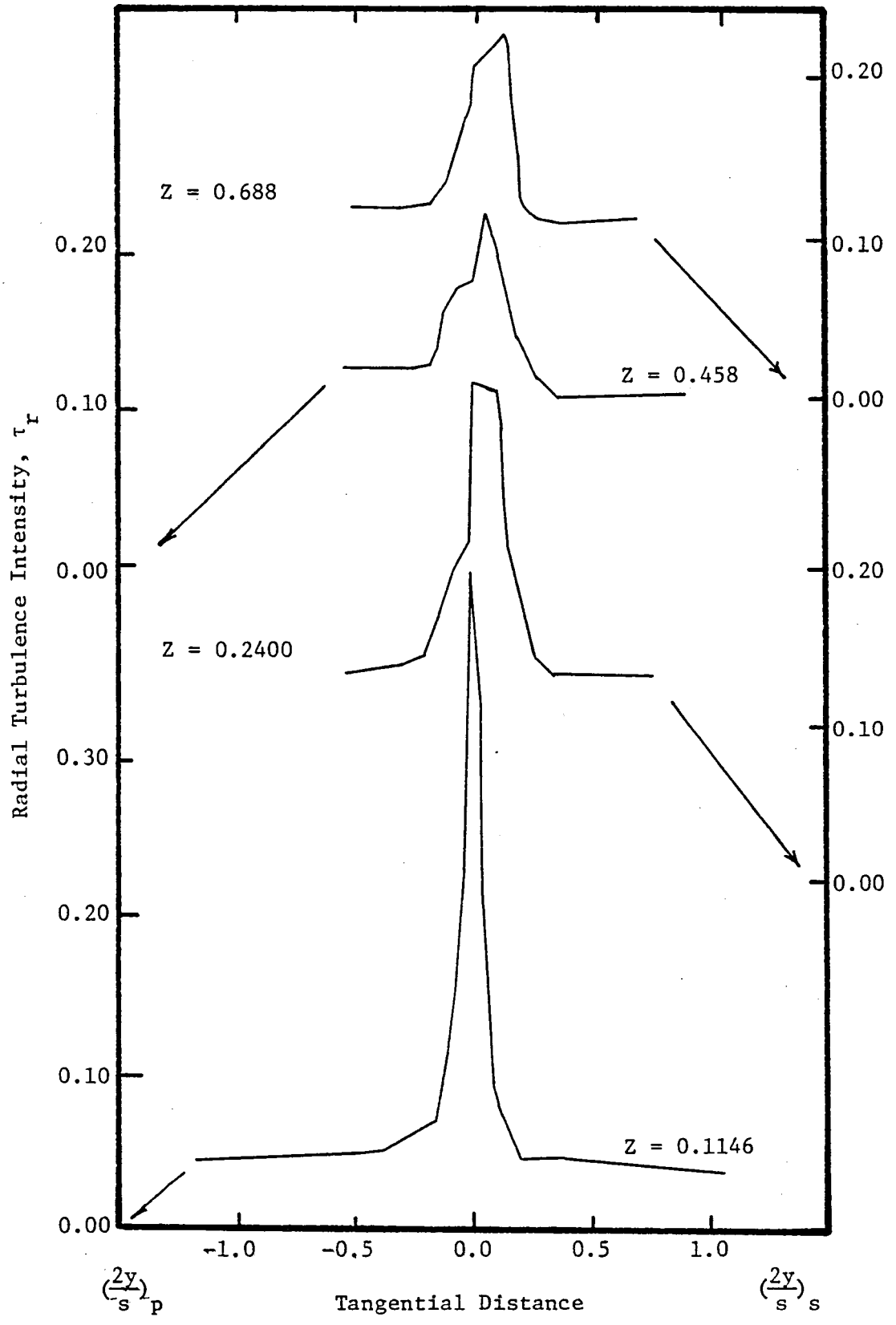

Figure 55. Radial Turbulence Intensity Profiles, R = 0.6581, ϕ = 0.56

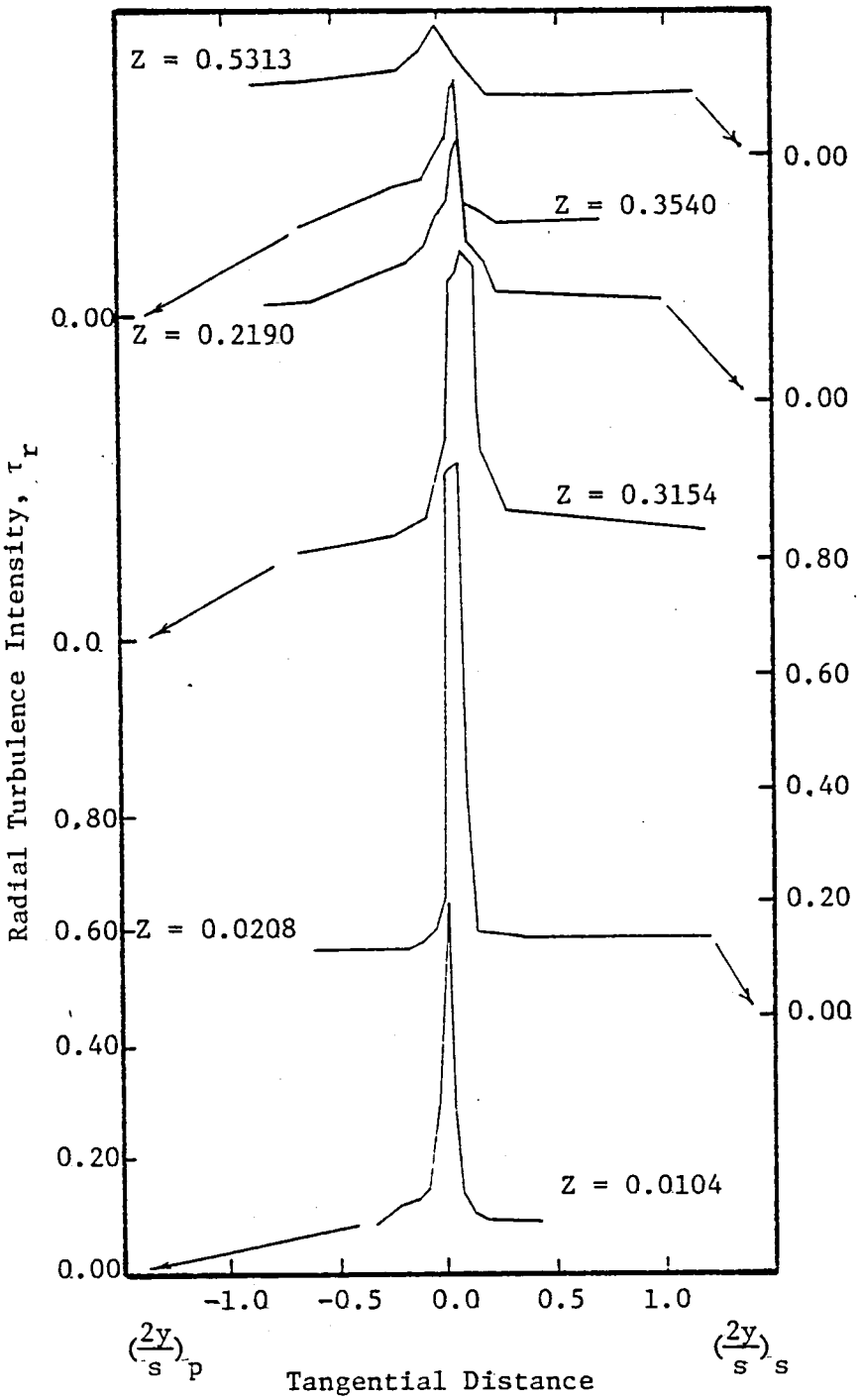

Figure 56. Radial Turbulence Intensity Profiles, R = 0.7297, ϕ = 0.56

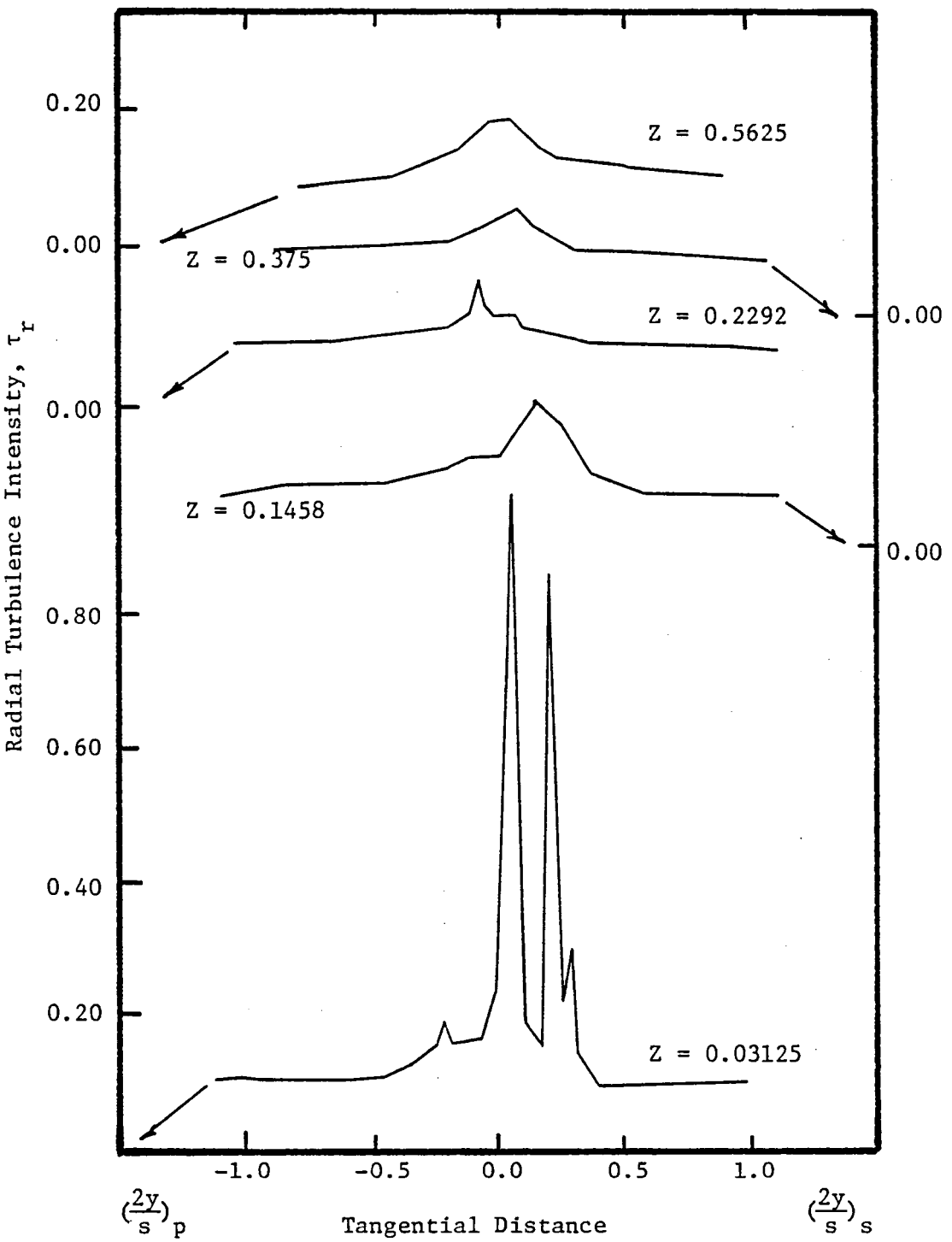

Figure 57. Radial Turbulence Intensity Profiles, R = 0.7973, ϕ = 0.56

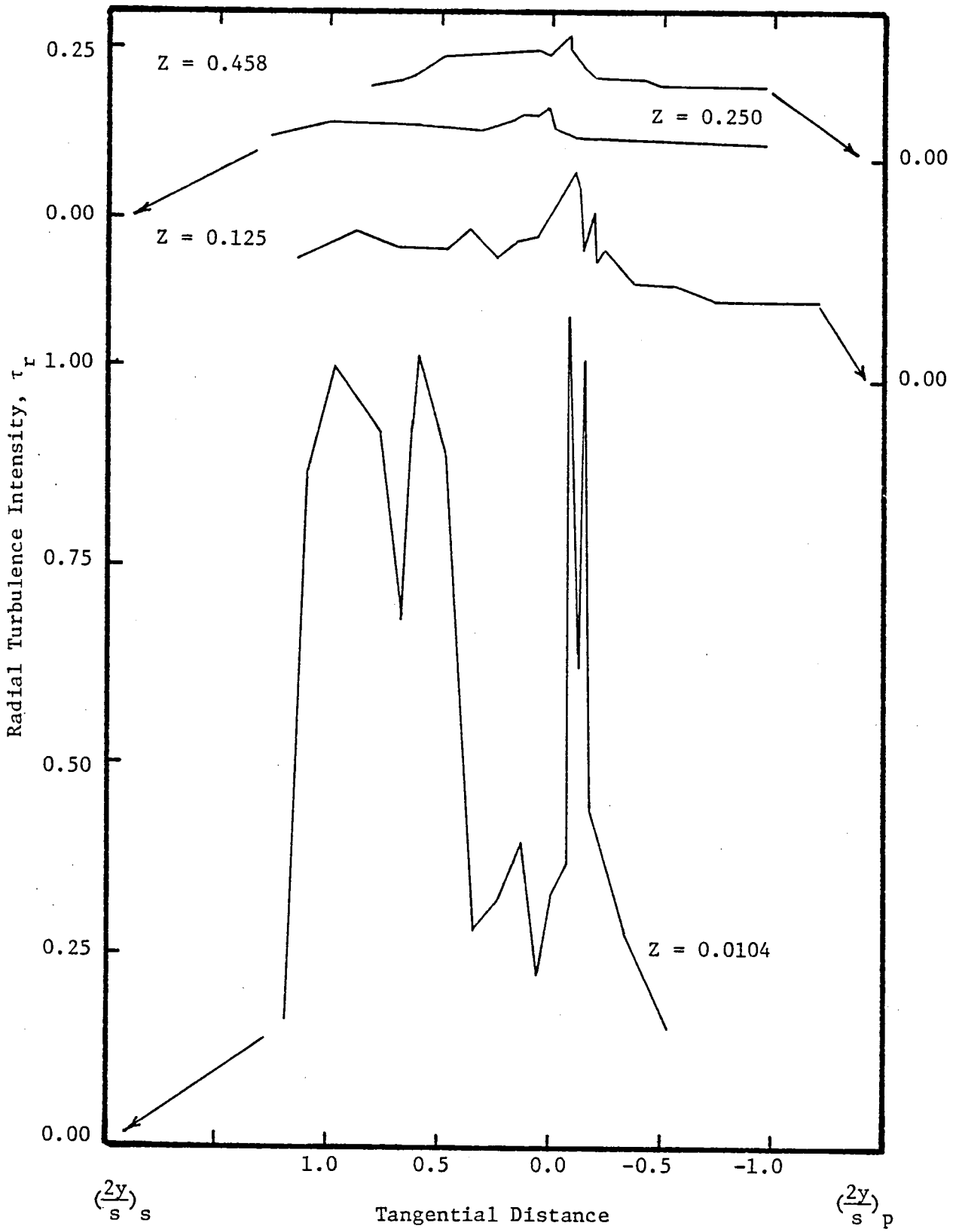

Figure 58. Radial Turbulence Intensity Profiles, R = 0.9324, θ = 0.56

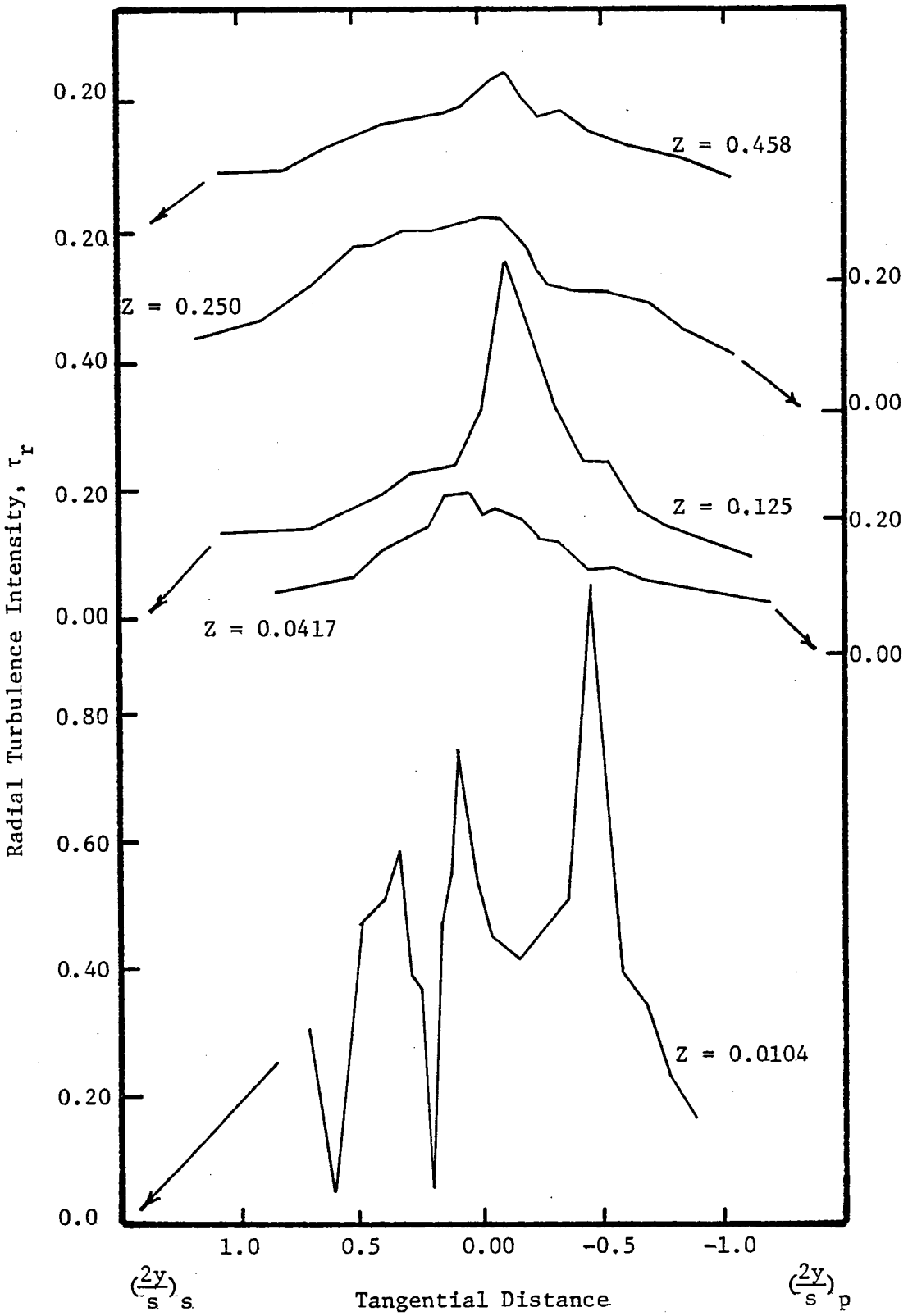

Figure 59. Radial Turbulence Intensity Profiles, R = 0.9595, ϕ = 0.56

As seen from Figure 56, for R = 0.7297 and at Z = 0.0104, the radial turbulence intensity reaches a value of 0.65 which at Z = 0.0208 becomes 0.96 which indicates the effect of the trailing vortex on the radial turbulence intensity. The increase in turbulence intensity at these two locations might indicate the development of the vortex which initially grows stronger before it starts to decay. At Z = 0.1354 the value of radial component of turbulence intensity is about 0.65 and beyond that the radial turbulence intensity decreases monotonically and reaches a value of nearly 0.25 at half-a-chord downstream.

The dip in profile that was observed in the case of axial intensity was noticed for the radial turbulence intensity for the wakes inside the annulus- and hub-wall boundary layers (Figures 54, 58, and 59). At R = 0.9595 another interesting feature was noted, namely that the intensities decayed rather rapidly increasing again before showing a peak. Beyond Z = 0.25 it decayed very slowly to a value of 0.2 at Z = 0.458. This shows the effect of tip vortex and secondary flow on the radial turbulence intensity. In general, at these locations the intensities were high and they covered one entire passage. The complex flow phenomena in this region can be attributed to the interaction of secondary flow, tip leakage-flow and the associated tip-vortex, and the annulus-wall boundary layer. The presence of vortex near the tip is clearly seen in Figures 58 and 59. There are two distinct profiles, one of which is due to the vortex and the other due to wake.

It was previously argued that the radial turbulence intensities are markedly influenced by the centrifugal forces arising due to rotation. This is very clearly seen for the wake at the radius R = 0.5676. Here the turbulence intensities are an order of magnitude lower than those at

the tip. Here also the dip in the intensity profiles is observed and the dip tends to persist for a longer distance downstream of the blade trailing-edge than at a higher radius. This might be due to the effect of secondary flow at the hub and the hub-wall boundary layer which has a tendency to slow down the decay.

Raj and Lumley (1976) and Lakshminarayana and Reynolds (1979) have given a theoretical explanation of the redistribution of energy between the three components of fluctuating velocities and have shown that the effect of Coriolis force is to redistribute the energy such that $\tau_r \geq \tau_s$ in a compressor. This trend is generally true in this case with the axial and radial intensities of the same order of magnitude. However in a non-rotating case $\tau_s > \tau_r$. It is also seen that beyond half-a-chord downstream of the blade the turbulence becomes isotropic with all the three components of intensities having nearly the same values.

3.5 Turbulence Shear Stress Profiles

The streamwise (τ_{sn}) and radial component (τ_{nr}) of the Reynolds stress as well as the correlation (τ_{sr}) are shown plotted in Figures 60 through 77. Only the data in the s-n-r (natural coordinates) are given as they are the ones which are of any practical interest. All the Reynolds stresses given here are normalized to the local dynamic pressure. The tangential distances are normalized to half the blade spacing. The turbulent stresses are very small in the free-stream and increase in magnitude near the wake center, where they reach a maximum value. This type of trend is to be expected as the production of stresses is brought about by velocity and turbulence intensity gradients.

The variation of the streamwise stress, τ_{sn}, across the wake is shown plotted in Figures 60 through 65. These plots show the expected

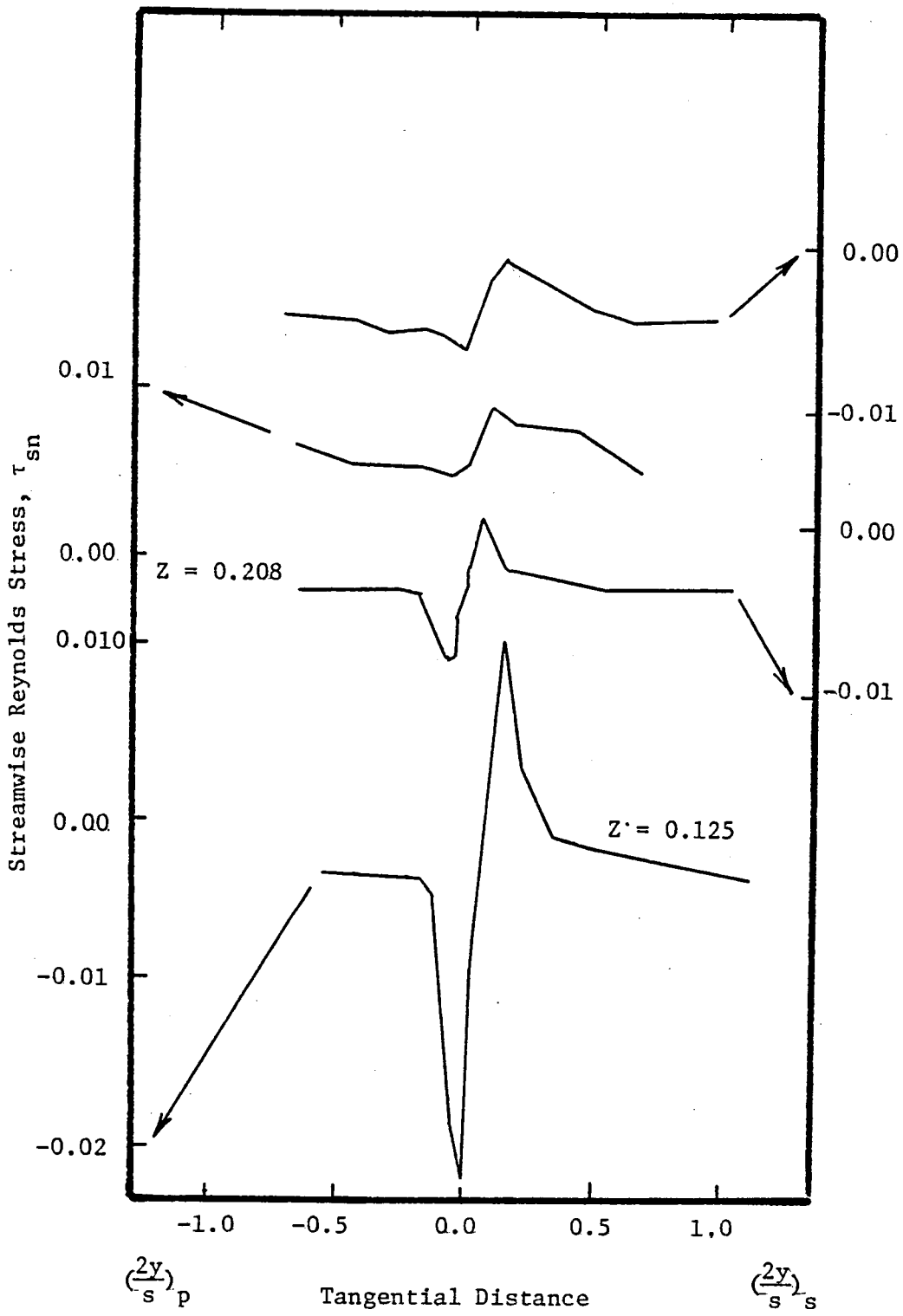

Figure 60. Streamwise Reynolds Stress Profiles, R = 0.5676, ϕ = 0.56

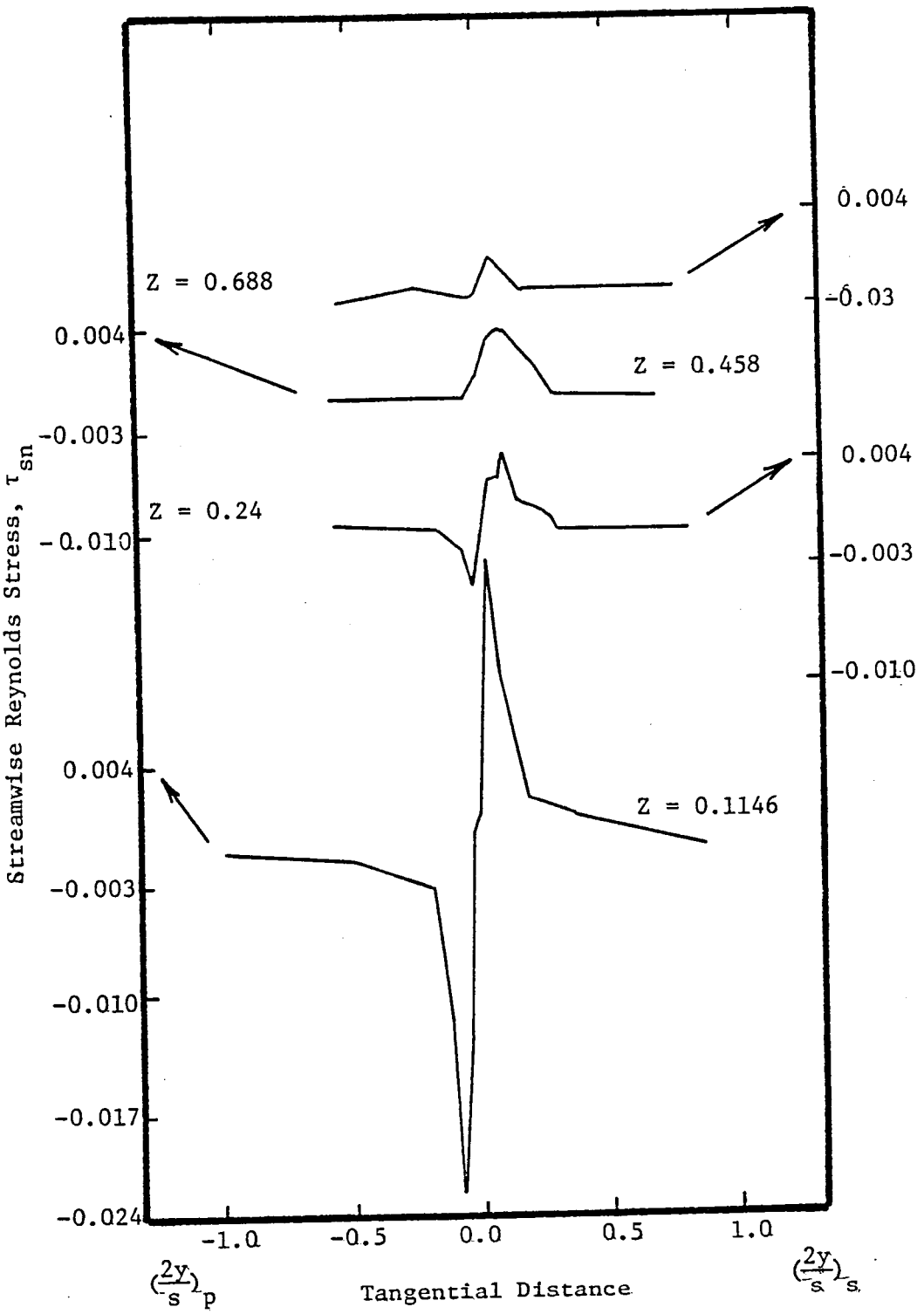

Figure 61. Streamwise Reynolds Stress Profiles, R = 0.6581, ϕ = 0.56

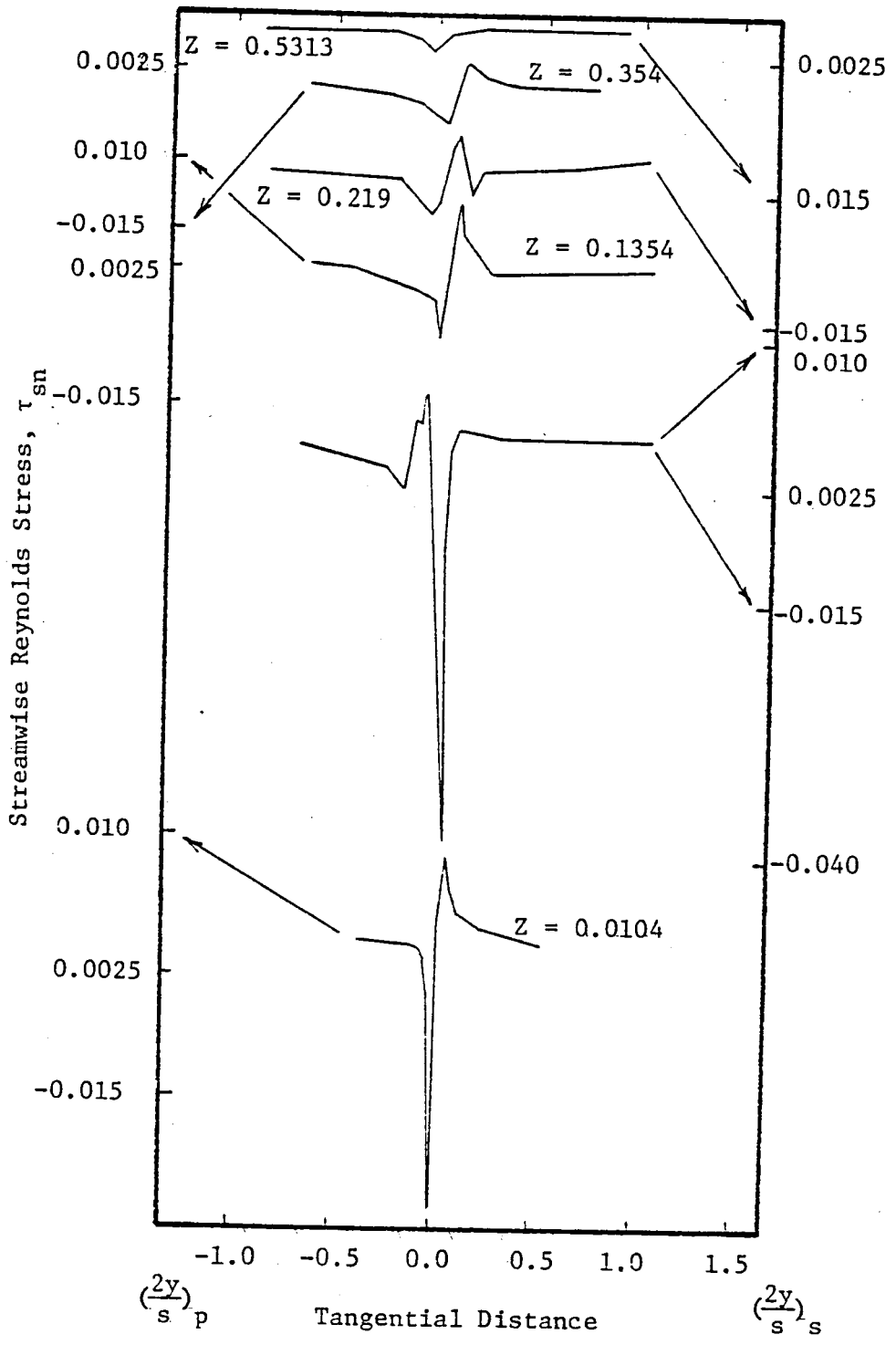

Figure 62. Streamwise Reynolds Stress Profiles, R = 0.7297, ϕ = 0.56

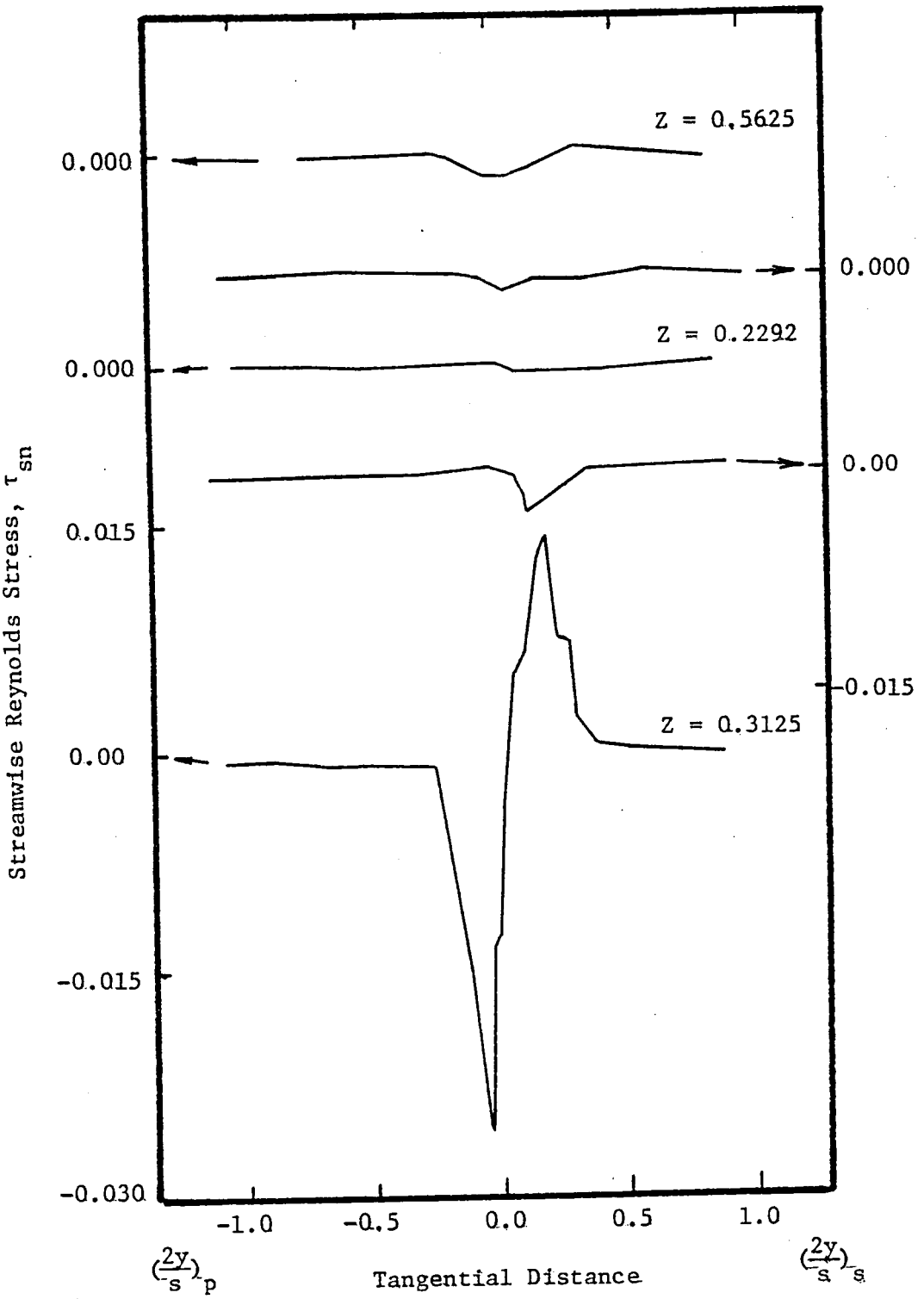

Figure 63. Streamwise Reynolds Stress Profiles, R = 0.7973, ϕ = 0.56

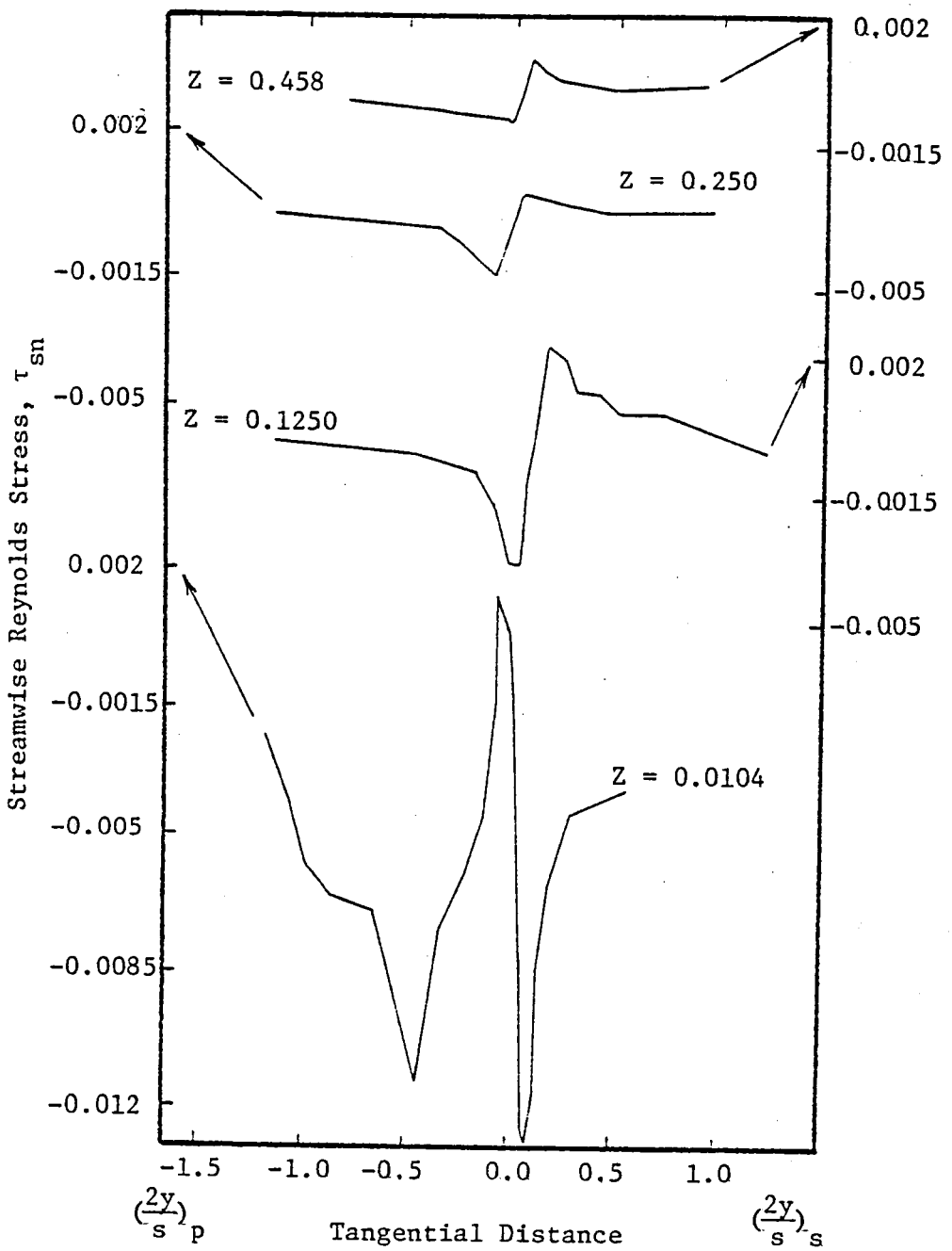

Figure 64. Streamwise Reynolds Stress Profiles, R = 0.9324, ϕ = 0.56

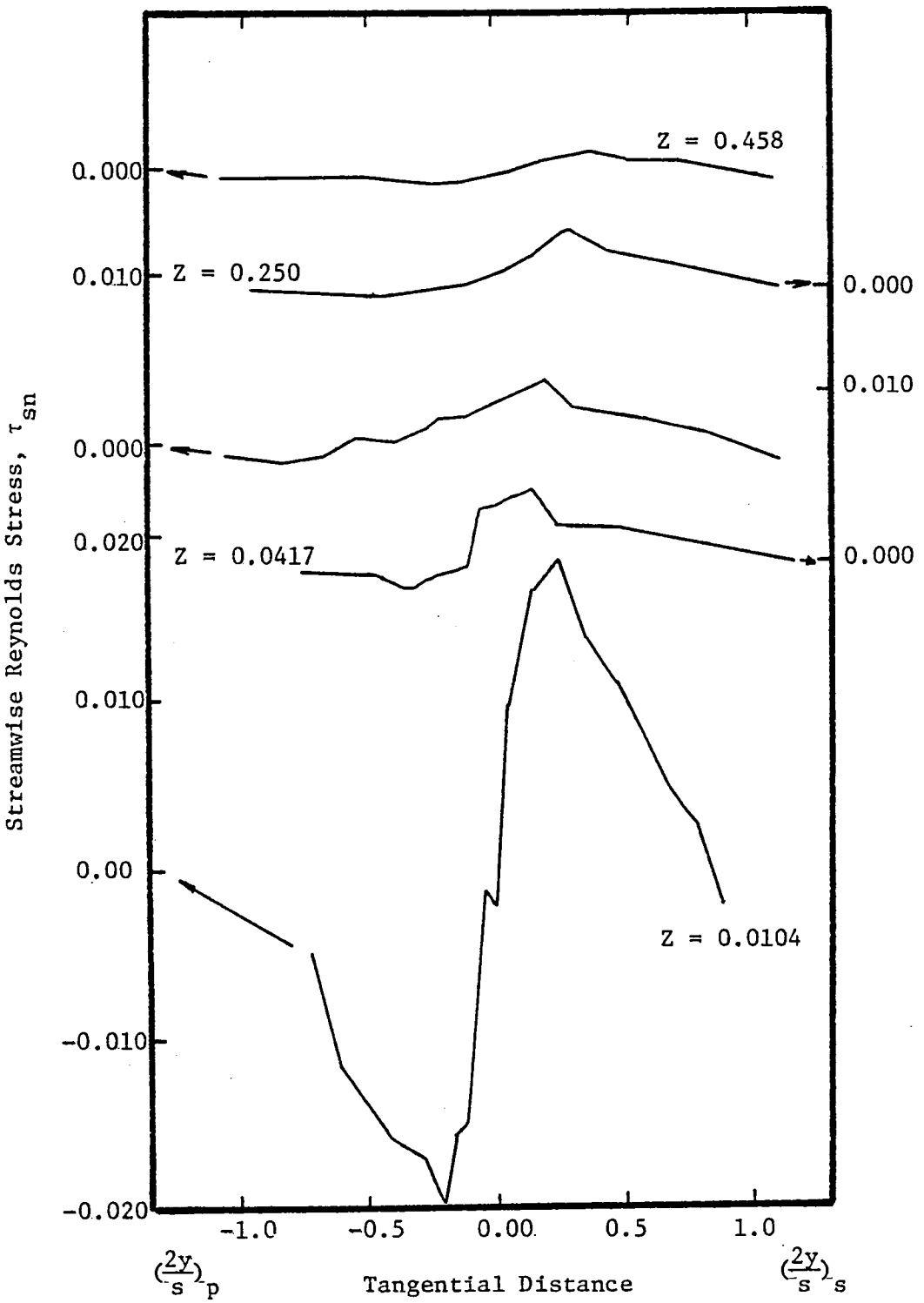

Figure 65. Streamwise Reynolds Stress Profiles, R = 0.9595, ϕ = 0.56

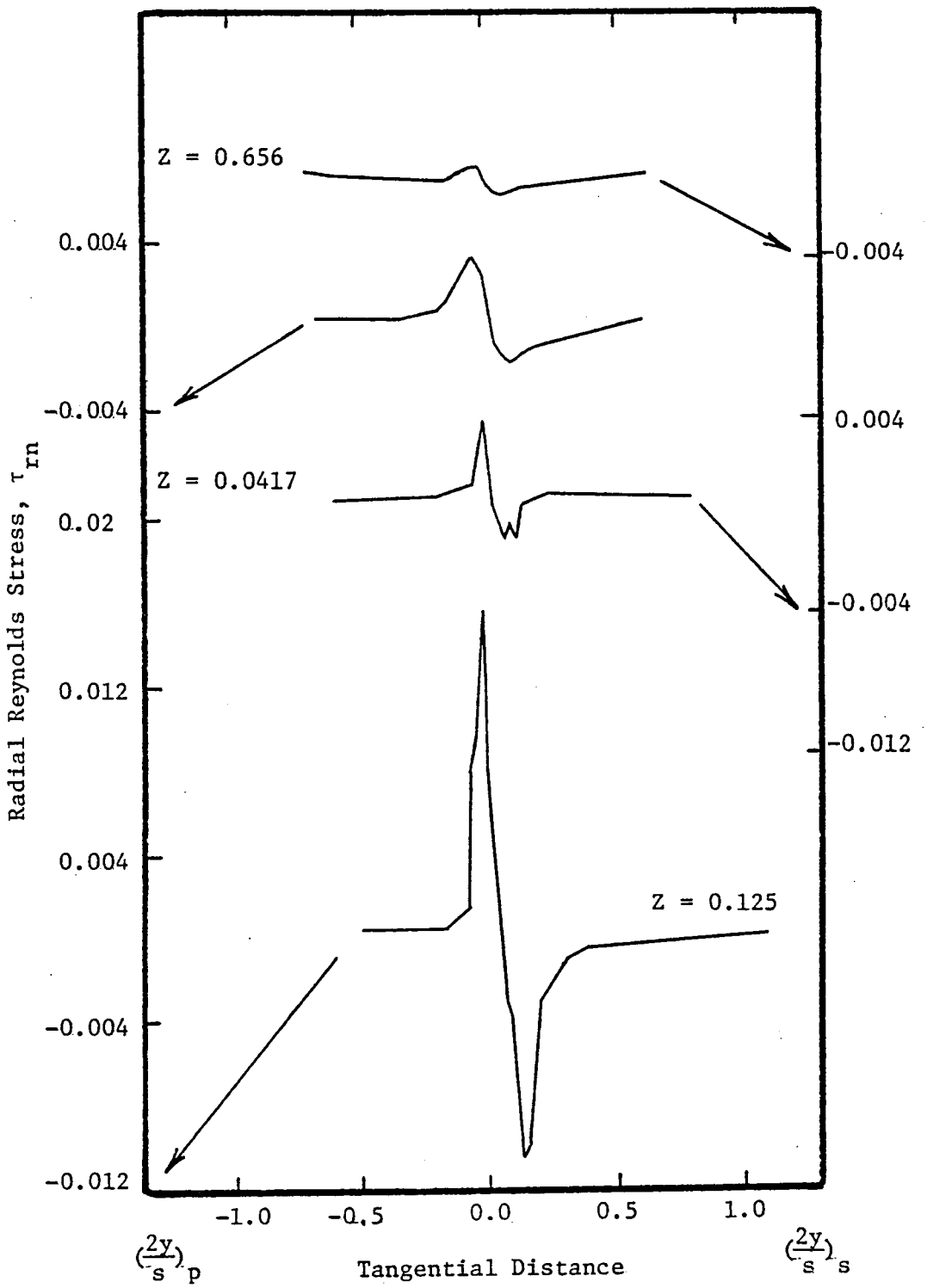

Figure 66. Radial Reynolds Stress Profiles, R = 0.5676, ϕ = 0.56

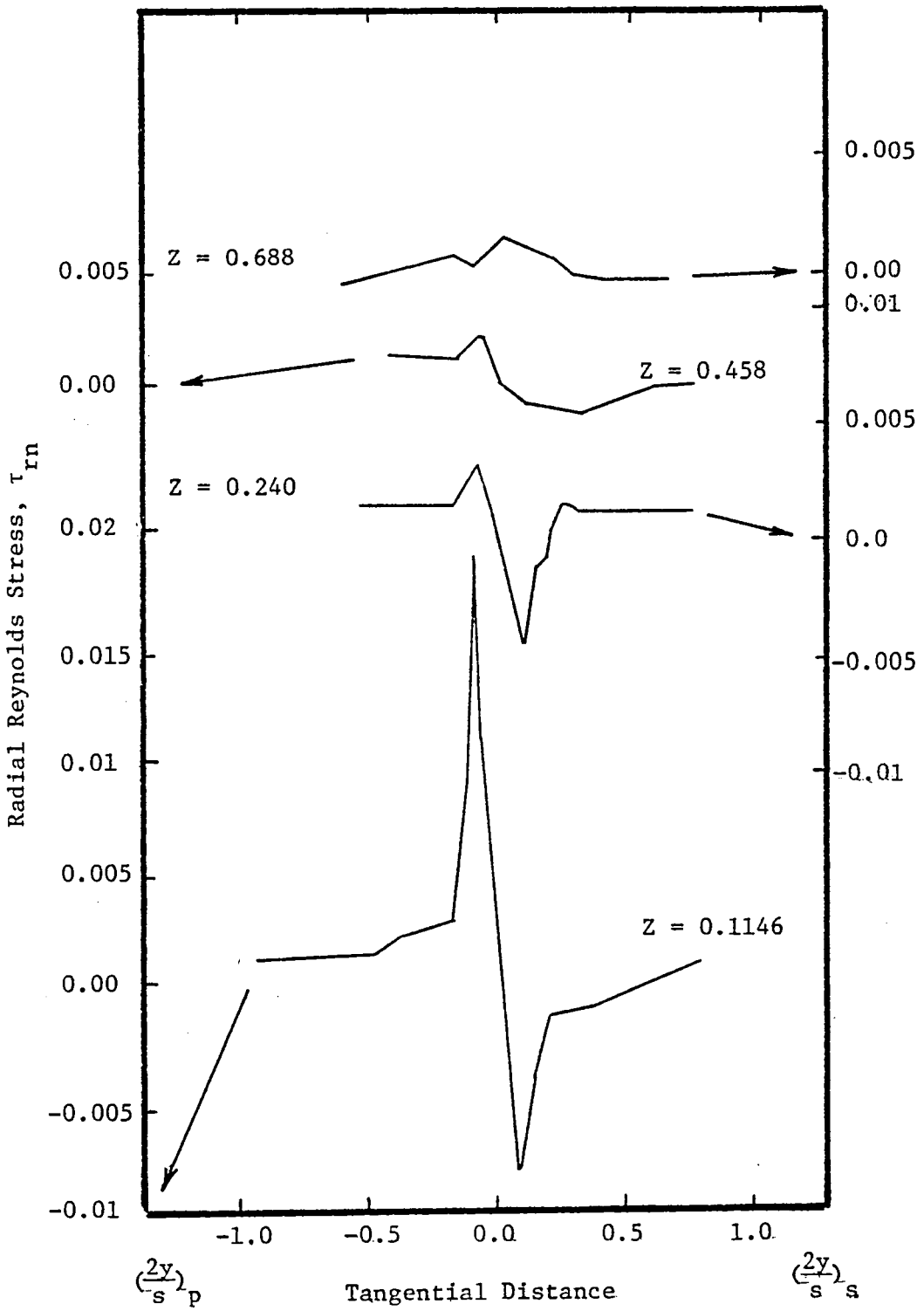

Figure 67. Radial Reynolds Stress Profiles, R = 0.6581, ϕ = 0.56

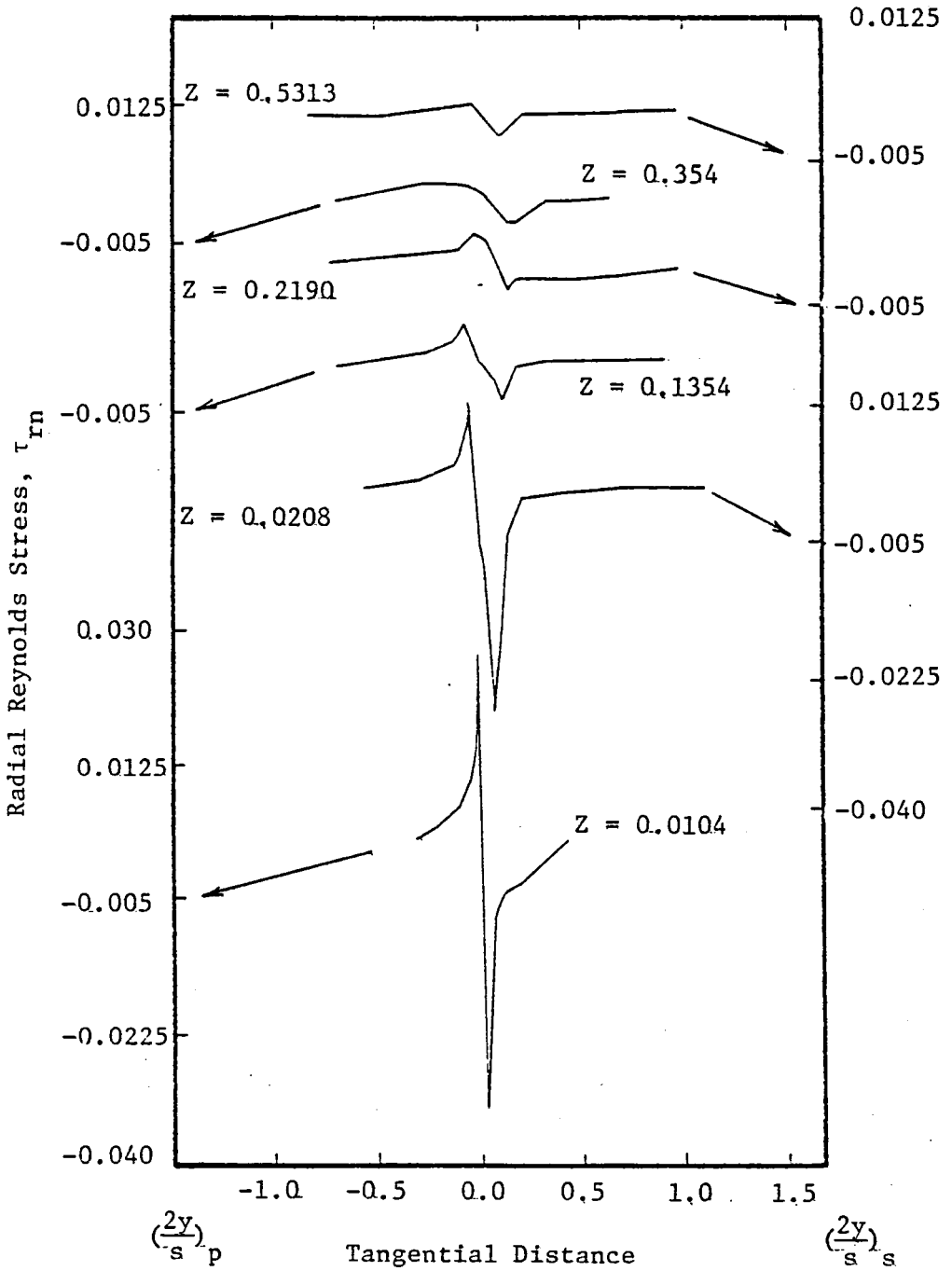

Figure 68. Radial Reynolds Stress Profiles, R = 0.7297, ϕ = 0.56

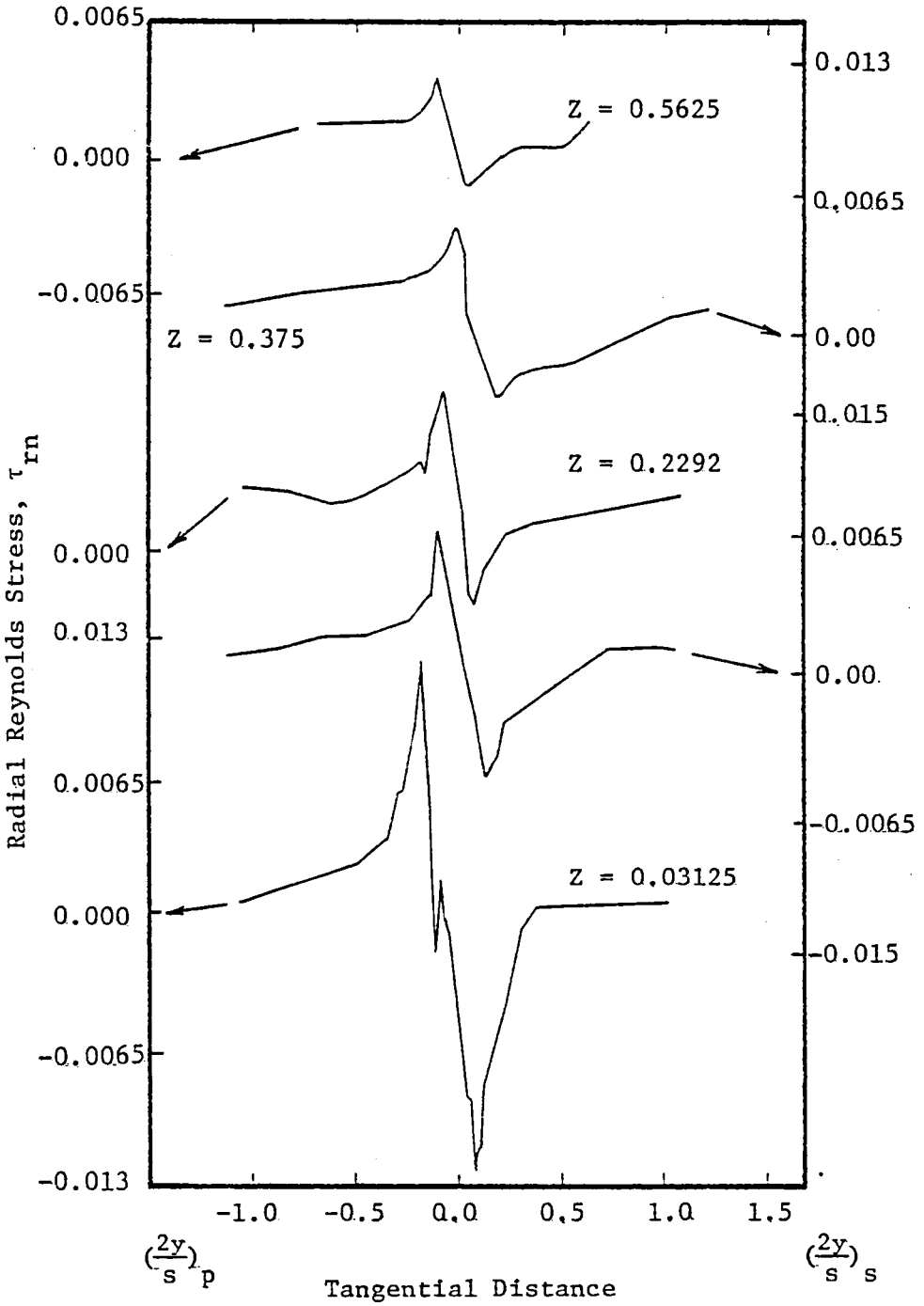

Figure 69. Radial Reynolds Stress Profiles, R = 0.7973, ϕ = 0.56

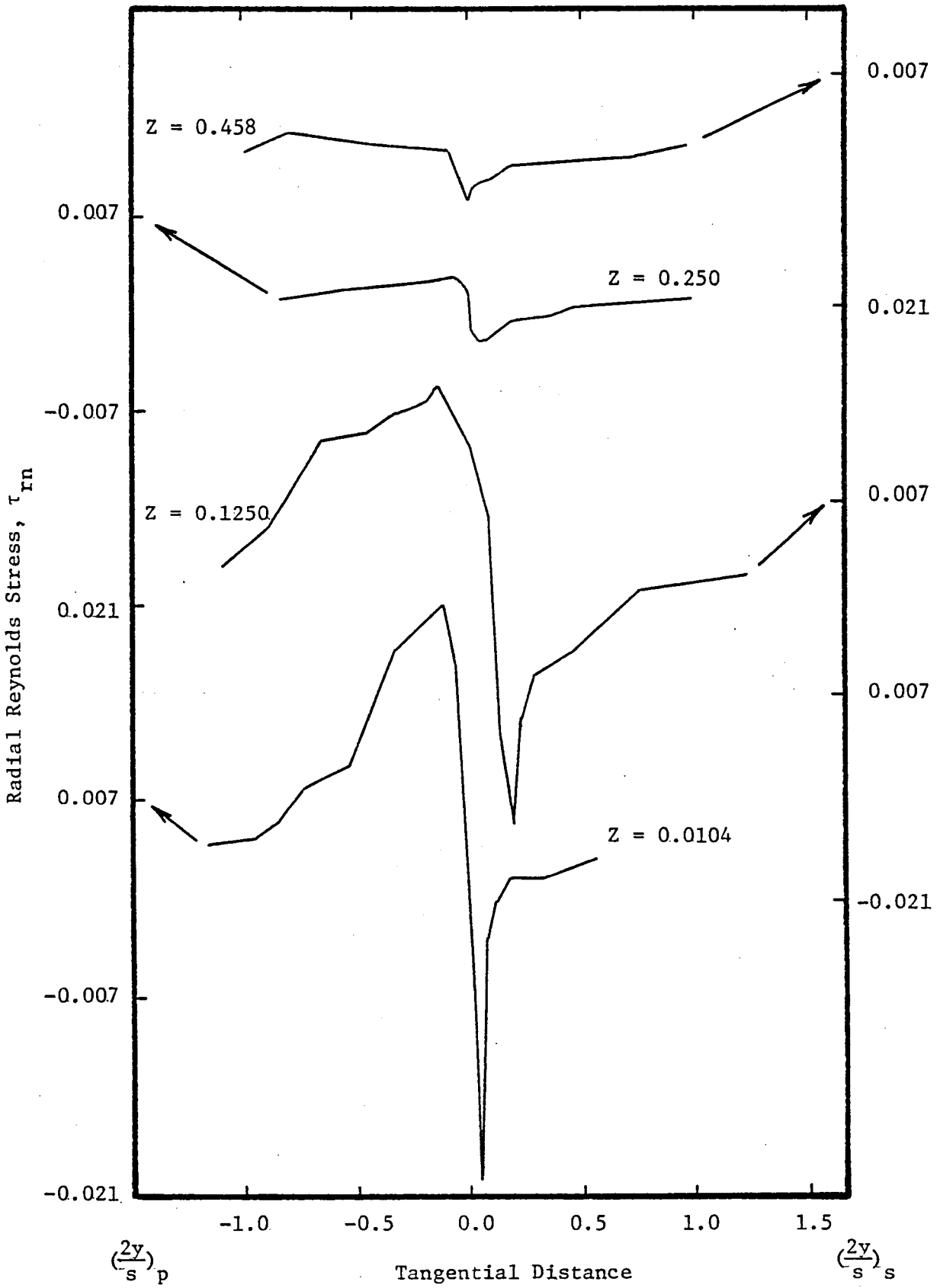

Figure 70. Radial Reynolds Stress Profiles, R = 0.9324, ϕ = 0.56

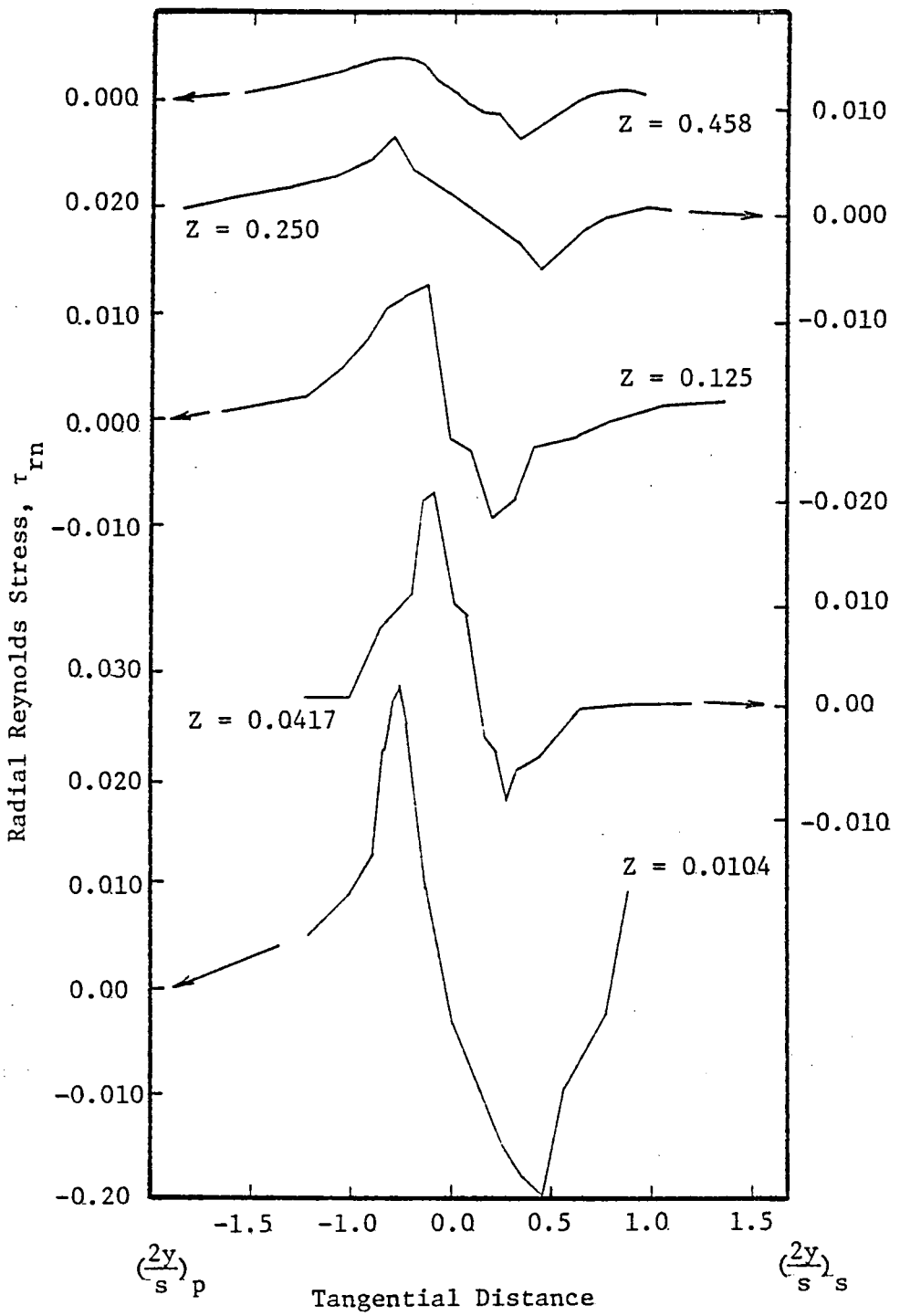

Figure 71. Radial Reynolds Stress Profiles, R = 0.9595, ϕ = 0.56

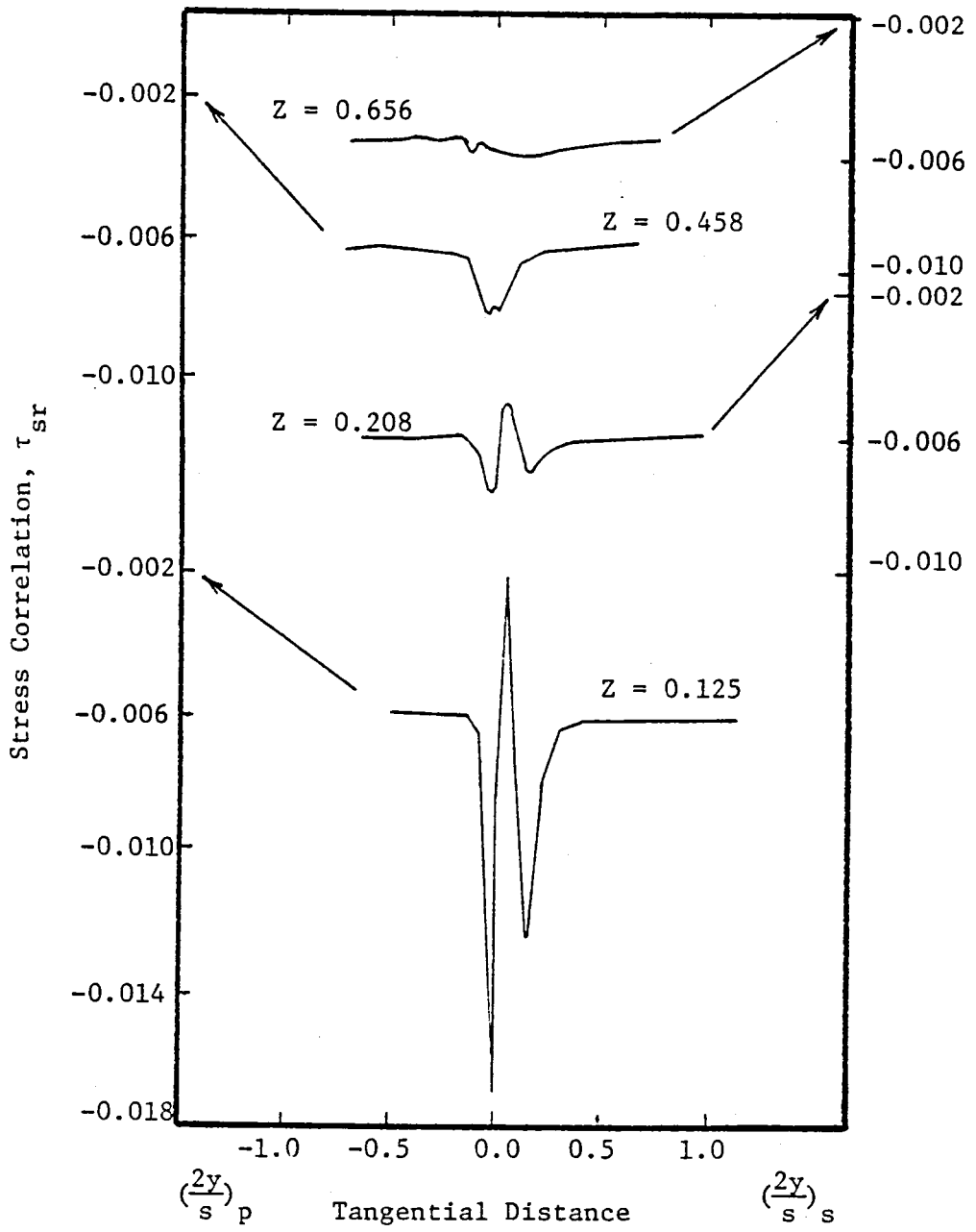

Figure 72. Stress Correlation Profiles, R = 0.5676, ϕ = 0.56

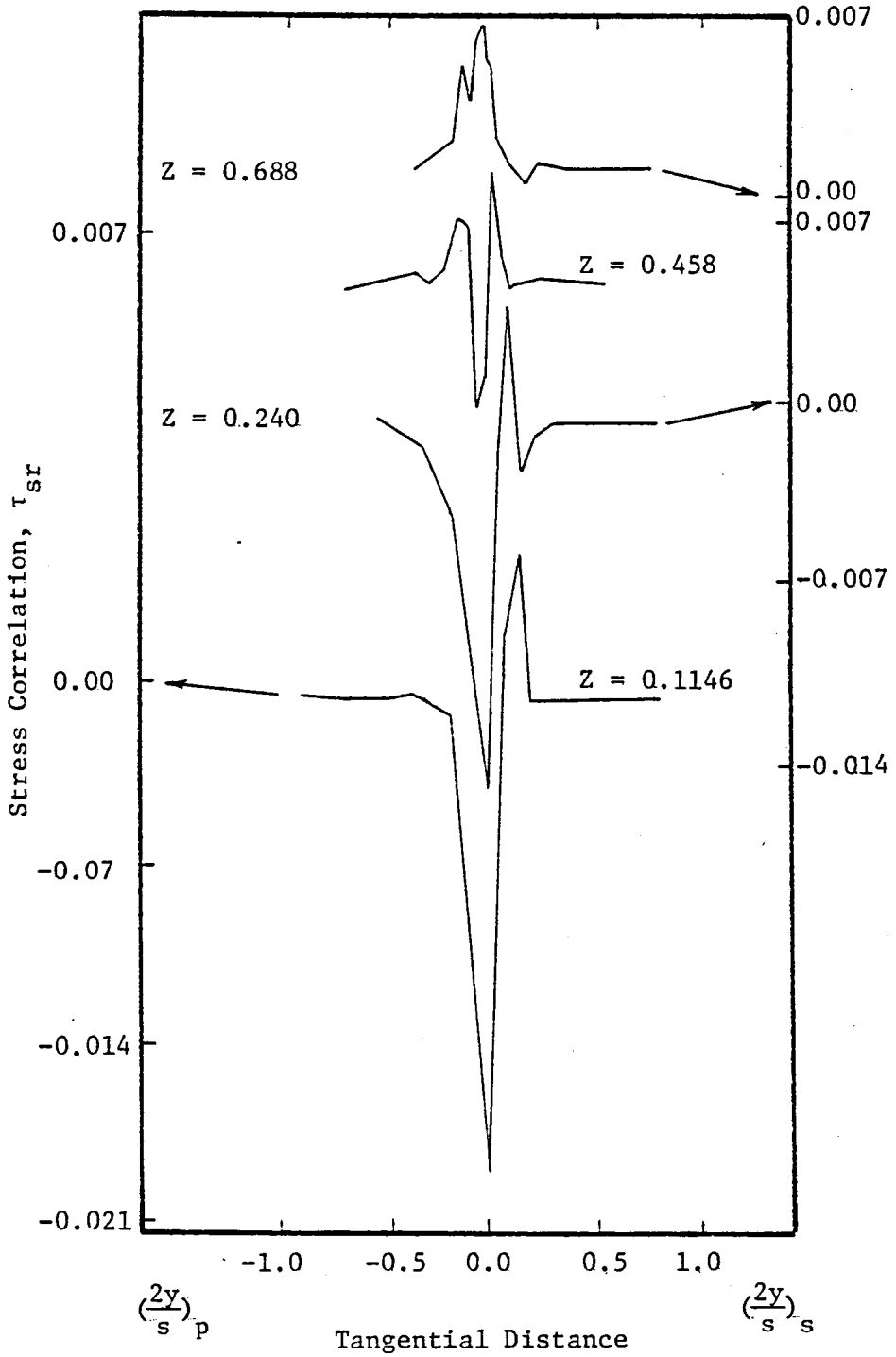

Figure 73. Stress Correlation Profiles, R = 0.6581, ϕ = 0.56

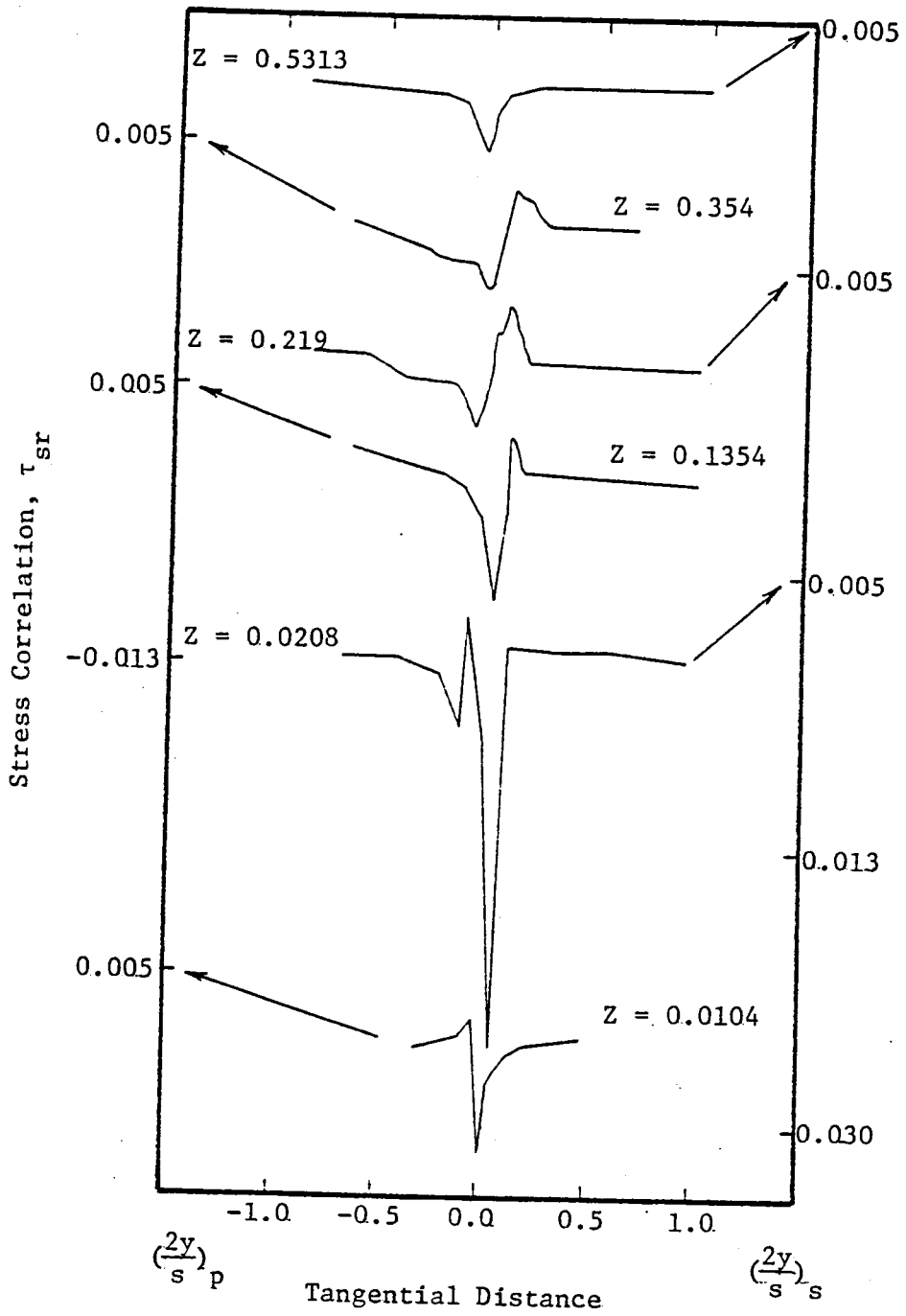

Figure 74. Stress Correlation Profiles, R = 0.7297, ϕ = 0.56

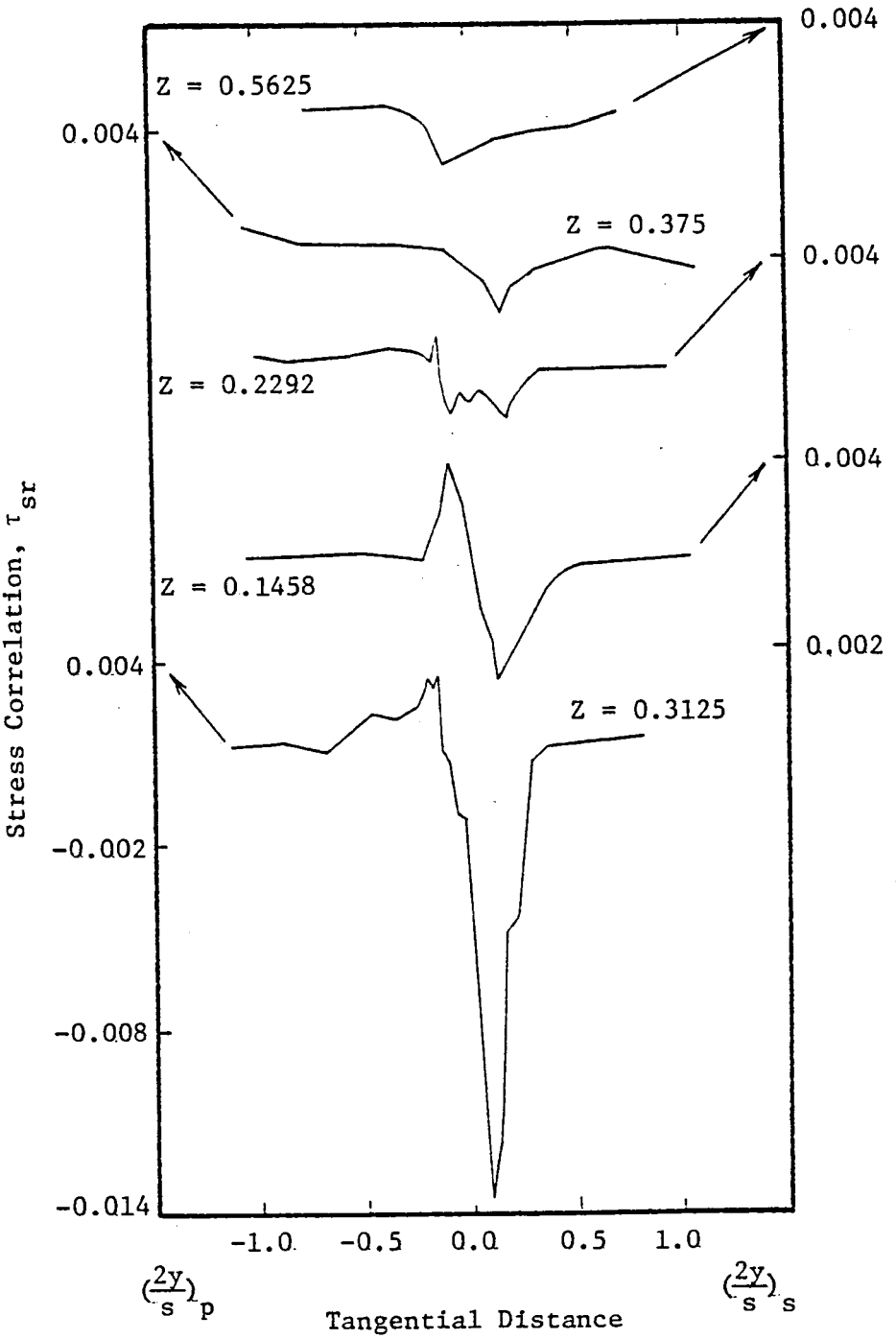

Figure 75. Stress Correlation Profiles, R = 0.7973, ϕ = 0.56

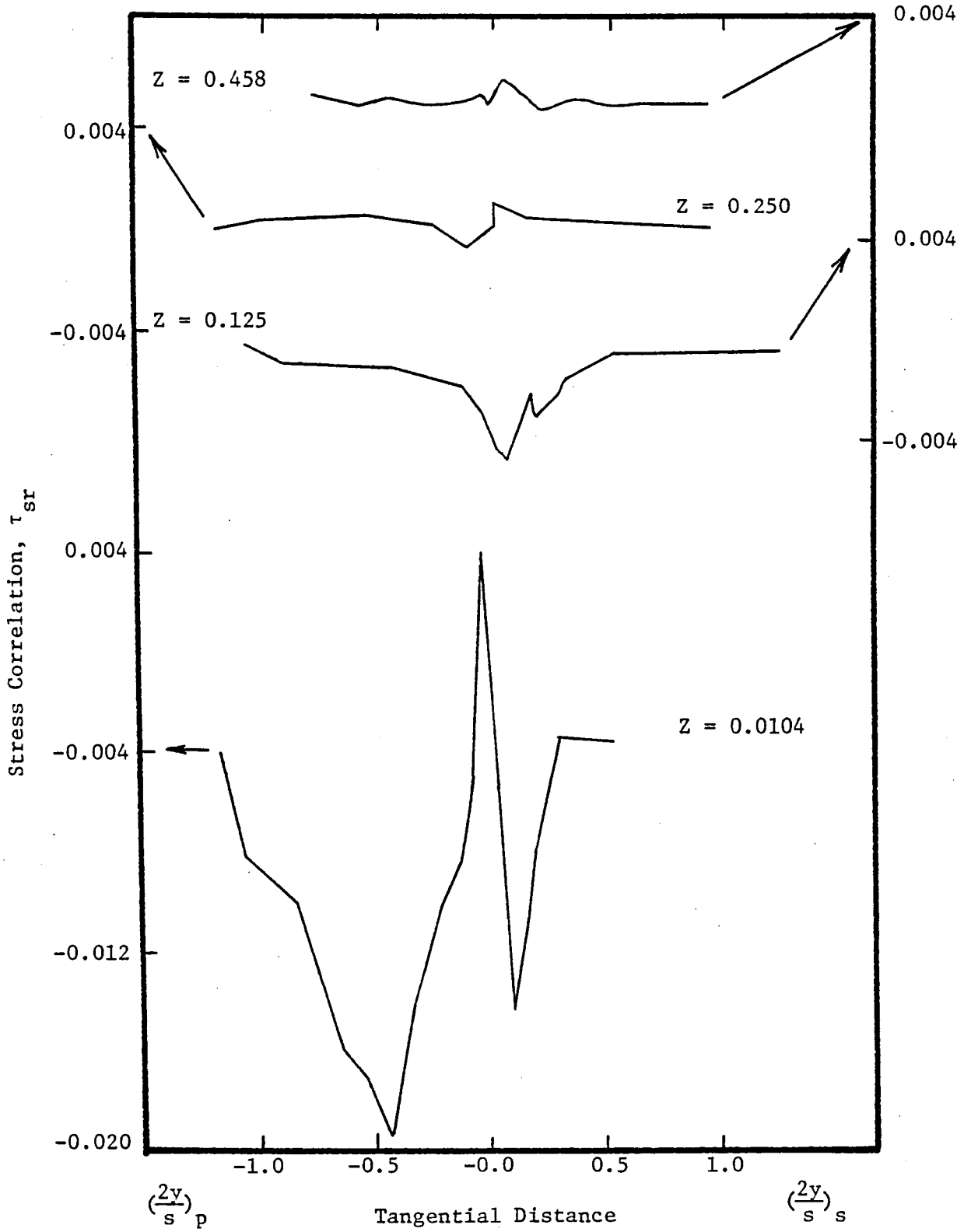

Figure 76. Stress Correlation Profiles, R = 0.9324, ϕ = 0.56

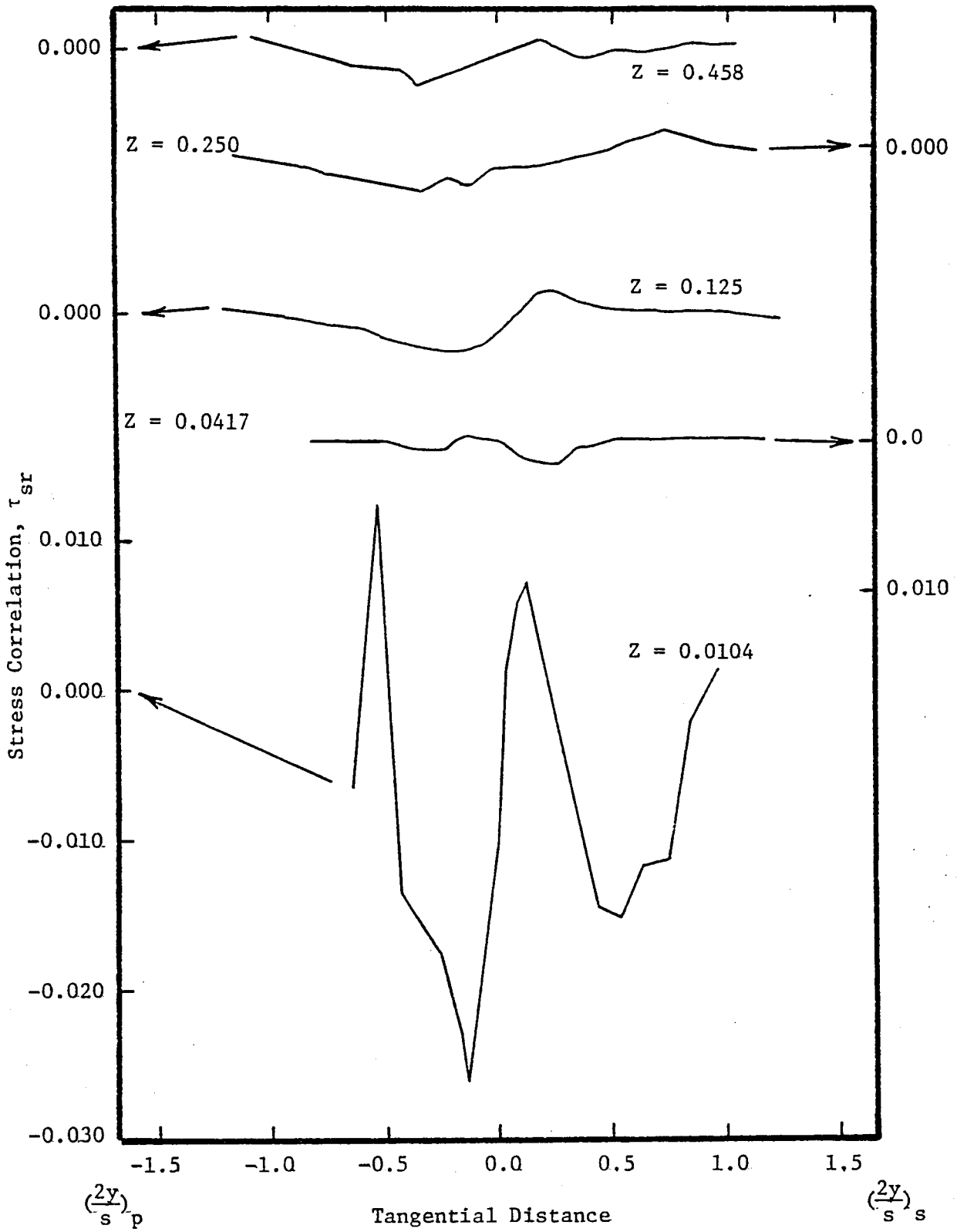

Figure 77. Stress Correlation Profiles, R = 0.9595, ϕ = 0.56

reversal of stress at the wake center. This positive and negative stress distribution results from opposite gradients of streamwise mean velocity about the wake center. The profiles are asymmetrical about the wake center with the pressure-surface stresses being higher than the suction-surface stresses. The location of the zero streamwise Reynolds stress occurs slightly away from where $\partial W/\partial n$ is zero. This characteristic has been measured and reported by Raj and Lakshminarayana (1973) and Lakshminarayana and Reynolds (1979). Hah (1980) used a stationary hot-wire and an ensemble average technique to evaluate the wake properties and has reported that the zero streamwise Reynolds stress occurs slightly away from where $\partial W/\partial n$ is zero. This implies that this characteristic is inherent for the wake and does not arise due to the spatial resolution of the hot-wire probes.

The profiles are asymmetric about the wake center and the decay of the stresses is extremely rapid in the trailing-edge region at all the radii and reach nearly zero values in the near-wake region. This rapid decay is expected as the steep gradients in mean velocity that exists in the trailing-edge region become very small for $Z > 0.15$. Further it is seen that at most of the radii the stresses in the free-stream have a value other than zero which might be due to the upstream inlet-guide-vane wakes. The dominant effect of the leakage vortex can be seen in Figures 64 and 65 for the radii $R = 0.9324$ and 0.9595, respectively. The vortex dissipates rapidly, very close to the trailing-edge, and the contribution to the Reynolds stress from this vortex also diminishes very rapidly.

The radial component of Reynolds stress for all the radii is shown in Figures 66 through 71. The radial stresses are opposite in sign to those of the streamwise stress. This is consistent with the mean velo-

city data presented in Section 3.2, where it was noted that the streamwise component of velocity increases on either side of the wake, while the radial component of velocity decreases. In the free-stream the value of the radial Reynolds stresses is around zero.

As the radial velocities are very much smaller than the streamwise velocities it has to be expected that the ratio of the radial stress to streamwise stress will be less than unity. But in the present case their ratio is greater than unity (trailing-edge and near-wake locations, outside the hub-wall boundary layer) indicating the effect of rotation on the stresses. This can be argued on the basis of the Reynolds stress equation in the rotating coordinate system (Lakshminarayana and Reynolds, 1979) where in the effect of rotation is to attenuate the streamwise stress component (τ_{sn}) and amplify the radial stress component (τ_{rn}). In the trailing-edge region the situation tends to be far more complicated because the trailing-vortex system dominates the flow. Their effect seems to make the radial velocity gradients steeper. In the trailing-edge and near-wake regions for R = 0.7297, the ratio of τ_{rn}/τ_{sn} is approximately 1.04. For the wakes inside the annulus-wall boundary layer the ratio is about 1.5. Thus it is seen that the effect of the vortex is, like rotation, to attenuate the radial component of Reynolds stress. But for the wakes inside the hub-wall boundary layer the streamwise component of stress seems to dominate. This has to be expected as the secondary flow and the hub-wall boundary layer interaction with the wake and their influence on the Reynolds stresses are not clearly understood. The ratio of the radial-to-streamwise Reynolds stress represents the deviation of the total stress vector from the streamwise direction. Comparison of these angles with those of Reynolds (1978) indicates the effect

of loading. The higher the loading the greater seems to be the deviation of the stress vector from the streamwise direction. This is to be expected as higher loading results in higher radial components of the velocity gradient and the higher the gradients, the larger are the radial stresses.

The stress correlations, τ_{sr}, are shown plotted in Figures 72 through 77. It is seen that the magnitude of this correlation is of the same order as that of streamwise stress. It has the same sense on either side of the wake.

The Reynolds stress data presented in Figures 60 through 77 must be studied with some caution. It is possible that the results are subject to spatial errors which are inherent in a tri-axial hot-wire probe. However the contribution to stress from eddies larger than the distance between the probe sensors is measured accurately. An estimate of the scales of flow and the expected orders of error is given in Appendix A2 and Appendix A3.

3.6 Wake Curvature and Flow Angle Variation

The locus of the wake centerline, which is a measure of the wake curvature, is shown plotted in Figure 78. The curvature of the rotor-wake is appreciable in the trailing-edge region and negligibly small in the far-wake region. As seen from the Figure 78, the wake curvature is towards the suction-surface of the blade in the near- and far-wake regions and the path is coincident with the blade outlet angles in the trailing-edge region. It is also found that the radius of curvature of the wake is higher at higher radii and continuously decreases as the hub-wall is approached where the trend of the curvature changes.

The curvature of the wake inside the annulus-wall boundary layer is affected greatly by the tip-vortex and secondary flows. Here the curva-

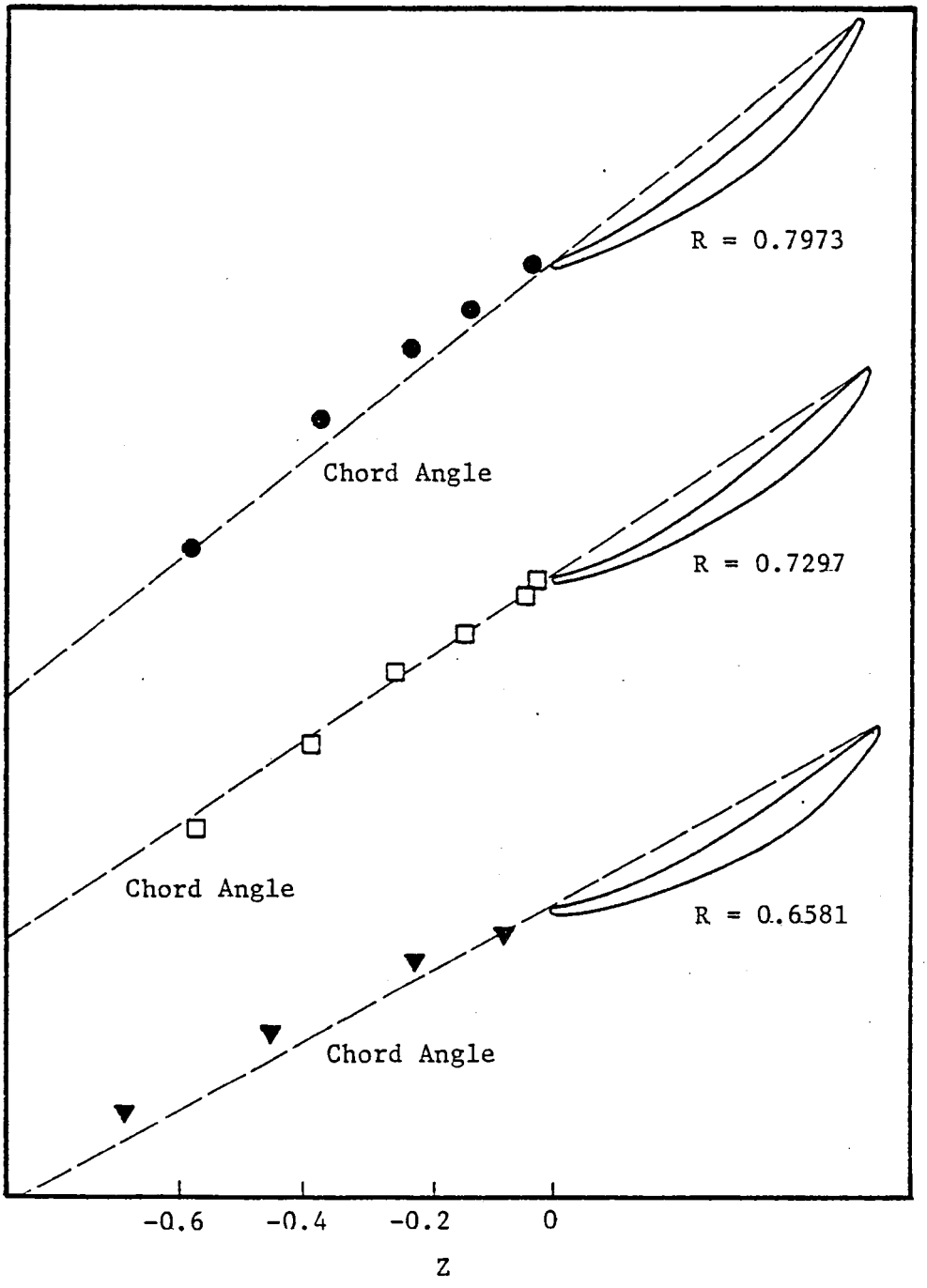

Figure 78. Curvature of the Rotor-Wake Centerline in Relative Frame of Reference

ture initially decreases and then starts to increase up to 0.12 chords beyond which it decreases gradually. This implies that outlet angle variation is considerable in the annulus-wall region, caused by different decay rates for axial and tangential velocities, coupled with the tip-vortex and the secondary flows which deflect the flow very strongly near the blade trailing-edge.

Curvature can also be thought of as the variation in flow angle at the wake center with downstream distance. The flow angle can be calculated from the velocity-triangles at each of the downstream locations. This plot is shown in Figures 79 through 84 where all the velocities are normalized to the free-stream axial velocity and the angle β is in degrees. In the trailing-edge region the flow is still developing where the trailing-vortex system may dominate the wake. As the axial component of velocity is very small and the radial velocities are large, the flow deflection is quite considerable resulting in small negative tangential relative velocities. This implies that the relative and the absolute velocities are in the same direction. As the wake travels downstream, the tangential relative velocity reverses its sign and becomes positive. The reversal of tangential velocity in its sign introduces a large angle variation which is reflected in the wake curvature in the trailing-edge region. Beyond $Z = 0.1354$ the flow angle variation is very small and consequently the curvature of the wake is also small.

The secondary flow and the tip-leakage flow which exist at the end-wall boundary layers have a pronounced influence on the tangential velocity and consequently, the curvature of the wake. The increased tangential velocity and widely differing decay rates of axial and tangential velocity defects in the trailing-edge region assisted by the tip-vortex

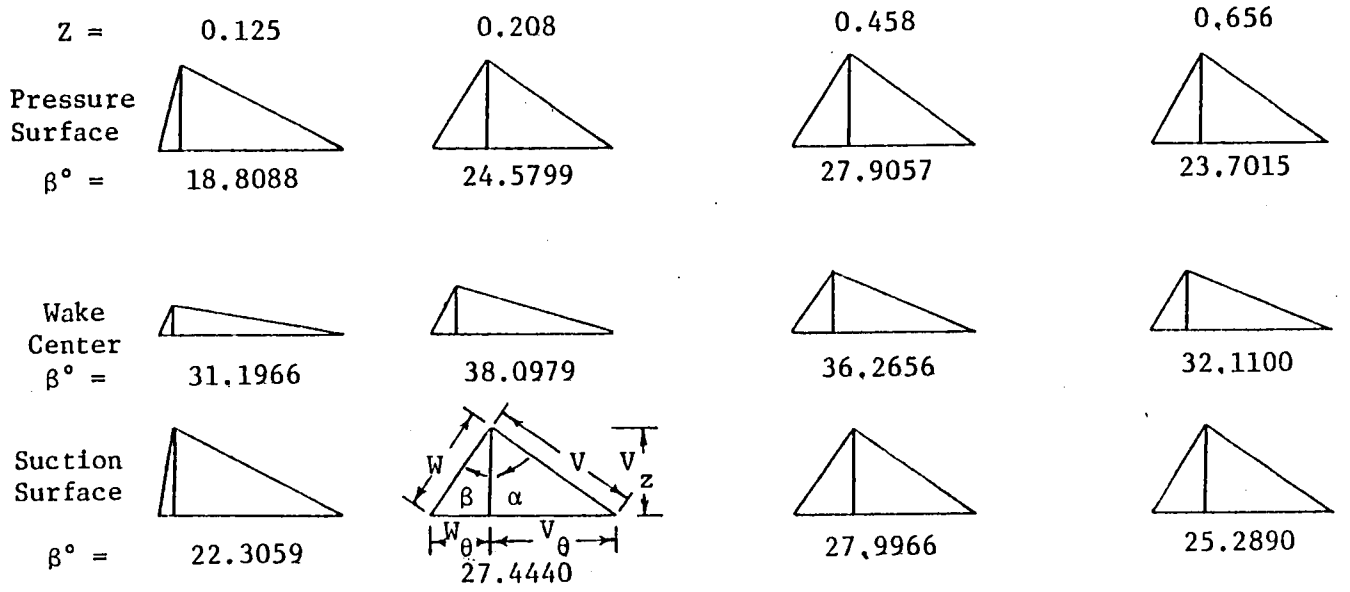

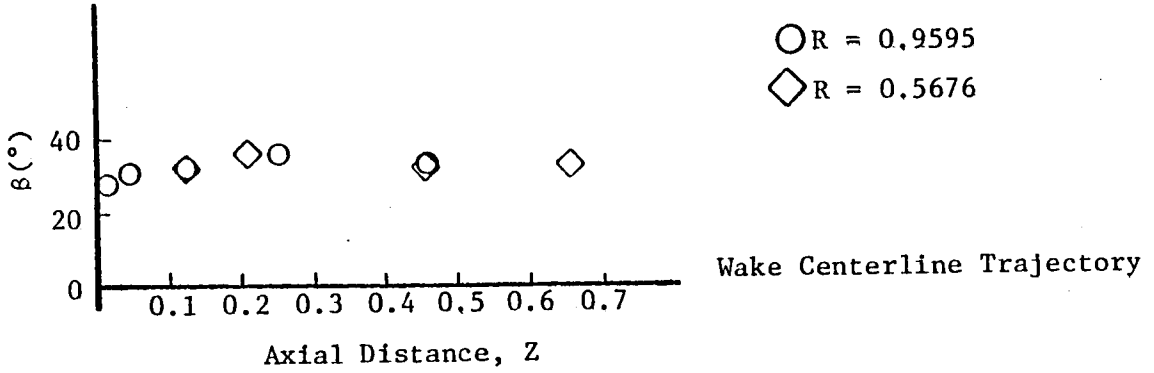

Figure 79. Velocity Triangles for R = 0.5676, ϕ = 0.56

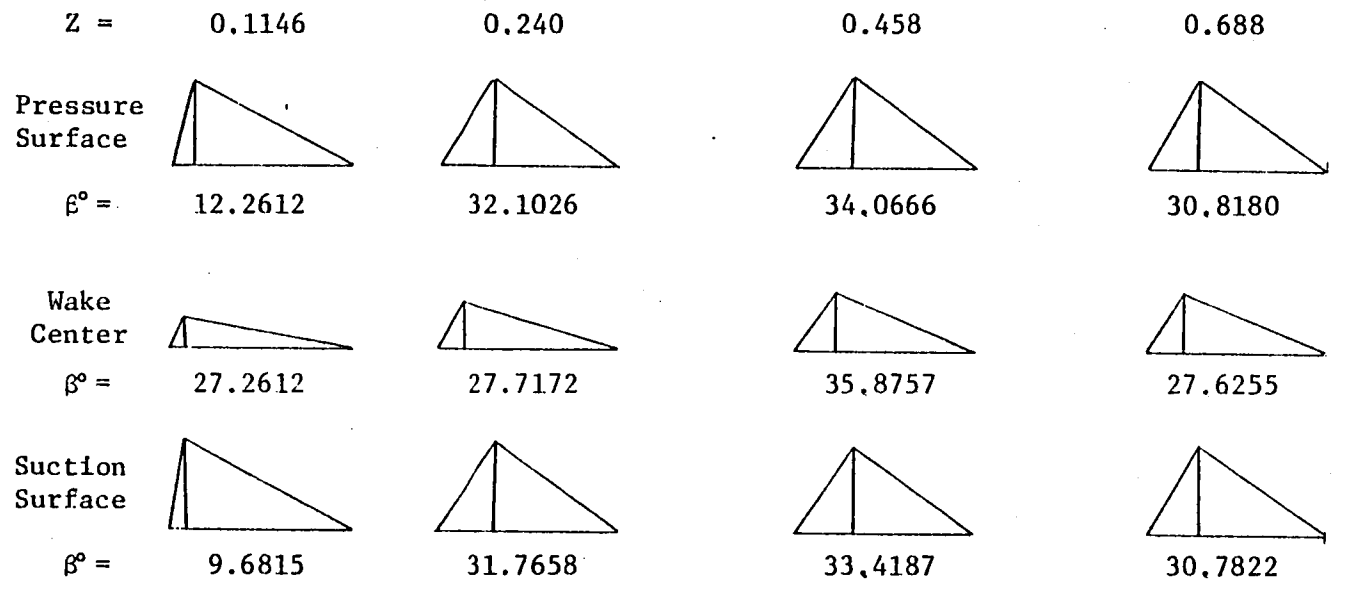

Figure 80. Velocity Triangles for R = 0.6581, ϕ = 0.56

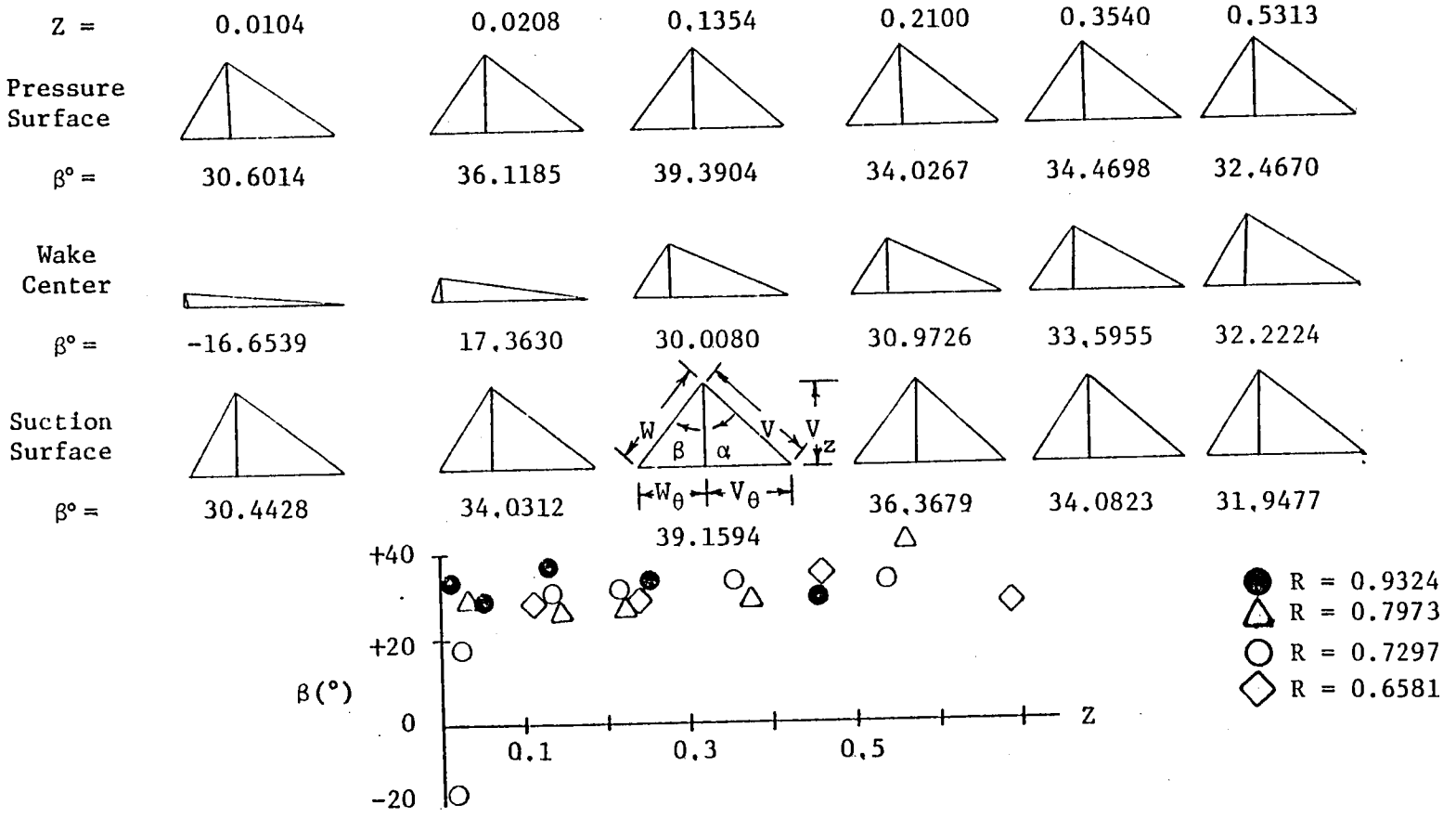

Figure 81. Velocity Triangles and Flow Angle Variation, R = 0.7297, ϕ = 0.56

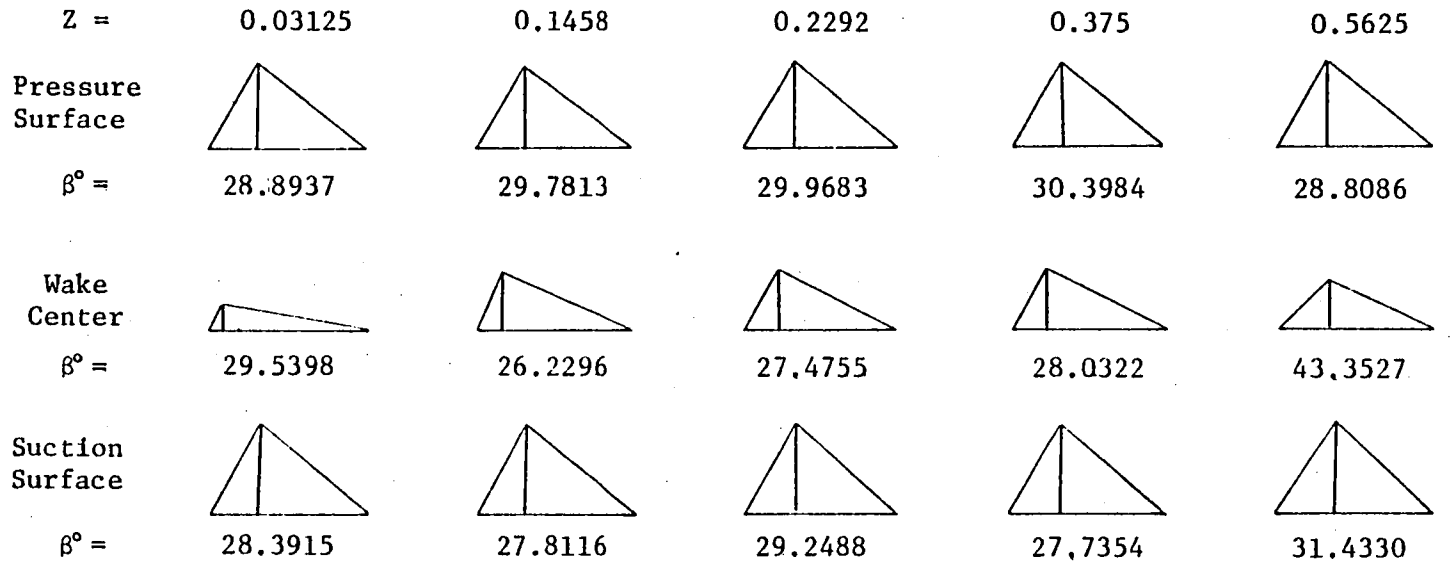

Figure 82. Velocity Triangles for R = 0.7973, ϕ = 0.56

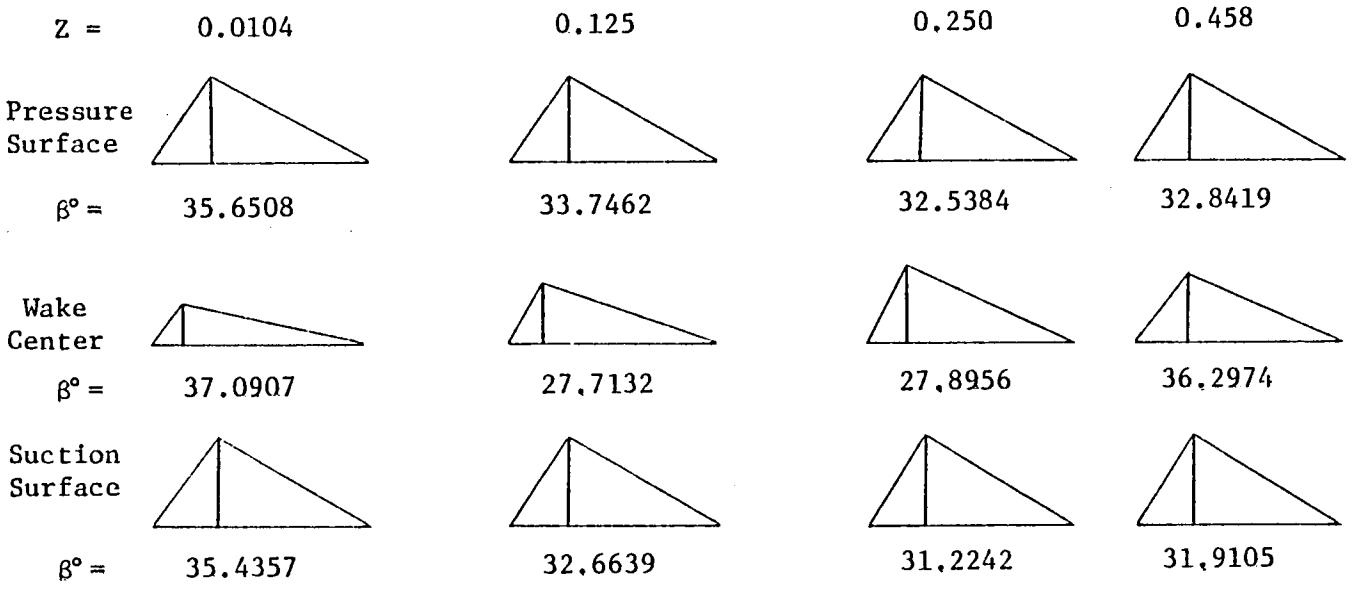

Figure 83. Velocity Triangles for R = 0.9324, ϕ = 0.56

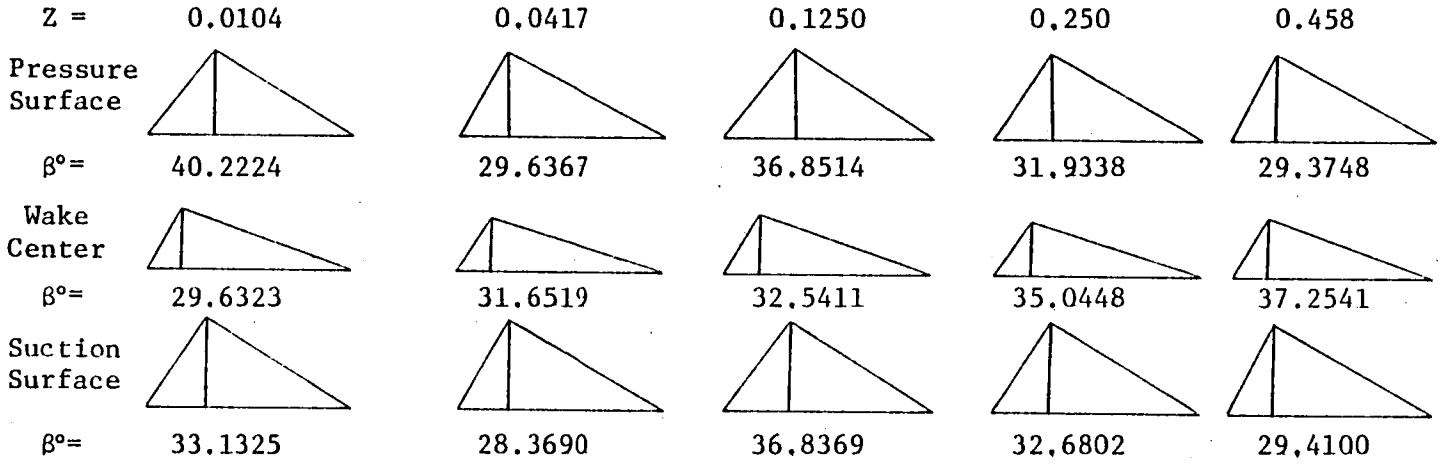

Figure 84. Velocity Triangles for R = 0.9595, ϕ = 0.56

tend to give a large "negative" curvature in the trailing-edge region. Beyond ten percent of the chord downstream of the blade the tip-vortex depletes in its strength and also the decay rates of both axial and tangential velocity defects are of the same magnitude and consequently the wake curvature becomes nearly asymptotic with the chord angle.

The effect of loading is to increase the curvature of the wake and is noted by comparing Figure 80 with Figure 10 of Reynolds, et al. (1978).

3.7 Rotor-Wake Decay

3.7.1 Decay of maximum defect in mean velocities

The decay of wake centerline velocity which reflects the decay of the wake is discussed in this section for all the three components of velocities as well as the resultant mean velocity.

Decay of the mean velocity defect is greatly influenced by the pressure gradients and turbulence fluctuations, as well as by the viscous effects that exist near the blade trailing-edge. The secondary flow that exists near the hub-wall as well as the secondary flow and tip-leakage-flow at the annulus-wall also contribute to the decay of the defect near the annulus- and hub-wall.

Decay of the defects of axial and tangential velocities is shown plotted in Figure 85 for the radii outside the end-wall boundary layers. Since the free-stream velocities on the pressure- and suction-side are different, the velocity defect based on these two velocities is shown plotted in the figure. The general trend observed for the decay of the defect in axial and tangential velocity is that they decay very rapidly in the trailing-edge region and the decay tends to be less rapid in the near- and far-wake regions. The very rapid decay in the trailing-edge region is attributed to large turbulence intensities, pressure gradients,

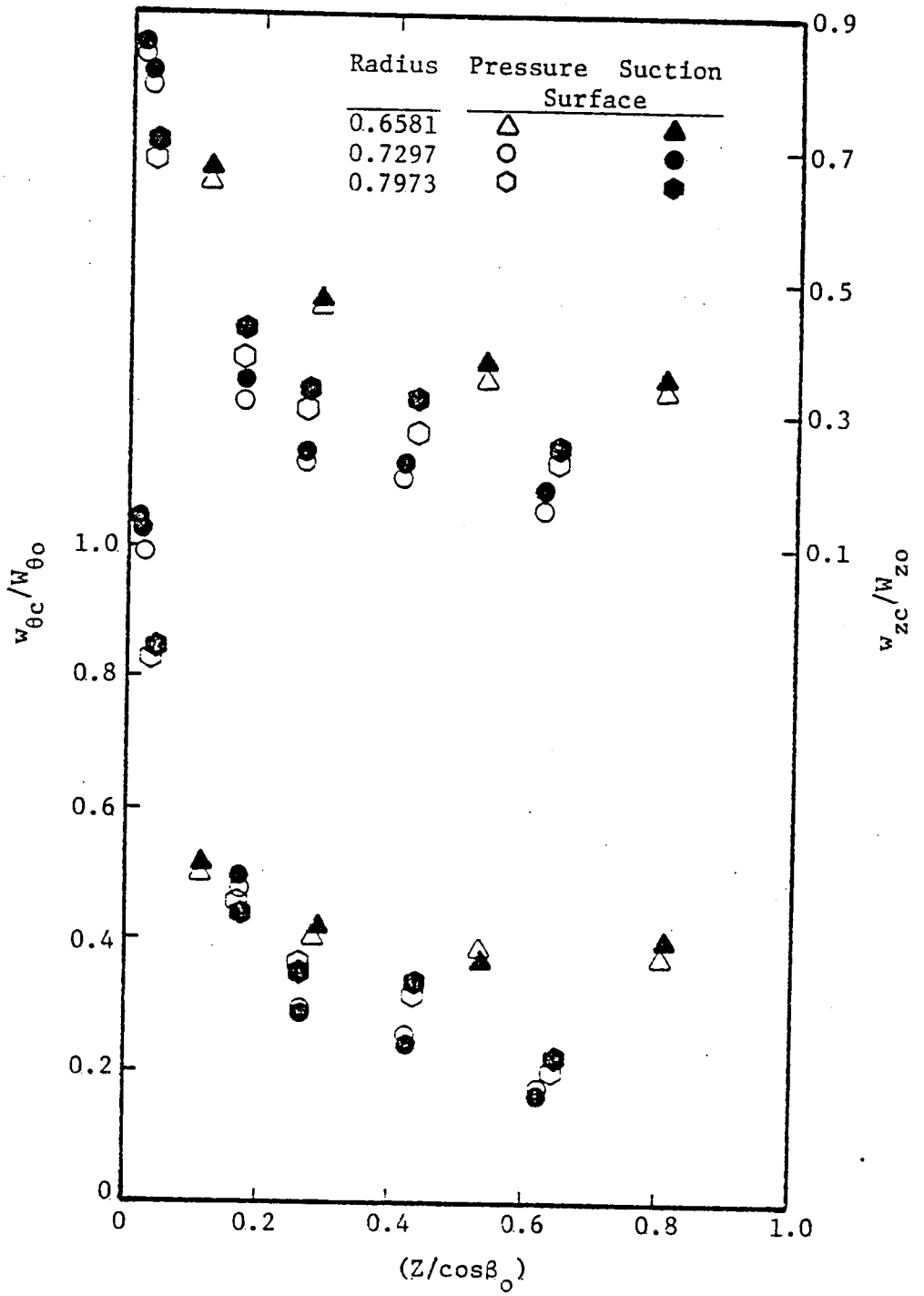

Figure 85. Decay of Axial and Tangential Mean Velocity Defects with Downstream Distance

and three-dimensional effects. The tangential velocity defect decays much more rapidly than the axial velocity defect. The contributing factor to the very rapid decay of the tangential velocities is the radial component of velocity as well as the radial distribution of free-stream tangential and axial velocities.

Figure 86 shows the decay of the maximum radial velocity for the wakes outside the annulus- and hub-wall boundary layers. It is clear that the decay is extremely rapid in the trailing-edge region and slows down considerably in the near- and far-wake region. Even at 0.6 chords downstream it is seen that there is a significant radial velocity component. This not only indicates that the decay of the radial velocity component is less rapid compared to the defect in axial and tangential velocities but also reflects the radial migration of flow in the rotor-wakes. The very rapid decay in the trailing-edge region can be attributed to not only the high turbulence intensities but also the decay of the trailing-vortex system which dominates the flow in this region. Also plotted in Figure 86 is the data on the maximum radial velocity from Raj and Lakshminarayana (1976), Reynolds, et al. (1978), Thompkins and Kerrebrock (1975), and Kool, et al. (1978). Comparison of the data from various sources indicates the effect of blade loading on the radial velocity. Higher blade loading induces larger radial velocities. Comparing the decay rates in the trailing-edge region with Figure 14 of Reynolds, et al. (1978) and Figure 7 of Lakshminarayana (1976) shows that the decay rate in this region is more rapid than the cascade, isolated airfoil, or even the wake of a lightly loaded rotor.

Comparison of the decay rates with those of Reynolds, et al. (1978) reflects the effect of blade loading. The higher the blade loading, the

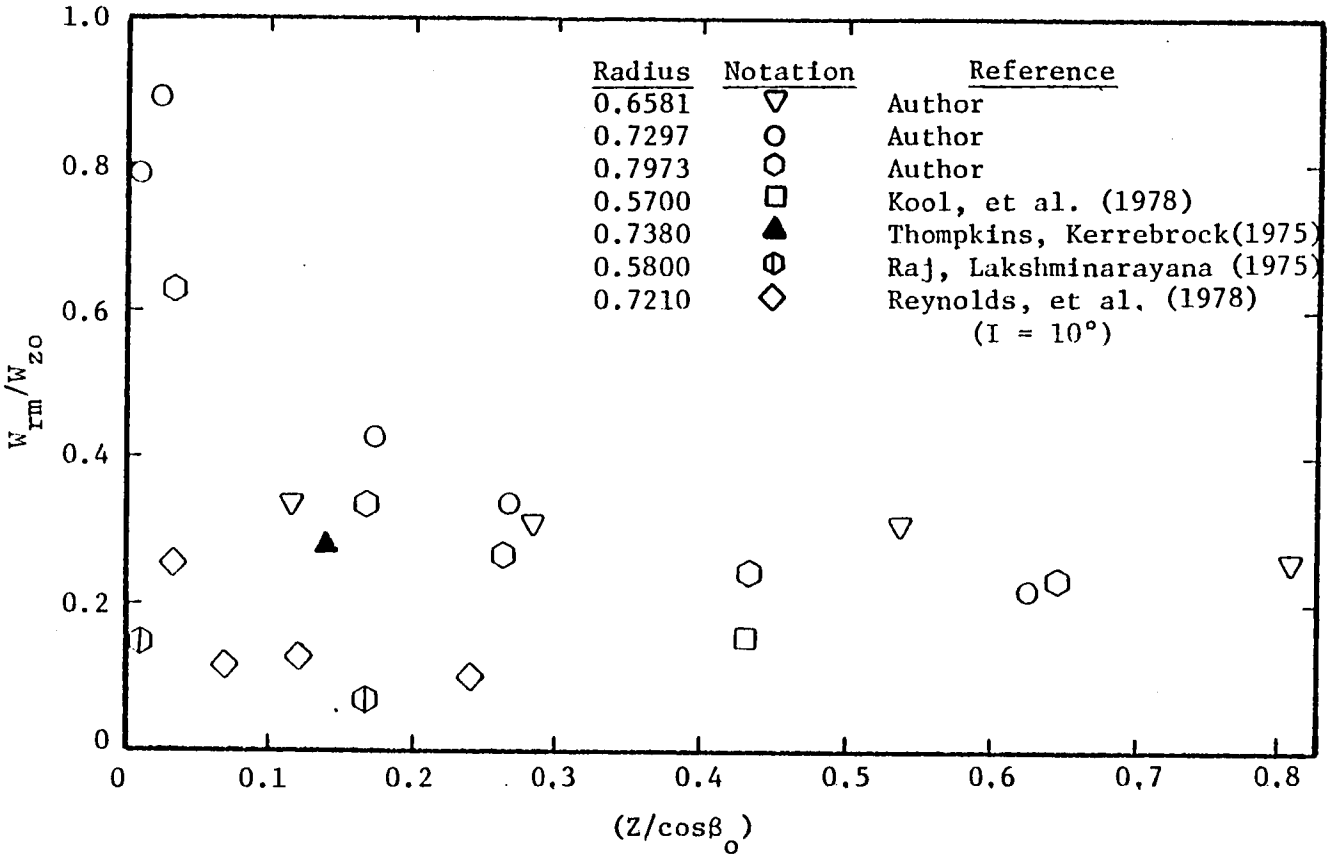

Figure 86. Decay of Maximum Radial Mean Velocity with Streamwise Distance

larger the wake defect. It is also observed that the wake decays much more slowly with increased blade loading. The effect of blade loading is shown to have a greater effect on the tangential velocity defect, more so than for the axial velocity defect.

The decay rates change drastically for the wakes inside the annulus- and hub-wall boundary layers. In the annulus-wall region, Figure 87, it is seen that the defect initially increases until 0.15 chords downstream before it monotonically decreases. This strange behavior is attributed to the tip-vortex in the tip region arising due to tip-clearance flow. It is also observed that the axial velocity defect is much smaller in the annulus-wall boundary layer compared to that in the hub-wall boundary layer. The interesting feature to be noted is that, though the defect is much larger in the hub-wall boundary layer, the decay rate in the far-wake region is about the same at approximately the same downstream distance from the trailing-edge.

The decay of the total relative velocity which is the resultant of axial, tangential, and radial velocity components is shown plotted in Figure 88 for the wakes outside the end-wall boundary layers. Some very interesting features are noted in the decay of the total velocity defect. For the radius R = 0.7297 and at Z = 0.0104, the defect in total velocity is 0.69 which increases to 0.735 at Z = 0.0208 and from then on it monotanically decays to a value of 0.13 at half-a-chord downstream. The data of Thomkins and Kerrebrock (1975) for a transonic rotor also follows the trend of the author data. The decay of the total velocity conforms more closely to the decay of the axial velocity. It is seen that at a half-a-chord downstream the defect in total velocity (w_c/W_o) is of the same order

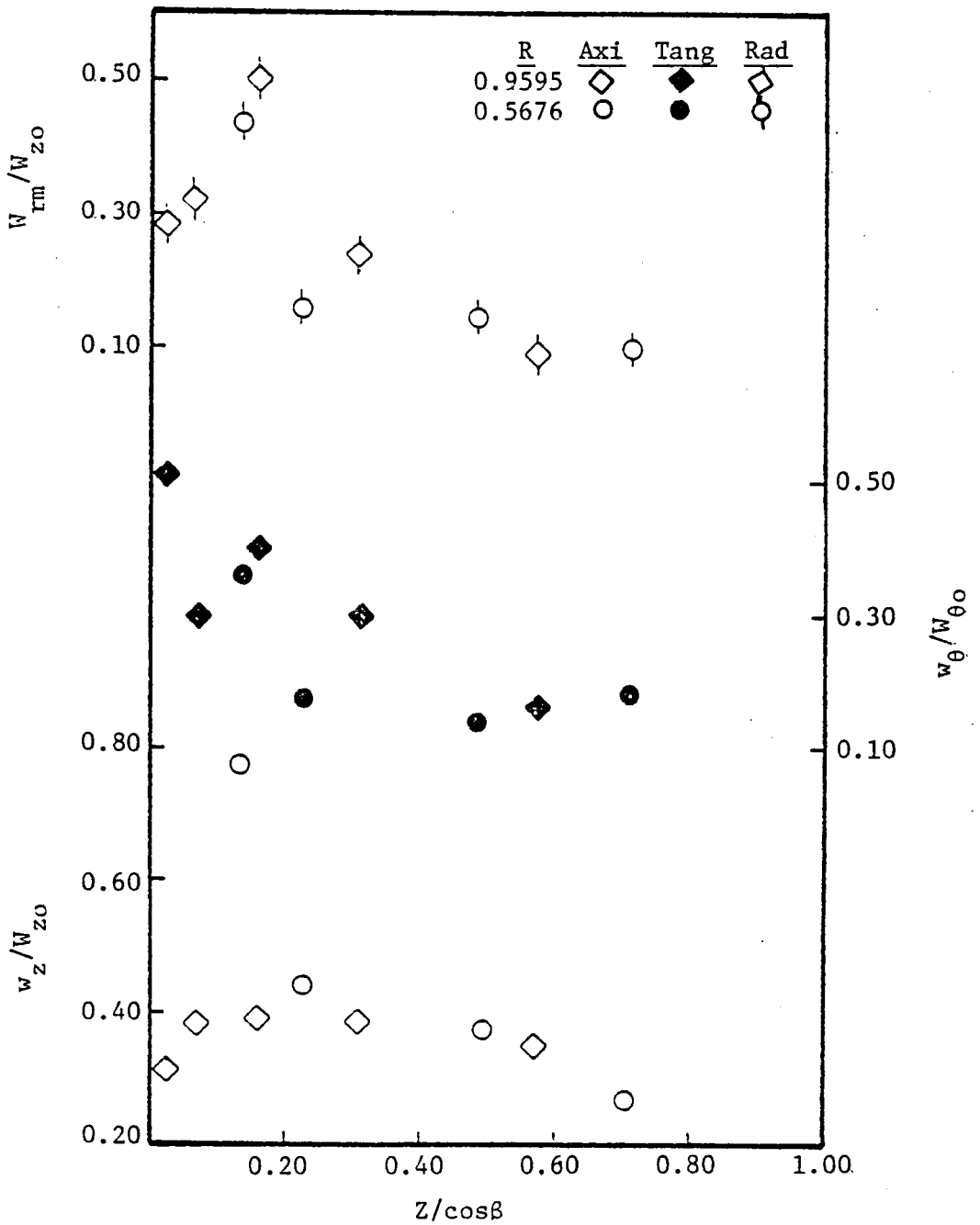

Figure 87. Decay of Defects of Axial and Tangential Mean Velocity and Maximum Radial Velocity for Wakes Inside Annulus- and Hub-Wall Boundary Layers

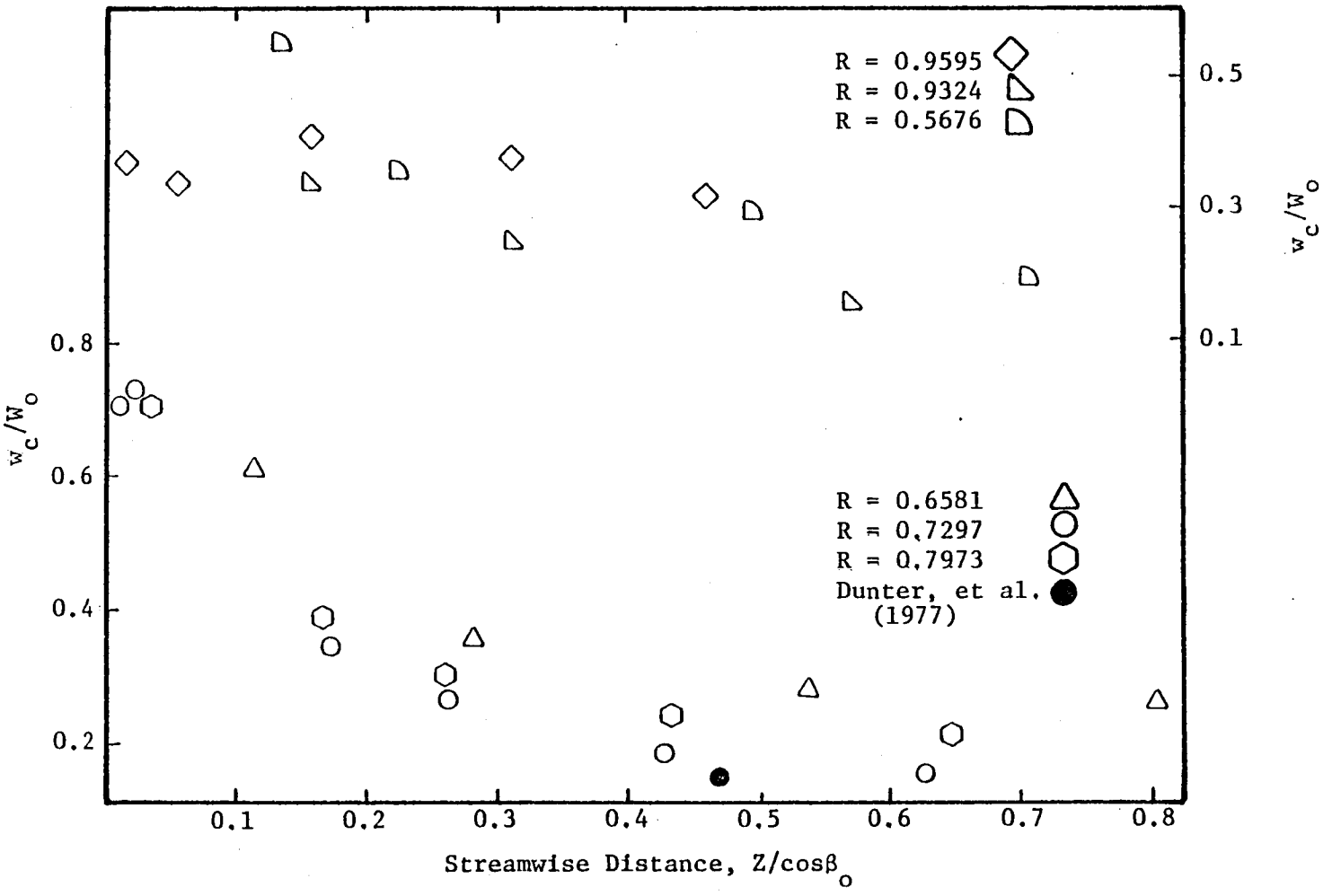

Figure 88. Decay of Total Mean Relative Velocity with Streamwise Distance

as that of axial velocity defect (w_{zc}/W_{zo}) while the tangential velocity defect ($w_{\theta c}/W_{\theta o}$) is much less than either the axial or the total velocity.

Not only do the defects of axial and tangential velocities and maximum radial velocities change in the downstream direction but also the free-stream velocity changes. This plot is shown in Figure 89. For the wakes outside the annulus- and hub-wall boundary layers it is seen that the free-stream velocity increases with downstream distance from the trailing-edge. This can be explained based on the continuity equation. As the wake decay is rather rapid in the trailing-edge region, increase in the free-stream velocity occurs. This is very clearly seen in Figure 88a for the radii R = 0.6581, 0.7297, 0.7973, and 0.9324. As the wake travels downstream the decay is less rapid and consequently we have a gradual increase in the free-stream velocity. For the wake inside the annulus-wall boundary layer the free-stream velocity decreases with distance, Figure 89b, contrary to those at other radii. This behavior can be explained based on the annulus-wall boundary layer growth. For the radius R = 0.9595 and at Z = 0.0104, the free-stream velocity normalized to the tip-speed is of the order of 0.664 which drops to 0.648 at Z = 0.458. This is due to the fact that at the same radius, but at different axial locations, the annulus-wall boundary layer would have grown and thus would represent a lower free-stream velocity. Thus the effect of the annulus-wall boundary layer on the free-stream velocity is opposite to that which occurs at some lower radii. For the wake at R = 0.9324, an interesting trend is noticed. Initially up to Z = 0.25 chord downstream the free-stream velocity increases and for Z > 0.25, the velocity shows a decreasing trend. This is due to the annulus-wall boundary layer at this radius beyond Z = 0.25. The same trend is noticed even for the wake

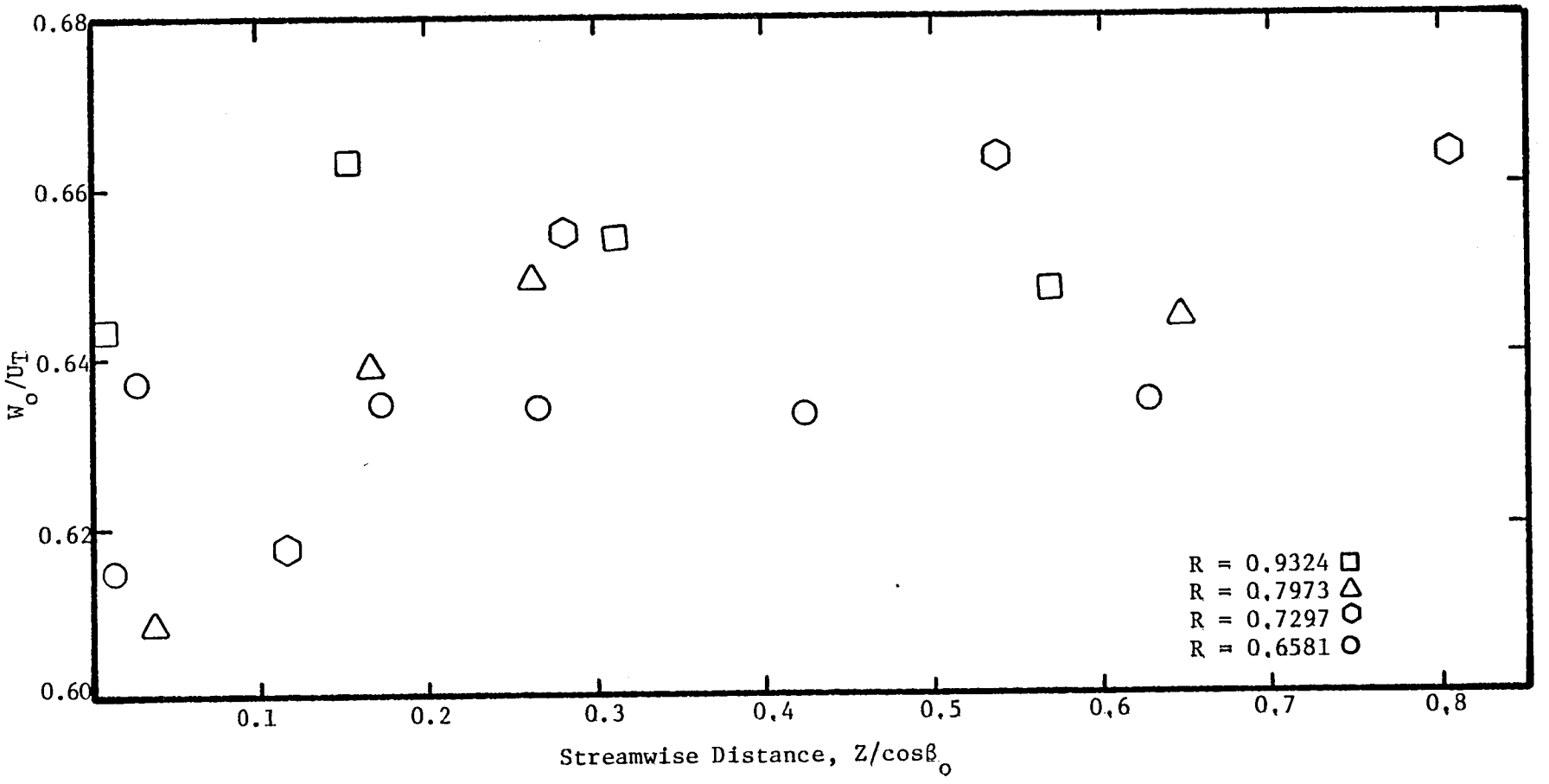

Figure 89a. Freestream Relative Velocity Variation with Streamwise Distance

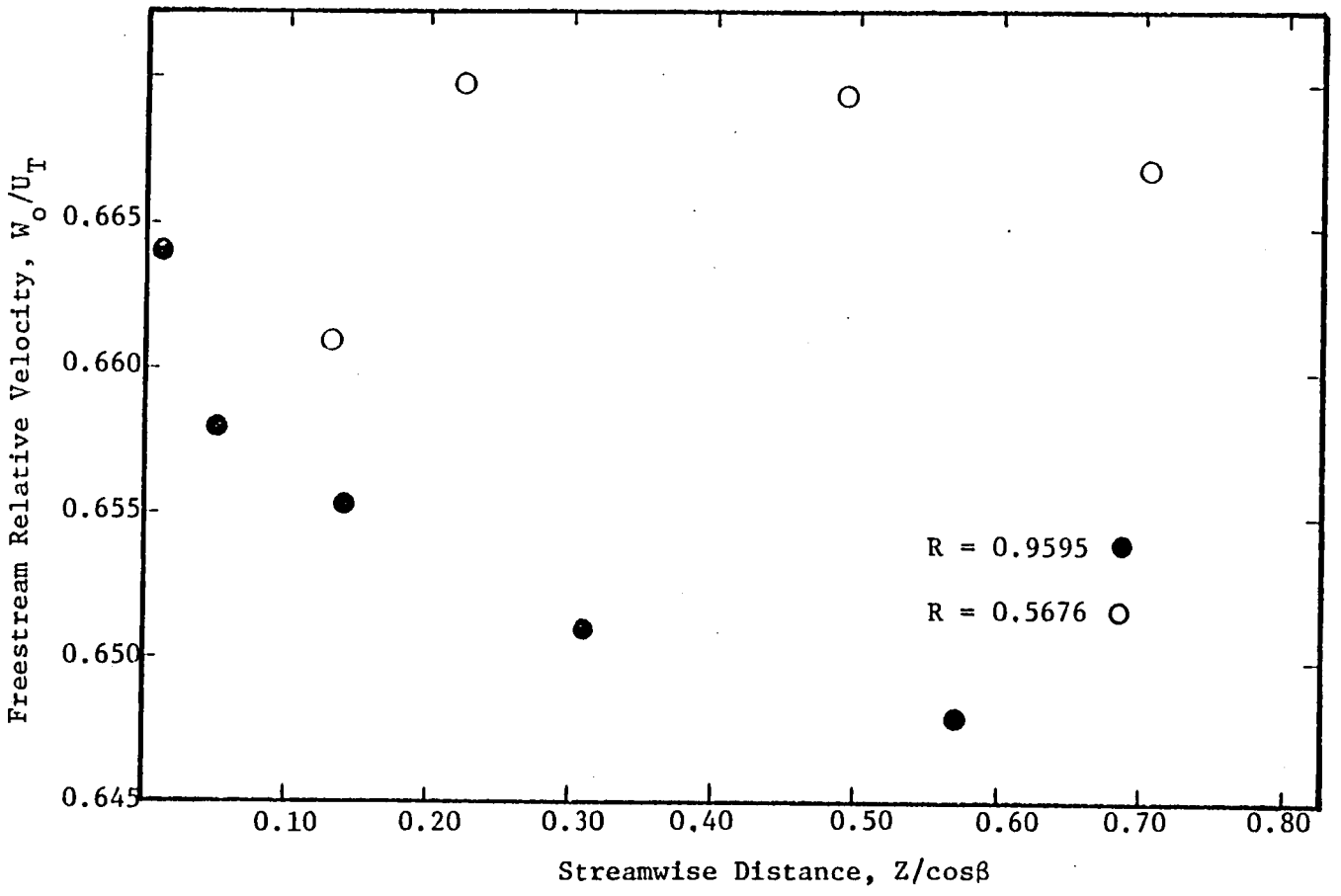

Figure 89b. Freestream Relative Velocity Variation with Streamwise Distance

at the radius R = 0.5676, which is clearly seen in Figure 89b. This trend is also reported by Ufer (1968) who has measured the annulus-wall boundary layer growth to nearly 20 percent of the blade height behind the rotor.

It is thus seen that the initial wake characteristics differ considerably in the radial direction and hence the decay rates are also different. The main controlling factor in the development of a wake is the section drag coefficient. So normalizing the decay by the drag coefficient should collapse all the data points on to a single decay curve. This correlation is reported in a later section.

3.7.2 Decay of maximum turbulence intensity

Decay of maximum axial, tangential, and radial turbulence intensities normalized to the local relative mean velocity is shown plotted in Figure 90, for the wakes outside the annulus- and hub-wall boundary layers. It is seen that the intensities are very high in the trailing-edge region and that they decay very rapidly in the trailing-edge region.

Lakshminarayana and Reynolds (1979) have given a qualitative analysis on the effects of rotation on turbulence and have shown that the turbulence structure is quite different compared to a stationary case. The radial intensities are likely to be higher than the axial and tangential components. The present data seems to confirm this analysis only at higher radius. For the radius R = 0.9324 at Z = 0.0104, the maximum radial component (normalized to the local axial velocity) is 0.99 while the axial and tangential components are 0.8316 and 0.8870, respectively. Further the data at this radius also confirms the analysis of Raj and Lumley (1976) who have shown that if the gradient of the radial component

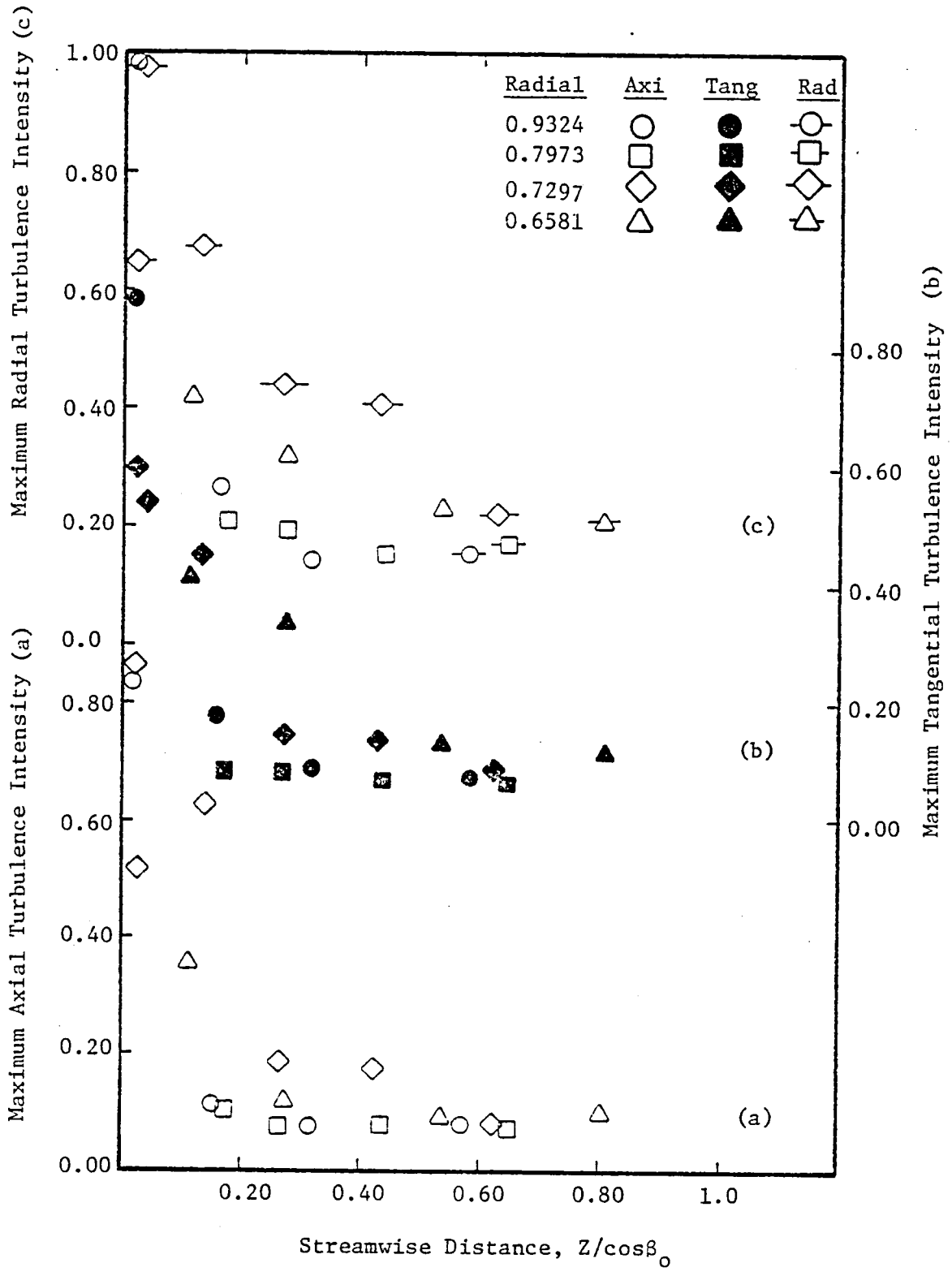

Figure 90. Decay of Maximum Axial, Tangential, and Radial Turbulence Intensity

of mean velocity across the wake is much larger than the angular velocity of the machine, then

$$\tau_r > \tau_\theta > \tau_z \quad . \tag{4}$$

But the data at lower radii does not agree with this reasoning.

Not only the magnitudes of the turbulence intensities at various radii are different so also are their decay rates. It is seen from Figure 90, that the decay of the axial and tangential components is about the same while the radial intensity decays much more slowly.

For the wakes inside the annulus- and hub-wall boundary layers it is seen, from Figure 91, that

$$\tau_z > \tau_r > \tau_\theta \quad . \tag{5}$$

It is also seen that the intensities for the wakes inside the annulus- and hub-wall boundary layers decay slower as compared to the ones outside the end-wall boundary layers.

Comparing these figures with those of Reynolds (1978), it is seen that the effect of loading is to increase the maximum axial, tangential, and radial intensities in the wake. Furthermore, the decay of intensities is also extremely rapid with increased blade loading.

3.7.3 Decay of maximum turbulent shear stress

The decay of the maximum turbulent shear stresses is shown plotted in Figure 92. The stresses are very high in the trailing-edge region decaying very rapidly downstream of the trailing-edge. The rate of decay seems to follow the same trend for the radii outside the annulus- and hub-wall boundary layers. But for the wakes inside the end-wall boundary layers the decay rates seems to be appreciably slower. The decay as shown in Figure 92 for the streamwise (τ_{sn}), radial (τ_{rn}), and the corre-

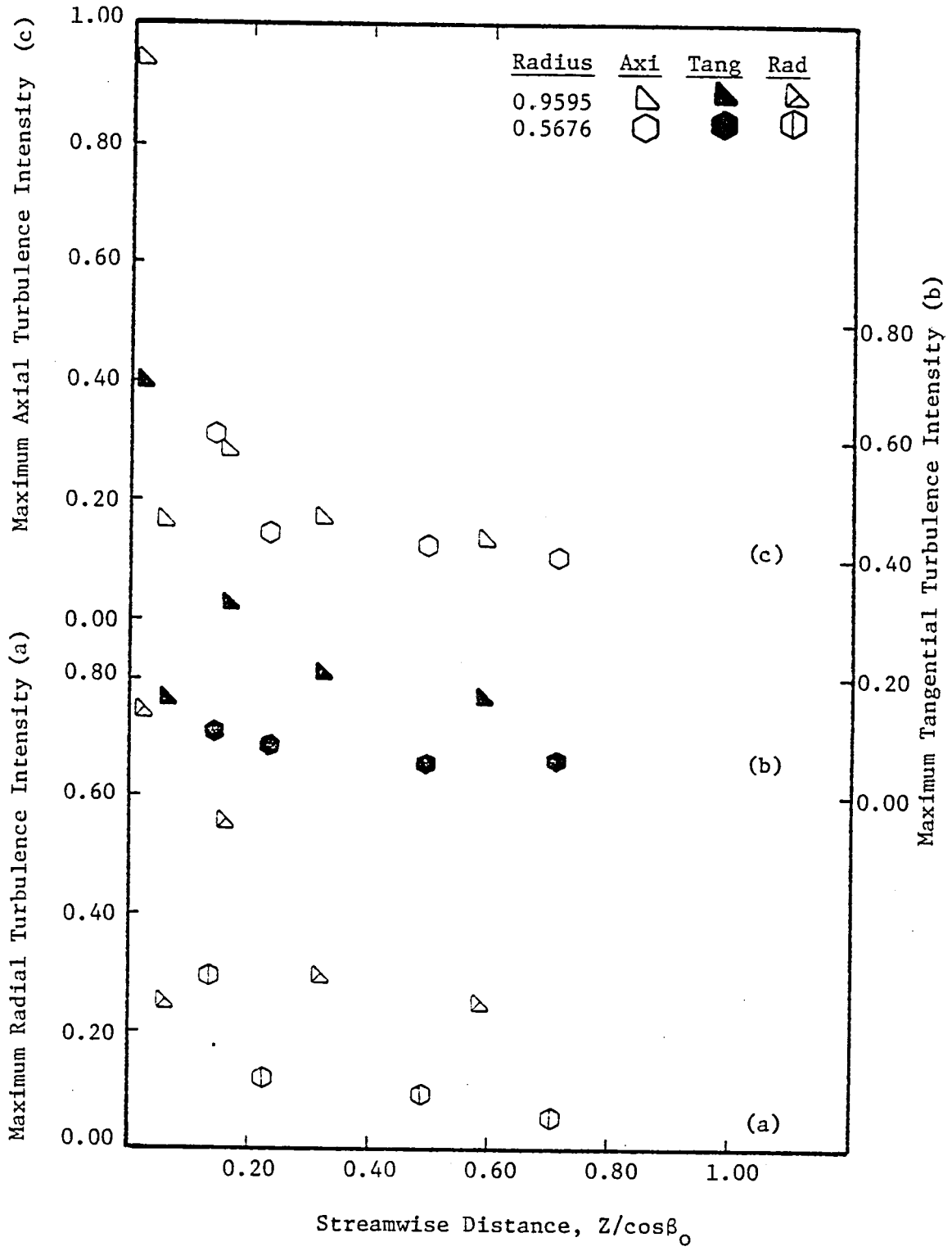

Figure 91. Decay of Maximum Axial, Tangential, and Radial Turbulence Intensity Inside Annulus- and Hub-Wall Boundary Layers

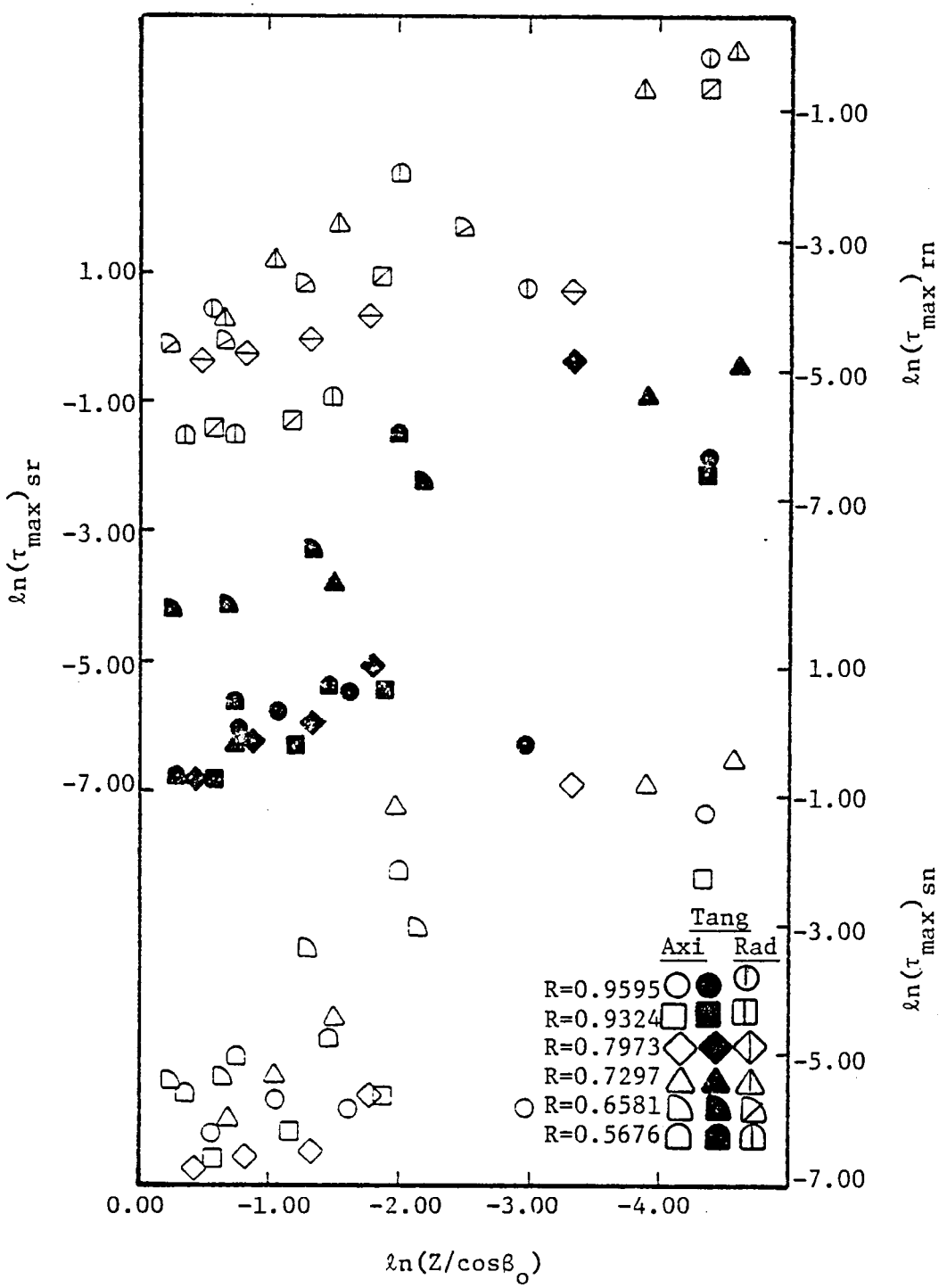

Figure 92. Decay of Maximum Shear Stress with Streamwise Distance

lation (τ_{sr}), seems to exhibit wide scatter for the different radii. This is to be expected as the wake development and decay are different at different radii. Normalizing the stresses by the corresponding values at the trailing-edge should collapse all the data onto a single curve, provided the stresses like the intensities and velocities depend only on their initial value. This correlation is attempted at a later section.

3.7.4 Static-pressure decay

The experimental evidence indicates that the static-pressure increases towards the wake center and as the wake travels downstream this difference decreases. For the data presented, R = 0.7297, Figure 93, the ratio of the static-pressure at the wake center to the corresponding static-pressure in the free-stream decays rather rapidly in the trailing-edge region and the decay is markedly slow in the near- and far-wake regions. The very rapid decay at the trailing-edge regions is attributed to the very rapid decay in velocity and turbulence intensity as well as to the existance of streamwise curvature.

The z-momentum can be written as: (neglecting viscous terms)

$$-\frac{1}{\rho}\frac{\partial p}{\partial z} = \frac{W_\theta}{r}\frac{\partial W_z}{\partial \theta} + W_r\frac{\partial W_z}{\partial r} + W_z\frac{\partial W_z}{\partial z} + \frac{\partial}{r\partial\theta}(\overline{W_\theta' w_z'}) - \frac{\partial}{\partial z}\overline{w_z'^2} \quad . \qquad (6)$$

In the above equation $\partial W_z/\partial\theta$ and $\partial W_z/\partial z$ are positive while $(\partial/\partial z)(\overline{w_z'^2})$ and $(\partial/r\partial\theta)(\overline{w_\theta' w_z'})$ are negative. If the decay in velocity gradients $[(\partial W_z/\partial\theta), (\partial W_z/\partial z)]$ dominate, the value $\partial p/\partial z$ should be negative. This means the decay in velocity gradients as well as the turbulence quantities contribute to the decay of the pressure difference across the wake. This static-pressure decay is shown plotted in Figure 93.

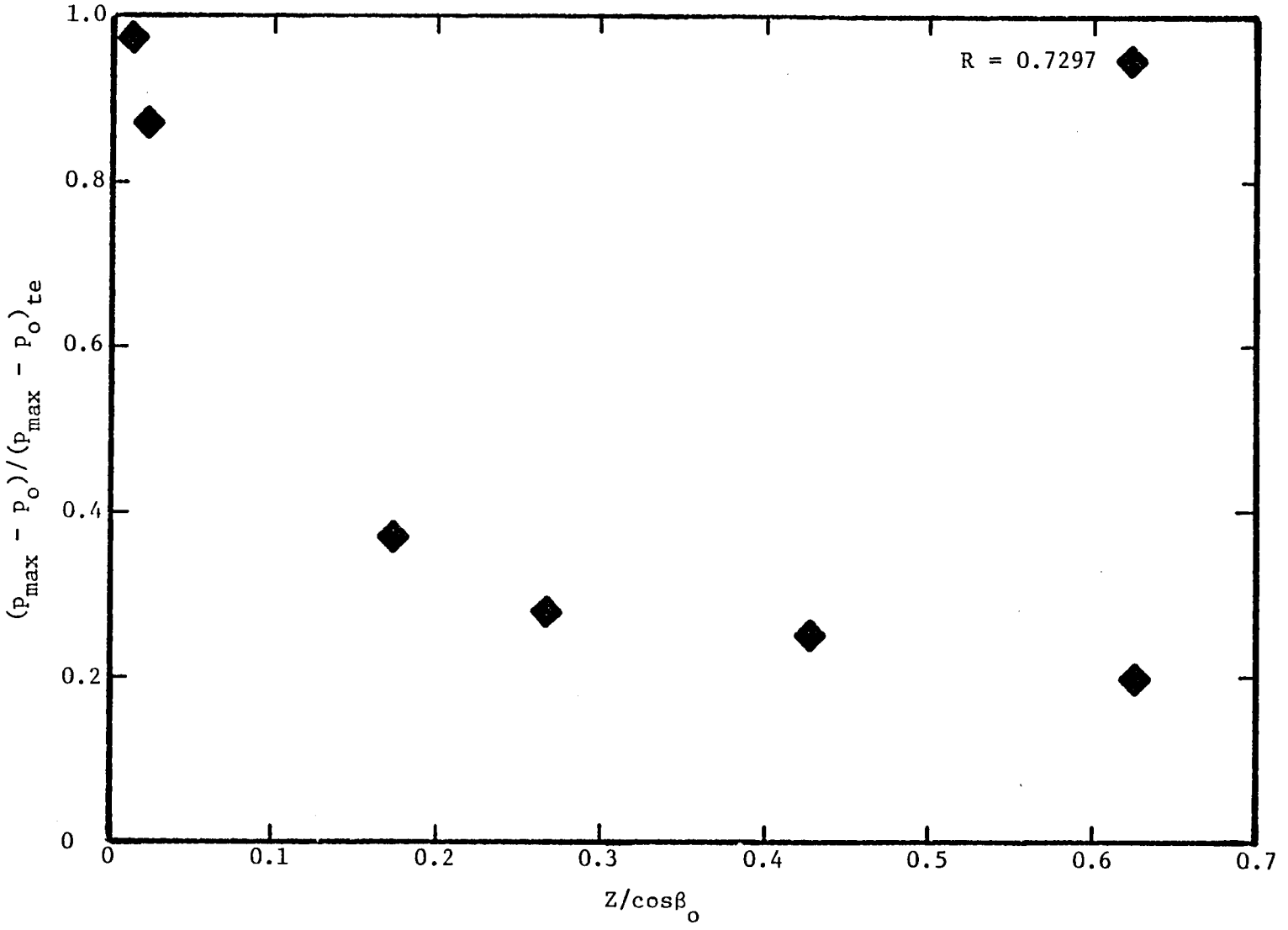

Figure 93. Static-Pressure Decay with Streamwise Distance

3.8 Semi-Wake Width Variation

The semi-wake width is defined as the width of the wake at half the defect of total relative velocity. The variation of this semi-wake width normalized by the blade spacing is shown plotted in Figure 94a for the radii R = 0.6581, 0.7297, 0.7973, and 0.9324. The wake width increases rapidly in the trailing-edge region and then the growth becomes very gradual in the near- and far-wake regions. As the interchange of momentum and energy is continuous on the two sides of the wake, the growth should also be continuous and this behavior is observed in Figure 94a. This is consistent with those observed for the isolated airfoil and the cascade wake. The wake width increases almost linearly with the downstream distance for $(Z/\cos\beta_o) > 0.2$ at all the radii, as shown in Figure 94a.

In the case of rotors, because of centrifugal effects, wakes at higher radius tend to be thicker compared to the wakes at lower radii. But as the hub- and annulus-wall regions are approached the wake width grows enormously due to the complex interaction of the wake with the end-wall boundary layers and secondary flow (and tip leakage in the case of annulus-wall region). The wake width variation in the annulus-and hub-wall boundary layers is shown plotted in Figure 94b. In the hub-wall region, at 0.6 chords downstream the wake has grown to approximately 30 percent of the passage while in the annulus-wall region at a Z-location of 0.458, the wake has grown to well beyond one passage. This implies that the adjoining wakes have already started interacting with one another.

The effect of loading on the wake width variation can be seen by comparing these results with those of Reynods, et al. (1978). One should be cautious in such a comparison as the wake width depends, besides other

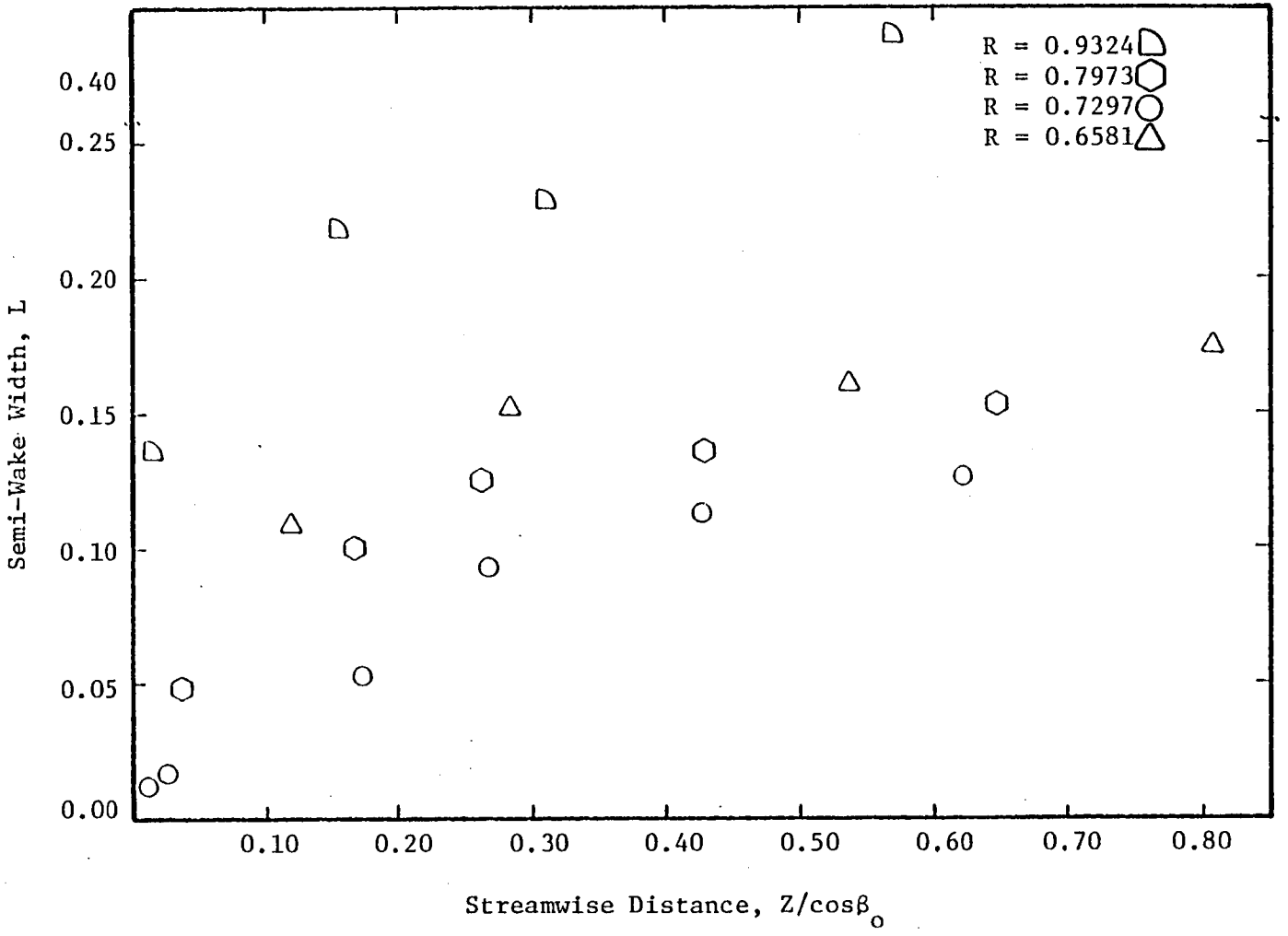

Figure 94a. Variation of Semi-Wake Width with Streamwise Distance

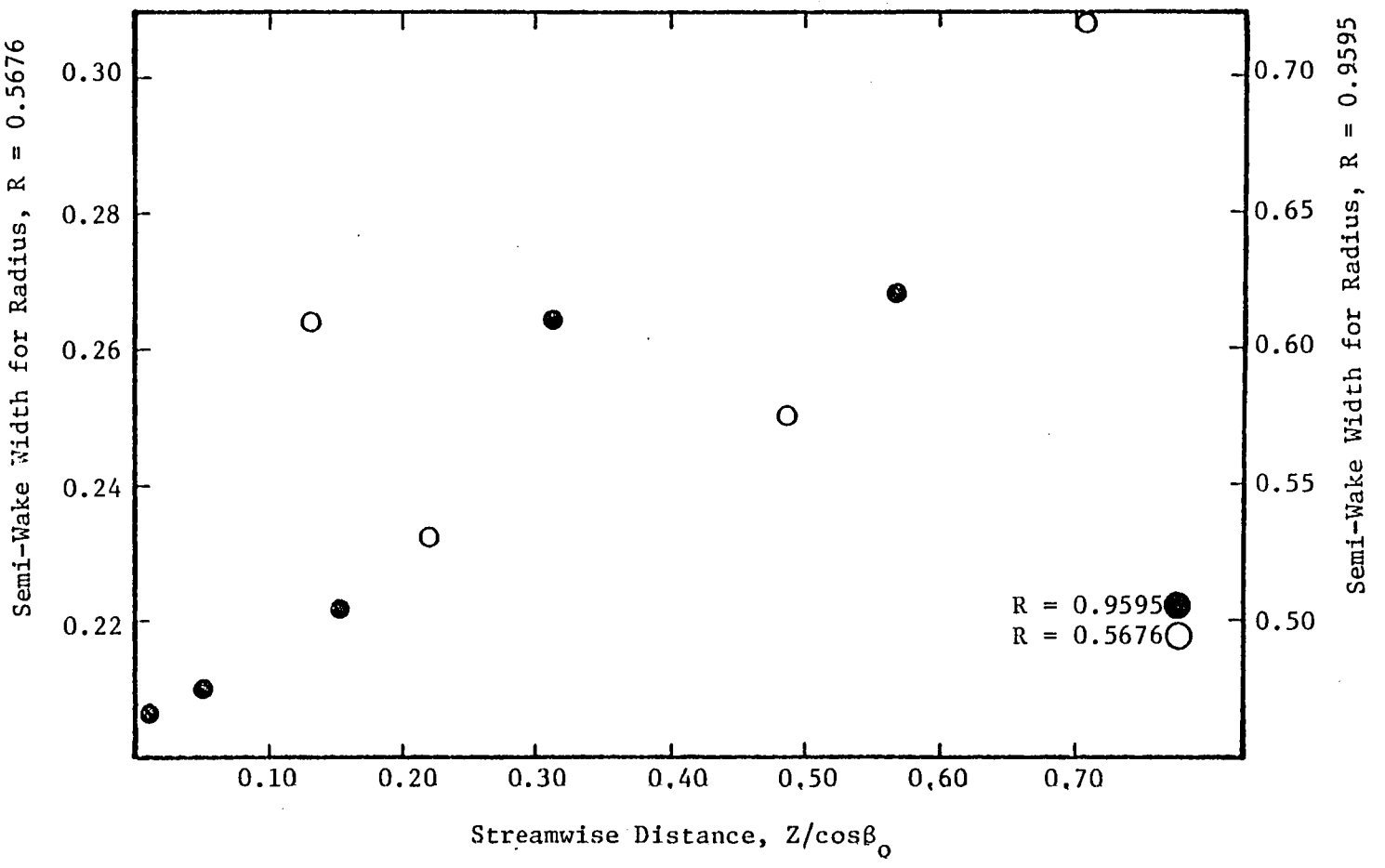

Figure 94b. Semi-Wake Width Variation with Streamwise Distance for Wakes Inside End-Wall Boundary Layers

factors, on the aerodynamic properties of the blade and in particular is strongly dependent on the section drag coefficient. So it is logical to compare the wake after its dependency on the drag coefficient (and consequently the radius) is removed. This correction is attempted in a subsequent section. But is should be commented that increased blade loading increases the wake width.

3.9 Wake Shape Factor and Momentum Thickness Variation

3.9.1 Wake shape factor

The wake shape factor (H) defined as the ratio of the displacement thickness to momentum thickness, is uniquely related to the velocity profile. The variation of the shape factor with downstream distance for all the radii is shown plotted in Figure 95. For the wakes outside the annulus-wall boundary layer the shape factor, shown in Figure 95, monotonically decreases with increasing distance from the trailing-edge and it asymptotically approaches the value of 1.2 at far downstream locations. In the hub-wall boundary layer region it is noted, Figure 95, that the value of the shape factor is very high, and this may be attributed to the pressure gradients. In the trailing-edge region for R = 0.7297, the value of the shape factor is greater than 1.8 which indicates that the flow shows a tendency to separate. For the wake inside the annulus-wall boundary layer the shape factor shows a very interesting trend. It initially decreases and beyond Z = 0.1 it starts to increase. This might be due to the merger of the tip-vortex with the wake. As the wake travels downstream from the trailing-edge, the vortex dominates the flow initially and later as the vortex dissipates the secondary flow and boundary layer flow dominate the flow. This may account for the unusual behavior of the shape factor variation in this region. It can thus be

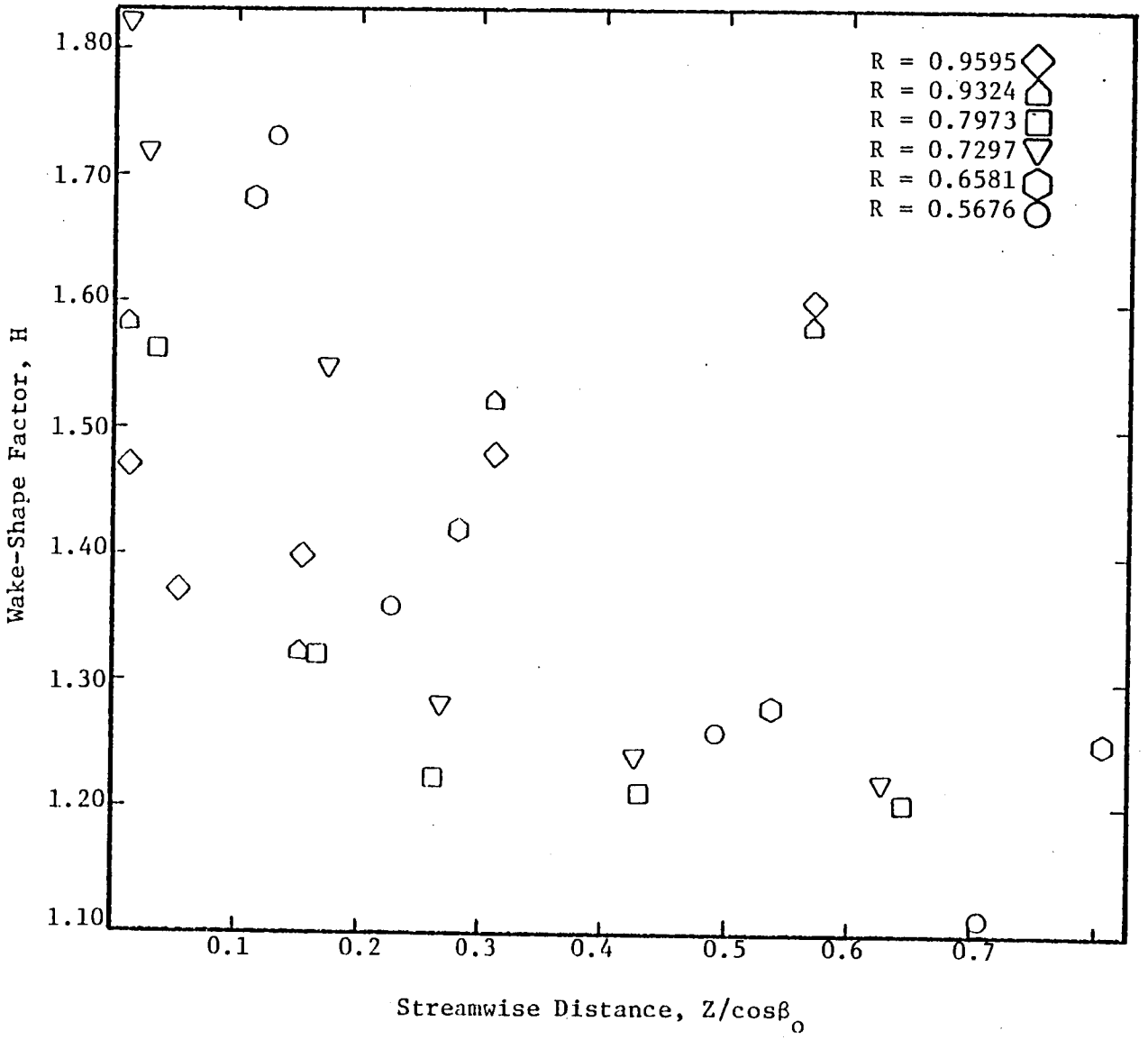

Figure 95. Variation of Wake Shape Factor with Streamwise Distance

concluded that for the wakes inside the annulus- and hub-wall boundary layers the variation of the shape factor is no longer controlled by the variation of the momentum thickness or the free-stream velocity variation.

The variation of the shape factor for isolated airfoils and cascades has experimentally been determined and reported by Lieblein and Roudebush (1956), Raj and Lakshminarayana (1973). Reynolds (1978) has given this variation for a lightly loaded fan. Comparison of the data from Reynolds (1978) with the present data (Figure 95) indicates the effect of loading on the shape factor. The higher the loading, the higher the shape factor. Compared to a lightly loaded blade the shape factor for a heavily loaded rotor decays much more slower. Thus the effect of loading is to slow down the decrease of the shape factor.

Raj and Lakshminarayana (1973) have shown that Spence's semi-analytical expression for the variation of the shape factor can be employed even to a cascade to accurately predict the downstream variation and that the agreement between the expression

$$(1 - \frac{1}{H}) = (1 - \frac{1}{H_{TE}})(b\,\frac{z}{c} + 1)^{-1/2} \qquad (7)$$

and the data is good, where the constant b takes the value of 40. But the same expression could not accurately predict the rotor-wake shape factor thus indicating highly three-dimensional nature of the rotor-wake. The magnitude of the shape factor based on this two-dimensional analysis yields very high values and this reflects the effects of three-dimensionality which dominate the flow in these regions.

3.9.2 Wake momentum thickness

Momentum thickness is defined as

$$\theta^* = \int_o^{\delta} \frac{w}{W_o}\left(1 - \frac{w}{W_o}\right) d(n/\delta) \qquad (8)$$

and is used as the characteristic boundary layer dimension. The momentum thickness implies the loss of momentum in the boundary layer, as compared with potential flow. In the case of the rotor-wake, this loss of momentum is defined in the wake, with the integration carried across one blade spacing and is given by

$$\theta^* = \frac{1}{s} \int_o^{s} \frac{w}{W_o}\left(1 - \frac{w}{W_o}\right) r d\theta \quad . \qquad (9)$$

The experimental variation of the wake momentum thickness with downstream distance is shown plotted in Figure 96 for various radial locations. Note the θ^* variation from one radius to another. These variations can be explained on the basis of conventional boundary layer momentum equation (two-dimensional) with zero shear stress as follows.

$$\frac{d\theta^*}{ds} = (H + 2)\frac{\theta^*}{W_o}\frac{dW_o}{ds} = 0 \qquad (10)$$

From this equation it is clear that the value of θ^* will increase if W_o decreases and it will decrease if W_o increases. A knowledge of the free-stream velocity variation will thus enable the determination of θ^* variation. A plot of this free-stream velocity variation with downstream distance is shown in Figure 89. A comparison of this figure with Figure 96 shows that the above reasoning is valid except in the trailing-edge and annulus-wall boundary layer regions. For the case of cascades and isolated airfoils this has experimentally been determined and reported by Raj and Lakshminarayana (1973) and Lieblein and Roudebush (1956). For the case of lightly loaded rotor it has been reported by Reynolds (1978).

As seen from Figure 96, for a moderately loaded compressor rotor, most of the increase in momentum thickness occurs very close to the trailing-edge where the change in shape factor and consequently the displacement thickness is greatest. For $Z > 0.2$ very little change in θ^* occurs indicating approximately constant free-stream velocity. Very close to the trailing-edge θ^* variations may not conform with the free-stream velocity variation due to the three-dimensional nature of the flow, the static-pressure gradients and the curvature induced Coriolis and centrifugal forces.

The wake inside the annulus-wall boundary layer behaves quite differently from that at other radii. Here the momentum thickness increases by nearly six percent until 0.4 chords downstream beyond which it stays approximately constant. This large momentum thickness might be attributed to the tip-vortex (leakage vortex) which might be continuously contributing to the wake defecit. Beyond 0.4 chords the strength of the tip-votex might be very weak and the flow is dominated by the wake.

The effect of blade loading can be observed by comparing Figure 96 with the data of Reynolds (1978). At the same Z-location, say $Z = 0.25$, $R = 0.7297$, for a moderately loaded compressor rotor the momentum thickness is 0.06 while for a lightly loaded rotor the value is only 0.02. (Actually θ/c should be compared. But both the rotors, in the present comparison, have the same chord length.) Thus the effect of blade loading is to increase the momentum thickness.

3.10 Variation of Wake Characteristics in the Radial Direction

In previous sections the decay of the wake properties as a function of the downstream distance from the trailing-edge was dealt with. In these studies it was realized that the wakes differ considerably in

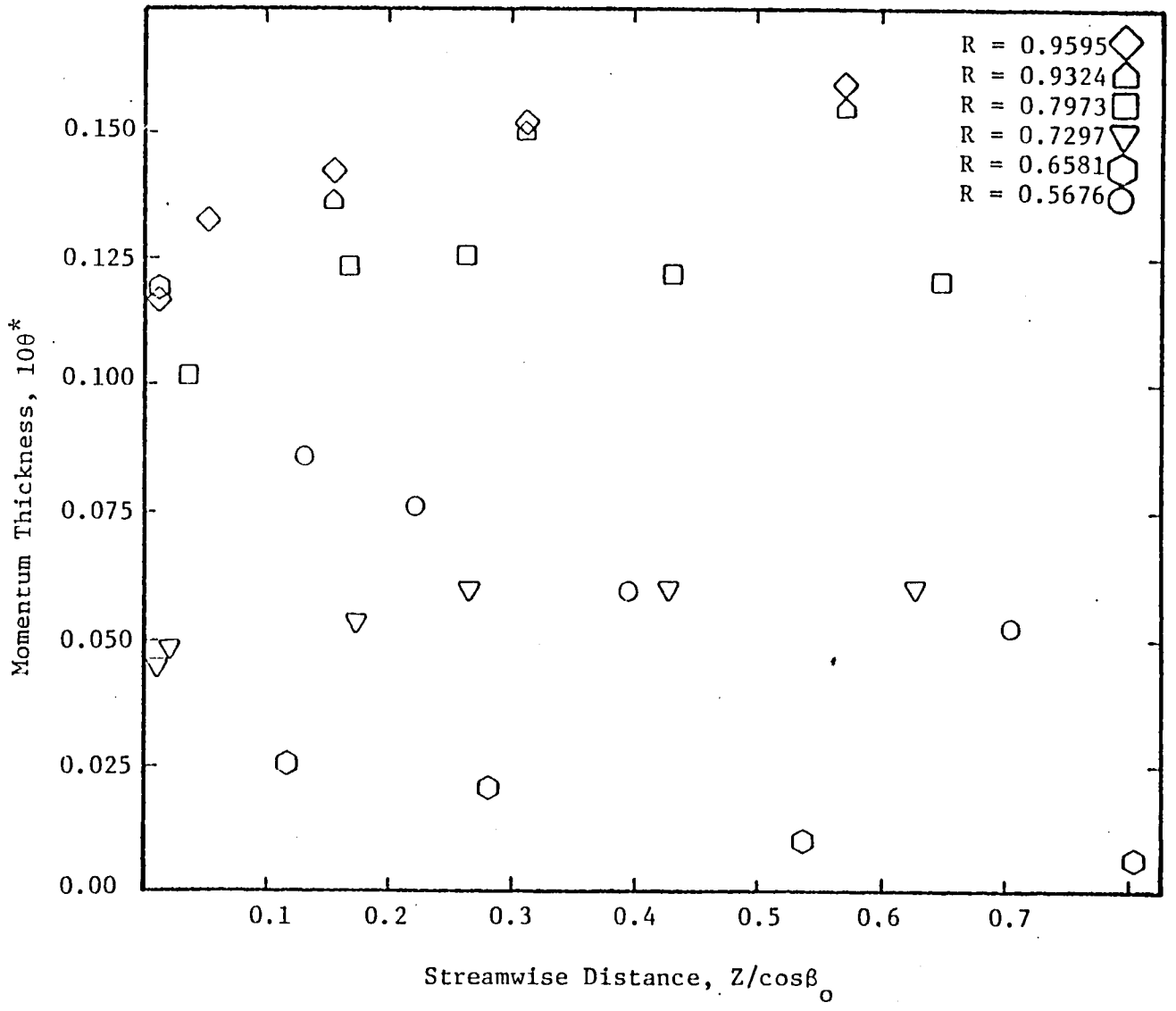

Figure 96. Variation of Momentum-Thickness with Streamwise Distance

the radial direction with regard to their decay and profile. This necessitated a search for variation of wake properties in the radial direction.

3.10.1 Wake characteristic velocity variation

Radial variations of the maximum axial, tangential velocity defects, and the maximum radial velocity of the rotor-wake are shown plotted in Figures 97, 98, and 99. Figure 100 shows the variation of the maximum velocity defects and the maximum radial velocity with radius for the station about 0.12 chords downstream of the blade trailing-edge. The proper parameter to be employed is the streamwise distance, $Z/\cos\beta_o$. The data points shown in Figures 97 to 109 are at Z-locations given in Table 3. Variations of β_o at various radial locations are given in Table 2. It is seen that the velocity defect is maximum near the hub and decreases with increasing radius. The variation is not appreciable beyond R = 0.7 and the defect remains fairly constant as the wake decays along the relative streamlines. At higher radii the streamwise distance downstream of the rotor in the relative frame of reference is higher. Hence the defect tends to be lower. For the same reason, at lower radii the defect will be larger. Inside the annulus- and hub-wall boundary layers the wake is greatly influenced by the secondary flows and the tip-leakage flows (essentially true only in the annulus-wall region) where the above reasoning may not apply.

Variation of the tangential velocity defect with radius is shown in Figure 98. The tangential defect increases with increasing radius up to 0.73 and starts to decrease beyond that. This clearly indicates the effect of the three-dimensional nature of the flow as well as the effect of secondary flow (tip-vortex in the case of annulus-wall region). The

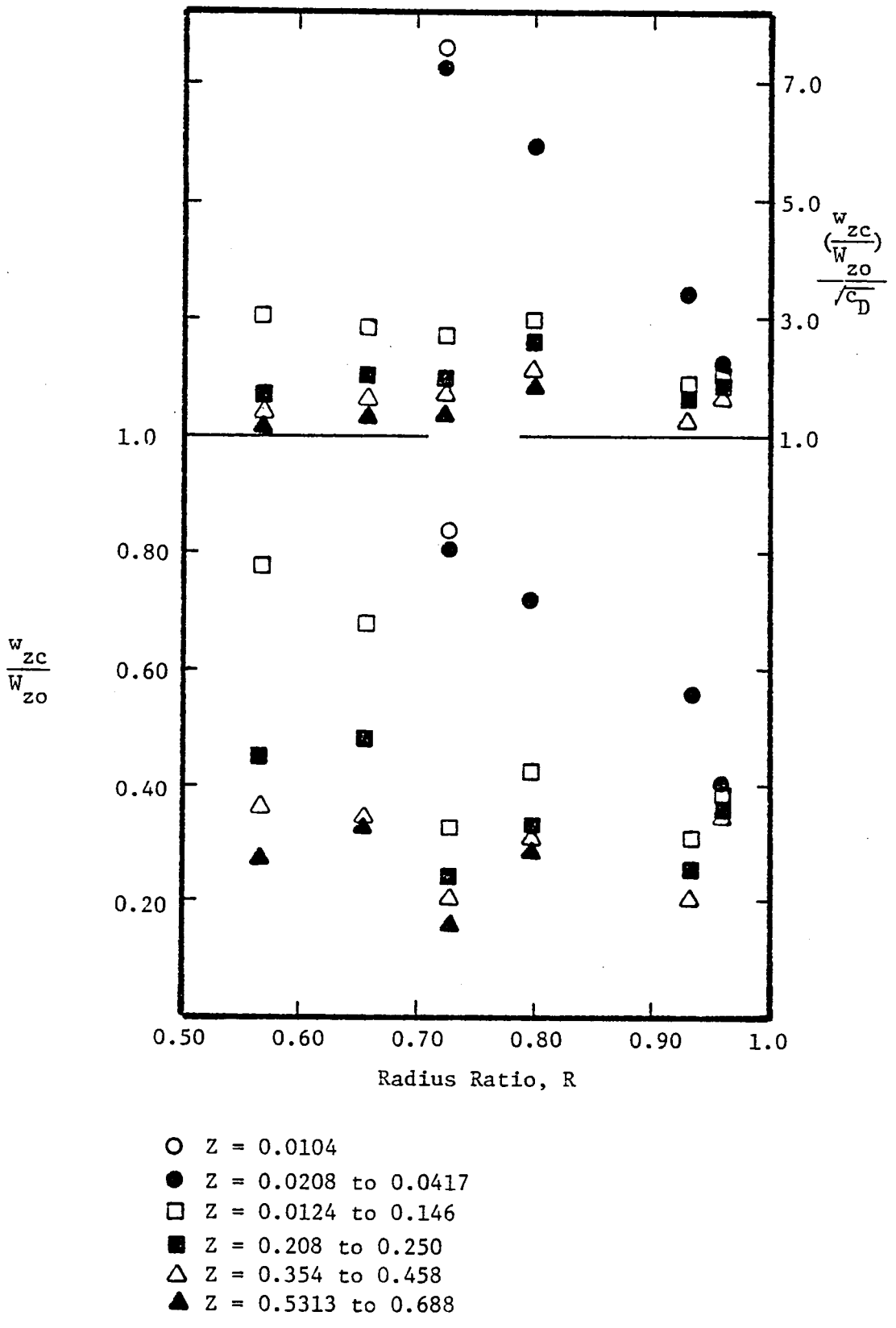

Figure 97. Radial Variation of Axial Mean Velocity

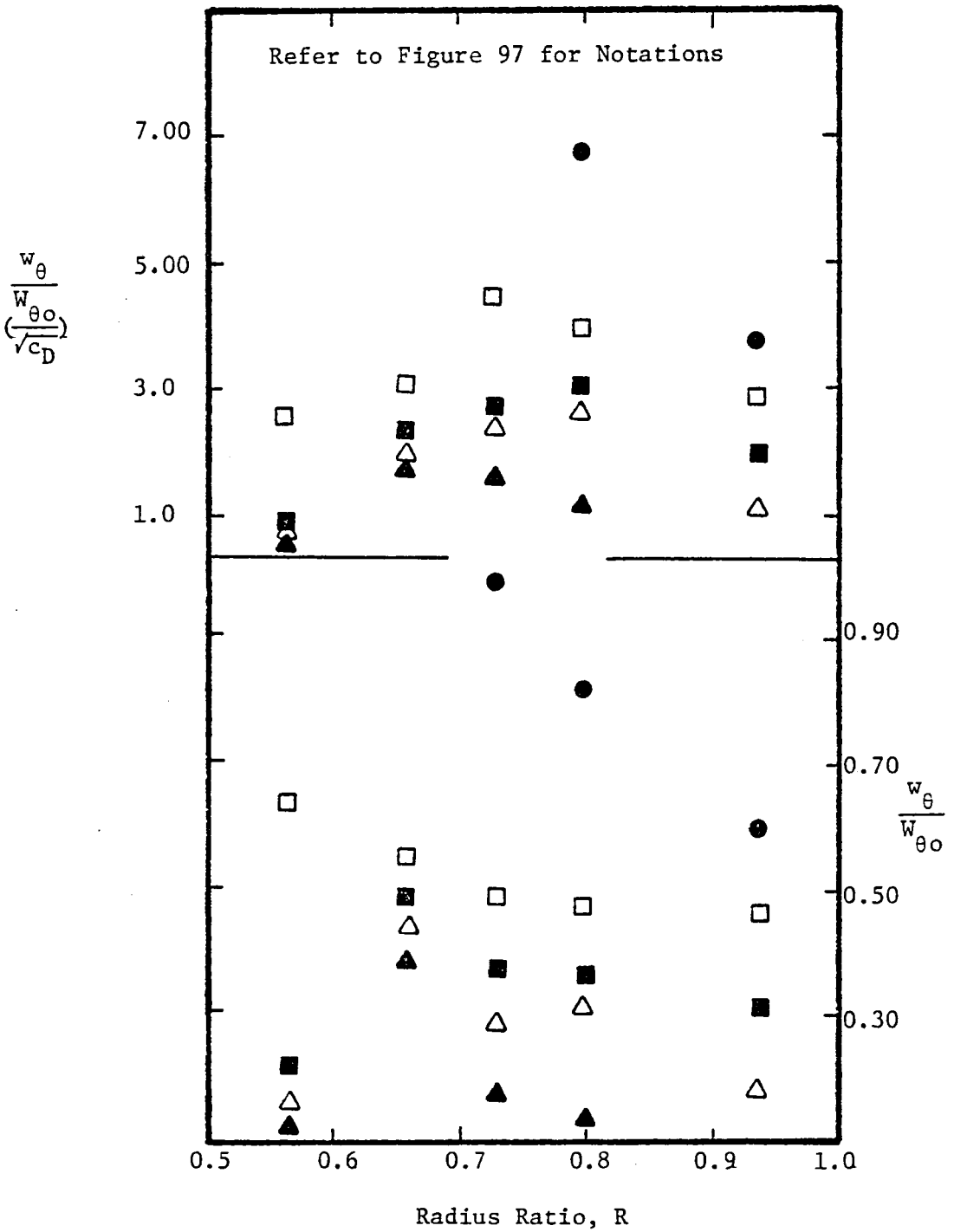

Figure 98. Radial Variation of Tangential Mean Velocity

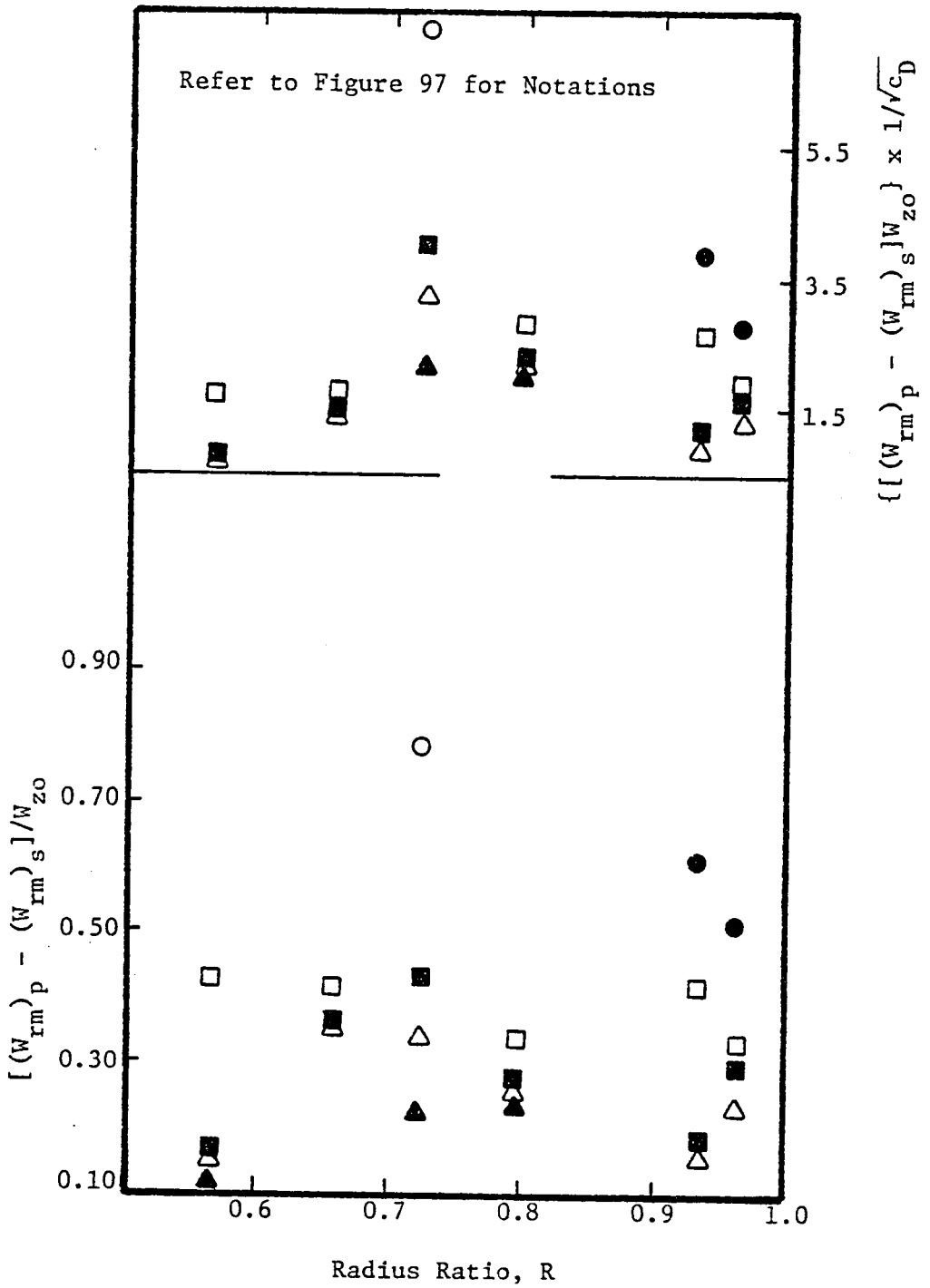

Figure 99. Radial Variation of Radial Mean Velocity

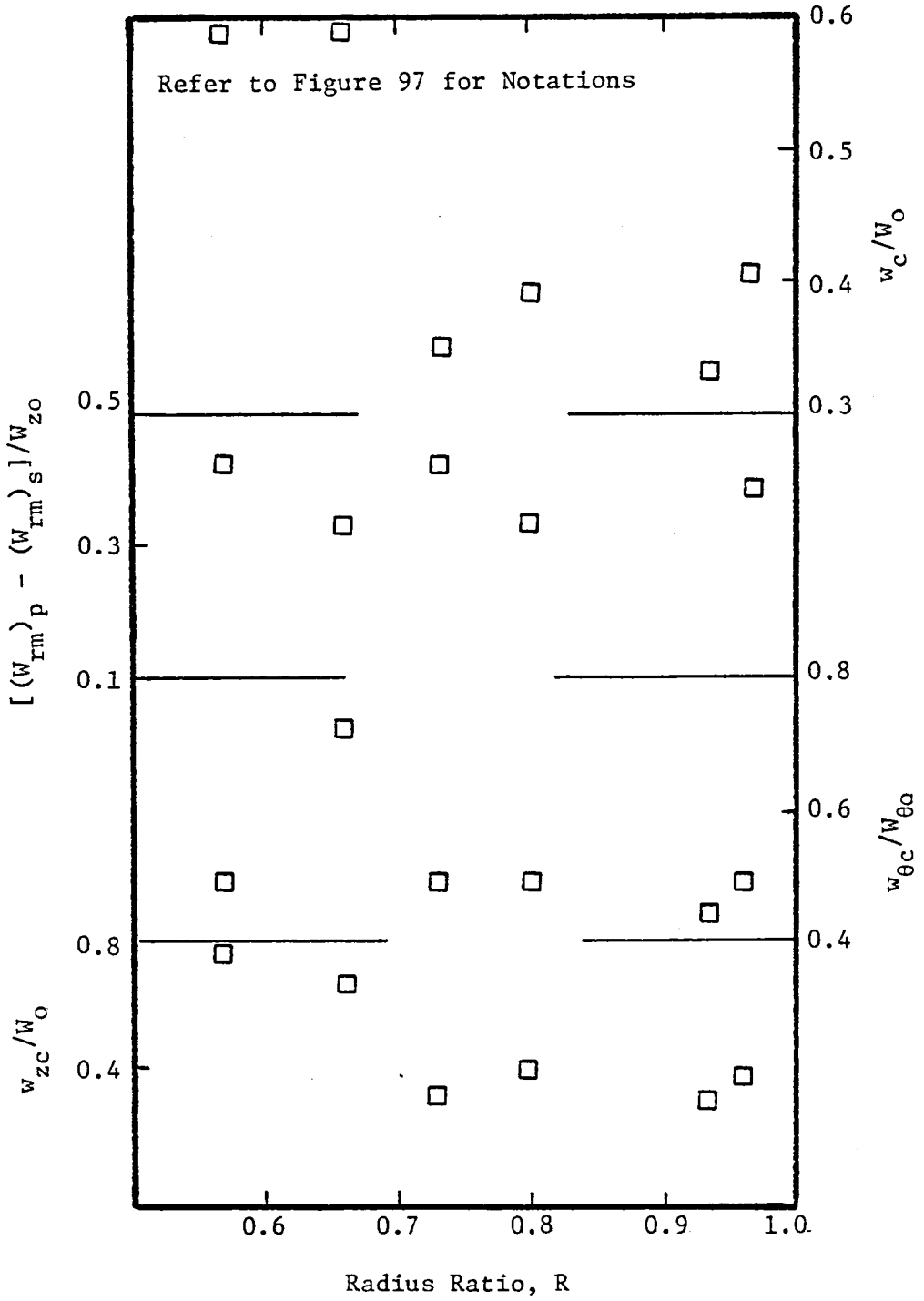

Figure 100. Radial Variation of Mean Velocities

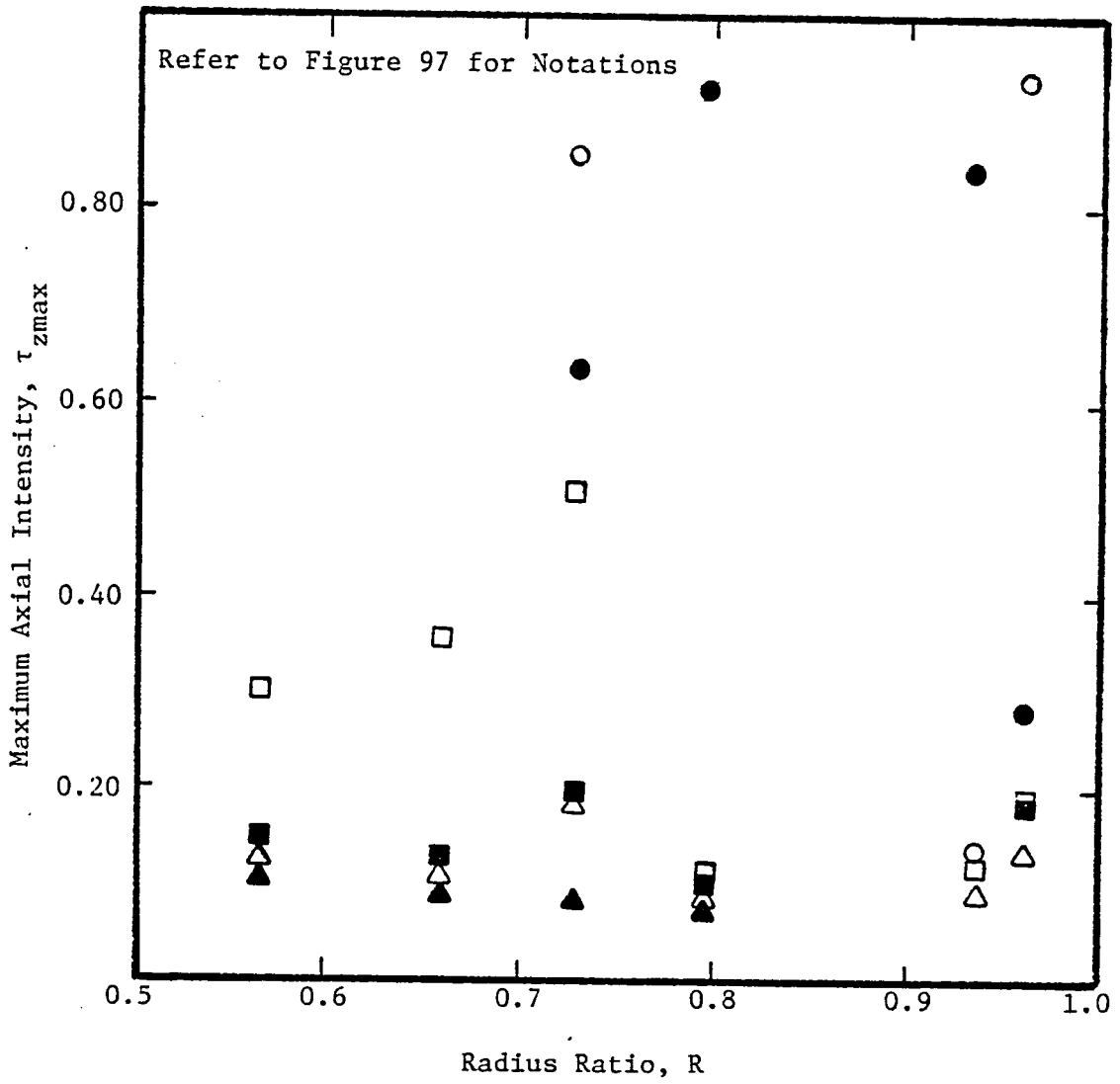

Figure 101. Radial Variation of Maximum Axial Turbulence Intensity

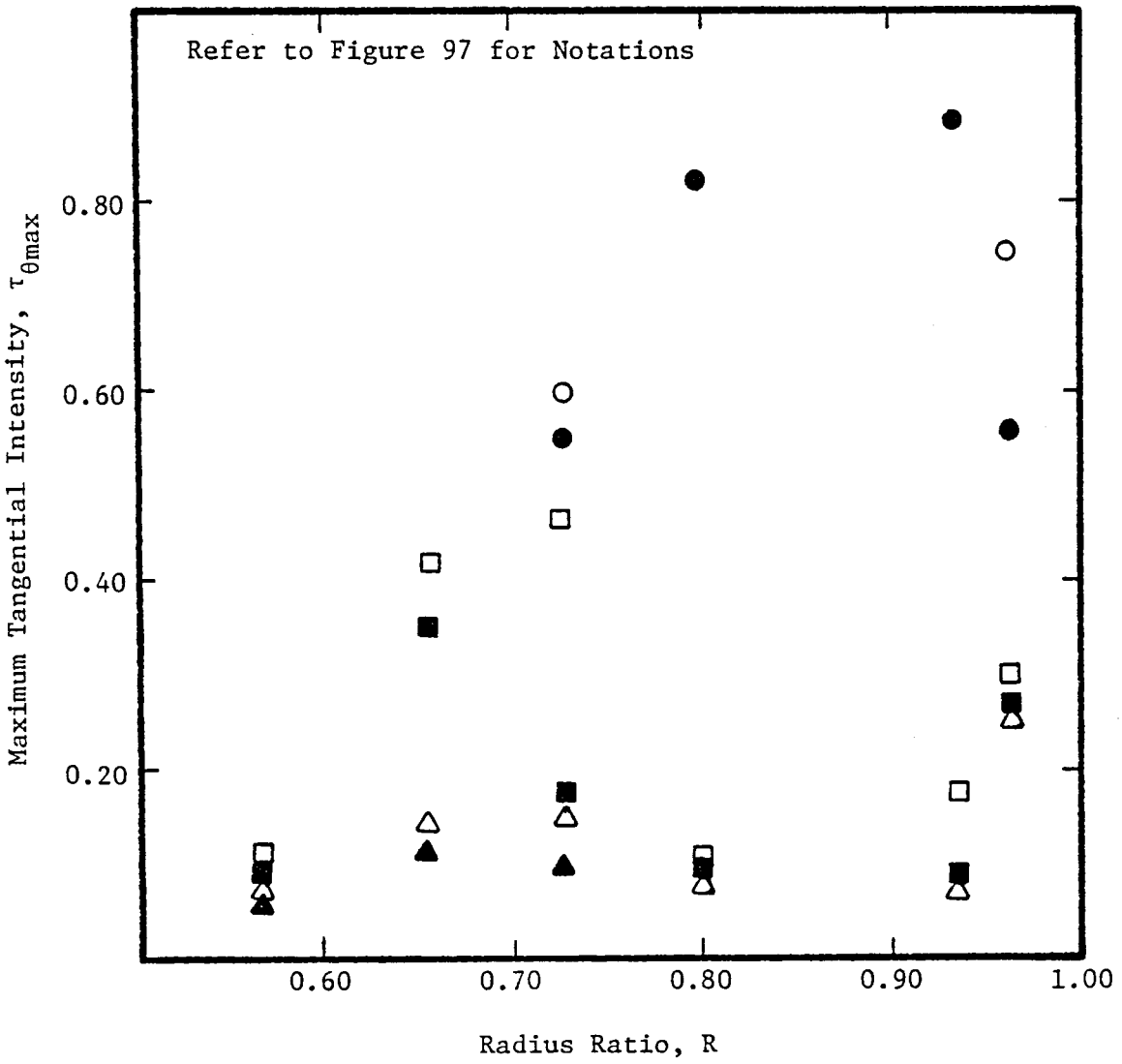

Figure 102. Radial Variation of Tangential Turbulence Intensity

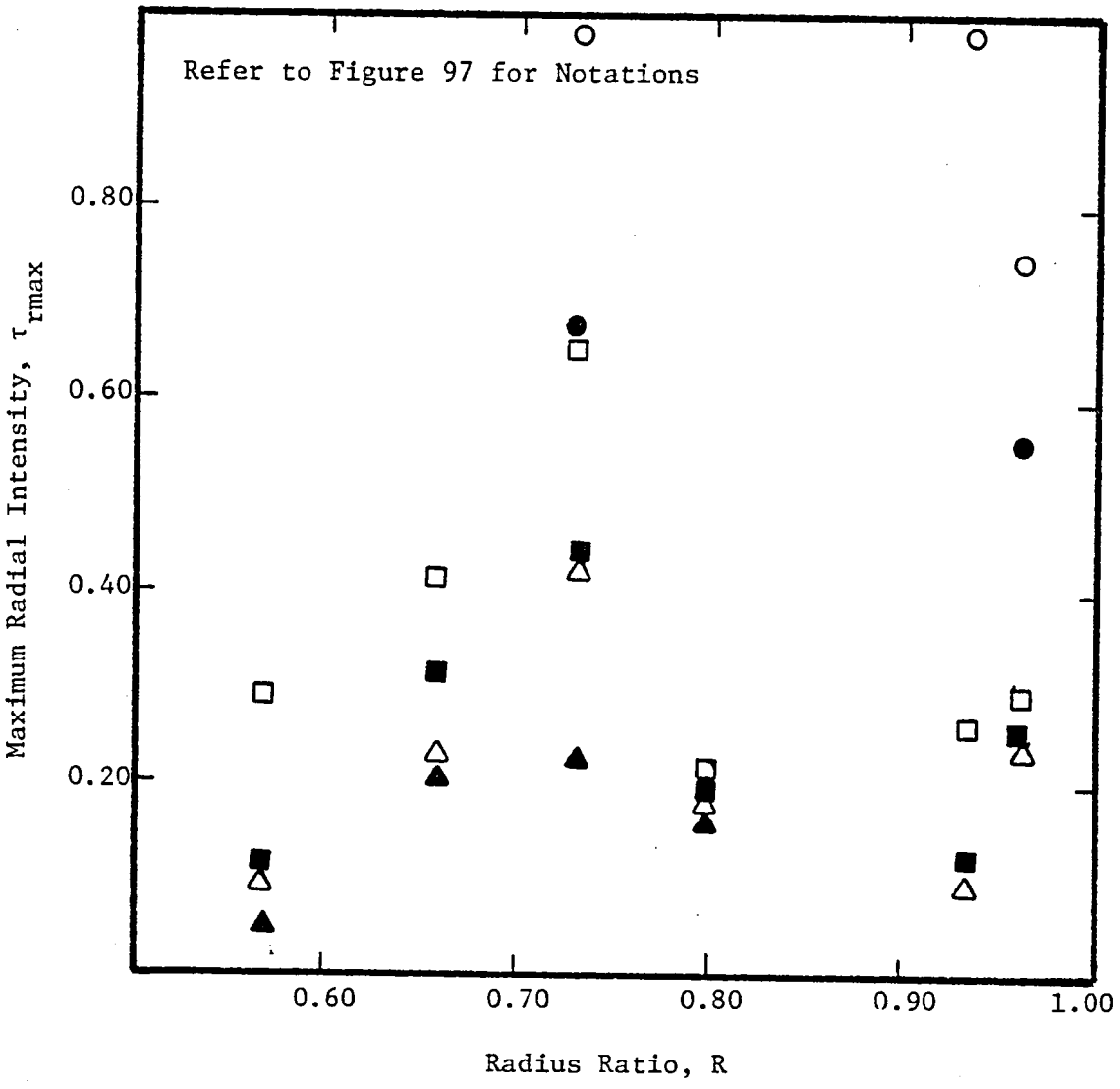

Figure 103. Radial Variation of Radial Turbulence Intensity

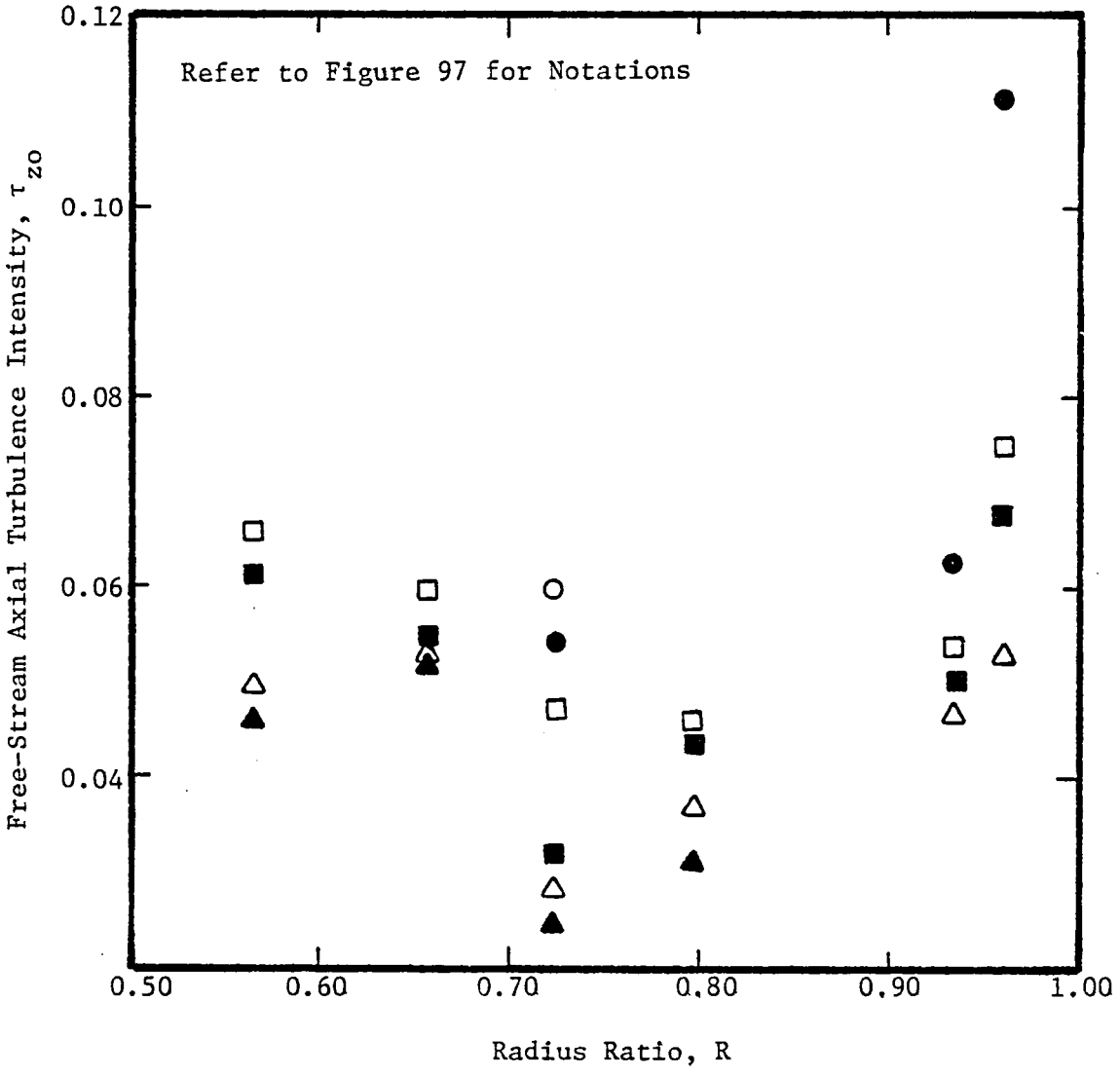

Figure 104. Radial Variation of Free-Stream Axial Turbulence Intensity

166

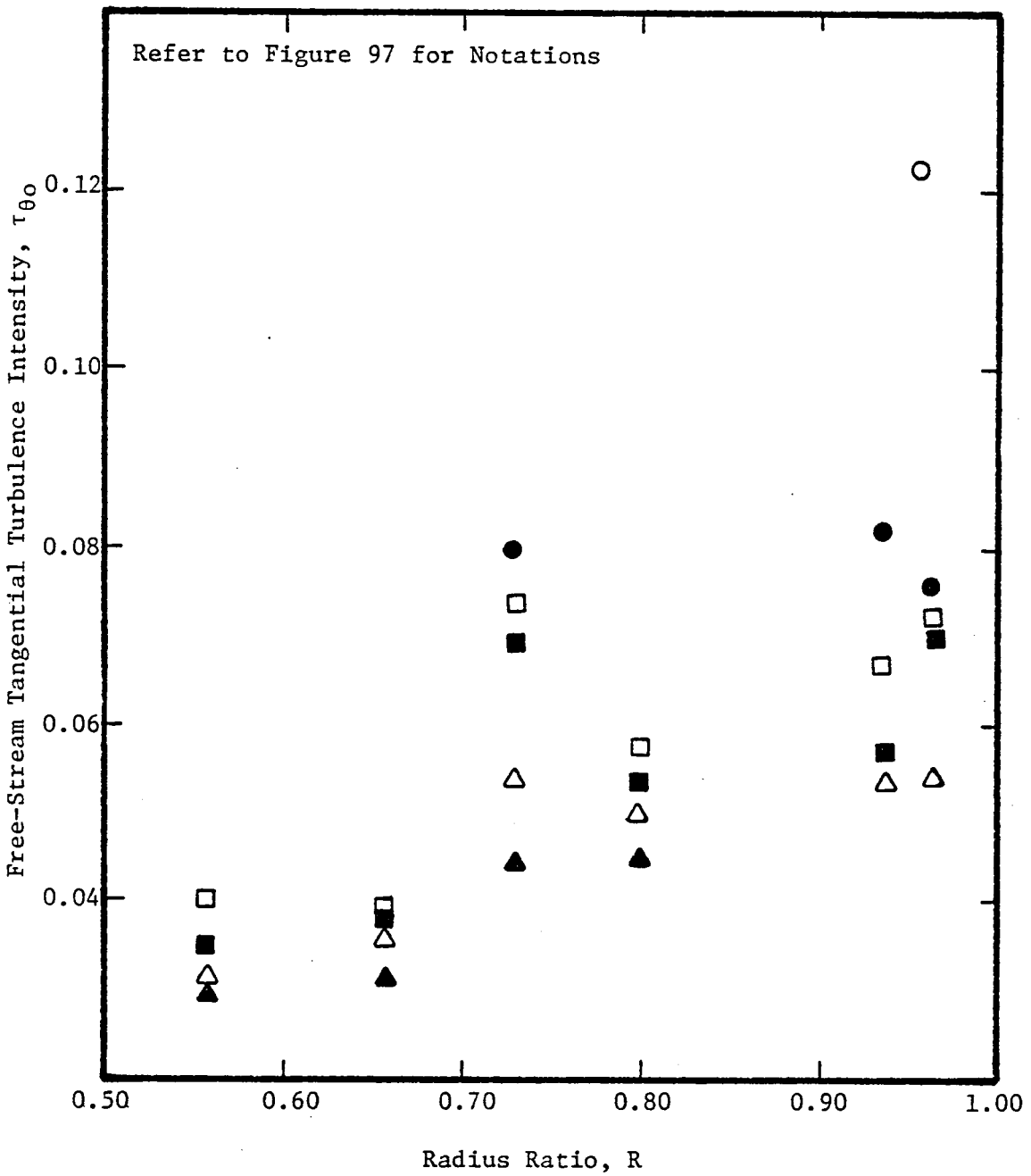

Figure 105. Radial Variation of Tangential Turbulence Intensity

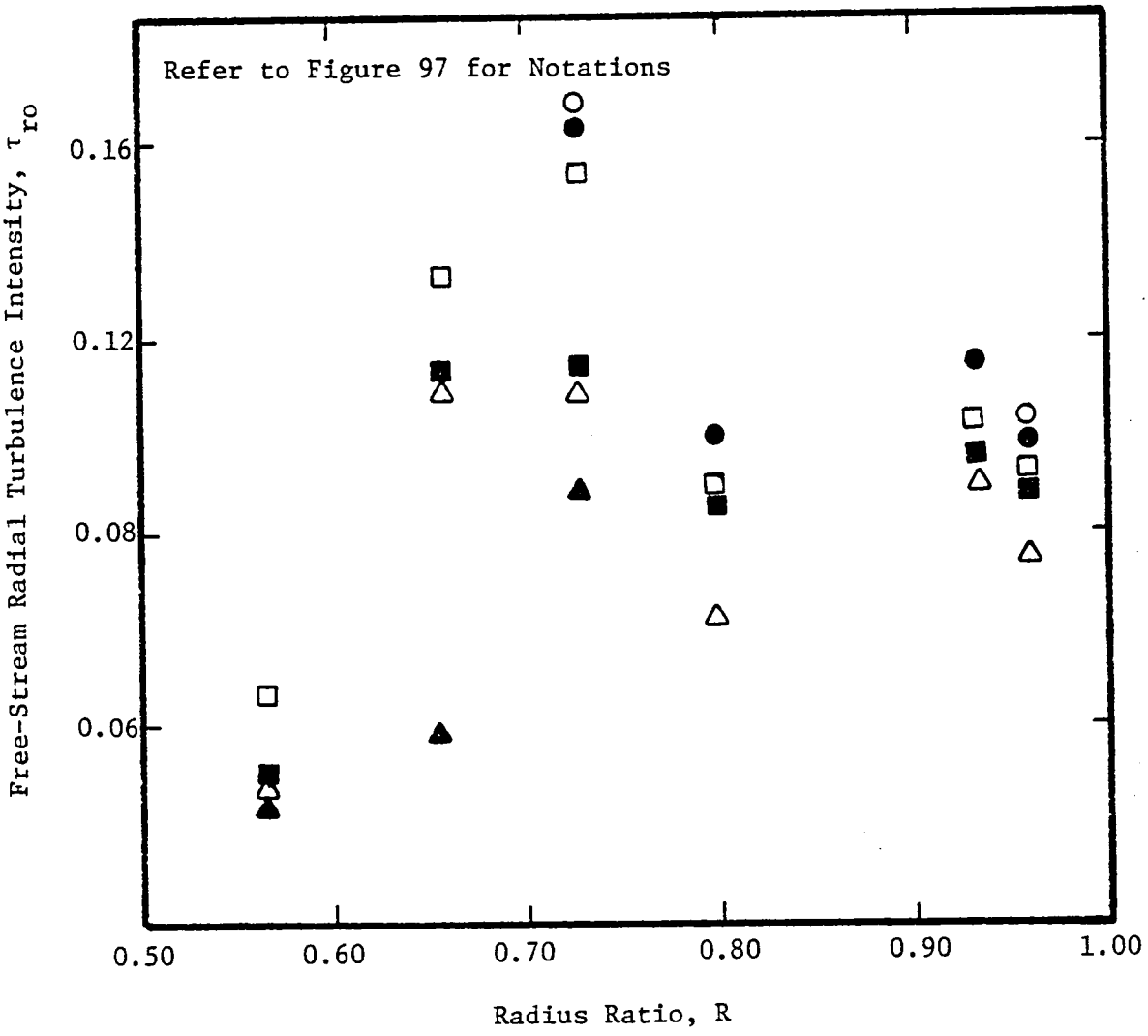

Figure 106. Radial Variation of Radial Turbulence Intensity

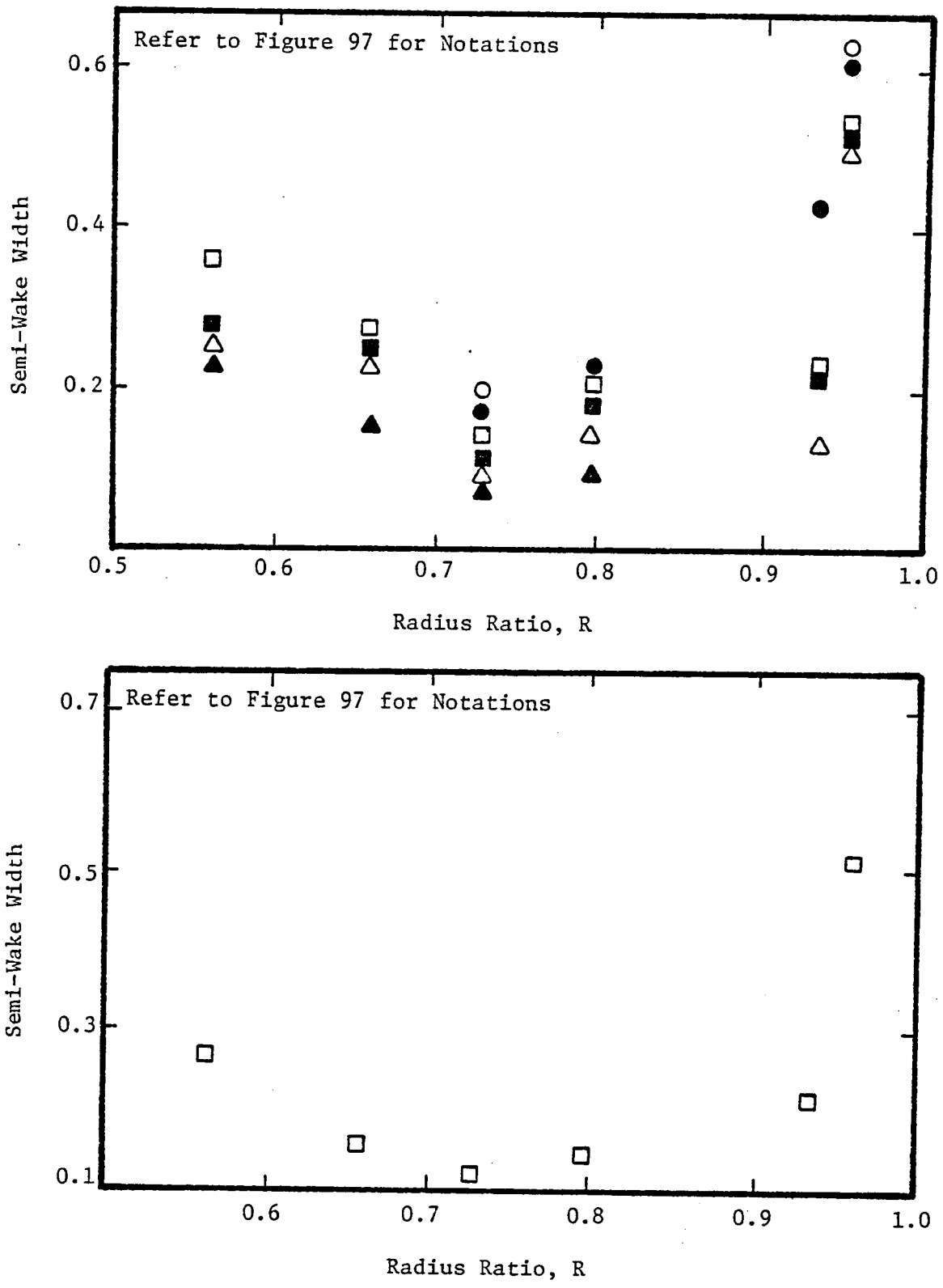

Figure 107. Radial Variation of Semi-Wake Width

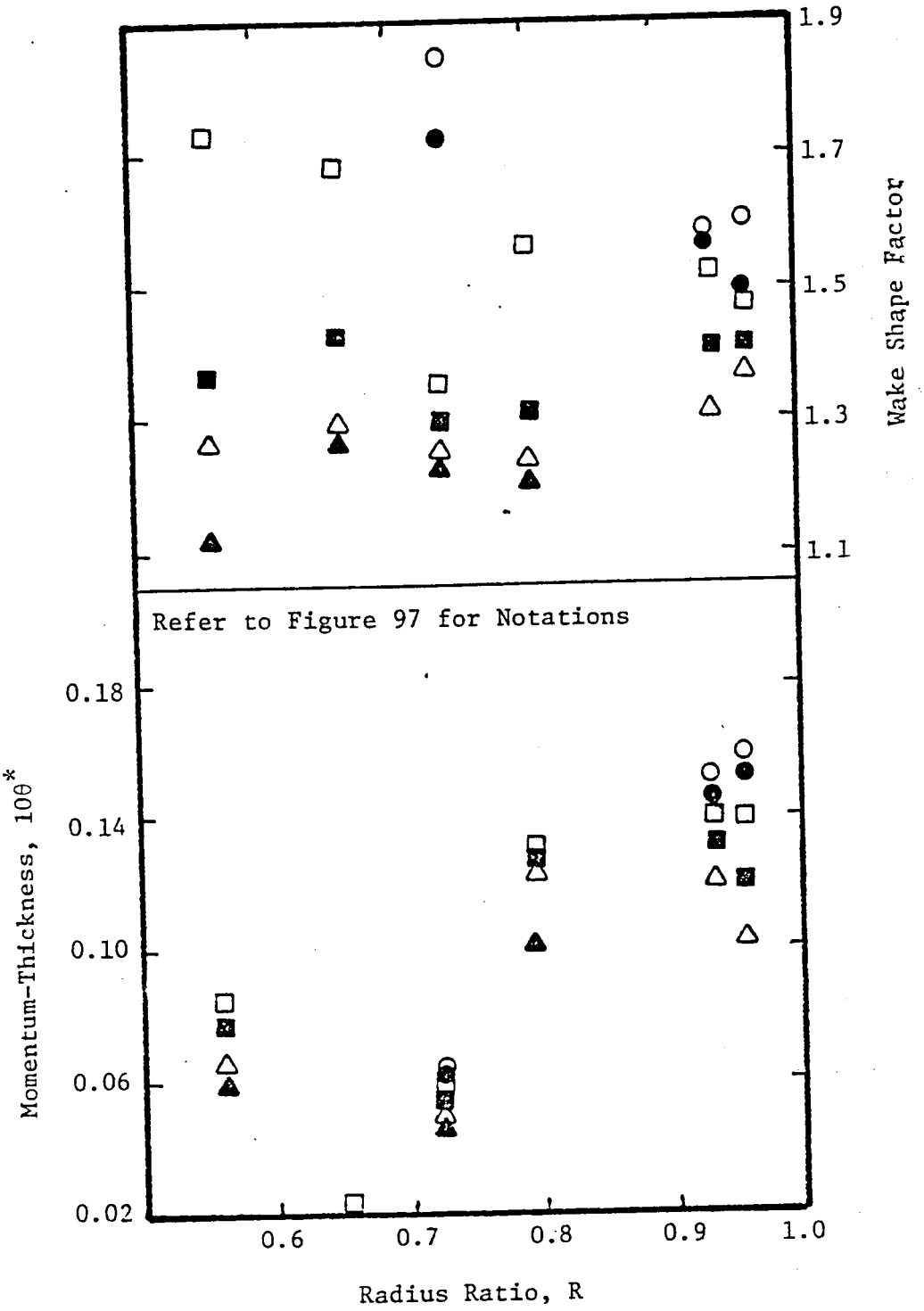

Figure 108. Radial Variation of Momentum-Thickness and Shape-Factor

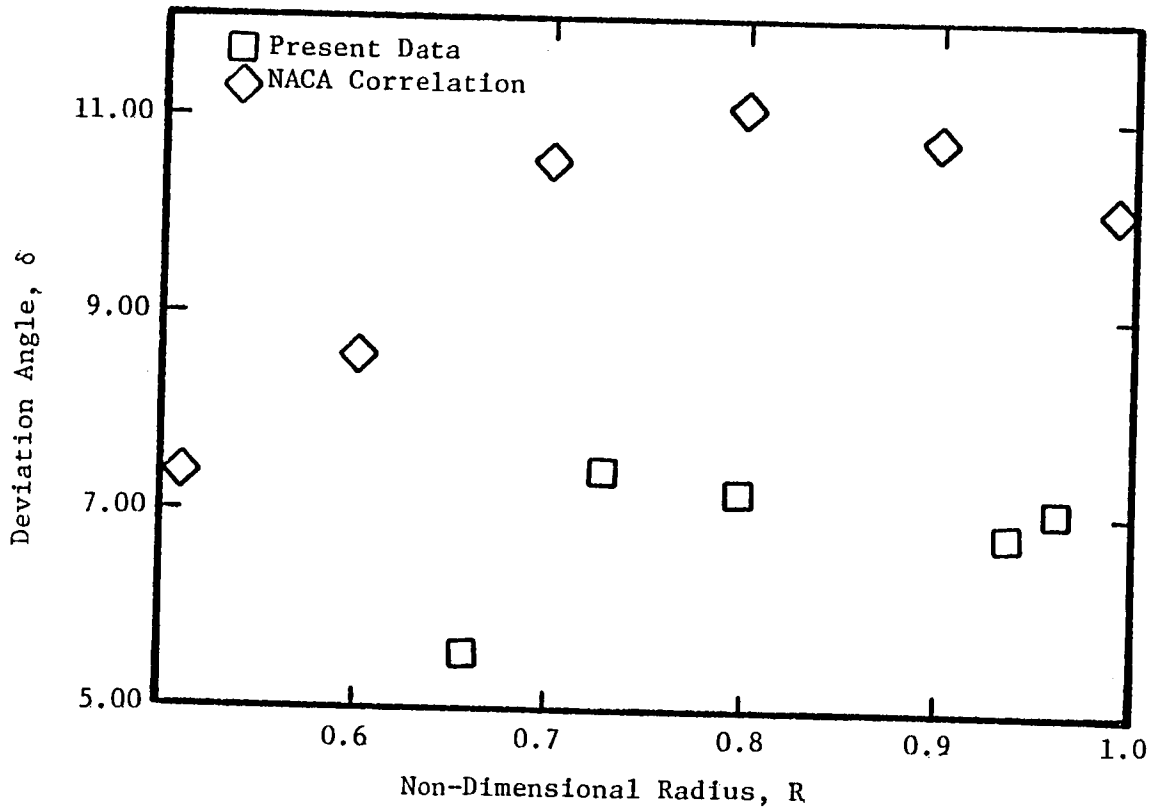

Figure 109. Variation of Deviation Angle with Radius

lower tangential velocity defects near the hub and annulus-wall can be attributed to the rapid decay of the wake caused by the tip-vortex and secondary flow.

The effect of blade loading on the tangential velocity defect can be discerned by comparing this figure with that of Reynolds (1978). Higher loading seems to give higher tangential defects. Comparing the two radii R = 0.7297 and 0.9595, at the same Z-location of 0.0104, it is noticed that at the lower radius the tangential velocity defect is larger. The same is true as the hub-wall is approached; in fact the tangential velocity defects are much more pronounced than the axial velocity defects.

The radial variation of the maximum variation in velocities $[(W_{rm})_p - (W_{rm})_s]/W_{zo}$ is shown plotted in Figure 99. As mentioned earlier the radial velocities are significant in the rotor-wakes and it varies considerably in the radial direction. Secondary flow, tip-leakage (and the associated tip-vortex) and the trailing-vortex system greatly influence the radial flows. The radial velocities are also influenced by the centrifugal and Coriolis forces which are not only a function of speed of rotation but also the radius. Radial velocities will also be induced by the trailing-shed-vortices and the unbalanced pressure gradients in the radial direction. The effect of all this is to make the radial variation of the radial velocity highly complex. Near the hub-wall boundary layer radial velocities are inward in nature (influence of secondary flows) and at higher radii the effect of secondary flow vanishes and the radial transport of mass, momentum, and energy influenced by the centrifugal forces dominates. As the annulus-wall region is approached the radial outward velocities have to vanish and may result in radially in-

ward velocity. The effect of these on the radial velocities is shown plotted in Figure 99.

3.10.2 Maximum turbulence intensity in the wake

The radial variation of maximum axial, tangential, and radial turbulence intensities in the wake is shown in Figures 101, 102, and 103.

Measurements in the trailing-edge region show that the turbulence intensities are maximum at the wake center (allowing for the probe's spatial error). These intensities are an order of magnitude higher than those that were measured in the near- and far-wake regions. These high intensities are attributed to the trailing-vortex system that dominates the flow at these locations. But the trailing-vortex's contribution to the wake-turbulence decays very rapidly (in less than five percent of the chord) and the wake-turbulence dominates over the vortex-turbulence beyond this downstream location.

Considering only the wake-turbulence it is noted that the turbulence intensity is maximum at the annulus-wall region and decreases steadily to a minimum at the mid-radius and starts to increases again towards the hub-wall region. (This is true for only near- and far-wake regions. For the trailing-edge locations the trailing-shed vortex contribution is substantial and may offset the above trend). This trend can be explained based on the tip-leakage-vortex, secondary flow, annulus- and hub-wall boundary layer and its interaction with the wake. Thus the intensities are fairly constant over a very narrow region across the annulus.

Of the three components of intensity the largest component is the radial intensity. Very close to the trailing-edge and in the near-wake regions the turbulence is highly anisotropic and has a tendency to become isotropic at far-downstream locations. Even though the turbulence struct-

ure was radially varying, free-stream turbulence for all the wakes outside the end-wall region was around four to five percent. The presence of maximum radial intensities of an order equal to or greater than that of axial and tangential components indicates the three-dimenisonal nature of the turbulence structure. This characteristic becomes less pronounced beyond 0.5 chords downstream. Reynolds (1978) has mentioned that radial intensities dominate even at far downstream locations. This might reflect on the effect of loading on the three-dimensionality of the turbulence structure. The higher the loading the faster is the tendency for the turbulence to tend towards isotropy.

3.10.3 Free-stream turbulence intensity

Variations of the free-stream axial, tangential, and radial turbulence intensities are shown plotted in Figures 104, 105, and 106. Here again the radial intensity is at a maximum, confirming the effect of rotation on the turbulence structure.

It is of interest to note the turbulence amplification through the blade row. A two percent free-stream axial and tangential turbulence and a less than one percent radial turbulence measured ahead of the blade row show up as rather high values in the free-stream after passing through the blade row. This amplification is probably caused by the blade force acting on the fluid.

In the case of radial intensity (Figure 106), a less than one percent turbulence intensity in front of the rotor gets amplified to nearly 16 percent in the trailing-edge region for R = 0.7297 and it drops off rather quickly to less than eight percent in half-a-chord downstream. The same is true at other radii except for those inside the annulus-wall boundary layer. Here the overall radial turbulence level was within the

range of eight to 11 percent indicating the effect of secondary flow and the tip-vortex on the turbulence structure. In the hub-wall region, as no trailing-edge measurements are available, the radial turbulence intensity remained fairly low in the range of 2.5 to 4.6 percent. All this clearly indicates the effect of centrifugal and Coriolis forces on the radial turbulence intensity.

A two percent axial and tangential intensity measured ahead of the rotor is found to have been amplified to nearly eight percent in the free-stream in the trailing edge and near-wake regions and drops off to around two percent in the far-wake region. So the free-stream axial and tangential turbulence intensity are of the same order of magnitude while the radial intensity is nearly twice the value of the axial and tangential components.

The free-stream turbulence structure does not in any way reflect the wake characteristics. It is helpful to the aerodynamicists and aeroacousticians in evaluating the inlet flow conditions to a subsequent stage. As is seen the axial and tangential components are of the same order while the radial turbulence structure is greatly affected by centrifugal forces. Near the hub- and annulus-wall, because of interactions of the wake, secondary flow and the end-wall boundary layers, the level of turbulence is high. At the tip region added to the above mentioned is the effect of tip-vortex.

Thus in a multi-stage machine there will be a spanwise gradient in turbulence intensity which would alter the flow situation into a succeeding blade row and consequently there will be a spanwise gradient in noise generation and propagation.

3.10.4 Semi-wake width

The variation of the semi-wake width with radius is shown plotted in Figure 107. It is seen that the wake width is a minimum in the mid-radius region and increases very rapidly towards annulus-wall and hub-wall region. This has to be expected as the radial transport of mass, momentum, and energy in the rotor-wake is towards the annulus-wall region and also the influence of the secondary flow (and the tip-leakage flow in the case of annulus-wall), on the wake is pronounced at these locations. Inside the annulus-wall boundary layer the wake width covers the entire blade passage. This is believed to have been caused by the tip-vortex and secondary flow and their interaction with the wake. Again as the hub-wall region is approached the wake width starts to grow because of the interaction of the two shear layers, namely the wake and the hub-wall boundary layer.

Semi-wake width is controlled by many parameters, the important ones being the section drag coefficient, blade spacing and the rate of decay. In the case of an isolated airfoil the wake has an infinite media in which it can expand. But in the case of a rotor, the wake growth is controlled by the adjacent blade wakes. Thus the wake growth is very rapid in the trailing-edge region and the growth slows down and becomes asymptotic in the far-wake region. It is also possible that the two adjacent wakes might merge together. In such an event the wake width would be greater than one blade passage and this is very clearly seen in Figure 107, where at the radius R = 0.9595, the wake width is greater than one passage. Such a growth might also be assisted by the tip-vortex at those locations.

3.10.5 Momentum thickness and shape factor

Momentum thickness and shape factor variation along the radius are shown plotted in Figure 108. Both the momentum thickness and shape factor are very high in the end-wall regions and they decrease towards mid-radius. With increased blade loading there will be greater radial outward transport of momentum and energy and consequently larger momentum deficit and larger values of shape factor. This can be observed by comparing these results with those of Reynolds (1978).

3.10.6 Variation of deviation angle

The deviation angle is defined as the angle between the average exit flow direction and the direction of a line tangent to the blade section camber line at the trailing-edge. A knowledge of the deviation angle is essential in predicting the losses and aerodynamic performance of compressors. Most of the compressor design done today is based on existing cascade correlations. Even the deviation angles are predicted based on cascade correlations. There may be a difference between the deviation angles derived from cascade correlation and the actual values in a rotor. In this section an attempt is made to evaluate the applicability of cascade correlation to the actual compressor rotor-blade data. The NACA/NASA deviation angle correlation as given by Serovy (1977) was employed to compare the results from the present experimental data.

The base equation for the NACA/NASA deviation angle correlation based on cascade data is given as:

$$\delta_{ref} = \delta_o + \frac{m_{\sigma=1}}{\sigma^b} \phi \qquad (11)$$

where:

δ_o = deviation angle measured from chord line for zero camber cascade with same fluid inlet angle and solidity as the cambered cascade.

δ_{ref} = cascade exit average deviation angle measured from tangent to blade trailing edge

$m_{\alpha=1}$ = rate of change of deviation angle with camber angle for cascade with solidity of 1.0

b = exponent to account for variable influence of solidity

σ = cascade solidity

ϕ = blade section camber angle.

For the present rotor the deviation angles were calculated using the above equation. The actual deviation for the rotor-blade was obtained to be the difference between the blade outlet angle and the fluid outlet angle. The fluid outlet angle can be obtained from the mean velocity data presented earlier. Figure 109 shows the plot of this variation of the deviation angle from hub-to-tip of the machine. It is seen that the cascade correlation overpredicts the deviation angle by as much as four to five degrees.

Thus it can be concluded that the deviation angles based on the cascade correlations will not yield true estimates in an actual rotor-blade. The failure of the cascade correlations to predict deviation angles correctly is the result of three-dimensional viscous and inviscid effects.

3.11 Structure of Turbulence

3.11.1 Correlation coefficient

The shear-correlation coefficient, defined as $(\tau_{sn}/\tau_s \cdot \tau_n)$ is a measure of the turbulence structure. This coefficient depends on the nature of turbulence.

For the rotor-wake this coefficient is shown plotted in Figure 110 at various downstream locations for the radius R = 0.7297. Ermshaus (1970) has given this correlation coefficient for the far-wake of axisymmetric bodies in a two-dimensional flow. The data indicates that this coefficient varies from 0.6 to -0.6 across the wake with nearly zero values at the center of the wake. It is known that a value of 0.4 to -0.4 represents an isotropic turbulence structure. Comparison of data from Ermshaus (1970) with the author's data, Figure 110, reflects the highly non-isotropic and asymmetric nature of turbulence, particularly in the near-wake region. Beyond Z = 0.5313 the coefficient becomes almost constant across the rotor-wake. This is due to very small Reynolds stress and turbulence intensity measured at these locations. The data in the trailing-edge region for the present case must be viewed with some caution. The wake width at trailing-edge locations being very small, the hot-wire with its spatial error might yield erroneous values.

In the trailing-edge and near-wake regions the outer regions of the wake display isotropic turbulence with the value around 0.4. But inside the wake where the radial intensities are dominant compared to streamwise and normal components this correlation coefficient takes on very high values indicating the highly non-isotropic nature of turbulence. In the far-wake region the wake turbulence is isotropic in nature.

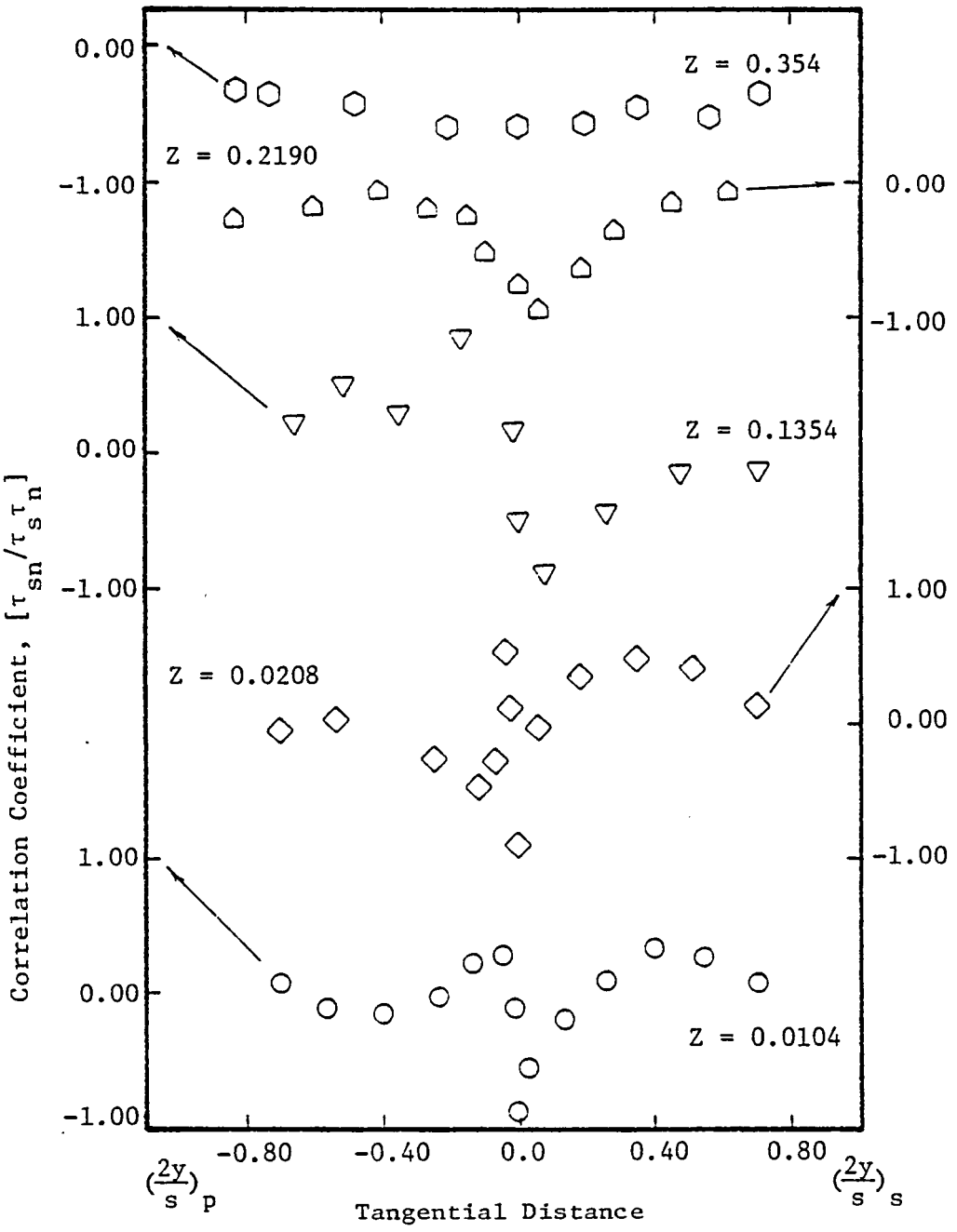

Figure 110. Variation of the Correlation Coefficient across the Rotor-Wake, R = 0.7297, ϕ = 0.56

3.11.2 Turbulence spectra

Real time spectrum analysis was carried out to evaluate the spectral content of the turbulence in the flow behind the rotor-blades. Such an energy spectrum was taken at various axial, radial, and tangential positions behind the rotor from a rotating hot-wire. The spectrum in the free-stream (between blades) as well as inside the wake (at the wake center) are presented and discussed in this section.

It is known (Hinze, 1959) that the slope of the energy spectrum is -5/3 in the inertial range of isotropic turbulence and -1 in the viscous convective range. It is of interest to know whether the rotor-wake spectrum also follows this boundary layer spectrum.

Figure 111 shows the spectrum taken at four representative radius in free-stream. The spectrum shows peaks at the blade passing frequency. If plotted on a linear scale, the area under the peaks would represent the fraction of the total fluctuating energy contained in the periodic oscillations influenced by the upstream inlet-guide-vane wakes while the area of the lower band would represent the fraction of the energy contained in the turbulent fluctuations. It is seen from Figure 111 that most of the energy in turbulence outside the wake is confined to the low frequency range (less than 2 KHZ) with a peak blade passing frequency corresponding to the inlet-guide-vane wakes. The blade passing frequency is obtained as,

$$BPF = \frac{\text{speed(rpm) x no. of IGV blades}}{60} \qquad (12)$$

$$= 0.74 \text{ KHZ} \quad .$$

It is evident that the rotating hot-wire senses the inlet-guide-vane wakes as a source of turbulence and hence its effect appears in the spectrum. The amplitude of the peaks represents the magnitude of the

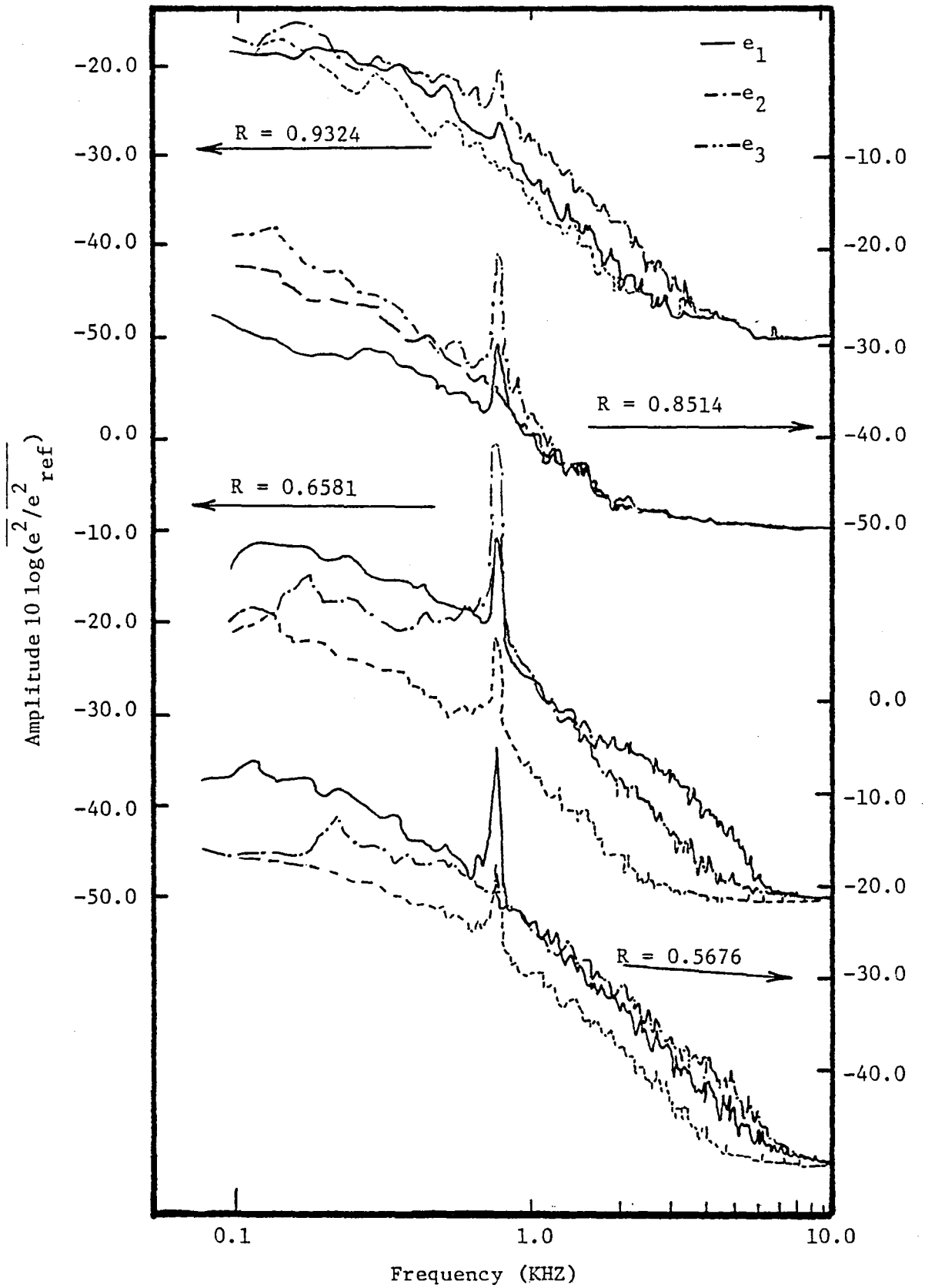

Figure 111. Turbulence Energy Spectra in the Relative Frame of Reference between the Blade Passage.

velocity defect that persists in the inlet-guide-vane wake after its passage through the rotor-blade. The figure also shows the radial variation of the velocity defect which is sensed by the rotating wire as a source of turbulence. The maximum defect seems to occur in the mid-radius region tapering off towards the end-wall zones.

Figure 112 shows the spectrum taken at different radii at the center of the wake. The effect of radius on the spectral content can be seen from this figure. The energy content in the turbulence fluctuations increases with increasing radius. Further there are no "peaks" in the energy spectrum indicating that the inlet-guide-vane wakes undergo substantial changes in the transport properties as it passes through the boundary layer of the rotor-blades. The spectrum also exhibits typical energy distribution that exists in turbulent flows with most of the energy contained within 10 KHZ.

The energy in the spectrum is given by

$$E(k) = I_{(k)} f(k)^{-2} \tag{13}$$

where:

$I_{(k)}$ = constant depending on the wave number

$f(k)$ = frequency of the turbulent fluctuations

n = exponent.

For the present case, the spectrums taken in the blade passages show a slope of -1 for the wakes in the higher radius region and -5/7 in the lower radius region. For the spectrums taken at the wake center the slopes are -5/3 at higher radii and -1 at lower radii. The -5/3 law is characteristic of an isotropic structure of turbulence.

It is of interest to note the length scales of eddies in the above spectrums. The eddy lengths in the frequency range of the present

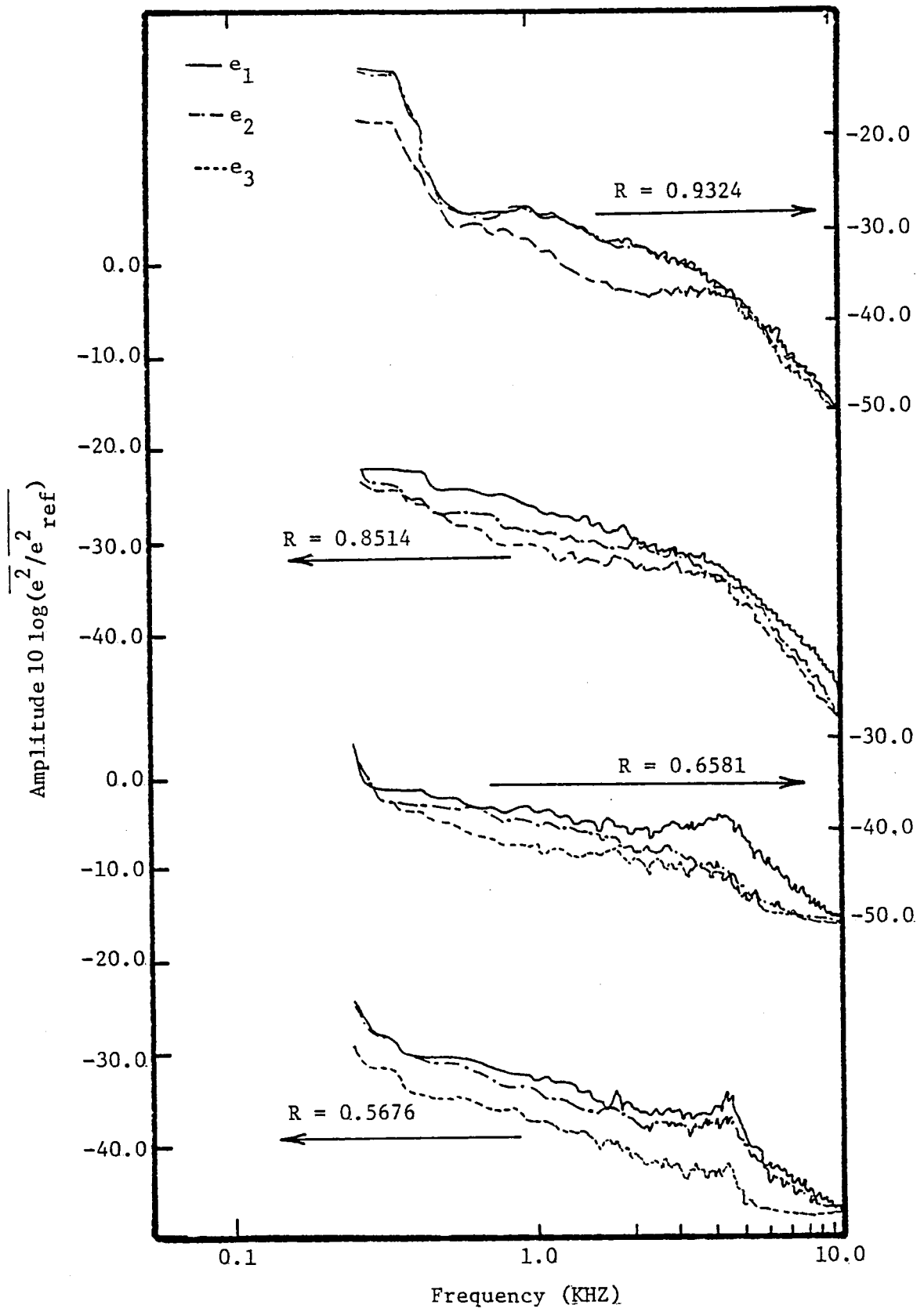

Figure 112. Turbulence Energy Spectra in the Relative Frame of Reference at the Wake Center

interest lie between 0.14 cm to 1.52 cm, the lower value approximately corresponding to the wake thickness in the trailing-edge region.

Chapter 4

SIMILARITY, CORRELATIONS, AND FOURIER ANALYSIS OF ROTOR-WAKES

4.1 Similarity Relations

Experimental evidence has shown that similarity exists in streamwise mean velocity profiles. This has been reported by Schlichting (1968) for wakes behind flat plates, circular cylinders and isolated airfoils. Schlichting has also given a semi-analytical expression for the similarity profiles and has shown that they follow a Gaussian distribution given by $Pe^{-k\eta 2}$, where P and k are constants and η is defined as the wake traverse distance normalized by half the wake-width. This prompted a search for the similarity for the wakes of isolated airfoils, cascades, and rotors. Raj and Lakshminarayana (1973) have reported the similarity for cascade wakes. Lakshminarayana (1976) and Reynolds (1978) have reported the similarity for lightly loaded fan blade wakes. In this section similarity is tried for the moderately loaded compressor rotor-blade wakes reported in an earlier chapter. Similarity is tried for both the mean velocities and turbulence intensities.

4.1.1 Mean velocity profiles

Lakshminarayana (1976) has shown that the normalized velocity components follow the Gaussian profile given by $e^{-0.693\eta^2}$. In this section similarity for the mean velocity are tried for the compressor rotor-wake reported in an earlier section.

4.1.1.1 Rotor-wake axial and tangential velocity profiles

Maximum velocity defect was used as the non-dimensionalizing velocity scale for the local velocity defect. The wake width at half the depth was taken as the characteristic length scale. Corresponding values L_s and L_p

were taken for the pressure and suction surfaces of the wake. Using this technique, similarity was examined for the axial and tangential velocity profiles and are shown plotted in Figures 113 and 114 for the radii R = 0.6581, 0.7297, and 0.7973. It is seen that similarity exists even in the case of a heavily loaded blade following the Gaussian distribution given by $e^{-0.693\eta^2}$. As seen from Figures 113 and 114, the discrepancy from the Gaussian curve for the wake in the trailing-edge region can be attributed to the fact that one is not only dealing with the wake but also dealing with the trailing-vortex system out of the trailing-edge of the blade. There is a susbstantial scatter from the Gaussian curve in the outer regions of the flow. The discrepancy is marked particularly for a heavily loaded blade (compare these figures with those of Reynolds, et al. (1978)). Townsend's (1947) approach of inclusion of an intermittancy factor into the Gaussian law in the form

$$\frac{u_d}{u_{dc}} = \exp[-c_1\eta^2\{1 + \frac{1}{3}(\frac{\eta}{\eta_1})\}^4] \qquad (14)$$

might yield better results. Here u_d is the velocity defect, c_1 and η_1 are constants.

Figures 115 and 116 show the plots of similarity profiles for the radii R = 0.9595, 0.9324, and 0.5676 which represent the wakes inside the annulus- and hub-wall boundary layers. As seen, the discrepancy from the Gaussian curve is considerable not only in the outer regions of flow but also at the wake center. It should be realized that at these locations not only the wake flow is dealt with but also the secondary flow, annulus- and hub-wall boundary layers and in the tip region the tip-vortex associated with the wake are also being dealt with. There is no analytical or experimental evidence, till now, to show that the velo-

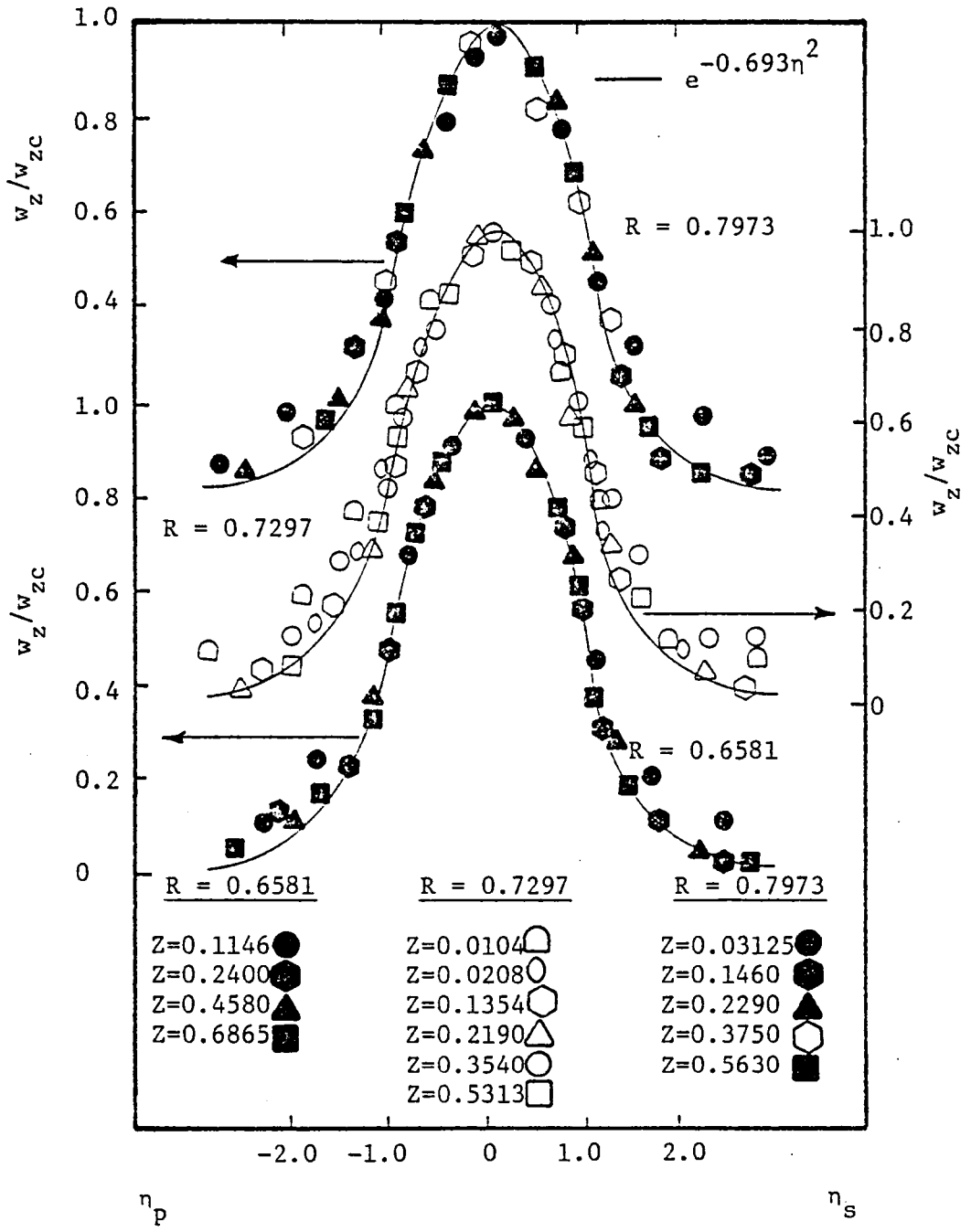

Figure 113. Axial Velocity Profile Similarity

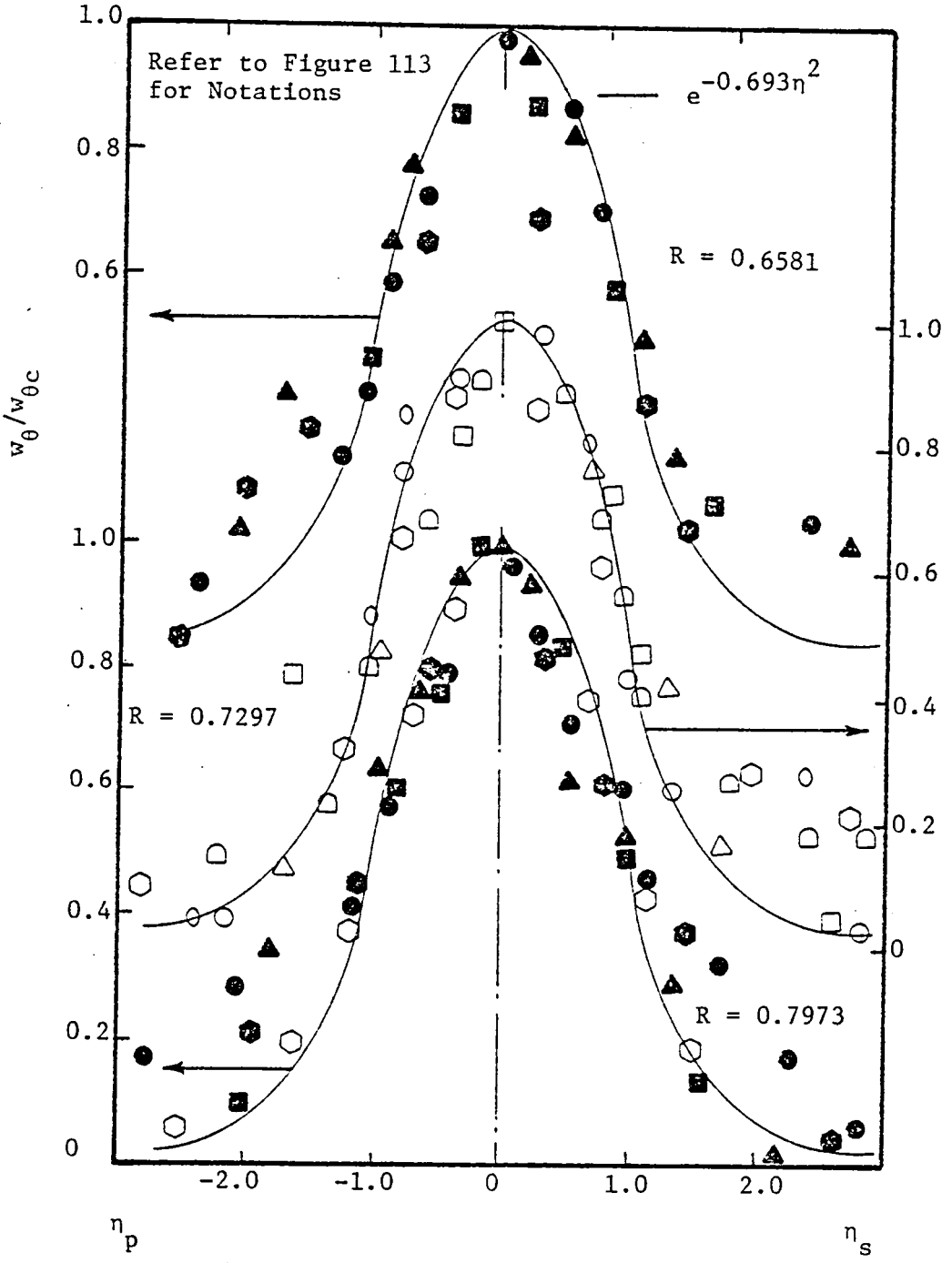

Figure 114. Tangential Velocity Profile Similarity

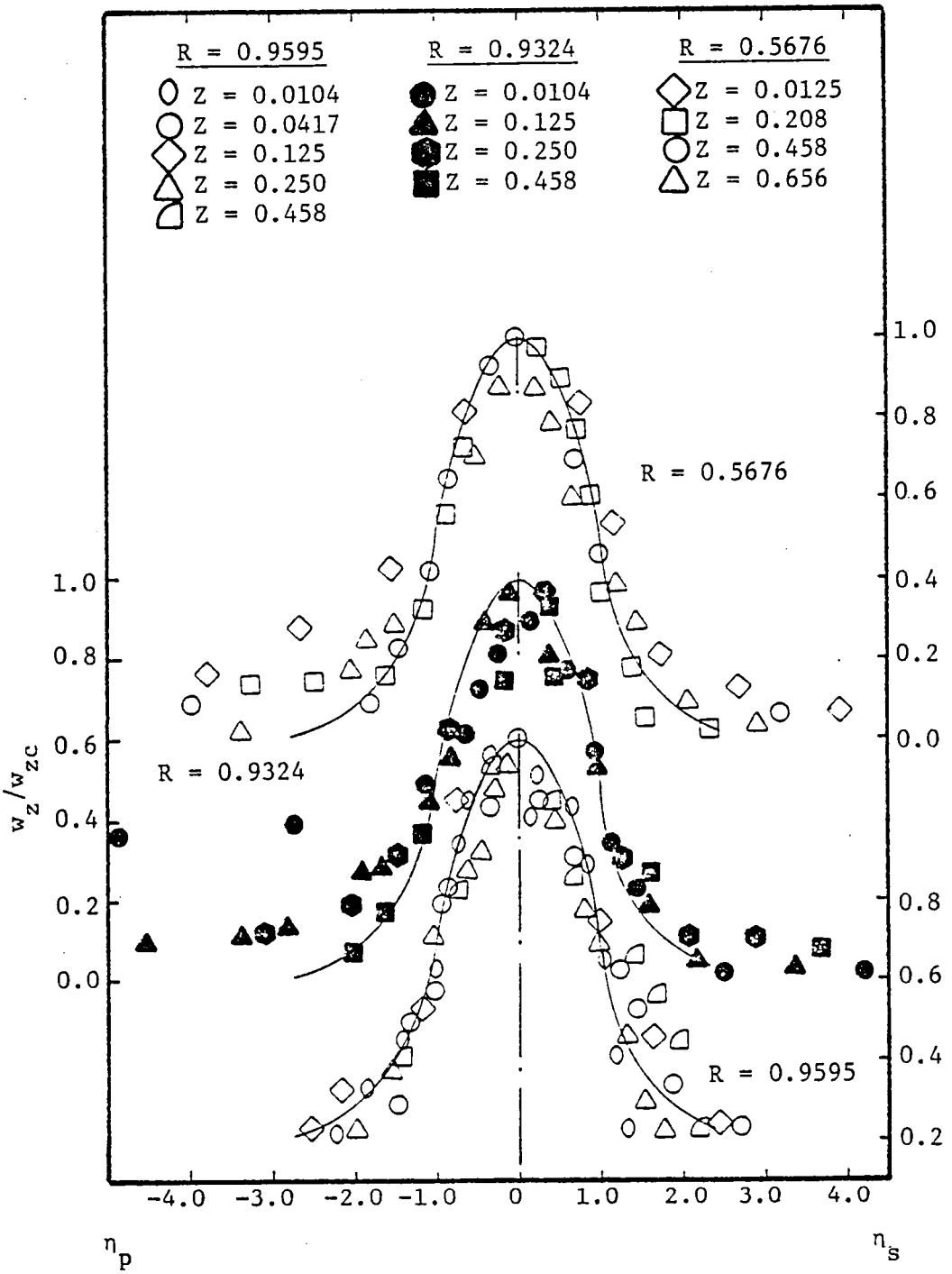

Figure 115. Axial Velocity Profile Similarity for Wakes Inside End-Wall Boundary Layers

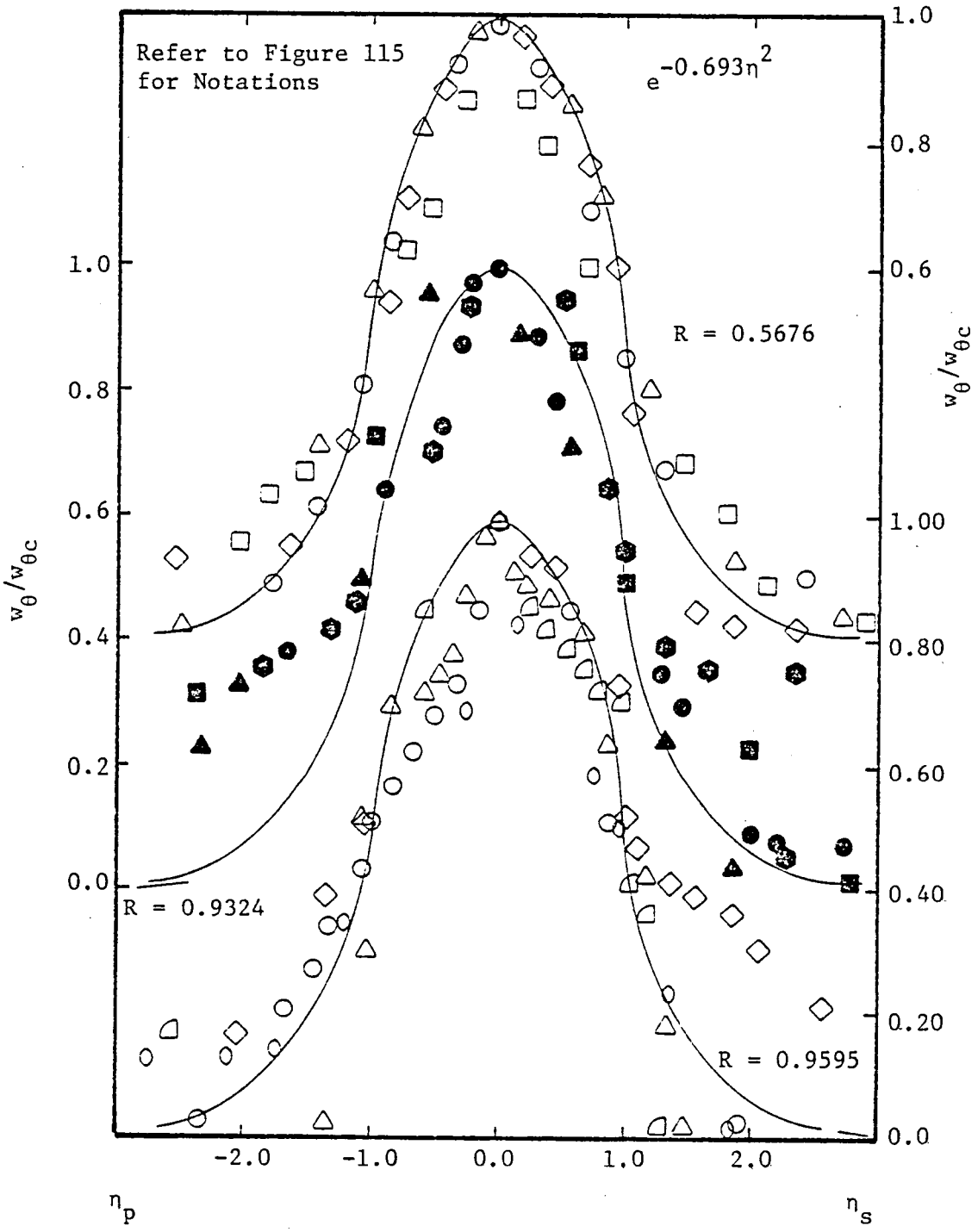

Figure 116. Tangential Velocity Profile Similarity for Wakes Inside End-Wall Boundary Layers

city profiles of such complicated flows should be similar and this is a first step in that direction. A better agreement might be obtained if a factor to include secondary flow and tip-vortex is included in the non-dimensionalizing parameter.

4.1.1.2 Rotor-wake radial velocity profiles

Radial velocities show two different trends, one trend in the trailing-edge region and the other in the near- and far-wake regions. For the far-wake region the similarity is quite good and is shown in Figure 117. The maximum radial outward velocity is taken as the normalizing velocity. The similarity for the wakes for R = 0.6581, 0.7297, and 0.7973 is quite good except for the scatter in the outer regions of the flow. This again indicates that even the radial velocities follow the trend of the Gaussian law. The similarity for the radial velocities inside the annulus- and hub-wall boundary layers represented by the radii R = 0.9595, 0.9324, and 0.5676 is shown plotted in Figure 118. It is seen that there is a considerable discrepancy between the data and the Gaussian curve. This shows that the secondary flow and the tip-vortex that exist at the hub and tip of the machine have considerable influence on the wake profile. It can also be noted that the secondary flow and the tip-vortex have considerably more influence on the radial velocity as compared to axial and tangential velocity components.

The radial velocities in the trailing-edge region exhibit two different types of velocity distribution with radially inward-flow on the pressure side and radially outward flow on the suction side of the wake. Here again, maximum radial velocity defect was used as the normalizing velocity (on the suction surface the absolute magnitude of the velocities were considered). The plots are shown in Figure 119. The agreement with

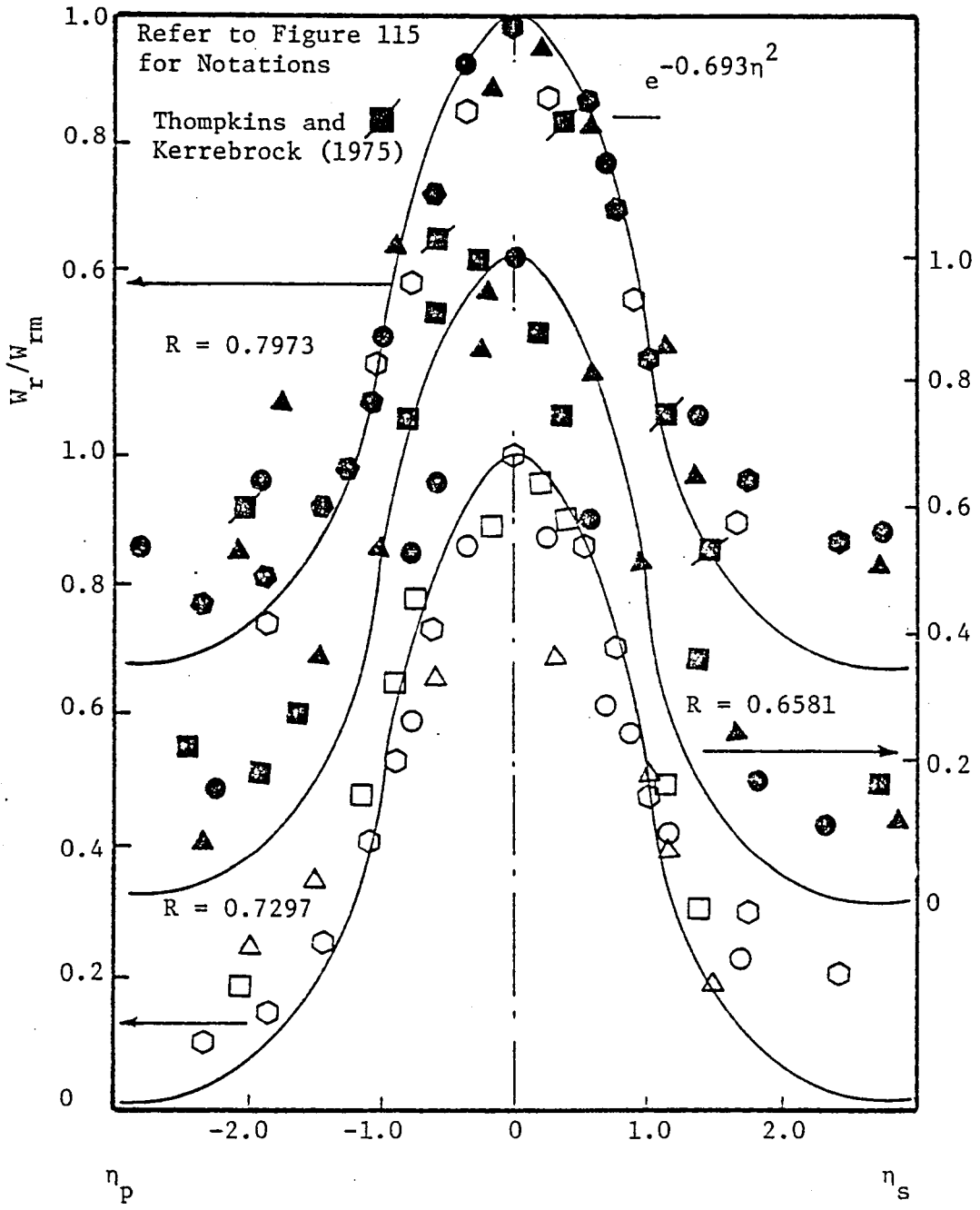

Figure 117. Radial Velocity Profile Similarity (Far-Wake Region)

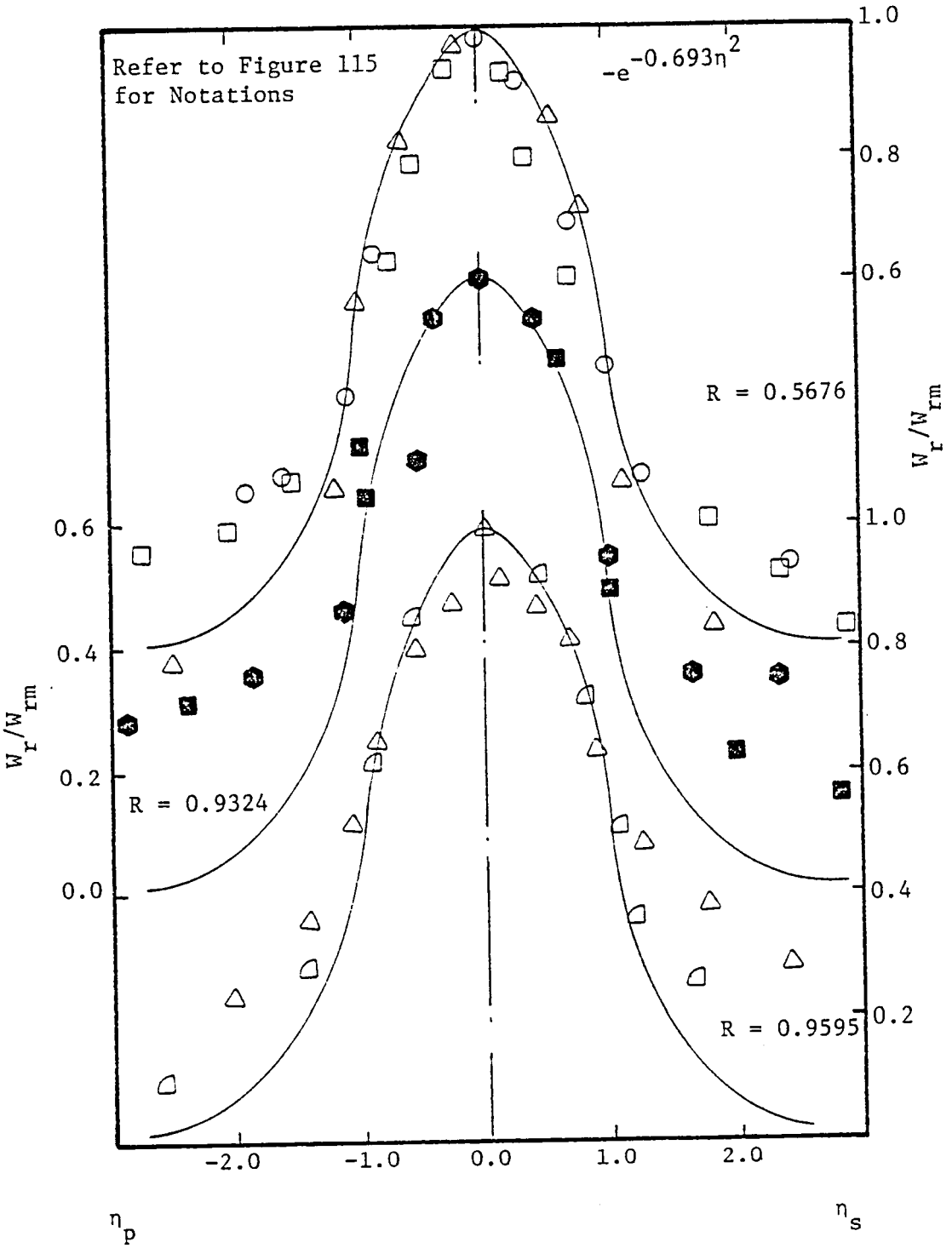

Figure 118. Radial Velocity Profile Similarity for Wakes Inside End-Wall Boundary Layers

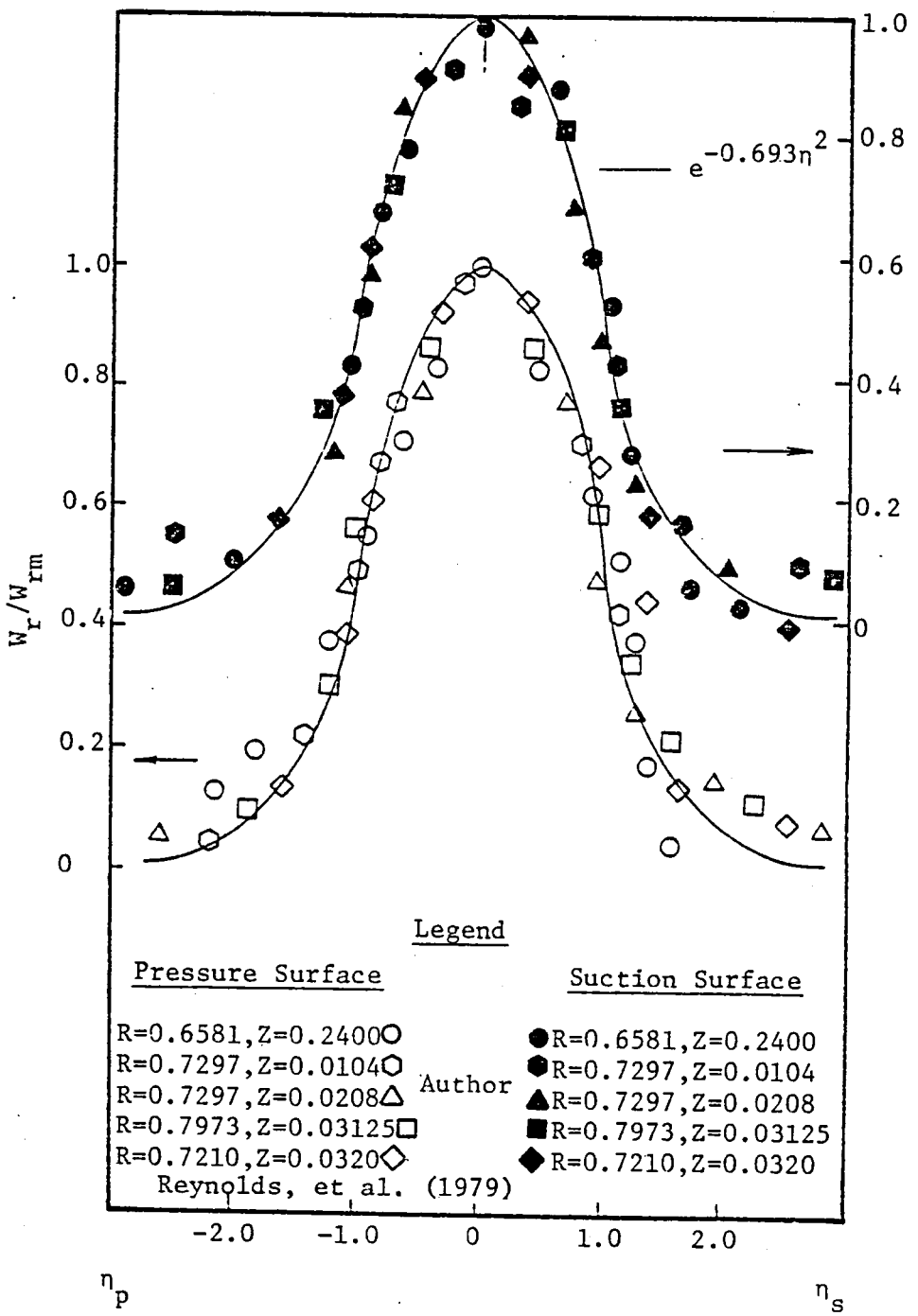

Figure 119. Radial Velocity Profile Similarity for Wake in the Trailing-Edge Region

the Gaussian distribution is fairly good. It has to be realized that at these Z-locations we are not only dealing with the boundary layer flow but also the trailing-vortex system (secondary flow, corner flows, tip-vortex in the end-wall regions). Similarity for such a complex flow phenomena has not been proven before and this is a first step in that direction. It is quite probable that inclusion of intermittency factors to account for the trailing-vortex and secondary flows might yield better correlation with the experimental data.

4.1.2 Turbulence intensity profiles

The similarity rule was examined for the axial, tangential and radial components of turbulence intensity for the entire wake region and the plots are shown in Figures 120, 121, and 122. In these plots the turbulence intensity has been normalized by the maximum turbulence intensity. In situations where a "dip" was noticed at the wake center, an extrapolated peak intensity near the wake center was taken. To study the intensity profiles in the wake alone, the free-stream value was subtracted from the local values. The distance from the wake centerline to the lotation where the maximum turbulence intensity minus the free-stream value is half was taken as the characteristic length scale ℓ_s and ℓ_p respectively on the pressure and suction side. Using this technique which is similar to the one employed to examine the velocity profile similarity, similarity was tried for the axial, tangential, and radial components of turbulence intensity.

Similarity was found for all the three components of intensity for the entire wake region. As in the case of velocity profile similarity, the discrepancy from the Gaussian curve was noticed in the outer regions of the flow as well as for the wakes in the trailing-edge region. For

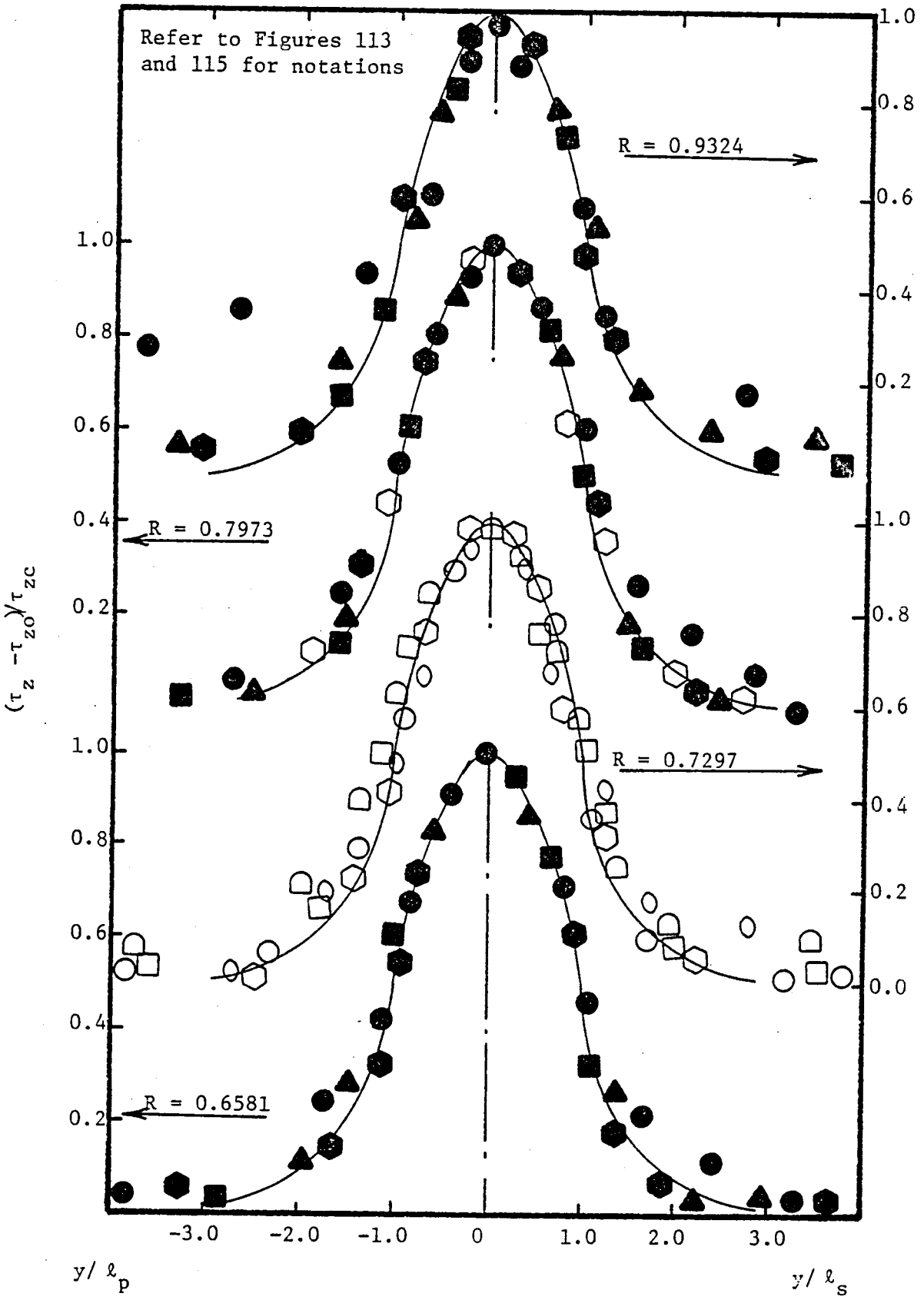

Figure 120. Axial Turbulence Intensity Profile Similarity

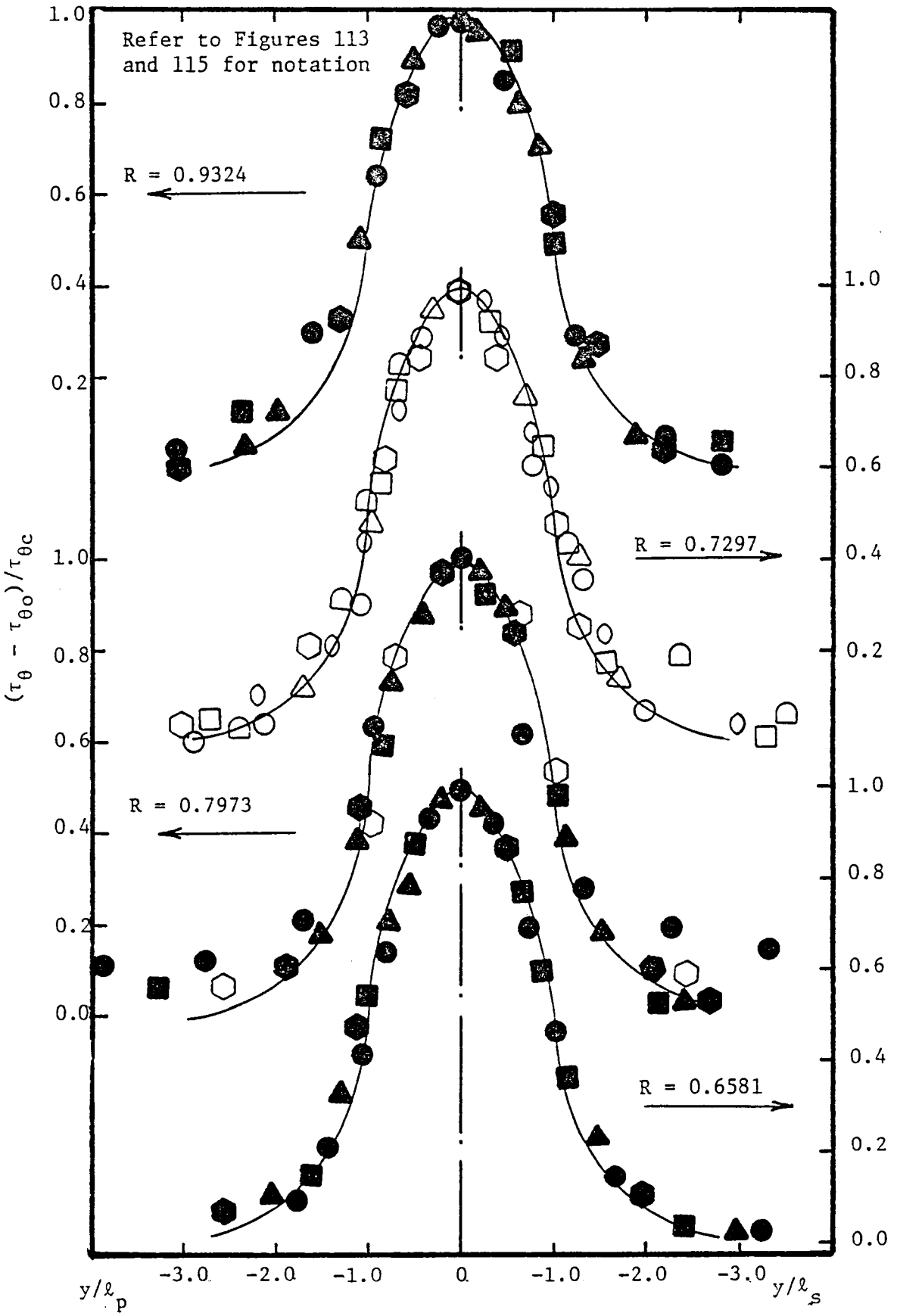

Figure 121. Tangential Turbulence Intensity Profiles

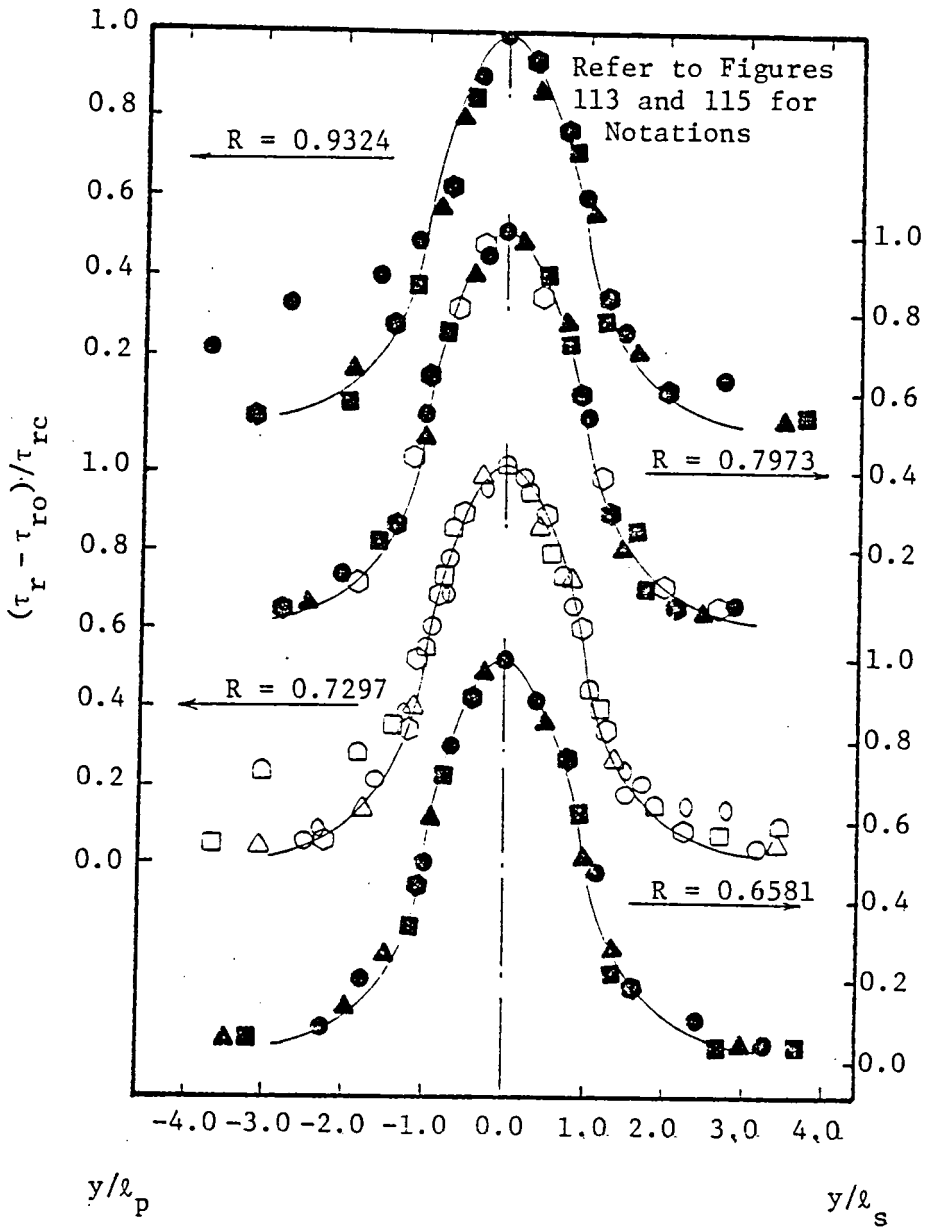

Figure 122. Radial Turbulence Intensity Profile Similarity

the wakes inside the annulus- and hub-wall boundary layers the deviation from the Gauss' curve was considerable, particularly for the wakes in the trailing-edge and near-wake regions. This is to be expected as in these regions the turbulence structure is markedly affected by the tip-vortex, secondary flow, and the interaction of the wake and annulus- and hub-wall boundary layers.

4.1.3 Static-pressure profiles

The similarity in static-pressure is examined using the characteristic values of the pressure (p_{max}) and lengths ℓ_s and ℓ_p. The plot of such a similarity is shown in Figure 123. The data follows the Gaussian distribution fairly closely and only in the outer regions of the flow substantial scatter from the $e^{-0.693\eta^2}$ curve is observed. This might be due to interference effects or the effect of the inviscid region located just outside the "wake" region. The data due to Thompkins and Kerrebrock (1975) also shows the existence of similarity in static-pressure distribution, Figure 123.

4.1.4 Velocity profile similarity for cascade, inlet-guide-vane, and stator-wakes

As previously reported, experimental evidence has shown that similarity in mean velocity profiles exists for the wakes of flat plates, circular cylinders, and isolated airfoils. Lakshminarayana (1975) has shown that the similarity follows the Gaussian distribution given by $e^{-k\eta^2}$. Raj and Lakshminarayana (1975) have examined the similarity for their cascade data. Lakshminarayana and Davino (1978) have shown that similarity exists for the wakes of inlet-guide-vanes and stators and that the distribution is Gaussian ($e^{-k\eta^2}$). In this section the similarity is tried for the cascade wakes (Pollard and Gastelow (1967), Sathyanarayana

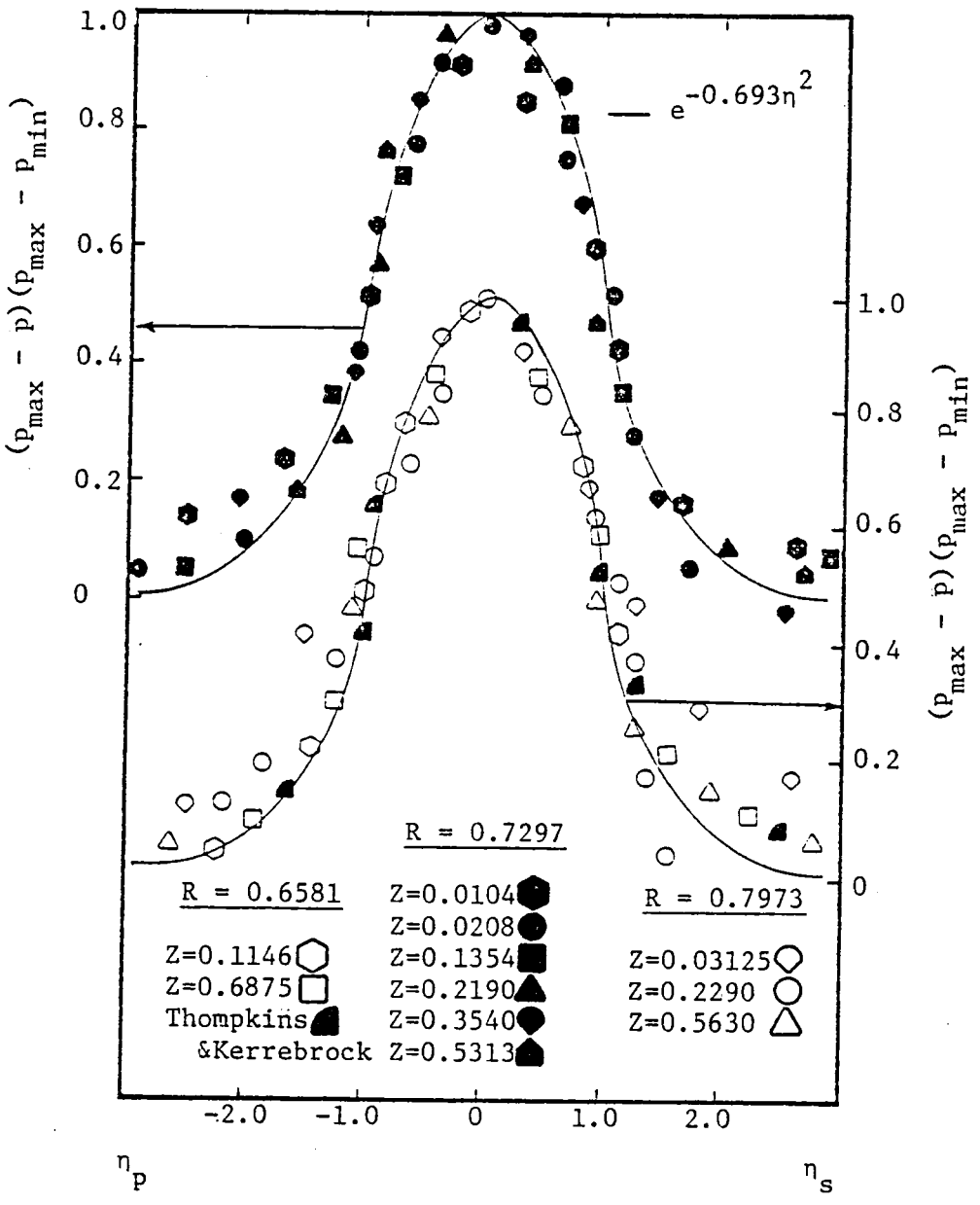

Figure 123. Static-Pressure Profile Similarity for the Wake

(1977), and Barna (1964)), Stators (Bitterslich and Rubner (1972) and Holbrook and Okiishi (1978)), and annulur cascades and inlet-guide-vanes (Daneshyar (1974) and Welsh (1973)). These are plotted in Figures 124a, 124b, and 124c. In all these cases, it is seen that the correlation is very good except in the outer regions of the flow.

4.2 Correlations for Decay of the Maximum Defect

4.2.1 Rotor-wake velocity correlation

The wake property is strongly dependent on the blade section parameters, the predominant one being the section drag coefficient. Schlichting (1968) has theoretically correlated wake properties using the drag coefficient and collapsed the mean velocity data from different configurations onto a single curve. The functional dependency for the mean velocity decay was given by Schlichting as

$$\frac{w_c}{W_o} = c_d^{1/2} f_1\left(\frac{s}{c}\right) \tag{15}$$

where s is the streamwise distance. This correlation has been tried for the rotor-wake data reported in this investigation and shown in Figure 125. The functional relationship for the decay of the axial and the tangential velocity defect as well as the radial velocity can be represented in the trailing-edge and near-wake region in the form,

$$\frac{w_c}{W_o} \times \frac{1}{\sqrt{c_D}} = k_1 \left(\frac{Z - Z_o}{\cos\beta_o}\right)^n \tag{16}$$

where the values of k_1, $(Z/\cos\beta_o)$ and n take different values for the three components of velocity. These relationships for the rotor-wake data are given by (in the trailing-edge and near wake region)

$$\frac{w_{zc}}{W_{zo}} \times \frac{1}{\sqrt{c_D}} = 0.592\left[(Z/\cos\beta_o) + 0.35\right]^{-2.39} \tag{17}$$

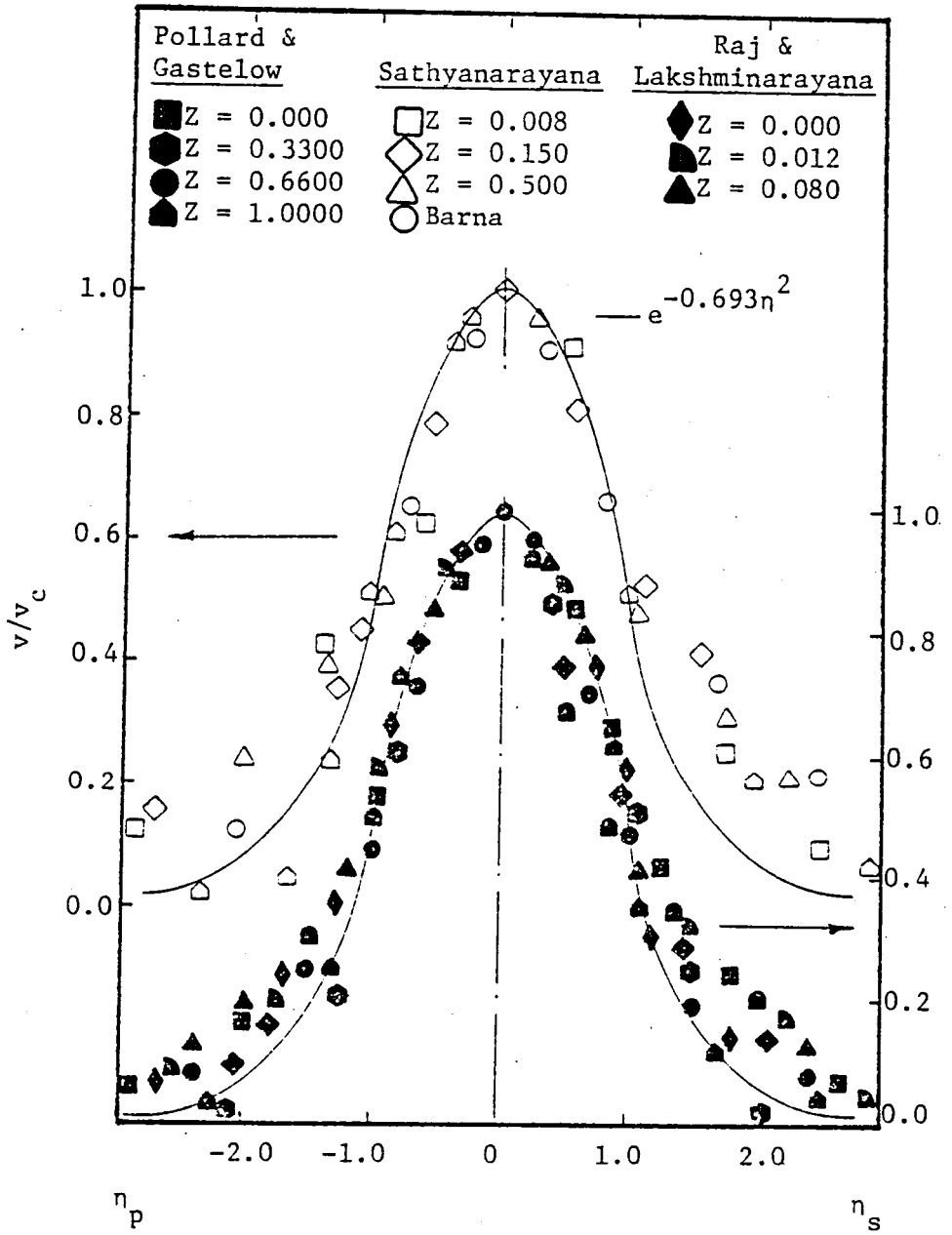

Figure 124a. Axial Velocity Similarity in Cascade Wakes

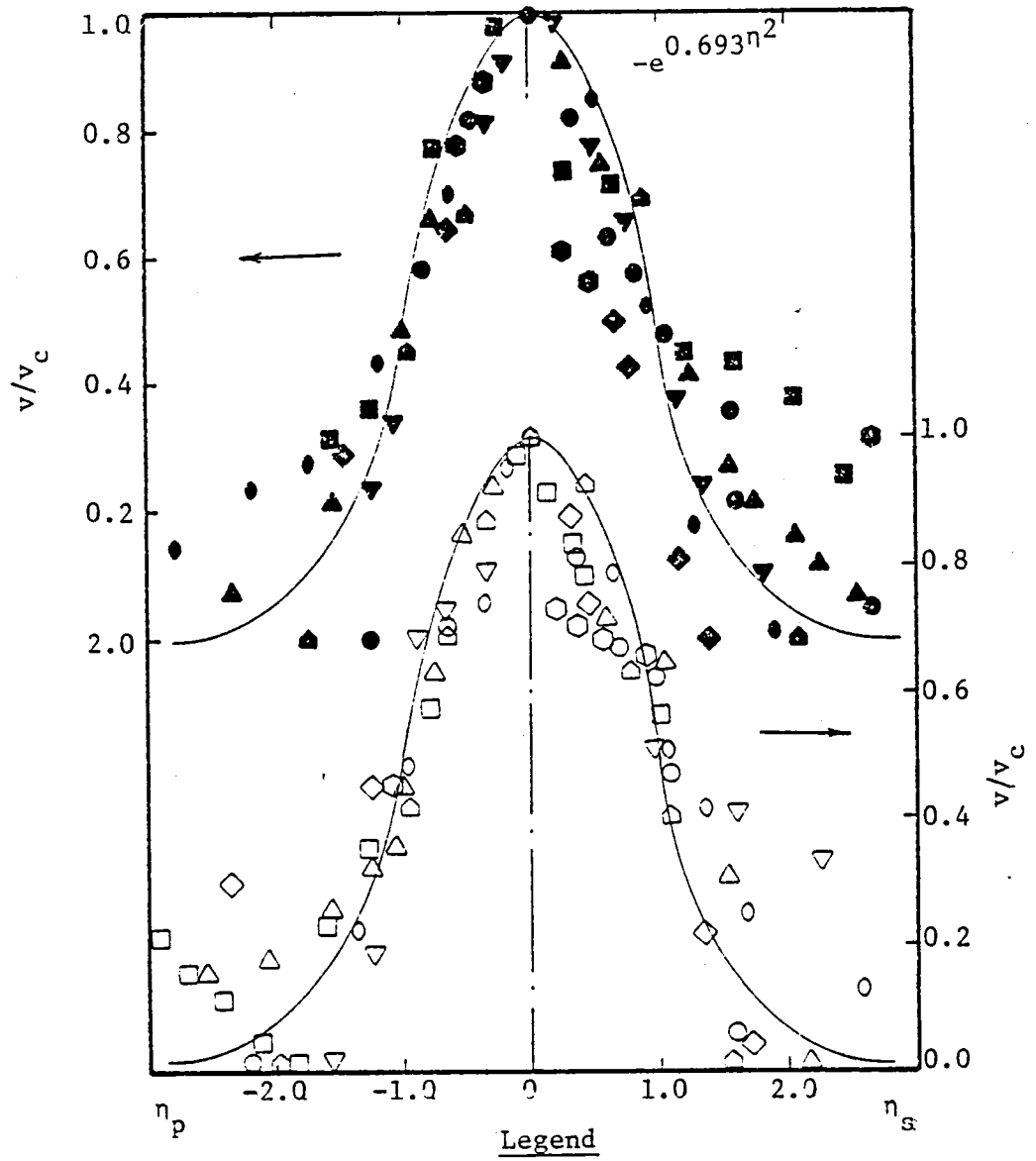

Figure 124b. Similarity in Velocity Profiles for Stator, Annular-Cascade and Inlet-Guide-Vanes

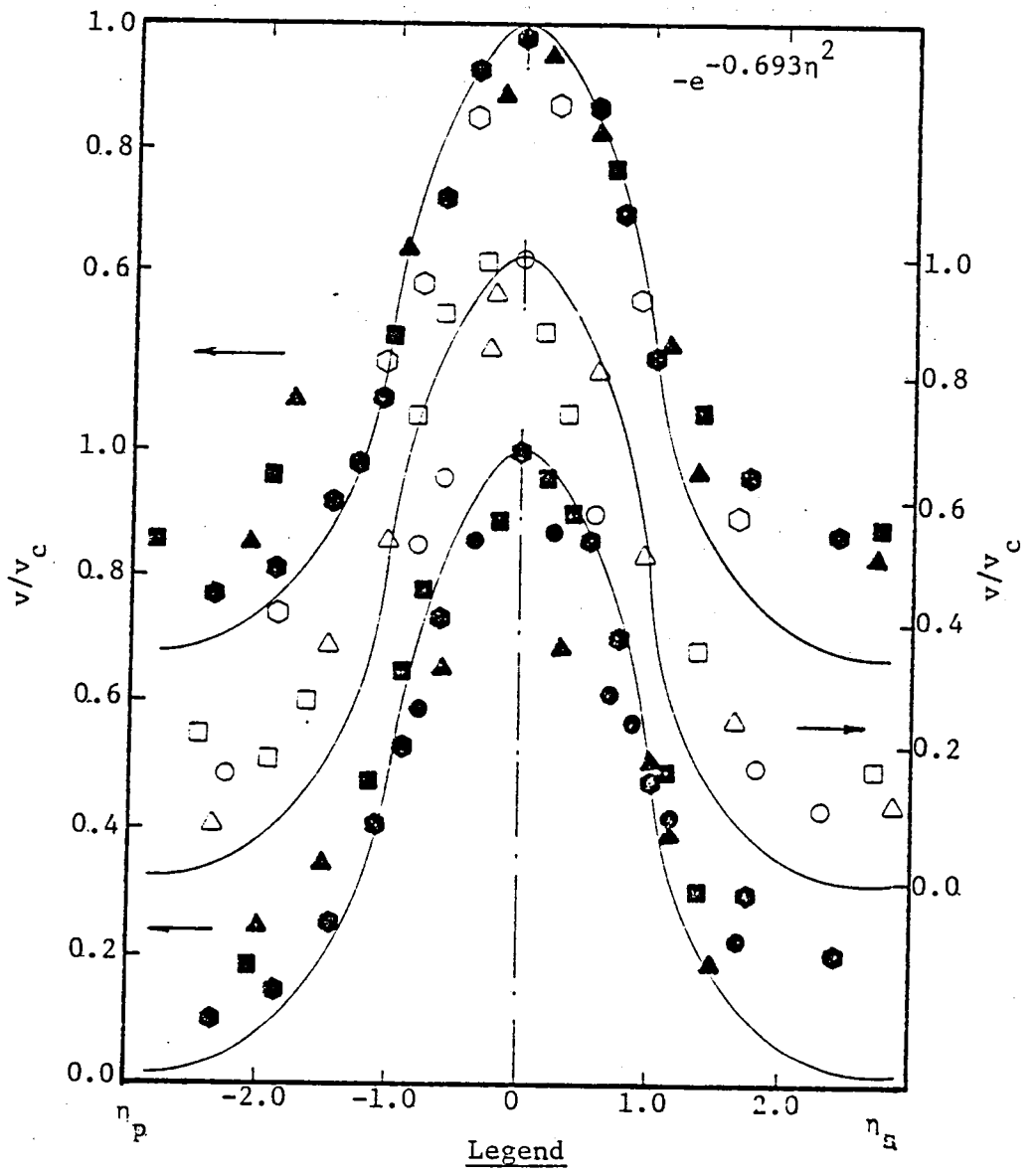

Bitterlish & Rubner (1972)

R = 0.8667
R = 0.7571
R = 0.6837
R = 0.5306
Stator

Holbrock & Okiishi

R = 0.90
R = 0.70
R = 0.30
Stator

Lakshminarayana & Davino (1979)

Z = 0.013, R = 0.75
Z = 0.053, R = 0.75
Z = 0.317, R = 0.75
Z = 0.846, R = 0.75

Figure 124c. Similarity in Velocity Profiles for Stator, Inlet-Guide-Vane and Annular-Cascade Wakes

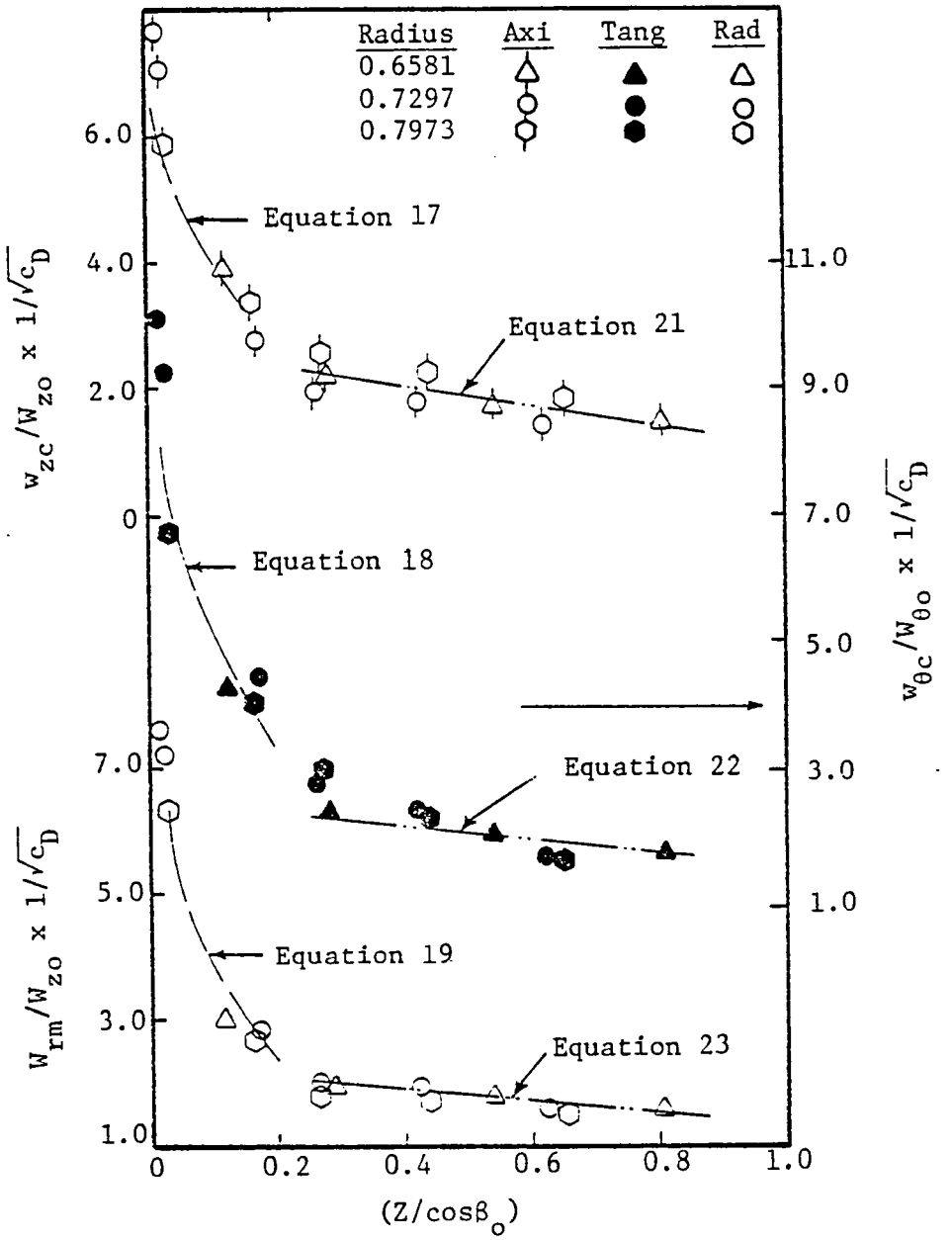

Figure 125. Correlation of Velocity Defects for Rotor-Wake

$$\text{for } 0.03 < \left(\frac{Z}{\cos\beta_o}\right) < 0.2$$

$$\frac{w_{\theta c}}{W_{\theta o}} \times \frac{1}{\sqrt{c_D}} = 0.778\left[\left(\frac{Z}{\cos\beta_o}\right) + 0.35\right]^{-2.39} \tag{18}$$

$$\text{for } 0.03 < \left(\frac{Z}{\cos\beta_o}\right) < 0.2$$

$$\frac{W_{rm}}{W_{zo}} \times \frac{1}{\sqrt{c_D}} = 0.566\left[\left(\frac{Z}{\cos\beta_o}\right) + 0.35\right]^{-2.39} \tag{19}$$

$$\text{for } 0.03 < \left(\frac{Z}{\cos\beta_o}\right) < 0.2$$

In the region $0.2 < Z/\cos\beta_o < 0.8$ the decay of the radial velocity and defects in axial and tangential velocities were found to vary linearly with $(z/\cos\beta_o)$ and can be represented by a general equation of the type,

$$\frac{w_c}{W_o} = k_2\left(\frac{Z}{\cos\beta_o}\right)^{-1} + k_3 \tag{20}$$

where again the constants k_2 and k_3 assume different values for the three different velocity components and are as follows:

$$\frac{w_{zc}}{W_{zo}} \times \frac{1}{\sqrt{c_D}} = 0.39\left(\frac{Z}{\cos\beta_o}\right)^{-1} + 0.984 \tag{21}$$

$$\text{for } 0.2 < \left(\frac{Z}{\cos\beta_o}\right) < 0.8$$

$$\frac{w_{\theta c}}{W_{\theta o}} \times \frac{1}{\sqrt{c_D}} = 0.221\left(\frac{Z}{\cos\beta_o}\right)^{-1} + 1.492 \tag{22}$$

$$\text{for } 0.2 < \left(\frac{Z}{\cos\beta_o}\right) < 0.8$$

$$\frac{W_{rm}}{W_{zo}} \times \frac{1}{\sqrt{c_D}} = 0.221\left(\frac{Z}{\cos\beta_o}\right)^{-1} + 1.20 \tag{23}$$

$$\text{for } 0.2 < \left(\frac{Z}{\cos\beta_o}\right) < 0.8 \quad .$$

The decay rates as represented by the above equations are shown plotted in Figure 125. It is seen that the data correlates quite well with these expressions.

For the wakes inside the annulus- and hub-wall boundary layers the data could not be collapsed on to a single curve using $c_D^{-0.5}$ as the normalizing parameter. This implies that the wakes at these locations are not only strongly dependent on the section drag coefficient but are also dependent on the secondary flows, tip-vortex, and the end-wall boundary layers. Inclusion of all these parameters into the correlating function might yield better results.

4.2.2 Cascade, stator, and inlet-guide-vane correlation

A correlation for the cascade wake data due to Raj and Lakshminarayana (1973), Pollard and Gastelow (1967), Sathyanarayana (1977) and Lieblein and Roudebush (1956) is shown plotted in Figure 126. The correlation seems to work well in the near- as well as far-wake region. But in the trailing-edge region it does not seem to yield good results. This has to be expected as in the trailing-edge region the flow is still developing and where no correlation is known to exist. Besides a correlation based on section drag coefficient might not yield good results as the properties of the wake might depend on a variety of other parameters. A functional dependency of the defect of velocity with streamwise distance was tried in the form

$$\frac{v_c}{V_o} \times \frac{1}{\sqrt{c_D}} = k\left[\left(\frac{Z}{\cos\beta_o}\right) - \left(\frac{Z_o}{\cos\beta_o}\right)\right]^n \qquad (24)$$

where:

v_c = velocity defect at the wake center

V_o = free-stream velocity

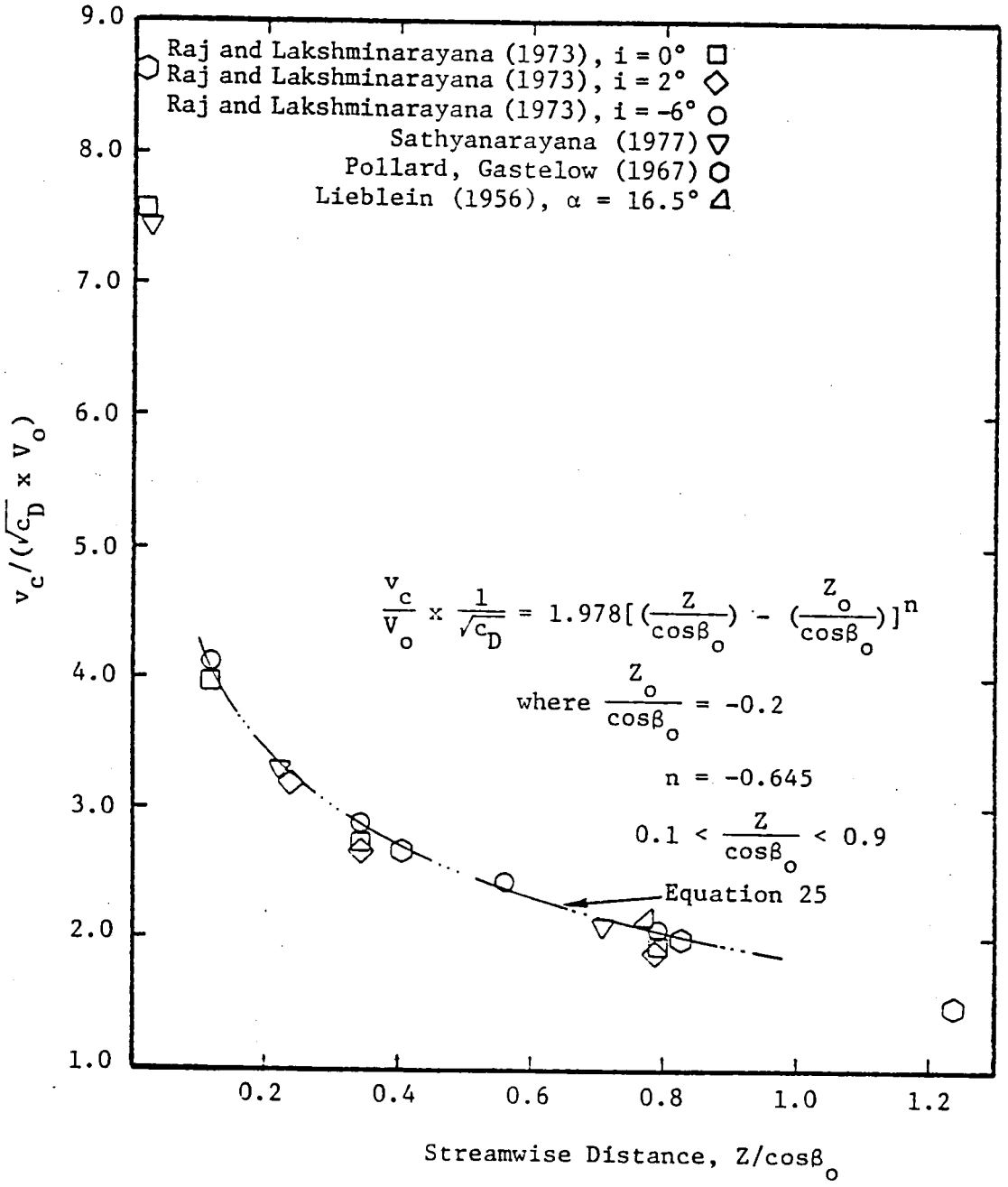

Figure 126. Correlation of Velocity Defect for Cascade Wake

$(Z/\cos\beta_o)$ = streamwise distance

$(Z_o/\cos\beta_o)$ = virtual origin

k = constant

n = exponent.

The relationship for the data presented in Figure 126 seems to follow the relationship

$$\frac{V_c}{V_o} \times \frac{1}{\sqrt{C_D}} = 1.978\left[\left(\frac{Z}{\cos\beta_o}\right) + 0.2\right]^{-0.645} \qquad (25)$$

$$\text{for } 0.1 < \left(\frac{Z}{\cos\beta_o}\right) < 0.9 \quad .$$

It is seen that the data correlates quite well with the above expression.

Figure 127 shows the correlation for the decay of stator-wake for the data from Lakshminarayana and Davino (1978) and Holbrock and Okiishi (1978). The data seems to correlate quite well using $C_D^{-0.5}$ as the normalizing parameter. All the three components of velocity have been plotted. It is interesting to note the variations of the exponent for the axial and tangential components in the near-wake region. It is seen that the tangential velocity component decays much slower compared to the axial component. Beyond $(Z/\cos\beta_o) = 0.4$, both axial and tangential velocity components seems to decay as $(Z/\cos\beta_o)^{-1}$. The functional relations for the decay of axial and tangential components of velocity for the stator-wake are as follows:

Near-Wake:

Axial Comp: $$\frac{V_{zc}}{V_{zo}} \times \frac{1}{\sqrt{C_D}} = 3.50\left[\left(\frac{Z}{\cos\beta_o}\right) + 0.95\right]^{-3.236} \qquad (26)$$

$$\text{for } 0.05 < \left(\frac{Z}{\cos\beta_o}\right) < 0.5$$

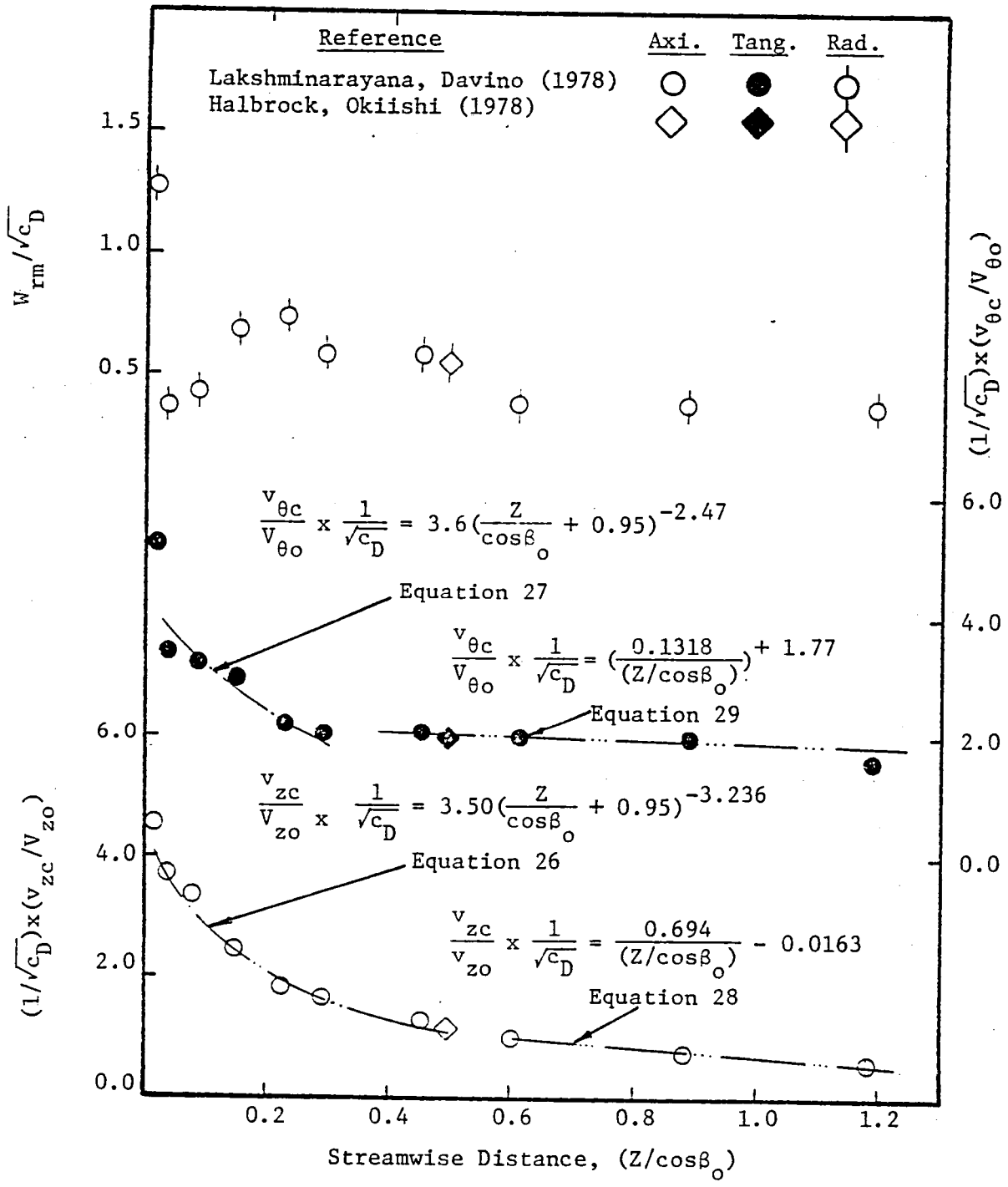

Figure 127. Correlation of Velocity Defect for Stator Wake

Tang. Comp: $$\frac{V_{\theta c}}{V_{\theta o}} \times \frac{1}{\sqrt{C_D}} = 3.60\left[\left(\frac{Z}{\cos\beta_o}\right) + 0.95\right]^{-2.470} \qquad (27)$$

$$\text{for } 0.05 < \left(\frac{Z}{\cos\beta_o}\right) < 0.3$$

Far Wake

Axial Comp: $$\frac{V_{zc}}{V_{zo}} \times \frac{1}{\sqrt{C_D}} = 0.694\left(\frac{Z}{\cos\beta_o}\right)^{-1} - 0.0163 \qquad (28)$$

$$\text{for } 0.6 < \left(\frac{Z}{\cos\beta_o}\right) < 1.2$$

Tang. Comp: $$\frac{V_{\theta c}}{V_{\theta o}} \times \frac{1}{\sqrt{C_D}} = 0.1318\left(\frac{Z}{\cos\beta_o}\right)^{-1} + 1.77 \qquad (29)$$

$$\text{for } 0.4 < \left(\frac{Z}{\cos\beta_o}\right) < 1.2 \ .$$

The radial velocity for the stator-wakes in the near-wake region seems to oscillate with $(Z/\cos\beta_o)$ and no functional dependency can be found.

The annular-cascade and inlet-guide-vane wake data from Lieblein and Raudebush (1956), Daneshyar (1974), and Lakshminarayana and Davino (1978) are shown plotted in Figure 128. The functional dependency for the decay as a function of streamwise distance seems to be similar to that of cascade wake.

Thus it is seen that the cascade, inlet-guide-vane, and annular-cascade wakes differ considerably from that of a stator-wake. The stator-wake tends to decay much more rapidly than the cascade wake. This is attributed to the very high swirl component of velocity that exists in the stator-wakes. Hill, et al. (1963) have shown that pressure gradients can have considerable influence on the boundary layer and wake develop-

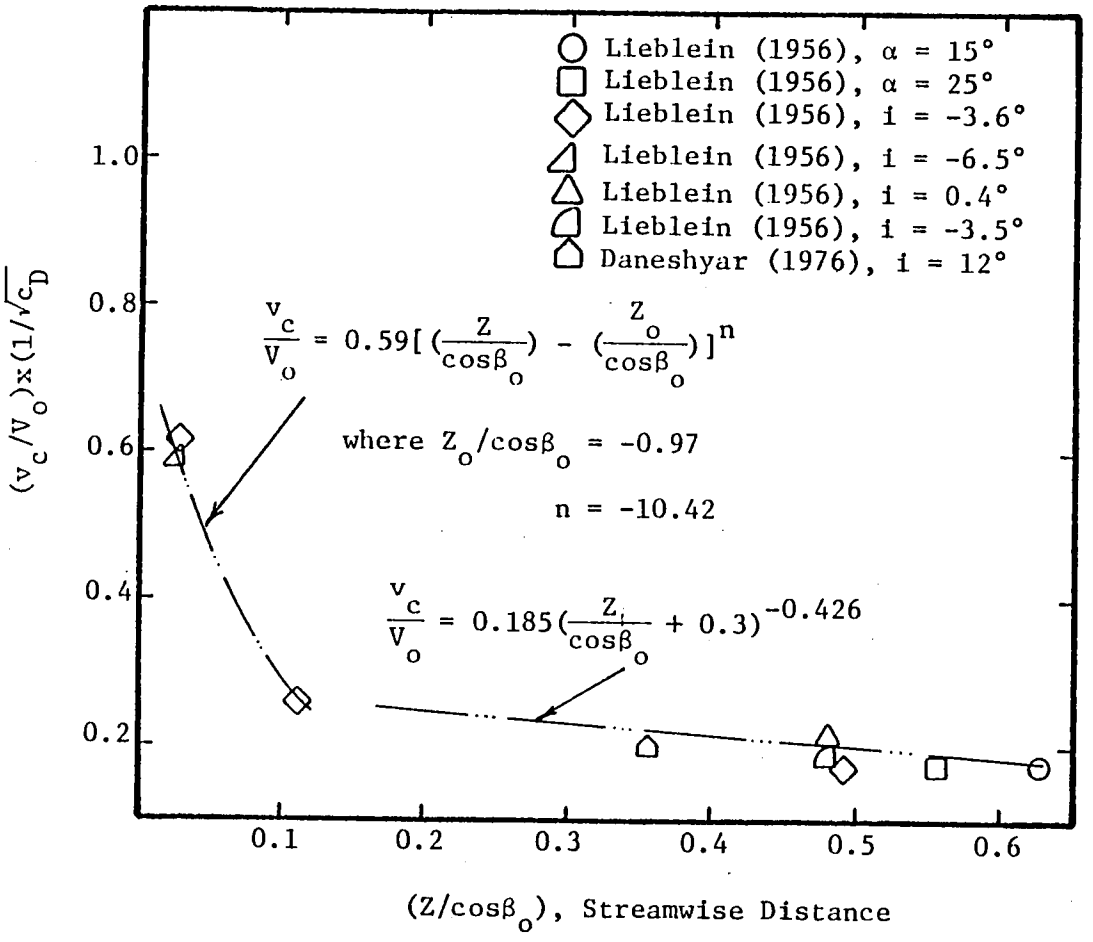

Figure 128. Correlation of Velocity Defect for Annular-Cascade and Inlet-Guide-Vane Wakes

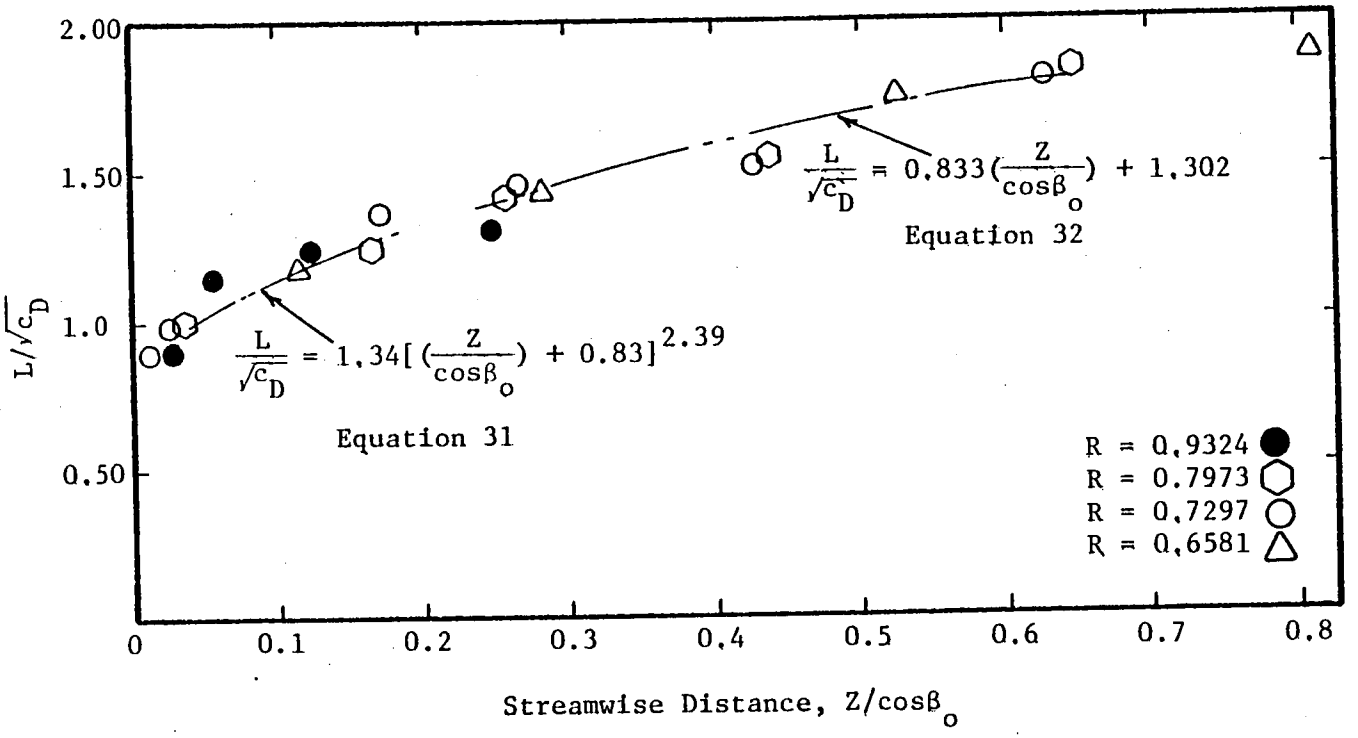

Figure 129. Wake Width Correlation with Downstream Distance

ment and decay. This may be the influencing factor in the observed phenomena.

4.3 Wake Width Correlation

4.3.1 Rotor-wake width correlation

Wake width depends on number of parameters like the blade thickness, initial flow conditions, blade turning angle, etc. But the most predominant parameter seems to be the section drag coefficient. So normalizing the wake width as a function of c_D should collapse all the data points on to a single curve. Figure 129 shows this correlation, where $c_D^{-0.5}$ has been used as the normalizing parameter. A functional dependency for the growth of wake width $(L/\sqrt{c_D})$ of the form

$$\frac{L}{\sqrt{c_D}} = k\left[\left(\frac{Z}{\cos\beta_o}\right) - \left(\frac{Z_o}{\cos\beta_o}\right)\right]^n \qquad (30)$$

can be used to represent the present data quite accurately. The constant k, and the exponent n, take on different values in the near- and far-wake regions and are found to be as follows:

$$\frac{L}{\sqrt{c_D}} = 1.34\left[\frac{Z}{\cos\beta_o}\right) + 0.83]^{2.39} \qquad (31)$$

$$\text{for } 0.01 < \left(\frac{Z}{\cos\beta_o}\right) < 0.2$$

Far-wake

$$\frac{L}{\sqrt{c_D}} = 0.833\left(\frac{Z}{\cos\beta_o}\right) + 1.302 \qquad (32)$$

$$\text{for } 0.25 < \left(\frac{Z}{\cos\beta_o}\right) < 0.8 \quad .$$

In Figure 130 is shown the plots of wake width normalized by L_o, the corresponding initial value at the first station. The wake spread can now be represented by the equation

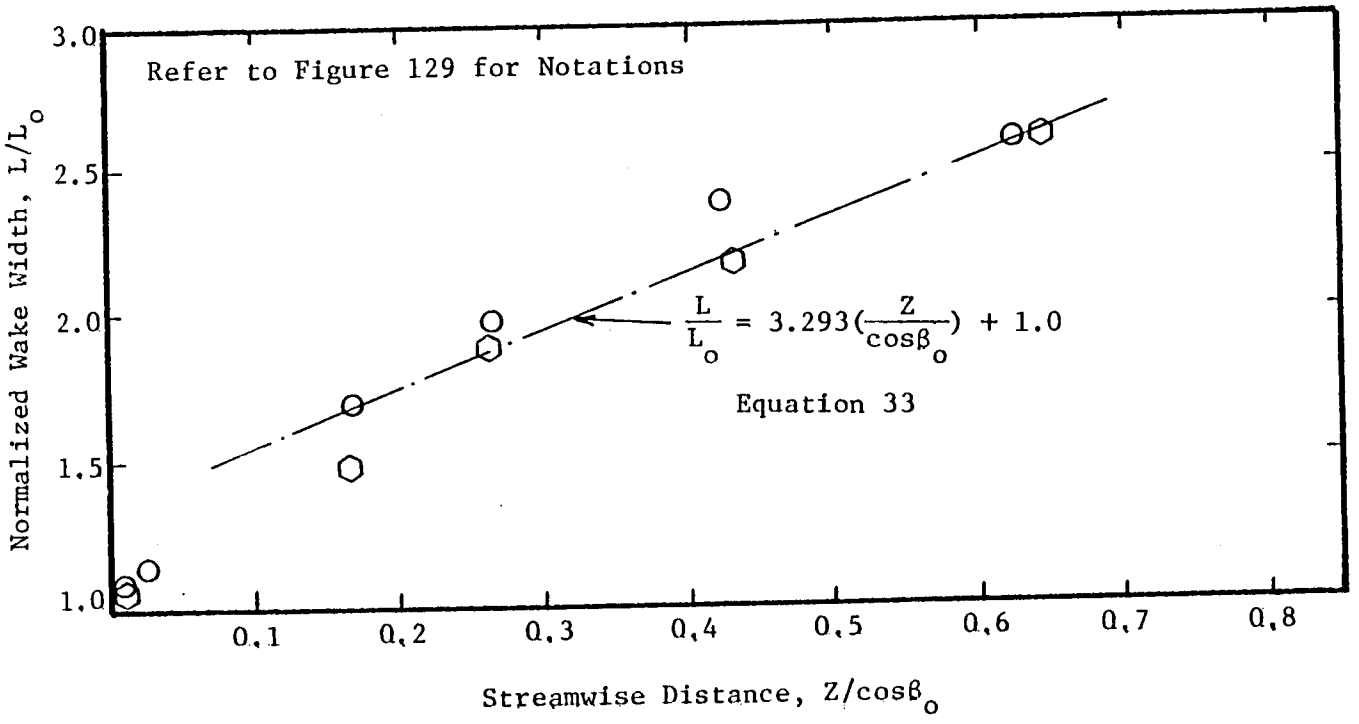

Figure 130. Wake Width Correlation with Downstream Distance

$$\frac{L}{L_o} = A_4 \left(\frac{Z}{\cos\beta_o}\right) + A_5 \qquad (33)$$

$$\text{for } 0.05 < \left(\frac{Z}{\cos\beta_o}\right) < 0.7$$

where the constants are found to be $A_4 = 3.292$ and $A_5 = 1.0$. Here L_o is the value of L at the trailing-edge. The constants depend on the type of blade row. These correlations are shown in Figure 130.

The wake decay and the wake width correlations discussed so far are for the data outside the annulus- and hub-wall boundary layers. Inside the end-wall boundary layers the wake behaves quite differently and a single functional dependency based on drag coefficient may not yield very good results. This correlation is shown in Figure 131. It is evident that the wake structure at these locations are very much dependent on the end-wall boundary layer characteristics. The correlations developed so far do not account for the end-wall boundary layers or the secondary flows (and in the tip region, the tip-vortex generated due to leakage flow). The complex interactions of these flows with the wake makes the flow highly complicated to be amenable to any simple correlation, based just on the section drag coefficient. Correlations to account for the secondary flow, tip-leakage flow, and some end-wall boundary layer properties might yield better results.

4.3.2 Cascade, inlet-guide-vane and stator-wake width correlation

As mentioned earlier the wake-width depends on many parameters like the thickness ratio, inlet flow conditions, section drag coefficient, etc. So in comparing wake widths from different blade geometries it may not be possible to collapse all the data on to a single curve. But an attempt has been made in this section to collapse the cascade wake width from

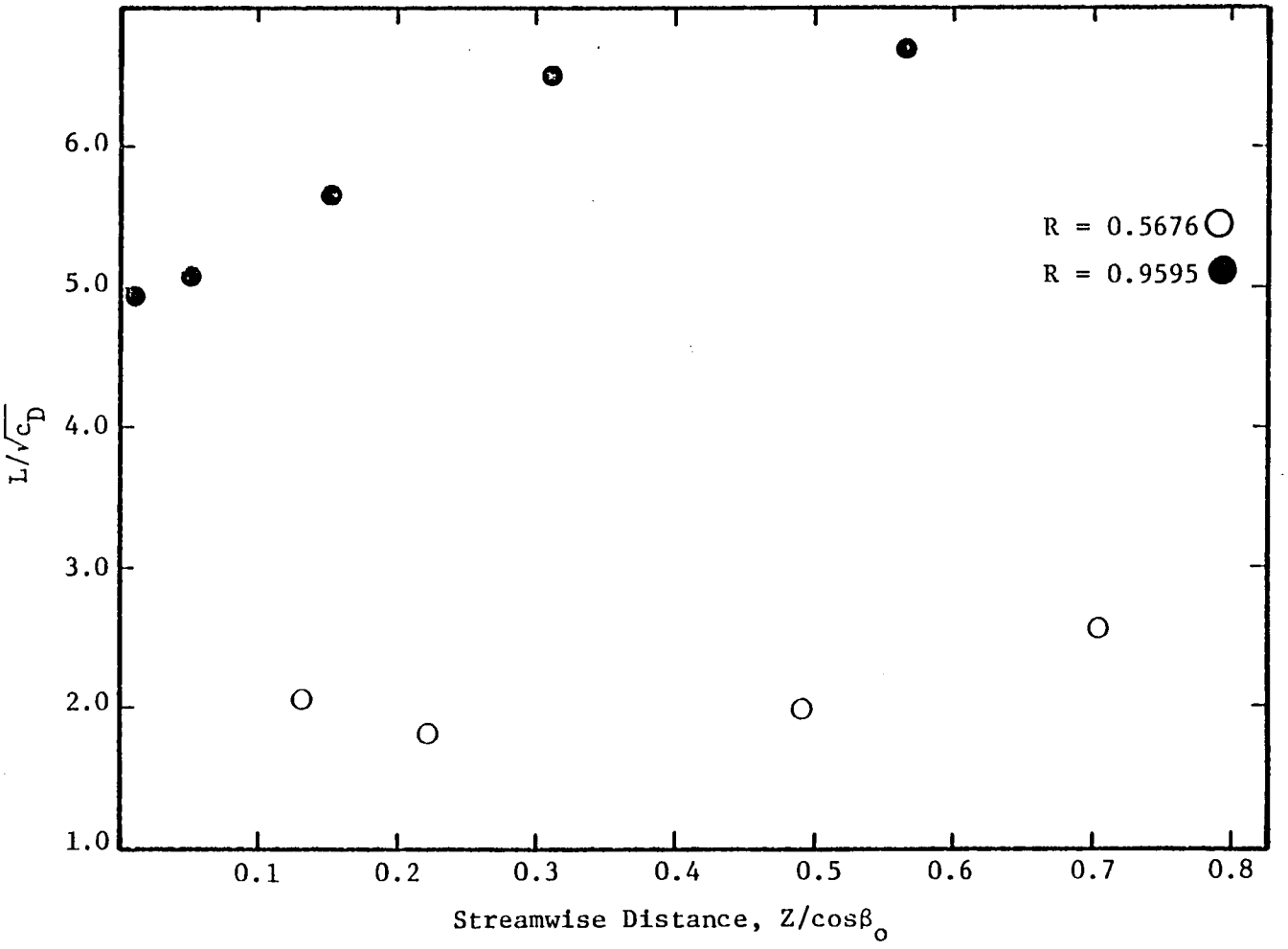

Figure 131. Wake Width Correlation with Downstream Distance for Wakes Inside End-Wall Boundary Layers

different blade geometries onto a single curve, using the wake width at the trailing-edge as the normalizing parameter. This is the most logical normalizing parameter as the initial wake width takes into account all the parameters that were mentioned earlier. This plot is shown in Figure 132. The correlation seems to work well for each set of rotor-blade individually and a overall correlation is not very satisfactory.

4.4 Turbulence Shear Stress Correlation

In an earlier section it was seen that the turbulence structure varies considerably in the radial direction. So normalizing the stresses by the value of the stress at the trailing-edge should collapse all the data points onto a single curve provided the value of the stress at the trailing-edge is a proper factor. Such a correlation is attempted in this section.

Raj and Lakshminarayana (1975) have shown that the decay of the stresses can be represented in the form

$$\tau_{ij} \propto \left(\frac{Z}{\cos\beta_o}\right)^n \tag{34}$$

where the exponent n assumes different values for the three components of stress. This plot is shown in Figure 133. A closer look at the present data indicates that the exponent n, assumes different values for the different radii. So other normalizing factors to include radial variations of mean-velocity and turbulence intensities, section drag coefficient might yield better results.

4.5 Fourier Decomposition of Rotor-Wake

In the aerodynamics and aeroacoustic analysis of rotors, it is convenient to represent the components of the wake velocities in terms of

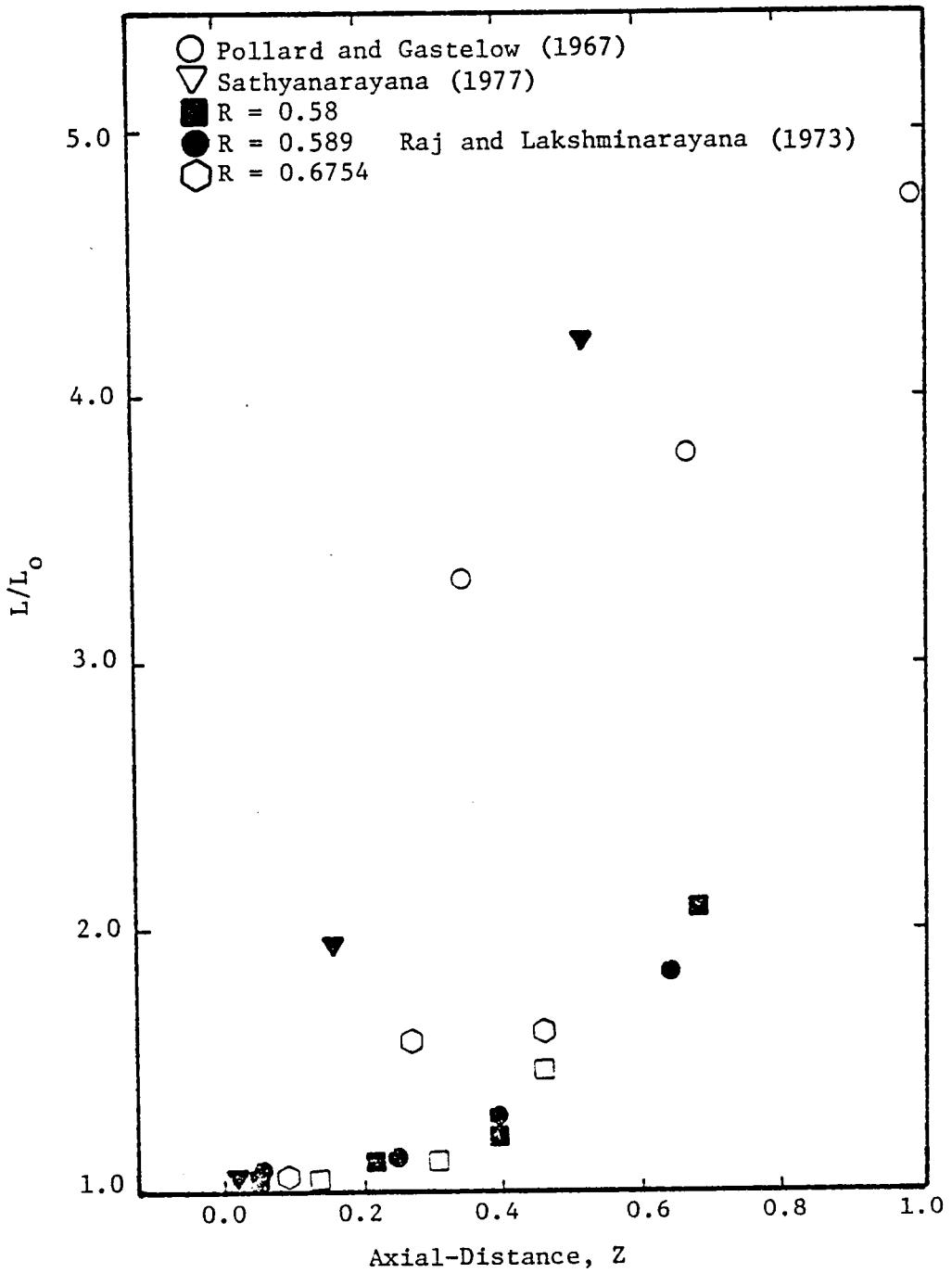

Figure 132. Wake Width Correlation with Downstream Distance for Cascade Wakes

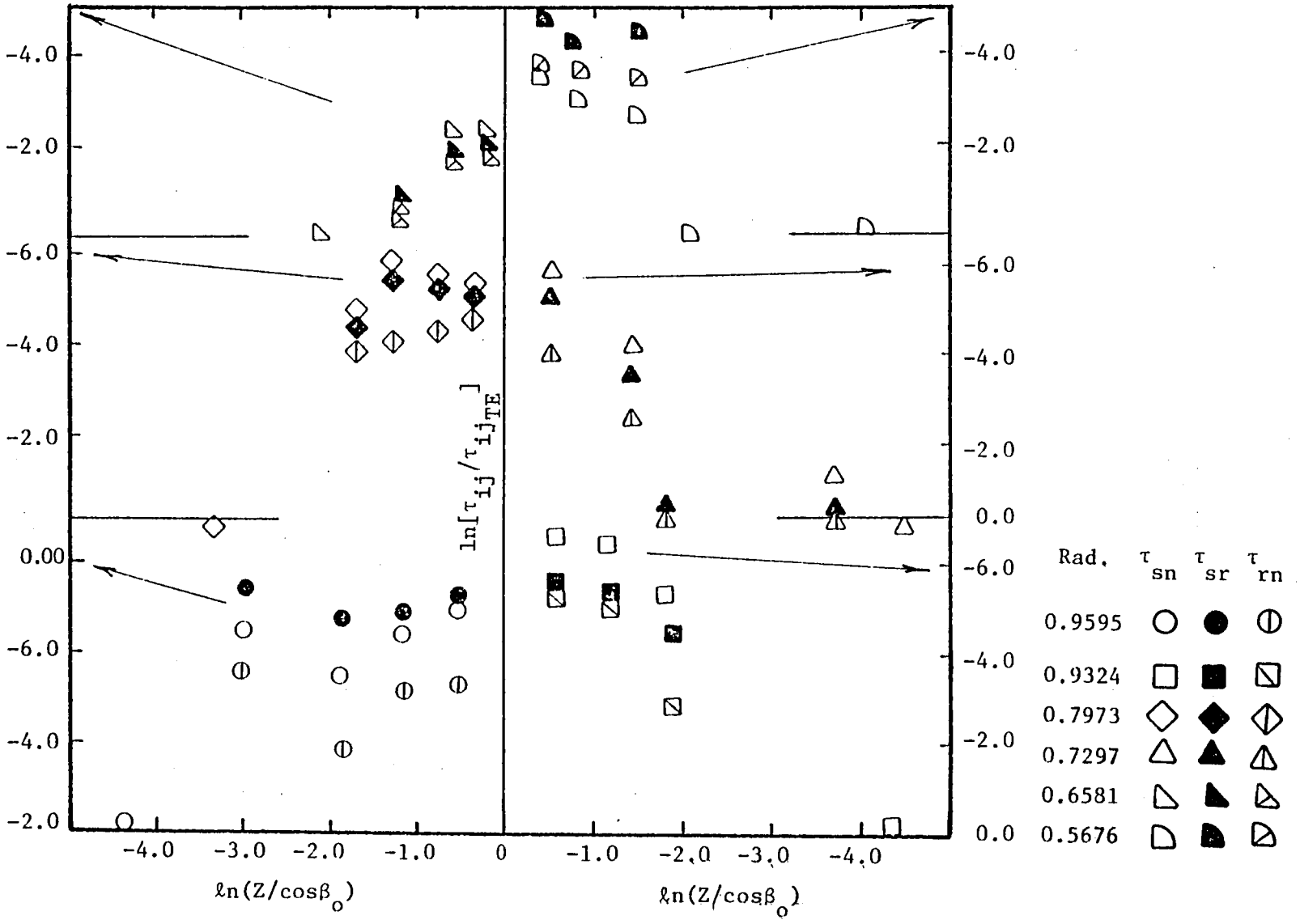

Figure 133. Decay of Normalized Shear-Stress with Downstream Distances

Fourier series. This representation is possible because the velocity distribution is periodic and continuous, as depicted in Figure 134. For example, the velocity at a point (r,θ,z) can be represented as

$$u_{dn}(r,\theta,z) = A_o + \sum_{n=1}^{\infty}[A_n(r,z)\cos\frac{n\theta}{\theta_L} + B_n(r,z)\sin\frac{n\theta}{\theta L}] \quad . \tag{35}$$

This type of representation was tried for the data of Raj and Lakshminarayana (1976) and the present data. The method of computation of the Fourier coefficients is based on the "FORIT" subroutine and is given in Appendix A-4. The subroutine uses recursive technique described by Ralston (1960).

Tjoennelano (1967) has investigated the repeatability of experimental velocity distributions inside the wake of a marine propeller. The Fourier coefficients calculated from the velocity distributions have shown that the variation between the experimental data and that obtained from the equation is of the order of $\pm$2.0 to 3.0 percent for the first four harmonics. Even for the present data the first four harmonics were found to be sufficient to get a close correlation with the data.

The coefficients of the Fourier series are given by,

$$A_n = \frac{\varepsilon_n}{L}\int_o^L \frac{u_d}{u_{dn}}\cos\frac{n\theta}{\theta_L}\, d(\frac{\theta}{\theta_L}) \tag{36}$$

and

$$B_n = \frac{\varepsilon_n}{L}\int_o^L \frac{u_d}{u_{dn}}\sin\frac{n\theta}{\theta_L}\, d(\frac{\theta}{\theta_L}) \tag{37}$$

where, ε_n = Neumann's factor

= 1 for n = 0

= 2 for n > 0

L = interval of integration (in the analysis only the wake portion is considered. The value of θ/θ_L at the wake center is π and at the edges 0 and 2π.)

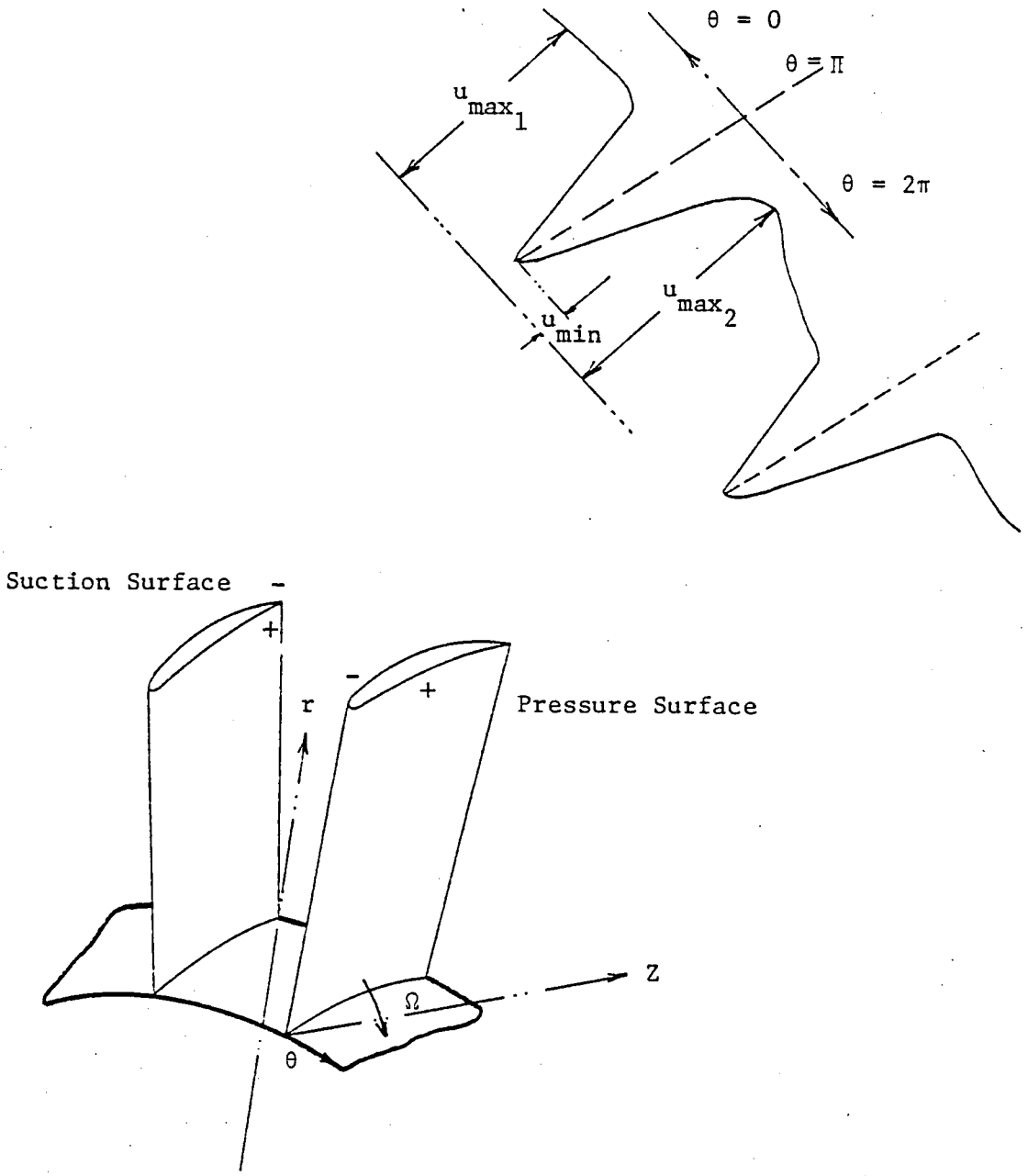

Figure 134. Typical Rotor-Wake and Coordinate System for Fourier Analysis

For n = 0,

$$A_o = \frac{1}{2\pi} \int_o^{2\pi} \frac{u_d}{u_{dn}} d\left(\frac{\theta}{\theta_L}\right) \quad . \tag{38}$$

This is the average defect across the wake. So A_o represents the average value across the wake and since the defect is normalized by the corresponding wake centerline defect, A_o should approximately remain constant with downstream distance. This is shown plotted in Figure 135 for the data of Raj and Lakshminarayana (1976) and the present data. The data of Raj and Lakshminarayana (1976) is at zero loading. The effect of loading is clearly seen in these plots. The higher the loading, the higher is the defect and correspondingly larger is the value of A_o.

The harmonic content in the wake is represented by the Fourier cosine coefficients and the asymmetry of the wake by the Fourier sine coefficients. As normalized velocity defects were used in the analysis the values of B_n were found to be very small indicating the axisymmetric nature of the normalized wake. The dominant coefficients are shown plotted in Figures 135, 136, and 137.

The Fourier curve correlates quite well with the data, considering only the first four harmonics. Figure 138 shows the plot of the scatter in the first four coefficients. The scatter is due to the asymmetry in the velocity defect profile in the outer regions of the flow, in particular, even after normalizing by the wake centerline velocity. As in this investigation only the wake portion is considered, the correlation with the Fourier curve seems to be good, with the correlation coefficient being about 0.989.

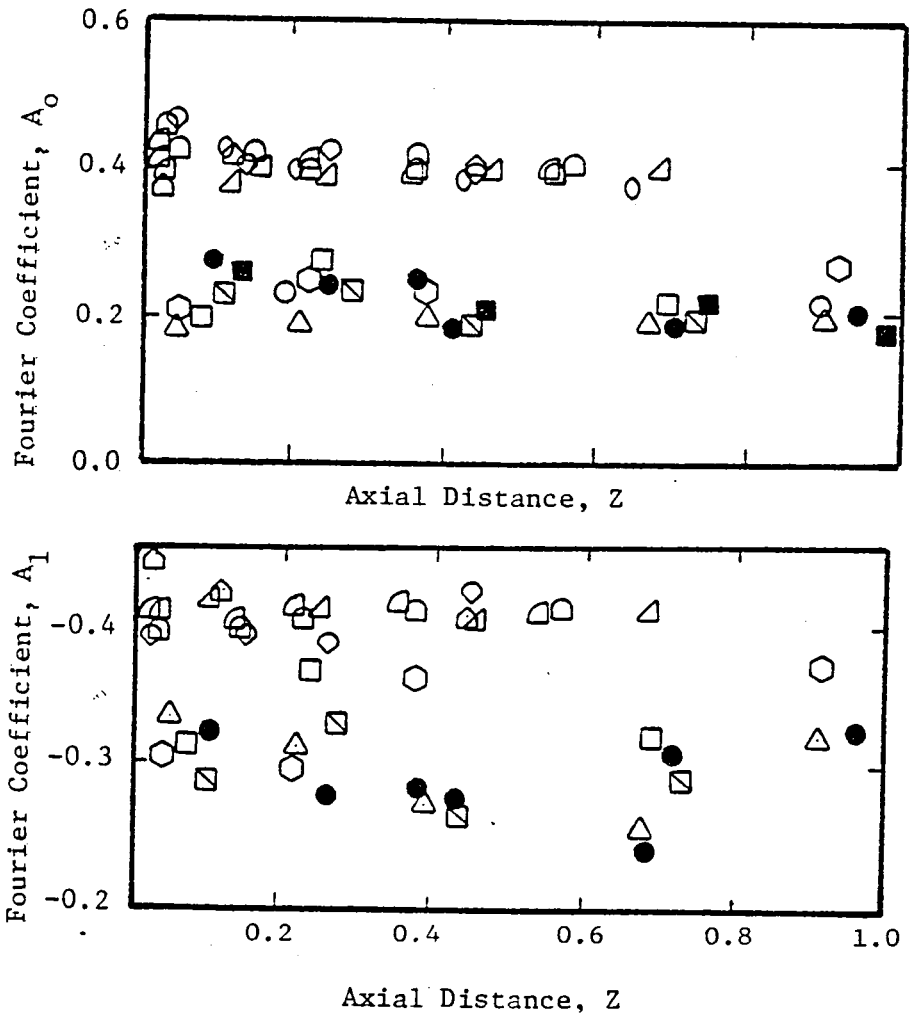

Legend

Author

R = 0.9595
R = 0.9324
R = 0.7973
R = 0.7297
R = 0.6581
R = 0.5676

Raj, Lakshminarayana (1976)

R = 0.493
R = 0.540
R = 0.587
R = 0.634
R = 0.728
R = 0.775
R = 0.822
R = 0.869

Figure 135. Variation of Fourier Coefficient A_o and A_1 with Downstream Distance

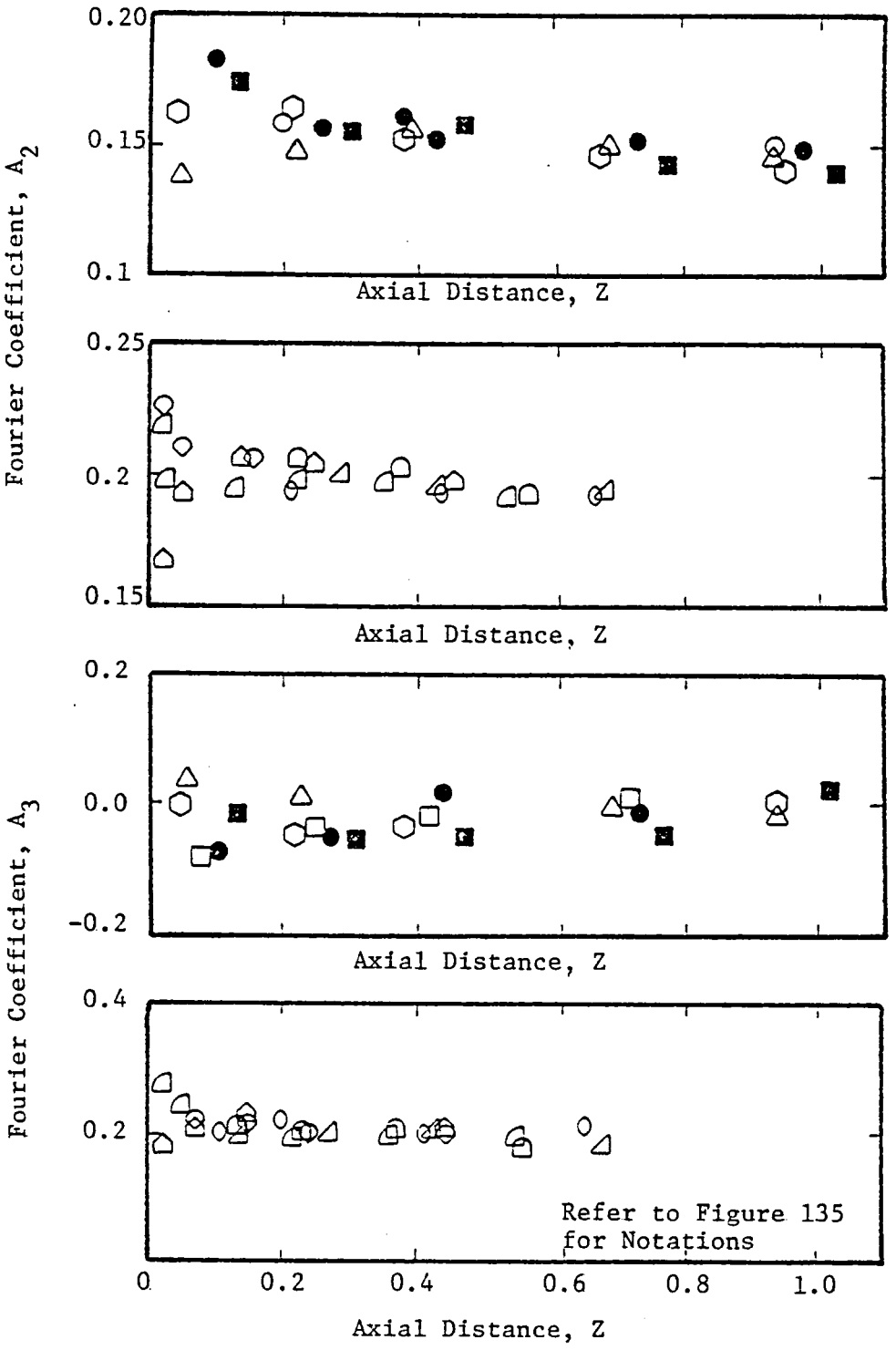

Figure 136. Variation of Fourier Coefficient A_2 and A_3 with Downstream Distance

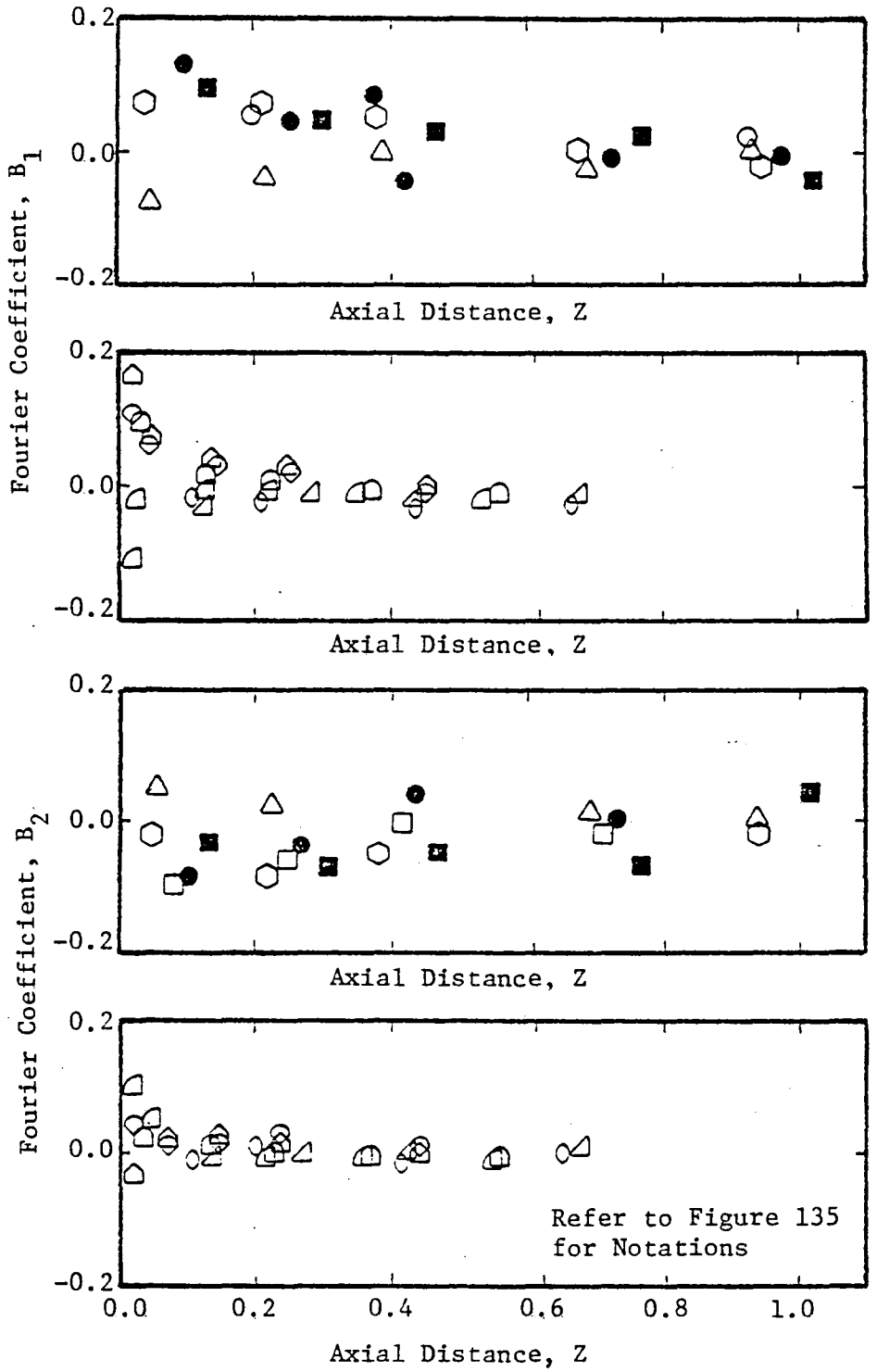

Figure 137. Variation of Fourier Coefficient B_1 and B_2 with Downstream Distance

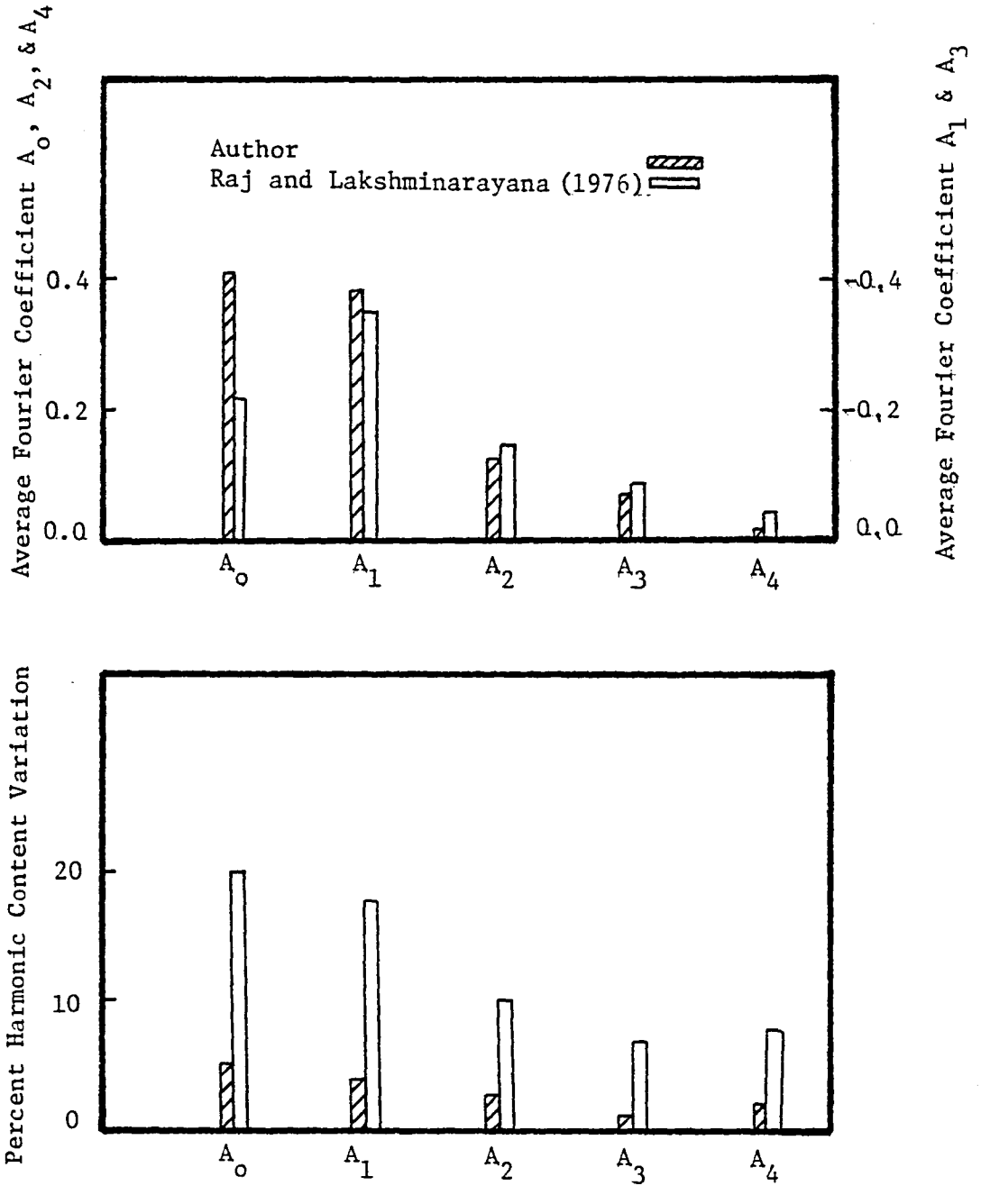

Figure 138. Average Fourier Coefficients and Scatter of Hormonic Content in Rotor-Wake

Chapter 5

CONCLUSIONS

The characteristics of the wake of a moderately loaded compressor rotor blade was investigated. The present set of measurements represent the first set of data in the trailing-edge region. All the measurements were acquired in the rotor frame of reference using a three sensor hot-wire probe and a direction insensitive static-stagnation pressure probe. Pressure survey indicated appreciable static-pressure gradient across the wake, particularly in the trailing-edge region. It was also found that the trailing-vortex system influences the mean velocities, particularly the radial velocity, in the trailing-edge region. Some of the important conclusions that can be drawn based on the results of the present investigation are as follows:

1. Mean velocity profiles in the trailing-edge and near-wake regions are asymmetrical and tend to become symmetrical in the far-wake region. In the end-wall regions, secondary flows (and tip-leakage flows in the case of annulus-wall region) affect the velocity profiles considerably resulting in vortex and wake type of distributions.

2. Radial velocities inside the annulus-wall layer are influenced by the secondary flow and the tip-leakage-flow. The tip-vortex, which is very strong in this case, dominates the radial velocity profile in this region.

3. Very large velocity defects were measured in the trailing-edge region. The defect was found to decay very rapidly in the trailing-edge and near-wake regions.

4. The defect in tangential velocity was found to be greater than the defect in axial velocity. The decay of the radial velocity in the

trailing-edge region was much more rapid than the axial and tangential components.

5. For the wake inside the annulus-wall boundary layer, the axial and tangential velocity defects and the maximum radial velocity initially increase and then start to decrease. This is attributed to the tip-vortex which initially increases in its strength and then decreases downstream of the blade. The decay of velocity defects inside the annulus- and hub-wall boundary layers is far slower compared to the decay rates outside the end-wall boundary layers. The slower decay is attributed to the combined effect of secondary flow (tip-vortex in the case of annulus-wall boundary layer) and the end-wall boundary layers on the wake.

6. The wake-width increases very rapidly in the trailing-edge region and the growth becomes very gradual in the far-wake region. Because of centrifugal effects, wake-width at higher radii is thicker. Inside the annulus- and hub-wall boundary layers the wake width is found to be very large due to the effect of secondary flow and tip-leakage flow.

7. For the wakes outside the end-wall boundary layers the wake shape factor monotonically decreases with downstream distance. It reaches an asymptotic value of nearly 1.2 at far downstream location. In the trailing-edge region the value is greater than 1.8 indicating the tendency of the flow to separate.

8. Variation of the momentum-thickness in the near- and far-wake regions is in close conformity with the free-stream velocity variation. For the wakes inside the annulus-wall boundary layer the momentum thickness grows very rapidly in the trailing-edge region and nearly remains

constant in the far-wake region. This behavior is due to the tip-vortex and the secondary flow at these locations.

9. There is a marked variation in the wake properties from one radius to the other. Not only the profiles, but also the defects and decay rates vary from one radius to the other.

10. For the wakes outside the end-wall boundary layers, the wake decay and wake width differ in the radial direction. But they correlate well with $\sqrt{c_d}$.

11. Similarity exists for axial, tangential, and radial velocity components. The radial velocities in the near- and far-wake regions also exhibit similarity. The radial velocities in the trailing-edge region show similarity only when the pressure and suction surface velocity profiles are separately considered.

12. Very strong static-pressure gradients across the wake were measured in the trailing-edge and near-wake regions. Static-pressure is found to increase towards the wake center. The difference in static pressure across the wake decays very rapidly in the trailing-edge region and the decay is very gradual in the far-wake region.

13. The turbulent stress profiles are asymmetrical about the wake center with the stresses near the pressure-surface being higher than those near the suction-surface. The streamwise Reynolds stress reaches zero value slightly away from the location where the velocity is minimum.

14. Decay of intensities and stresses are very rapid in the trailing-edge region and this trend slows down in the far-wake region. The rapid decay in the trailing-edge region is attributed to the trailing-vortex system.

15. Radial turbulence intensity decays slowest compared to axial and tangential components. The radial component of turbulence intensities was found to be the largest and this phenomenon is attributed to rotation effects.

16. The turbulence structure of the rotor-wake is highly asymmetric and non-isotropic in the trailing-edge region and becomes nearly isotropic and symmetric at half-a-chord downstream.

17. The free-stream turbulence in the wakes outside the end-wall boundary layers is about the same at all radii. But for the wakes inside the annulus- and hub-wall boundary layers, the magnitude of the free-stream turbulence is higher indicating the influence of secondary and tip-leakage as well as wall boundary layers on the turbulence intensity.

18. Similarity relationship was also found for all the three components of turbulence intensity. Discrepancy from the Gaussian curve, $e^{-0.693\eta^2}$, was observed only in the outer regions of flow as well as for wakes in the trailing-edge region.

19. The wake profiles could be represented by a Fourier series. The magnitude of the coefficients decreases rapidly, with the first three coefficients being the dominant ones.

REFERENCES

Anand, A. K., "An experimental and theoretical investigation of three-dimensional turbulent boundary layer inside the passage of a turbomachinery rotor," Ph.D. thesis, Department of Aerospace Engineering, The Pennsylvania State University, May 1976. (Also as NASA CR 28887, 1977)

Anand, A. K. and Lakshminarayana, B., "An experimental study of three-dimensional turbulent boundary layer and turbulence characteristics inside a turbomachinery rotor passage," ASME paper 78-GT-114, 1978.

Barna, P. S., "Investigations on the aerodynamic behavior of circular arc sheet metal airfoils in a two-dimensional accelerating cascade for stagger angles 7 1/2 and 15 degrees and gap-chord ratios 0.5, 0.75, and 1.0, respectively," Auburn University Report, Bulletin 46, 1964.

Berger, S. A., Laminar wakes, American Elsevier, New York, 1971.

Betchov, R., Verh. K. Akad. Wet, 51, pp. 721-730, 1948.

Bitterlich, W. and Rubner, K., "Annulus-wall boundary layer in axial-flow turbomchines," AGARDograph, 164, pp. 397-413, 1972.

Champagne, F. A., Sleicher, C. A., and Wehrmann, O. H., "Turbulence measurements with inclined hot-wires," Part I and Part II, J. Fluid Mech., 28, pp. 153-183, 1967.

Corrson, S., "Turbulence: Experimental methods," Handbook of Physics, 8/2, Springer, Berlin, 1963.

Daneshyar, M., "Annulus-wall boundary layer in turbomachines," Ph.D. thesis, Cambridge University, 1974.

Dunker, R. J., Strinning, P. E., and Weyer, H. B., "Experimental study of the flow field within a transonic axial compressor rotor by laser velocity and comparison with through-flow calculation," ASME Paper 77-GT-28, 1977.

Eagleson, P. S., Huval, C. J., and Perkins, F. E., "Turbulence in the early wake of a fixed flat plate," MIT Hydrodynamic Lab., TR No. 46, 1961.

Ermshaus, R., "Typical features of turbulent wake flows," translated from Mitt. ans dem Max-Plank-Inst. für strömungsforschung u. der Acrodyn. versuchsanst, Göttingen, No. 46, 1970.

Evans, R. L., "Turbulence and unsteady measurements downstream of a moving blade row," Tran. ASME, J. of Engy. for Power, Vol. 97, pp. 131-139, 1975.

Goldstein, S., "On the two-dimensional steady flow of a viscous fluid behind a solid body," appendix by Fage, Proc. Royal Society, Vo. 142, 1953.

Gorton, C. A. and Lakshminarayana, B., "A method of measuring the three-dimensional mean flow and turbulence quantities inside a rotating turbomachinery passage," Trans. ASME, J. of Engy. for Power, Vol. 98, No. 2, pp. 137-146, 1976.

Gustafson, W. A., David, Jr., D. W., and Deffenbaugh, F. D., "Analysis of turbulent wake of a cascade airfoil," J. Aircraft, Vol. 14, No. 2, pp. 35-356, 1977.

Hah, C. and Lakshminarayana, B., "Effect of rotation on a rotating hot-wire," J. of Phys. E: Sci. Instrum., Vol. 11, 1978.

Hah, C., "Numerical and experimental analysis of turbulent wake of airfoil, cascade, and turbomachinery rotor blade," Ph.D. thesis, Department of Aerospace Engineering, The Pennsylvania State Univeristy, 1980.

Hill, P. G., Schaub, V. W., and Senoo, Y., "Turbulent wakes in pressure gradients," Trans. ASME, J. of Applied Mechanics, Series E, pp. 518-524, 1963.

Hinze, J. O., Turbulence, McGraw-Hill, 1959.

Holbrock, G.J. and Okiishi, T. H., "The influence of compressor inlet-guide-vane/stator relative circumferential positioning on blade wake transport and interaction," Iowa State University Report, ERI-AMES-79037, 1978.

Hortog, D., Mechanical Vibrations, McGraw-Hill, 3rd Edition, 1947.

Klebanoff, P. S., "Characteristics of turbulence in a boundary layer with zero pressure gradient," NACA TN 3178, 1954.

Kool, P., DeRuyck, J., and Hirsch, C. H., "The three-dimensional flow and blade wake in an axial plane downstream of an axial compressor rotor," ASME Paper 78-GT-66, 1978.

Lakshminarayana, B., "The nature of flow distortions caused by rotor blade wakes," AGARD CP-177, 1976.

Lakshminarayana, B. and Davino, R., "Mean velocity and decay characteristics of the guide-vane and stator-blade wake of an axial-flow compressor, ASME Paper 78-GT-9, 1978.

Lakshminarayana, B. and Jabbari, B., and Yamaoka, H., "Turbulent boundary layer on a rotating helical blade," J. of Fluid Mech., Vol. 5, Part 3, pp. 545-569, 1972.

Lakshminarayana, B and Reynolds, B., "Turbulence characteristics in the near-wake of a compressor rotor blade," AIAA Paper 79-0280, 1979.

Lieblein, S. and Roudebush, W. H., "Low-speed wake characteristics of two-dimensional cascade and isolated airfoil sections," NACA TN 3771, 1956.

Lumley, J. L., "On the interpretation of time spectra measured in high intensity shear flows," Physics of Fluids, Vol. 8, No. 6, 1965.

Olivari, D., "Effects on the wire supports on the frequency response of hot-wire anemometers," Von Karman Institute for Fluid Dynamics, TN 118, 1976.

Pollard, D. and Gastelow, J. P., "Some experiments at low speed on compressor cascades," Tran. ASME, J. of Engy. for Power, pp. 427-436, 1967.

Raj, R. and Lakshminarayana, B., "Characteristics of the wake behind a cascade of airfoils," J. of Fluid Mech., Vol. 61, Pt. 4, pp. 707-730, 1973.

Raj, R. and Lakshminarayana, B., "On the investigation of cascade and turbomachinery rotor-wake characteristics," NASA-CR-134680, 1975.

Raj, R. and Lakshminarayana, B., "Three-dimensional characteristics of turbulent wakes behind axial flow turbomachinery," J. Engineering for Power, Vol. 98, pp. 218-228, April 1976.

Raj, R. and Lumley, J. L., "A theoretical investigation on the structure of fan wakes," ASME Paper 76-WA/FE-22, 1976.

Ralston, H., Numerical methods for digital computers, Chap. 24, John Wiley & Sons, 1960.

Reynolds, B., "Characteristics of lightly loaded fan rotor blade wakes," M.S. thesis, Department of Aerospace Engineering, The Pennsylvania State University, Dec., 1978.

Reynolds, B., Lakshminarayana, B., and Ravindranath, A., "Characteristics of the near-wake of a compressor or fan rotor blade," AIAA Journal, Sept., 1978.

Sathyanarayana, B., "Unsteady wake measurements of airfoils and cascades," AIAA J., Vol. 15, No. 5, pp. 613-618, 1977.

Schlichting, H., Boundary layer theory, McGraw-Hill, 1968.

Serovy, G, K., "Deviation angle/turning angle prediction for advanced axial-flow compressor blade row geometries," AFADL-TR-77-81, Iowa State University, Technical Report, 1977.

Silverstein, A., Katzoff, S., and Bullivant, W. K., "Downwash and wake behind plain airfoils," NACA Report No. 651, 1939(a).

Smith, Jr., L. H., "Three-dimensional flow in an axial-flow turbomachinery," QADC, Technical Report 55-348, Vol. II, Johns Hopkins University, 1956, also WADC Technical Report 55-348.

Tennekes, H. and Lumley, J. L., A first course in turbulence, MIT Press, Cambridge, 1972.

Thompkins, W. T. and Kerrebrock, J. L., "Exit flow from a transonic compressor rotor," AGARD CP-177, 1975.

Tjoennelano, J. P., "An investigation into the repeatability of wake survey data and the effects of small yaw angles on the wake velocities," MIT Department of Naval Architecture and Marine Engineering, Rep. No. 67-5, 1967.

Townsend, A. A., "Measurements in the turbulent wake of a cylinder," Proc. of the Royal Society, London, Series A, Vol. 190, pp. 551-561, 1947.

Ufer, H., "Analyse der Geschwindigkeitsverteilung an den Schaufelspitzen von Axialgeblä Sen," Tech. Mitt Krupp (Forschungsberichte), Vol. 26, No. 2, pp. 33-45, 1968 (also NASA TTF-16366, 1975).

Welsh, J. K., "Experimental investigation of the effect of tip clearance and end losses on axial compressor performance," M.S. thesis, Department of Aeronautics, U.S. Naval Postgraduate School, 1973.

Appendix A1

ROTATING HOT-WIRE DATA REDUCTION COMPUTER PROGRAM

The FORTRAN-IV computer program described in this appendix reduces the rotating hot-wire data to obtain the mean velocity, turbulence intensity, and Reynolds stresses in any arbitrary coordinate system. This program was developed by Gorton and Lakshminarayana (1976). Later it was modified by Anand (1976) and Reynolds (1978) to include many of the corrections, including temperature and E_o variation. The author modified the program by incorporating the effects of varying rotational speed, inlet velocity, and test section temperature. This modified version of the program was employed to reduce the data reported in the thesis.

Reference is made to Gorton and Lakshminarayana (1976) for the basic analysis and mathematical interpretation. Only the information required to run this program and to interpret the output is given below.

A1.1 Description of Input and Output

The principal inputs for the program are the correction factors to account for the deviation from the cosine law rule, calibration voltages of the hot-wire probe, the direction cosines of the hot-wire sensors, and the mean and the root mean square value of the fluctuating components of voltage at each measuring location. The output of the program include three components of mean velocity and three components of intensity, and Reynolds stress and other relevant data.

A1.1.1 Input

The input variables are read into the program on punched data cards. The first input card sets a switch depending on whether it is the last data set or another data set will follow (for example, a blank card will

allow the program to proceed to the next set of data and 2.0 in the first two columns terminates the program with that particular data set.)

The second card is a title card which serves for problem identification. Any information can be put in the first 72 columns and the rotor tip speed, which is used as a normalizing parameter is punched in the 73rd to 80th column.

The third card sets the number of iteration and the tolerance limit in the program. Any limit on these two parameters can be set, depending upon the accuracy needed for the problem under consideration.

The next card is for setting the attenuation of the input electrical data. This is a nongeometric parameter and has to be obtained from the instruments used during the experimentation.

The fifth card is the K-factor employed to account for the deviation of hot-wire response from the cosine law. This factor has to be calculated based on the length-to-diameter ratio as well as the angle the sensors make with the flow direction.

The program can take either individual or multiple sets of calibration and this is punched in the sixth card of the input data. The temperature at which the calibration is carried out and the number of calibration curves employed for the data reduction are punched in the next two cards. The ninth card accounts for the number of calibration points. The tenth and eleventh cards are used for the initial and final values of voltages of the hot-wire sensors at zero flow velocity. The next sets of cards take values of the flow velocity in the calibration tunnel in inches of water and the voltages of the hot-wire sensors at various flow velocities in the tunnel. The next card in the input deck is used to designate the number of radial stations in that particular survey and

also the number of tangential positions across the wake for that particular measurement. In the next three cards are punched the angles which each of the sensors make with the system of coordinates choosen. The set of cards that follow these carry the D.C. voltages, wall static pressure, temperature in the tunnel, the rotor speed, as well as the output from the sum and difference unit at each of the data points.

The input variables described above have to be in some consistant units. Only a list of the input variables are given below and reference is made to Gorton and Lakshminarayana (1976) for detailed description of the program and program variables.

RAVI	control card to set a switch to indicate whether the data set following is the last one in the deck or whether succeeding data sets will follow that particular data set.
NTITLE	title card to designate problem identification
UTIP	tip speed of rotor for that particular experiment (m/sec or ft/sec)
NREPS	number of iterations desired
EPS	expected tolerance limit
ATTEN	attenuation of the input signal
KK	K-factor. The factor that accounts for the deviation from the cosine law
CALA	defines whether single or multiple sets of calibration is employed in the program
TEMP,NTER	temperature at which calibration was carried out (°C or °K)
NCAL	number of calibration curves employed in the subroutine
NPTS	number of calibration points in that particular data set

EO	value of the voltage from the hot-wire sensor at zero flow velocity (volts)
V	velocity in the calibration tunnel as pressure head (inches or cms of water colum)
CALE	calibration voltage of the sensor (volts)
POWER	slope of the calibration curve (multiple calibration)
NOR,JRAD	number of radial stations in the data set
NOT,THETA	number of tangential positions across the wake in the data set
A1	angle the sensor number one makes with the one of three coordinates, usually streamwise or axial, in degrees
B1	angle the sensor number one makes with the second coordinate, usually normal or tangent direction, in degrees
C1	angle the sensor number one makes with the third coordinate, usually the radial direction, in degrees
D1,E1,F1	angles the sensor number two makes with the coordinate system (s,n,r or z,θ,r, respectively) in degrees
GI,XHI,XI1	angles the sensor number three makes with the coordinate system (s,n,r or z,θ,r, respectively) in degrees
IPRO	number of probes employed for the data set
DSLOP	slopes of the calibration curve (simultaneous calibration)
VCHAN	voltage output from sensor at operating conditions (volts)
T	temperature in the test section (°F)
PW	wall static pressure (a measure of through flow velocity into the test section) (cm or inches of water column)
N	rotational speed at which the data set was taken (rpm)

FV15,FV25,FV35 root mean square voltage of the fluctuating component of flow for the three sensors (volts)

E12,E23,E13 root mean square voltage output from the summing circuits between two hot-wire signals (volts)

E21,E32,E31 voltage output from the differencing circuits between two hot-wire signals (volts)

A1.1.2 Output

A sample of input variables as they are punched on the data cards is given at the end of the program listing.

The printed output from the program is in the form of three mean velocity components, three turbulent intensities, and turbulent shear stresses. The output is also in the form of punched cards. Consistent with the assumptions made in the program the output which will be in the form of velocities, turbulence intensities, and stresses will be in the natural coordinate system. The punched output is used in a subsequent coordinate transformation program to convert the velocities and turbulence quantities from the streamline coordinate system to the coordinate system of interest. A listing of the same is also given after the sample data input listing.

Below is listed the printed output directory.

WS streamwise component of total mean velocity normalized by blade tip speed

WN normal component of total mean velocity normalized by blade tip speed

WR radial component of total mean velocity normalized by blade tip speed

W total mean velocity normalized by blade tip speed

FWS	streamwise component of turbulent intensity normalized by local mean velocity
FWN	normal component of turbulent intensity normalized by local mean velocity
FWR	radial component of turbulent intensity normalized by local mean velocity
B(4)	streamwise component of Reynolds stress normalized by local dynamic pressure
B(5)	normal component of Reynolds stress normalized by local dynamic pressure
B(6)	radial component of Reynolds stress normalized by local dynamic pressure
RESSTR	resultant of streamwise, normal, and radial components of Reynolds stress

A1.2 Program Listing

This program utilizes about 460 records for a 22 points data set on the IBM 370 system. The run time for this program is 5 seconds. A listing of the program begins on the next page.

```
C      ROTATING HOT-WIRE DATA REDUCTION PROGRAM
       IMPLICIT LOGICAL*1 ($)
        DIMENSION SLOPE1(99),SLOPE2(99),SLOPE3(99),NTITLE(20)
       DIMENSION FVEL1(6,99),FVEL2(6,99),FVEL3(6,99)
       DIMENSION V1(4,25),V2(4,25),V3(4,25)
       DIMENSION NPTS(25),CINCH(4,25),CVEL(4,25)
       DIMENSION VEL1(6,99),VEL2(6,99)
       DIMENSION VEL3(6,99)
       DIMENSION RRAD(6)
       DIMENSION THETA(99),RAD(6)
        DIMENSION FV1S (99), FV2S (99), FV3S (99), FV12S(99),FV13S(99),
      1 FV23S (99),DATA(200,30)
       DIMENSION C(3,3),A(6,6),ERROR(6),ATTEN(3),TIME(3),TEMP(  99),XI(6)
       COMMON VCHAN1(4,6,99),VCHAN2(4,6,99),VCHAN3(4,6,99),EO1,EO2,EO3,EO
     C4,EO5,EO6,EO7,EO8,EO9,CALE1(4,25),CALE2(4,25),CALE3(4,25),NOT
       COMMON JJ,CALV1(4,25),CALV2(4,25),CALV3(4,25)
       REAL*8 CC(3,3),AA(6,6),D(3),B(6),DET
 5553  CONTINUE
       READ(5,5555)RAVI
 5555  FORMAT(F10.4)
       FACT=SQRT(2.)/2.
       FACTOR=0.0
       RAT=3.14159/180.
       READ(5,83)(NTITLE(I),I=1,18),UTIP
       WRITE(6,98)
  98   FORMAT(////////)
       WRITE (6,95) (NTITLE(I),I=1,18)
       WRITE(6,666)
  666  FORMAT(////)
       READ(5,82)NREPS,EPS
        EPS = EPS * UTIP
        READ(5,45) (ATTEN(L),L=1,3)
C
C      READ IN HOTWIRE CONSTANTS FOR L/D
C
       READ(5,70)XK1,XK2,XK3
```

```
      READ(5,6)CALA1,CALA2,CALA3
      CALA1=CALA1*RAT
      CALA2=CALA2*RAT
      CALA3=CALA3*RAT
C
C     READ IN CALIBRATION CURVES
C
       READ(5,32) (TEMP(LL),LL=1, 6)
      READ(5,5)NCAL
      DO 100 I=1,NCAL
      READ(5,10)NPTS(I)
      JJ=NPTS(I)
      READ(5,15)E04,E05,E06
      READ(5,15)E07,E08,E09
      DO 105 J=1,JJ
      READ(5,15)V1(I,J),CALE1(I,J),V2(I,J),CALE2(I,J),V3(I,J),CALE3(I,J)
     X,T
      IF(T.LT.50.0) T=1.8*T+32.0
      IF (T.EQ.0.0) T=73.0
C     CORRECTION TO ACCOUNT FOR THE DIFFERENCE IN EO VALUES
      DE1=0.0
      DE2=0.0
      DE3=0.0
C
C  TEMPRATURE CORRECTION TO VELOCITIES & VOLTAGES
      TEMP(J)=T
      CALE1(I,J)=CALE1(I,J)  *(1.0+ 0.0014*( TEMP(J)-73.0))
      CALE2(I,J)=CALE2(I,J)  *(1.0+ 0.0014*( TEMP(J)-73.0))
      CALE3(I,J)=CALE3(I,J)  *(1.0+ 0.0014*( TEMP(J)-73.0))
C     CORRECT CALIBRATION CURVE FOR SKEWED PROBE
C
      V1(I,J)=66.7*(1.0+0.001*(TEMP(J)-73.0))*SQRT(V1(I,J))
      V2(I,J)=66.7*(1.0+0.001*(TEMP(J)-73.0))*SQRT(V2(I,J))
      V3(I,J)=66.7*(1.0+0.001*(TEMP(J)-73.0))*SQRT(V3(I,J))
  105 CONTINUE
  100 CONTINUE
```

```
C
C       READ IN CALIBRATION CONSTANTS OF HOT WIRES
C
        READ (5,6) POWER1,POWER2,POWER3,KOUNTR
C
C       WRITE OUT CALIBRATION CURVES
C
        DO 101 I=1,NCAL
        WRITE(6,99)
        WRITE(6,50)I
         WRITE(6,54)
        JJ=NPTS(I)
        DO 102 J=1,JJ
        VSQ1=V1(I,J)**POWER1
        VSQ2=V2(I,J)**POWER2
        VSQ3=V3(I,J)**POWER3
        E1SQ=CALE1(I,J)**2.
        E2SQ=CALE2(I,J)**2.
        E3SQ=CALE3(I,J)**2.
        CALV1(I,J)=CALE1(I,J)
        CALV2(I,J)=CALE2(I,J)
        CALV3(I,J)=CALE3(I,J)
        WRITE(6,55)J,CVEL(I,J),V1(I,J),V2(I,J),V3(I,J),CALE1(I,J),CALE2(I,
       1J),CALE3(I,J),VSQ1,VSQ2,VSQ3,E1SQ,E2SQ,E3SQ
C
C        USE VOLTAGE SQUARED VS. ROOT VELOCITY CURVE FOR CALIBRATION
C
        CALV1(I,J)=CALE1(I,J)**2.
        CALV2(I,J)=CALE2(I,J)**2.
        CALV3(I,J)=CALE3(I,J)**2.
        V1(I,J)=V1(I,J)**POWER1
        V2(I,J)=V2(I,J)**POWER2
        V3(I,J)=V3(I,J)**POWER3
  102 CONTINUE
  101 CONTINUE
        WRITE(6,99)
```

```
      READ(5,20)NOR,NOT
      READ(5,32)(RAD(I),I=1,NOR)
      DO 112 I=1,NOR
      RRAD(I)=(10.75-RAD(I))/10.75
  112 CONTINUE
C
C     WRITE OUT INPUT DATA
C
      WRITE(6,32)(RRAD(I),I=1,NOR)
C
C     READ IN DIRECTION COSINES
C
      READ(5,70)A1,B1,C1
      READ(5,70)D1,E1,F1
      READ(5,70)G1,XH1,XI1
      WRITE (6,87)A1,B1,C1,D1,E1,F1,G1,XH1,XI1
C
       A1= A1* RAT
       B1= B1* RAT
       C1= C1* RAT
      A1=COS(A1)
      B1=COS(B1)
       C1= COS(C1)
       A2= 0.00
       D2= 0.00
       G2= 0.00
       BX= SQRT( B1*B1+C1*C1 )
       B2= C1/BX
       C2= -B1/C1*B2
       BY= C1*B2-C2*B1
       BSQ= A1*A1+BY*BY
       BSQ= SQRT(BSQ)
       A3= BY/BSQ
       B3= A1*C2/BSQ
       C3= -A1*B2/BSQ
       D1= D1* RAT
```

```
      E1= E1* RAT
      F1= F1* RAT
      D1= COS(D1)
      E1= COS(E1)
      F1= COS(F1)
      EX= SQRT( E1*E1+F1*F1 )
      E2= F1/EX
      F2= -E1/F1*E2
      EY= F1*E2-F2*E1
      ESQ= D1*D1+EY*EY
      ESQ= SQRT(ESQ)
      D3= EY/ESQ
      E3= D1*F2/ESQ
      F3= -D1*E2/ESQ
      G1= G1* RAT
     XH1=XH1* RAT
     XI1=XI1* RAT
      G1= COS(G1)
     XH1= COS(XH1)
     XI1= COS(XI1)
      EX= SQRT( XH1*XH1+XI1*XI1)
     XH2= XI1/EX
      XI2= -XH1/XI1*XH2
      EY= XI1*XH2-XI2*XH1
      ESQ= G1*G1+EY*EY
      ESQ= SQRT(ESQ)
     G3=  EY/ESQ
      XH3= G1*XI2/ESQ
     XI3= -G1*XH2/ESQ
      WRITE(6,74)
      WRITE(6,75) A1,B1,C1,D1,E1,F1
      WRITE(6,75) G1,XH1,XI1,B2,E2,XH2
     WRITE (6,88)A1,B1,C1,A2,B2,C2,A3,B3,C3
     WRITE (6,88)D1,E1,F1,D2,E2,F2,D3,E3,F3
     WRITE (6,88)G1,XH1,XI1,G2,XH2,XI2,G3,XH3,XI3
C    CALCULATE EQUATION COEFFICIENTS
```

```
C
      A4=XK1*XK1*A1*A1+A2*A2+A3*A3
      B4=XK1*XK1*B1*B1+B2*B2+B3*B3
      C4=XK1*XK1*C1*C1+C2*C2+C3*C3
      D4=2.*(XK1*XK1*A1*B1+A2*B2+A3*B3)
      E4=2.*(XK1*XK1*A1*C1+A2*C2+A3*C3)
      F4=2.*(XK1*XK1*B1*C1+B2*C2+B3*C3)
C
      A5=XK2*XK2*D1*D1+D2*D2+D3*D3
      B5=XK2*XK2*E1*E1+E2*E2+E3*E3
      C5=XK2*XK2*F1*F1+F2*F2+F3*F3
      D5=2.*(XK2*XK2*D1*E1+D2*E2+D3*E3)
      E5=2.*(XK2*XK2*D1*F1+D2*F2+D3*F3)
      F5=2.*(XK2*XK2*E1*F1+E2*F2+E3*F3)
C
      A6=XK3*XK3*G1*G1+G2*G2+G3*G3
      B6=XK3*XK3*XH1*XH1+XH2*XH2+XH3*XH3
      C6=XK3*XK3*XI1*XI1+XI2*XI2+XI3*XI3
      D6=2.*(XK3*XK3*G1*XH1+G2*XH2+G3*XH3)
      E6=2.*(XK3*XK3*G1*XI1+G2*XI2+G3*XI3)
      F6=2.*(XK3*XK3*XH1*XI1+XH2*XI2+XH3*XI3)
C
      WRITE(6,76)A4,B4,C4,D4,E4,F4
      WRITE(6,76)A5,B5,C5,D5,E5,F5
      WRITE(6,76)A6,B6,C6,D6,E6,F6
C
      C(1,1)=SQRT(A4)
      C(1,2)=D4/(2.*C(1,1))
      C(1,3)=E4/(2.*C(1,1))
      C(2,1)=SQRT(A5)
      C(2,2)=D5/(2.*C(2,1))
      C(2,3)=E5/(2.*C(2,1))
      C(3,1)=SQRT(A6)
      C(3,2)=D6/(2.*C(3,1))
      C(3,3)=E6/(2.*C(3,1))
C
```

```
      DO 107 I=1,3
      WRITE(6,75)(C(I,J),J=1,3)
  107 CONTINUE
C
C     READ IN MEAN AND FLUCTUATING VOLTAGES, FIND CORRESPONDING VELOCITIES
C
      READ(5,82) NTER, THETAI
      READ(5,40)IPRO,JRAD
      WRITE(6,99)
      IPROBE=IPRO
      READ(5,6) DSLOP1 ,DSLOP2 ,DSLOP3
      DO 110 I=1,JRAD
      READ(5,45) ERROR(I),XI(I),TIME(I)
       DO 300 J=1,NOT
      READ(5,45)VCHAN1(IPROBE,I,J),VCHAN2(IPROBE,I,J),VCHAN3(IPROBE,I,J)
     X,T,PW,N
      AN=N
      IF (J.EQ.1) AN1=AN
      IF(AN.EQ.0.0) AN=AN1
      IF(J.EQ.1) UT1=UTIP
      UT1=0.3147*0.02780*18.5*AN
      UT=UT1*AN/AN1
      IF (T.EQ.0.0) T=73.0
      IF(T.LT.50.0) T=1.8*T+32.0
      PWALL=(1.000/1.0000)*PW
      TEMP(J)=T
      IF(J.EQ.1) PWALL1=PWALL
      IF(PWALL.EQ.0.0) PWALL=PWALL1
      DT=T-73.0
      RHO=(1.0-0.001*DT)**2
      IF(J.EQ.1)RHO1=RHO
       READ(5,45) FV1S (  J),FV2S (  J),FV3S (  J)
      READ (5,45) E12,E23,E13
      READ (5,45) E21,E32,E31
      FV12S(J)=(E12*E12-E21*E21)/4.0
      FV23S(J)=(E23*E23-E32*E32)/4.
```

```
      FV13S(J)=(E13*E13-E31*E31)  /4.0
      WRITE(6,46)VCHAN1(IPROBE,I,J),VCHAN2(IPROBE,I,J),VCHAN3(IPROBE,I,J)
     C),FV1S(J),FV2S(J),FV3S(J),FV12S(J),FV13S(J),FV23S(J)
      THETA(J)=THETAI+1
  300  CONTINUE
      WRITE(6,88) (THETA(IJ),IJ=1,3)
      IF (KOUNTR.EQ.0) GO TO 302
      IX=I
      NOTT=NOT-1
      DO 301 JX=1,NOTT
      J=JX+1
      VCHAN2(IPROBE,IX,JX)=2.0*VCHAN2(IPROBE,IX,JX)-VCHAN2(IPROBE,IX,J)
      VCHAN3(IPROBE,IX,JX)=0.5*VCHAN3(IPROBE,IX,JX)+VCHAN3(IPROBE,IX,J)
      FV2S (JX)=2.0*FV2S (JX)-FV2S (J)
      FV3S (JX)=0.5*(FV3S (JX)+FV3S (J))
      FV12S(JX)=0.5*(3.0*FV12S(JX)-FV12S(J))
      FV13S(JX)=0.25*(3.*FV13S(JX)+FV13S(J))
      FV23S(JX)=0.25*(5.0*FV23S(JX)-FV23S(J))
  301 CONTINUE
      IY=I
      VCHAN2(IPROBE,IY,NOT)=VCHAN2(IPROBE,IY,NOTT)
      VCHAN3(IPROBE,IY,NOT)=(3.*VCHAN2(IPROBE,IY,NOT)-VCHAN3(IPROBE,IY,
     CNOTT))*0.5
      FV12S(NOT) = 0.5*(FV12S(NOT)+FV12S(NOTT))
      FV2S(NOT)=FV2S(NOT-1)
      FV3S(NOT)=0.5*(3.*FV3S(NOT)-FV3S(NOTT))
      FV13S(NOT)=0.25*(3.0*FV13S(NOT)+FV13S(NOTT))
      FV23S(NOT)=0.25*(3.0*FV23S(NOT)+FV23S(NOTT))
  302 CONTINUE
      DO 115 J=1,NOT
C
      FV1SQ=FV1S(J)
      FV2SQ=FV2S(J)
      FV3SQ=FV3S(J)
      FV12=FV12S(J)
      FV13=FV13S(J)
```

```
      FV23=FV23S(J)
       NJ= J+7
      TEMP(J)=73.0
       TCORR= 1.0 + 0.0028*(TEMP( J)-73.0)
       VCHAN1(IPROBE,I,J)=VCHAN1(IPROBE,I,J)*VCHAN1(IPROBE,I,J)*TCORR
       VCHAN2(IPROBE,I,J)=VCHAN2(IPROBE,I,J)*VCHAN2(IPROBE,I,J)*TCORR
       VCHAN3(IPROBE,I,J)=VCHAN3(IPROBE,I,J)*VCHAN3(IPROBE,I,J)*TCORR
      JJ=NPTS(IPROBE)
      CALL CALIB(IPROBE,J)
      DO 120 K=1,JJ
      IF(VCHAN1(IPROBE,I,J).GT.CALV1(IPROBE,K))GO TO 120
       IF( K.GT.2) GO TO 170
       SLOPE1(J)=(CALV1(IPROBE,K)- CALV1(IPROBE,K-1))/ (V1(IPROBE,K)-V1
     1 (IPROBE,K-1)) + DSLOP1 * J / NOT
       GO TO 171
  170  SLOPE1(J)=(CALV1(IPROBE,K)- CALV1(IPROBE,K-2))/ (V1(IPROBE,K)-V1
     1 (IPROBE,K-2)) + DSLOP1 * J / NOT
  171 RATIO=(VCHAN1(IPROBE,I,J)-CALV1(IPROBE,K-1))/ SLOPE1(J)
      VEL1(I,J)=V1(IPROBE,K-1)+RATIO
      VEL1(I,J)=VEL1(I,J)**(1.0/POWER1)
      K1=K
      GO TO 121
  120 CONTINUE
  121 JJ=NPTS(IPROBE)
      DO 125 K=1,JJ
      IF(VCHAN2(IPROBE,I,J).GT.CALV2(IPROBE,K))GO TO 125
       IF( K.GT.2) GO TO 173
       SLOPE2(J)=(CALV2(IPROBE,K)- CALV2(IPROBE,K-1))/ (V2(IPROBE,K)-V2
     1 (IPROBE,K-1)) + DSLOP2  *J/NOT
       GO TO 174
  173  SLOPE2(J)=(CALV2(IPROBE,K)- CALV2(IPROBE,K-2))/ (V2(IPROBE,K)-V2
     1 (IPROBE,K-2)) + DSLOP2  *J/NOT
  174 RATIO=(VCHAN2(IPROBE,I,J)-CALV2(IPROBE,K-1))/ SLOPE2(J)
      VEL2(I,J)=V2(IPROBE,K-1)+RATIO
      VEL2(I,J)=VEL2(I,J)**(1.0/POWER2)
      K3=99
```

```
      K2=K
      GO TO 122
  125 CONTINUE
  122 JJ=NPTS(IPROBE)
      DO 130 K=1,JJ
      IF(VCHAN3(IPROBE,I,J).GT.CALV3(IPROBE,K))GO TO 130
       IF( K.GT.2) GO TO 176
       SLOPE3(J)=(CALV3(IPROBE,K)- CALV3(IPROBE,K-1))/ (V3(IPROBE,K)-V3
     1 (IPROBE,K-1)) + DSLOP3*J/NOT
       GO TO 177
  176  SLOPE3(J)=(CALV3(IPROBE,K)- CALV3(IPROBE,K-2))/ (V3(IPROBE,K)-V3
     1 (IPROBE,K-2)) + DSLOP3*J/NOT
  177 RATIO=(VCHAN3(IPROBE,I,J)-CALV3(IPROBE,K-1))/SLOPE3(J)
      VEL3(I,J)=V3(IPROBE,K-1)+RATIO
      VEL3(I,J)=VEL3(I,J)**(1.0/POWER3)
      K3=K
      GO TO 135
  130 CONTINUE
C
CC    USE NEWTON-RAPHSON METHOD TO CALCULATE MEAN VELOCITIS
C
C     FIND INITIAL VALUES OF VELOCITY USING DLEQD METHOD
C
  135 D(1)=VEL1(I,J)
      WRITE(6,3334)
 3334 FORMAT(' ','     MEASURED VOLTAGES AND VELOCITIES FOR EACH WIRE ')
      WRITE(6,76)VCHAN1(IPROBE,I,J),VCHAN2(IPROBE,I,J),VCHAN3(IPROBE,I,J
     C),VEL1(I,J),VEL2(I,J),VEL3(I,J)
      D(2)=VEL2(I,J)
      D(3)=VEL3(I,J)
      DO 111 II=1,3
      DO 111 JJ=1,3
      CC(II,JJ)=C(II,JJ)
  111 CONTINUE
      CALL DLEQD(CC,D,3,1,3,3,DET)
      U0=D(2)
```

```
      V0=D(1)
      W0=D(3)
      WRITE(6,61)V0,U0,W0
      VINIT=V0
      UINIT=U0
      WINIT=W0
C
C       BEGIN NEWTON-RAPHSON ITERATION
C
      AA1=SQRT(A4)
      AA2=SQRT(A5)
      AA3=SQRT(A6)
      BB1=D4/(2.*AA1)
      BB2=D5/(2.*AA2)
      BB3=D6/(2.*AA3)
      CC1=AA1*(B4/(2.*A4)-D4*D4/(8.*A4*A4))
      DD1=AA1*(F4/(2.*A4)-D4*E4/(4.*A4*A4))
      EE1=E4/(2.*AA1)
      FF1=AA1*(C4/(2.*A4)-E4*E4/(8.*A4*A4))
      CC2=AA2*(B5/(2.*A5)-D5*D5/(8.*A5*A5))
      DD2=AA2*(F5/(2.*A5)-D5*E5/(4.*A5*A5))
      EE2=E5/(2.*AA2)
      FF2=AA2*(C5/(2.*A5)-E5*E5/(8.*A5*A5))
      CC3=AA3*(B6/(2.*A6)-D6*D6/(8.*A6*A6))
      DD3=AA3*(F6/(2.*A6)-D6*E6/(4.*A6*A6))
      EE3=E6/(2.*AA3)
      FF3=AA3*(C6/(2.*A6)-E6*E6/(8.*A6*A6))
      DO 200 N=1,NREPS
      GG1=AA1*V0+BB1*U0+CC1*U0*U0/V0+DD1*U0*W0/V0+EE1*W0+FF1*W0*W0/V0
     1-VEL1(I,J)
      GG2=AA2*V0+BB2*U0+CC2*U0*U0/V0+DD2*U0*W0/V0+EE2*W0+FF2*W0*W0/V0
     1-VEL2(I,J)
      GG3=AA3*V0+BB3*U0+CC3*U0*U0/V0+DD3*U0*W0/V0+EE3*W0+FF3*W0*W0/V0
     1-VEL3(I,J)
      G1WV=AA1-CC1*U0*U0/(V0*V0)-DD1*U0*W0/(V0*V0)-FF1*W0*W0/(V0*V0)
      G2WV=AA2-CC2*U0*U0/(V0*V0)-DD2*U0*W0/(V0*V0)-FF2*W0*W0/(V0*V0)
```

```
G3WV=AA3-CC3*U0*U0/(V0*V0)-DD3*U0*W0/(V0*V0)-FF3*W0*W0/(V0*V0)
G1WU=BB1+2.*CC1*U0/V0+DD1*W0/V0
G2WU=BB2+2.*CC2*U0/V0+DD2*W0/V0
G3WU=BB3+2.*CC3*U0/V0+DD3*W0/V0
G1WW=EE1+DD1*U0/V0+2.*FF1*W0/V0
G2WW=EE2+DD2*U0/V0+2.*FF2*W0/V0
G3WW=EE3+DD3*U0/V0+2.*FF3*W0/V0
D(1)=-GG1 *10
D(2)=-GG2 *10
D(3)=-GG3  *10
 CC(1,1)= G1WV* 10.0
 CC(1,2)= G1WU* 10.0
 CC(1,3)= G1WW* 10.0
 CC(2,1)= G2WV* 10.0
 CC(2,2)= G2WU* 10.0
 CC(2,3)= G2WW* 10.0
 CC(3,1)= G3WV* 10.0
 CC(3,2)= G3WU* 10.0
 CC(3,3)= G3WW* 10.0
CALL DLEQD(CC,D,3,1,3,3,DET)
DELV=D(1) /10
DELU=D(2)   /10
DELW=D(3)  /10
RLX=1.0
DELU=RLX*DELU
DELV=RLX*DELV
DELW=RLX*DELW
 V0= V0+DELV
 U0=U0+DELU
 W0= W0+DELW
 GRES= SQRT((GG1*GG1+GG2*GG2+GG3*GG3)/ 3.0)
 EPX= EPS
 IF(ABS(GRES).GT.EPX) GO TO 210
 WV=V0
 WU=U0
 WW=W0
```

```
C
C       SOLUTION CONVERGED
C
        WRITE(6,84)N
        WRITE(6,61)WV,WU,WW
        WR=WU/UTIP
        WT=WV/UTIP
        WZ=WW/UTIP
        W=SQRT(WT*WT+WR*WR+WZ*WZ)
        CONST=SQRT(PWALL/RHO*RHO1/PWALL)
        WT=WT/CONST
        WR=WR/CONST
        WZ=WZ/CONST
        WRITE(6,61)WT,WR,WZ,W
        DATA(J,1)=WT
        DATA(J,2)=WR
        DATA(J,3)=WZ
        DATA (J,11)=W
        GO TO 220
  210   IF( N.EQ. 20) GO TO 211
        IF ( N .EQ. 40) GO TO 211
        IF ( N .EQ. 60) GO TO 211
        IF ( N .EQ. 80) GO TO 211
        GO TO 200
  211   EPX= 2.0*EPX
  200 CONTINUE
C
C       SOLUTION FAILED TO CONVERGE
C
        WRITE(6,86)NREPS
   86 FORMAT(5X,'MEAN VELOCITIES DID NOT CONVERGE AFTER',I5,' ITERATIONS'
     C')
         WRITE(6,61) V0,U0,W0
C
C       USE INITIAL VALUES OF VELOCITY FOR TURBULENCE CALUULATIONS
C
```

```
      WV=VINIT
      WU=UINIT
      WW=WINIT
      WR=WU/UTIP
      WT=WV/UTIP
      WZ=WW/UTIP
      W=SQRT(WT*WT+WR*WR+WZ*WZ)
      WRITE(6,61)WT,WR,WZ,W
      DATA(J,1)=WT
      DATA(J,2)=WR
      DATA(J,3)=WZ
      DATA (J,11)=W
C
C       CORRECT INPUT FLUCTUATING VOLTAGES FOR TIME ERROR
C
  220 FV1SQ=FV1SQ/TIME(I)
      FV2SQ=FV2SQ/TIME(I)
      FV3SQ=FV3SQ/TIME(I)
      FV12=(FV12/TIME(I))
      FV13=(FV13/TIME(I))
      FV23=(FV23/TIME(I))
C
C       USE LINEARIZED THEORY TO CALCULATE FLUCTUATING VELOCITIES
C
      FACT1=2.0*SQRT(VCHAN1(IPROBE,I,J))*VEL1(I,J)**(1.0-POWER1)/SLOPE1
     C(J)/POWER1
      FACT2=2.0*SQRT(VCHAN2(IPROBE,I,J))*VEL2(I,J)**(1.0-POWER2)/SLOPE2
     C(J)/POWER2
      FACT3=2.0*SQRT(VCHAN3(IPROBE,I,J))*VEL3(I,J)**(1.0-POWER3)/SLOPE3
     C(J)/POWER3
      WRITE(6,45)SLOPE1(J),SLOPE2(J),SLOPE3(J)
      FV1=SQRT(FV1SQ)/ATTEN(1)
      FV2=SQRT(FV2SQ)/ATTEN(2)
      FV3=SQRT(FV3SQ)/ATTEN(3)
       FV12= FV12/(ATTEN(1)*ATTEN(2))
       FV13= FV13/(ATTEN(1)*ATTEN(3))
```

```
      FV23= FV23/(ATTEN(2)*ATTEN(3))
      U1=FACT1*FV1
      U2=FACT2*FV2
      U3=FACT3*FV3
C
      FVEL1(I,J)=U1*U1
      FVEL2(I,J)=U2*U2
      FVEL3(I,J)=U3*U3
      FVEL12=FACT1*FACT2*FV12
      FVEL13=FACT1*FACT3*FV13
      FVEL23=FACT2*FACT3*FV23
C
C
C     CALCULATE FLUCTUATING VELOCITY COEFFICIENTS
C
      AA1=C(1,1)
      AA2=C(1,2)
      AA3=C(1,3)
      AA4=AA1*(B4/(2.*A4)-D4*D4/(8.*A4*A4))
      AA5=AA1*(C4/(2.*A4)-E4*E4/(8.*A4*A4))
      AA6=AA1*(F4/(2.*A4)-D4*E4/(4.*A4*A4))
       AA7=  AA4/2.0
       AA8=  AA5/2.0
      AA9=AA6
       BB1 = C(2,1)
       BB2 = C(2,2)
       BB3 = C(2,3)
      BB4=BB1*(B5/(2.*A5)-D5*D5/(8.*A5*A5))
      BB5=BB1*(C5/(2.*A5)-E5*E5/(8.*A5*A5))
      BB6=BB1*(F5/(2.*A5)-D5*E5/(4.*A5*A5))
       BB7=  BB4/2.0
       BB8=  BB5/2.0
      BB9=BB6
       CC1 = C(3,1)
       CC2 = C(3,2)
       CC3 = C(3,3)
```

```
CC4=CC1*(B6/(2.*A6)-D6*D6/(8.*A6*A6))
CC5=CC1*(C6/(2.*A6)-E6*E6/(8.*A6*A6))
CC6=CC1*(F6/(2.*A6)-D6*E6/(4.*A6*A6))
 CC7=  CC4/2.0
 CC8=  CC5/2.0
CC9=CC6
AAA1=AA1
AAA2=BB1
AAA3=CC1
BBB1=AA2+AA7*WR/WT+AA6*WZ/WT
BBB2=BB2+BB7*WR/WT+BB6*WZ/WT
BBB3=CC2+CC7*WR/WT+CC6*WZ/WT
CCC1=AA3+AA8*WZ/WT+AA6*WR/WT
CCC2=BB3+BB8*WZ/WT+BB6*WR/WT
CCC3=CC3+CC8*WZ/WT+CC6*WR/WT
A(1,1)=AAA1*AAA1
A(1,2)=BBB1*BBB1
A(1,3)=CCC1*CCC1
A(1,4)=2.*AAA1*BBB1
A(1,5)=2.*AAA1*CCC1
A(1,6)=2.*BBB1*CCC1
A(2,1)=AAA2*AAA2
A(2,2)=BBB2*BBB2
A(2,3)=CCC2*CCC2
A(2,4)=2.*AAA2*BBB2
A(2,5)=2.*AAA2*CCC2
A(2,6)=2.*BBB2*CCC2
A(3,1)=AAA3*AAA3
A(3,2)=BBB3*BBB3
A(3,3)=CCC3*CCC3
A(3,4)=2.*AAA3*BBB3
A(3,5)=2.*AAA3*CCC3
A(3,6)=2.*BBB3*CCC3
A(4,1)=AAA1*AAA2
A(4,2)=BBB1*BBB2
A(4,3)=CCC1*CCC2
```

```
      A(4,4)=AAA1*BBB2+AAA2*BBB1
      A(4,5)=AAA1*CCC2+AAA2*CCC1
      A(4,6)=BBB1*CCC2+CCC1*BBB2
      A(5,1)=AAA1*AAA3
      A(5,2)=BBB1*BBB3
      A(5,3)=CCC1*CCC3
      A(5,4)=AAA1*BBB3+AAA3*BBB1
      A(5,5)=AAA1*CCC3+AAA3*CCC1
      A(5,6)=BBB1*CCC3+CCC1*BBB3
      A(6,1)=AAA2*AAA3
      A(6,2)=BBB2*BBB3
      A(6,3)=CCC2*CCC3
      A(6,4)=AAA2*BBB3+AAA3*BBB2
      A(6,5)=AAA2*CCC3+AAA3*CCC2
      A(6,6)=BBB2*CCC3+CCC2*BBB3
      DO 108 II=1,6
  108 CONTINUE
      B(1)=FVEL1(I,J)
      B(2)=FVEL2(I,J)
      B(3)=FVEL3(I,J)
      B(4)=FVEL12
      B(5)=FVEL13
      B(6)=FVEL23
      DO 113 II=1,6
      DO 113 JJ=1,6
      AA(II,JJ)=A(II,JJ)
  113 CONTINUE
      CALL DLEQD(AA,B,6,1,6,6,DET)
      WRITE(6,65)(B(K),K=1,6)
      WRITE(6,66)DET
      B(1)=DSQRT(B(1))
      B(2)=DSQRT(B(2))
      B(3)=DSQRT(B(3))
C
C     CORRECT FLUCTUATING VELOCITIES FOR HIGH TURBULENCE INTENSITIES
C
```

```
      ARG1=1.+FACTOR*(B(1)/(W*UTIP))**2.
      ARG2=1.+FACTOR*(B(2)/(W*UTIP))**2.
      ARG3=1.+FACTOR*(B(3)/(W*UTIP))**2.
      B(1)=B(1)/SQRT(ARG1)
      B(2)=B(2)/SQRT(ARG2)
      B(3)=B(3)/SQRT(ARG3)
C
      FWT=B(1)/(W*UTIP)
      FWR=B(2)/(W*UTIP)
      FWZ=B(3)/(W*UTIP)
      FW=ABS(FWR*WR/W)+ABS(FWT*WT/W)+ABS(FWZ*WZ/W)
      WRITE(6,62)FWT,FWR,FWZ,FW
      B(4)=B(4)/(W*W*UTIP*UTIP)
      B(5)=B(5)/(W*W*UTIP*UTIP)
      B(6)=B(6)/(W*W*UTIP*UTIP)
      RESSTR=DSQRT(B(4)*B(4)+B(5)*B(5)+B(6)*B(6))
      Q=SQRT(FWR*FWR+FWZ*FWZ+FWT*FWT)
      QSQD=Q*Q
      WRITE(6,67)Q,QSQD
       RATIO1= B(4)/QSQD
       RATIO2= B(5)/QSQD
       RATIO3= B(6)/QSQD
       RATIO= RESSTR/ QSQD
       WRITE(6,68) RATIO1, RATIO2, RATIO3,RATIO
        CR1=-B(4)/(FWT*FWR)
       CR2=-B(5)/( FWT*FWZ)
       CR3=-B(6)/(FWR*FWZ)
       CRR= RESSTR/ QSQD
      DATA (J,4)=FWT
      DATA (J,5)=FWR
      DATA (J,6)=FWZ
      DATA (J,7)=FW
      DATA (J,8)=B(4)
      DATA (J,9)=B(5)
      DATA (J,10)=B(6)
      DATA (J,12)=RESSTR
```

```
      DATA (J,13)=Q
      DATA (J,14)=QSQD
      DATA (J,15)=RATIO1
      DATA (J,16)=RATIO2
      DATA (J,17)=RATIO3
      DATA (J,18)=RATIO
      DATA (J,19)=CR1
      DATA (J,20)=CR2
      DATA (J,21)=CR3
      DATA (J,22)=CRR
  115 CONTINUE
      DO 1124 J=1,12
      AMAX = DATA(1,J)
      AMIN = DATA(1,J)
      DO 1122 II=2,NOT
      IF(AMAX.LT.DATA(II,J))AMAX=DATA(II,J)
      IF(AMIN.GT.DATA(II,J))AMIN=DATA(II,J)
 1122 CONTINUE
      WRITE(6,1123)J,AMAX,AMIN
      IF(J.EQ.11)AMA = AMAX
 1124 CONTINUE
 1123 FORMAT(' ',5X,I3,10X,F10.4,10X,F10.4)
      DO 1112 J=1,NOT
      DATU=DATA(J,1)/AMA
      DATAI=DATA(J,2)/AMA
      DATAO=DATA(J,3)/AMA
      WRITE(6,7777) DATU,DATAI,DATAO,
     X            (DATA(J,L),L=4,6),(DATA(J,L),L=8,10),DATA(J,12)
 7777 FORMAT(10F13.4)
 1112 CONTINUE
  97  FORMAT(5F10.4)
      WRITE (6,85)
      DO1111 J=1,NOT
      WRITE (6,96) J,DATA(J,1),DATA(J,2),DATA(J,3),DATA(J,11),(DATA(J,KN
     X),KN=4,10)
1111  CONTINUE
```

```
      WRITE (6,89)
      DO 110J=1,NOT
      WRITE (6,96) J,(DATA(J,KN),KN=12,22)
   96 FORMAT (I3,1X,11(F10.4,1X))
   85 FORMAT(//16X,'MEAN VELOCITIES',24X,'TURBULENCE INTENSITIES',20X,
     X'TURBULENCE STRESSES' /' J',5X,'WS',9X,'WN',9X,'WR',10 X,'W',9X,'FW
     XWS',8X,'FWN',8X,'FWR',9X,'FW',7X,'B(4)',7X,'B(5)',7X,'B(6)'/)
   89 FORMAT(//' TOTAL STRESS',9X,'TOTAL ENERGY',9X,'STRESS/INTENSITY RATI
     XTIOS',20X,'CORRELATION COEFFICIENTS' /' J',4X,'RESSTR',7X,'Q',8X,'
     XQSQD',6X,'RATIO1',5X,'RATIO2',5X,'RATIO3',5X,'RATIO',8X,'CR1',8X,
     X'CR2',8X,'CR3',8X,'CRR'/)
  110 CONTINUE
C
C      FORMAT STATEMENTS
C
    5 FORMAT(9X,I1)
   6  FORMAT (3F10.5,I3)
   10 FORMAT(8X,I2)
   15 FORMAT(8F10.5)
   16 FORMAT ( '  CALIBRATION CURVE OF PROBES',4F15.6)
   20 FORMAT(9X,I1,8X,I2)
   32 FORMAT(6F10.5)
   40 FORMAT  (2I10)
   44  FORMAT( 5X, ' MEAN & AVERAGED FLUCTUATING VOLTAGES')
   45 FORMAT(5F10.6,I4)
   46 FORMAT ( ' MEAN & FLUCTATING VOLTAGES--',9F10.5)
   50 FORMAT(5X,' VALUES FOR CALIBRATION CURVE ',I2//)
   54  FORMAT( 3X,'J',3X,'CVEL',7X,'V1',6X,'V2',6X,'V3',5X,'CALE1',
     1 4X,'CALE2',4X,'CALE3',4X,'VSQ1',5X,'VSQ2',5X,'VSQ3',5X,'E1SQ',
     2 5X,'E2SQ',5X,'E3SQ' )
   55 FORMAT(1X,I3,13F9.5)
   60 FORMAT(5X,'THETA STATION NUMBER ',I2,'   PROBE CALIBRATION CURVE '
     C,I1,'  NO. OF RADIAL STATIONS ',I2//)
   61 FORMAT(10X,'MEAN VELOCITIES :',4E15.5)
   62 FORMAT(10X,'TURBULENCE INTENSITIES :',4E15.5)
   63 FORMAT(10X,'TURBULENCE STRESSES :',4E15.5)
```

```
   65 FORMAT(1X,'SOLUTION MATRIX',6F16.6)
   66 FORMAT(1X,'DETERMINANT =',F16.8)
   67 FORMAT(10X,'TOTAL ENERGY :',2E15.5)
   68 FORMAT(10X,'STRESS/INTENSITY RATIOS:', 4F10.5)
   70 FORMAT(3F10.5)
   71  FORMAT ( 10X, ' CORRELATION COEFICIENTS:',4F10.5)
   74  FORMAT( 5X,'DIRECTION COSINES OF WIRES ' )
   75 FORMAT(6F10.6)
   76 FORMAT(6E15.5)
   80 FORMAT(5I5,9F12.5)
   82 FORMAT(5X,I5,F10.5)
  83  FORMAT (18A4,F8.3)
   84 FORMAT(5X,'MEAN VELOCITIES CONVERGED IN',I5,'  ITERATIONS')
   95 FORMAT (30X,20A4)
  87  FORMAT ('  PROBE D.C. ANGLES ',9F10.4)
   88  FORMAT( 1X,10F10.5)
   99 FORMAT(1X,//)
      IF(RAVI.EQ.2.0) GOTO 5554
      GO TO 5553
 5554 CONTINUE
      STOP
      END
      SUBROUTINE CALIB(I,K)
      COMMON VCHAN1(4,6,99),VCHAN2(4,6,99),VCHAN3(4,6,99),EO1,EO2,EO3,EO
     C4,EO5,EO6,EO7,EO8,EO9,CALE1(4,25),CALE2(4,25),CALE3(4,25),NOT
      COMMON JJ,CALV1(4,25),CALV2(4,25),CALV3(4,25)
      AJ=K-1
      AN=NOT-1
      D1 = (EO7-EO4)/AN
      D2 = (EO8-EO5)/AN
      D3 = (EO9-EO6)/AN
      EO1 = EO4+AJ*D1
      EO2 = EO5+AJ*D2
      EO3=EO6+AJ*D3
      DO 1155 J=1,JJ
      IF(J.NE.1)GO TO 1156
```

```
      DE1=CALE1(I,1)*CALE1(I,1)-EO1*EO1
      DE2=CALE2(I,1)*CALE2(I,1)-EO2*EO2
      DE3=CALE3(I,1)*CALE3(I,1)-EO3*EO3
 1156 CALE1(I,J)=SQRT(CALE1(I,J)*CALE1(I,J)-DE1)
      CALE2(I,J)=SQRT(CALE2(I,J)*CALE2(I,J)-DE2 )
      CALE3(I,J)=SQRT(CALE3(I,J)*CALE3(I,J)-DE3)
      CALV1(I,J)=CALE1(I,J)**2.0
      CALV2(I,J)=CALE2(I,J)**2.0
      CALV3(I,J)=CALE3(I,J)**2.0
 1155 CONTINUE
      RETURN
      END
```

```
AFC ROTOR WAKE: X/C=0.00104,R/RT=0.7297,I=5: DATED;04/18/1978          169.578
       1000.01
1.0        1.0        1.0
0.175      0.175      0.175

73.0       73.0       73.0       73.0       73.0       73.0
          1
          9
1.791      1.867      1.732
1.6689     1.745      1.6014
0.000      1.758      0.000      1.795      0.000      1.732
0.355      2.280      0.328      2.326      0.3380     2.462
0.756      2.400      0.963      2.499      0.5970     2.572
1.622      2.518      1.813      2.608      1.170      2.690
3.025      2.621      2.328      2.654      2.400      2.832
4.599      2.697      3.844      2.754      3.889      2.929
6.021      2.747      5.247      2.817      4.536      2.963
6.600      2.767      6.117      2.850      5.738      3.014
6.875      2.778      6.814      2.875      6.662      3.050
0.516      0.545      0.476
          1          21
7.75
40.0641    47.2406    97.6157
```

```
66.4042    105.7630   148.2960
55.4258    128.3390   59.5102
         7321.0
           1          1

                      50.0
2.556       2.767      2.830      23.5       1.594      1051
0.0190      0.0160     0.020
0.0240      0.0280     0.0240
0.010       0.0150     0.0180
2.513       2.756      2.805      24.0       1.587      1050
0.020       0.0170     0.0180
0.0250      0.0280     0.0240
0.020       0.0220     0.020
C      REMAINING SET OF DATA
```

```
C      COORDINATE TRANSFORMATION PROGRAM
       DIMENSION DATA(12,100)
       DIMENSION WORD1(80),WORD2(80)
C      COMPUTER PROGRAM TO CONVERT VELOCITIES AND TURBULENCE QUANTITIES
C      FROM ONE COORDINATE SYSTEM TO ANOTHER COORDINATE SYSTEM
C
C      READ IN DIRECTION COSINES
C
       READ(5,21)AL11,AL12,AL13,AL21,AL22
   21  FORMAT(5F10.4)
       READ(5,22)AL23,AL31,AL32,AL33
   22  FORMAT(4F10.4)
```

```
 1000 CONTINUE
      UMAX=0.0
C
C     READ IN RAVI NOT EQUAL TO ZERO FOR LAST DATA SET
C
      READ(5,18)RAVI
   18 FORMAT(F10.4)
C
C     READ IN DATA SET DESIGNATION
C
      READ(5,1)(WORD1(L),L=1,80)
C
C     READ IN BLANK CARD
C
      READ(5,1)(WORD2(L),L=1,80)
    1 FORMAT(80A1)
C
      WRITE(6,2)(WORD1(M),M=1,80)
      WRITE(6,2)(WORD2(M),M=1,80)
    2 FORMAT(' ',80A1)
C
C     READ IN NUMBER OF POINTS IN DATA SET
C
      READ(5,10)N
   10 FORMAT(I5)
      DO 100  I=1,N
      READ(5,20)US,UN,UR,FS,FN,FR,B4,B5,B6,RES
   20  FORMAT(5F10.4)
C
C     MEAN VELOCITY TRANSFORMATION
C
      UX=AL11*US+AL12*UN+AL13*UR
      UY=AL21*US+AL22*UN+AL23*UR
      UZ=AL31*US+AL32*UN+AL33*UR
      IF(UX.GT.UMAX)UMAX=UX
C
```

```
C      TURBULENCE QUANTITIES
C
       FX=AL11*AL11*FS*FS + AL12*AL12*FN*FN + AL13*AL13*FR*FR + 2.0*(AL11
      C*AL12*B4 + AL11*AL13*B5 + AL12*AL13*B6)
       FY= AL21*AL21*FS*FS + AL22*AL22*FN*FN + AL23*AL23*FR*FR + 2.0*(AL2
      C1* AL22*B4 + AL22*AL23*B6 + AL21*AL23*B5)
       FZ=AL31*AL31*FS*FS + AL32*AL32*UN*UN + AL33*AL33*FR*FR + 2.0*(AL31
      C*AL32*B4 + AL31*AL33*B5 + AL32*AL33*B6)
       FXY=AL11*AL21*FS*FS +AL12*AL22*FN*FN + AL13*AL23*FR*FR + (AL12*AL2
      C1 + AL11*AL22)*B4+ (AL13*AL21 + AL11 * AL23)*B5 + (AL13*AL22 + AL1
      C2*AL23)*B6
       FXZ=AL11*AL31*FS*FS + AL12*AL32*FN*FN + AL13*AL33*FR*FR + (AL11*AL
      C32 + AL12*AL31)*B4 + (AL11*AL33  + AL13*AL31)*B5 +(AL12*AL33 + AL1
      C3*AL32) *B6
       FYZ = AL21*AL31*FS*FS + AL22*AL32*FN*FN + AL23*AL33*FR*FR + (AL21*
      CAL32 + AL22*AL31) *B4 + (AL21*AL33 + AL23*AL31)*B5 + (AL23*AL32 +
      CAL22*AL33)*B6
       FX=SQRT(FX)
       FY=SQRT(FY)
       FZ=SQRT(FZ)
       DATA(1,I)=UX
       DATA(2,I)=UY
       DATA(3,I)=UZ
       DATA(4,I)=FX
       DATA(5,I)=FY
       DATA(6,I)=FZ
       DATA(7,I)=FXY
       DATA(8,I)=FXZ
       DATA(9,I)=FYZ
       DATA(10,I)=RES
  100  CONTINUE
       DO 200 J=1,10
       AMAX=DATA(J,1)
       AMIN=DATA(J,1)
       DO 201 II=2,N
       IF(AMAX.LT.DATA(J,II))AMAX=DATA(J,II)
```

```
      IF(AMIN.GT.DATA(J,II))AMIN=DATA(J,II)
  201 CONTINUE
      IF(J.EQ.1)AMA=AMAX
      AMAX=AMAX/AMA
      AMIN = AMIN/AMA
      WRITE(6,1123)J,AMAX,AMIN
 1123 FORMAT(' ',5X,I3,10X,F10.4,10X,F10.4)
  200 CONTINUE
      DO 202 IJ=1,10
      DO 203 IK=1,N
      DATA(IJ,IK)=DATA(IJ,IK)/AMA
  203 CONTINUE
  202 CONTINUE
      WRITE(6,1124)UMAX
 1124 FORMAT(' ',' UMAX=',F10.4)
      DO 204 KK=1,N
      WRITE(7,20)(DATA(JK,KK),JK=1,10)
      WRITE(6,98)(DATA(JK,KK),JK=1,10)
   98 FORMAT(10F10.4)
  204 CONTINUE
      IF(RAVI.EQ.0.0) GO TO 1000
      STOP
      END
```

Appendix A2

SCALES AND OTHER PARAMETERS OF FLOW

The flow parameters and various scales of turbulence encountered in the present study are given below.

A2.1 Free-Stream Turbulence

The values, in the relative frame of reference, inside and outside the end-wall boundary layers and in the trailing-edge and far-wake regions at the operating speed and flow coefficients are given by

R	Z	W_o/U_T	W_o m/sec (ft/sec)	R_e
0.5676	0.1250	0.6604	34.217 (112.261)	17.42x 10^5 (Based on Tip Conditions)
0.5676	0.6560	0.6639	34.399 (112.858)	
0.7297	0.0104	0.6145	31.843 (104.470)	
0.7297	0.5313	0.6500	33.6804 (110.500)	
0.9595	0.0104	0.6639	34.412 (112.900)	
0.9595	0.458	0.6457	33.467 (109.800)	

A2.2 Semi-Wake Thickness

Semi-wake thickness is considered to be the characteristic rotor-wake thickness. The values at representative radii inside and outside the end-wall boundary layers are:

R	Z	L (Semi-Wake Width)	ℓ (Wake Width) m(ft)
0.5676	0.1250	0.2650	0.0211 (0.0694)
0.5676	0.6560	0.3200	0.0255 (0.0838)
0.7297	0.0104	0.0190	0.0020 (0.0064)
0.7297	0.5313	0.1313	0.0135 (0.0442)
0.9595	0.0104	0.413	0.0557 (0.1828)
0.9595	0.458	0.620	0.0836 (0.2744)

Overall turbulence level is about two percent in free-stream and 45 per-center at wake center.

Reynolds number based on tip velocity is 17.42×10^5.

A2.3 Length Scales

In order to calculate the errors involved in the measurement of turbulent flow as well as in categorizing the type of turbulent flow, it is necessary to make an estimation of the length scales that are encountered in the rotor-wake data. The three important scales of turbulence are:

1. Large eddy length scale (ℓ)
2. Taylor's microscale (λ_g)
3. Kolmogorov scale (η)

The large eddy length scale is proportional to the boundary layer thickness. In the case of wakes, it is proportional to the semi-wake width. It is known that the semi-wake width varies depending on the radius and downstream location. Typical values are given below

R	Z	L (Semi-Wake Width)	ℓ (Wake Width) m(ft)
0.5676	0.1250	0.2650	0.0211 (0.0694)
0.5676	0.6560	0.3200	0.0255 (0.0838)
0.7297	0.0104	0.0190	0.0020 (0.0064)
0.7297	0.5313	0.1313	0.0135 (0.0442)
0.9595	0.0104	0.4130	0.0557 (0.1828)
0.9595	0.458	0.6200	0.0836 (0.2744)

The Reynolds number based on the turbulence intensity is also an important parameter in determining the structure of turbulent flow. It varies with the radius as well as the downstream distance. Typical values are ($R_e = u'\ell/\nu$, u' is turbulence intensity and ν is the kinematic viscosity).

R	Z	R_e
0.5676	0.1250	1.54×10^5
0.5676	0.6560	6.30×10^4
0.7297	0.0104	2.53×10^4
0.7297	0.5313	4.65×10^4
0.9595	0.0104	8.04×10^5
0.9595	0.4580	4.65×10^5

Taylor's microscale: This scale λ_g is defined as

$$\varepsilon = \frac{15\nu u'^2}{\lambda_g^2}$$

where ε is the turbulent dissipation rate. An estimate of ε based on Tennekes and Lumely (1972) is

$$\varepsilon = \frac{u'^3}{\ell}$$

For the rotor-wake under consideration, the typical values are,

R	Z	ε
0.5676	0.1250	$4.31 \times 10_3^3$ (4.64×10^4)
0.5676	0.6560	$1.65 \times 10_3^6$ (1.78×10^4)
0.7297	0.0104	$1.72 \times 10_4^6$ (18.47×10^6)
0.7297	0.5313	$4.7 \times 10_4^4$ (5.06×10^4)
0.9595	0.0104	$5.53 \times 10_4^4$ (5.95×10^5)
0.9595	0.458	4.95×10^3 (5.33×10^4)

Taylor's miscroscale will then be,

R	Z	λ_g (cm (inch)
0.5676	0.1250	0.063 (0.0248)
0.5676	0.6560	0.117 (0.0462)
0.7297	0.0104	0.018 (0.0070)
0.7297	0.5313	0.102 (0.040)
0.9595	0.0104	0.102 (0.040)
0.9595	0.458	0.152 (0.060)

Kolmogrov scale represents the small scale eddies in the dissipation range and is defined as:

$$\eta = (\nu^3/\varepsilon)^{1/4} \quad .$$

Again the representative values inside and outside the end-wall boundary layers are:

R	Z	η
0.5676	0.1250	0.0345 (1.36×10^{-2})
0.5676	0.6560	0.0132 (5.20×10^{-3})
0.7297	0.0104	0.008 (3.14×10^{-3})
0.7297	0.5313	0.0348 (1.37×10^{-2})
0.9595	0.0104	0.0191 (7.52×10^{-3})
0.9595	0.458	0.0345 ($o.36 \times 10^{-2}$)

A2.4 Wave Number

Wave number for the turbulent flow is defined as:

$$K = \frac{2\pi\omega}{u} \simeq \frac{1}{\ell_c}$$

where ω is the frequency at which the contribution due to a correlation between two fluctuating velocity components to the Reynolds stress is being considered. u is the mean flow velocity at which an eddy of length ℓ_e, corresponding to that wave number is convected. The wave number which is expressed in centimeter units is required in calculating the errors in Reynolds stress correlations. The distance between the sensors is 1.5 mm, while the sensors are 1 mm long. The wave number corresponding to an eddy of sesnor length is 10 cm^{-1} and the wave number corresponding to an eddy equal to distance between wires is 6.67 cm^{-1}.

A2.5 Thermal Inertia of the Wire

The temperal error due to thermal inertia at any frequency is given by Hinze (1959) as:

$$e(\omega) = \frac{1}{\sqrt{(1 + \omega^2 M^2)}}$$

where M is the time constant of the wire and is equal to

$$\frac{e_L c_w (\theta_w - \theta_f)}{I^2 R_f}$$

where:

e_L = conversion constant between heat and electrical units,

c_w = specific heat of the wire material

θ_w = temperature to which the wire is heated

θ_f = working fluid temperature

I = amperage in the circuit

R_f = resistance of the wire at fluid temperature.

The time constant is $M = 1.56 \times 10^{-4}$ sec. So the thermal inertia order at

1 KHZ	e (1 KHZ)	= 0.897
5 KHZ	e (5 KHZ)	= 0.789
10 KHZ	e (10 KHZ)	= 0.540

Appendix A3

ESTIMATION OF ERRORS IN MEASUREMENTS

Hot-wire and pressure measurements are prone to numerous errors, some of which can be compensated for by inclusion of correction factors. Some of the errors are inherent in the measurement technique and call for detailed and elaborate equipment to overcome them. Broadly the errors can be divided into three categories: probe errors, instrumentation errors, and mechanical errors. A detailed discussion is given by Anand (1976).

A3.1 Probe Error

The major source of error arising due to probe and the sensors are:

1. Inclination of the wire to the flow streamlines (deviation from cosine law).

2. Effects of wire supports on the frequency response and heat-transfer properties of hot-wires.

3. Spatial resolution of the probe (eg. finite length of probe sensors).

4. Aging of hot-wire and variation of resistance due to ambient conditions.

5. Ambient temperature and test section temperature drift.

6. Wall proximity effects.

7. Inaccuracies in angle measurements.

As mentioned earlier some of these errors can be eliminated by use of correction factors while some are inherent in the measurement technique. Some estimates and reductions of the above losses are discussed below.

1. Effective cooling velocity on the wire is given by Hinze (1959) as:

$$U_{eff} = U_n^2 + K^2 U_a^2$$

where U_n and U_a are velocity components normal and parallel to the wire. K is a correction factor which depends on the length-to-diameter ratio and its variation with ℓ/d can be calculated using the relation

$$K^2 = \cot^2\alpha\{[b + \frac{1 - b}{\cos^{1/2}\alpha}]^4 - 1\}$$

where α = angle of incidence between free-stream direction and the normal to the axis of the wire.

b = parameter that depends on ℓ/d ratio. For standard wires, the value can be obtained from Champane, et al. (1967).

For the departure from cosine law, Hizne (1958) gives a semi-analytical expression of the form:

$$U_{eff} = U(\cos^2\phi + b^2\sin^2\phi)^{1/2} \quad .$$

Finite dimensions of the wire with respect to the local parameters to be measured might yield errors like,

a. Temperature distribution along the wire.

b. Modifications of the time constnat of the wire.

2. Effects of wire supports on the frequency response and heat-transfer properties of hot-wires.

a. Betchov (1948) and Corrson (1963) give the heat loss to the support, based on theoretical deductions, around seven to ten percent.

b. The prongs have negligible influence on the frequency response and transient response of the hot-wire, when operated in constant temperature mode, and its effect is reported by Olivari (1976).

3. Spatial resolution of the hot-wire. When the wire length is not negligible compared with the characteristic length of interest in mean velocity and turbulence, an imperfect spatial resolution occurs because of "inactive" wire length. The source of error introduced by this may be appreciable, particularly in the highly three-dimensional flow-field that exists in the trailing-edge region of the blades. Besides the wake width at these locations will be of the same order or smaller than the effective length of the sensor. In effect there will be a error in the measurement of mean velocity, fluctuating quantities, and correlations.

The error in a cross correlation to spatial resolution is the minimum eddy size the probe can correlate because of separation between the two wires. The wave number corresponding to these distances are 10 cm^{-1}. The error e in the correlation is given by Lumley (1965) as:

$$e\overline{(u_i'u_j')} = \frac{\overline{u_i'u_j'} - u_i'u_j'(K)}{u_i'u_j'} \quad .$$

Anand (1978) has shown that $\overline{u_i'u_j'}$ correlation is directly related to measured fluctuating voltage correlation $\overline{e_ie_j}$. Using these relations, the maximum anticipated errors in the measured voltage correlations are:

Radius	Axial Loc.	Error in		
		$\overline{e_1e_2}$	$\overline{e_2e_3}$	$\overline{e_3e_1}$
R	Z	(in Percent)		
0.5676	0.1250	8.7	9.2	7.9
0.5676	0.6560	7.2	8.1	6.5
0.7297	0.0104	34.5	42.5	47.9
0.7297	0.5313	9.8	11.9	7.2
0.9595	0.0104	14.7	17.2	12.6
0.9595	0.4580	6.3	7.1	8.2

The inaccuracies introduced by the "cold lengths" can be overcome by individual calibration of the wire which would give a proper slope in the King's law. The error arising due to this is discussed by Anand (1976) and the order of error in the far-wake region is about the same.

The error arising due to the aging of the hot-wire and the variation due to ambient conditions which is reflected in the wire resistance and voltage at zero flow conditions can be corrected for by calibrating the wires before and after the experiment and incorporating the variation in the data reduction process. The error arising due to this cannot be evaluated as it is a function of time, environment in which it operates, over-heat ratios employed, to mention a few variables.

The error arising due to the ambient temperature variation (and consequently the test section temperature variation) has been discussed by Anand (1976) and has been incorporated in the data reduction computer program given in Appendix A1. Hence this error is not discussed in this section.

A3.2 Instrumentation Errors

The errors arising due to instrumentation may be due to:

1. Improper integration time constant in voltmeter and rms meters.
2. Not properly balanced anemometers.
3. Improper gain adjustments in the sum and difference circuits.

As most of these factors can be easily checked, it is assumed that they do not contribute any error to the data.

A3.3 Mechanical Errors

There are many errors introduced because of mechanical problems. Most of these errors are easy to recognize and can be solved to an

extent when they do not actually influence the data. The probable errors are:

1. Probe body vibration. The vibration of the probe body due to rotation, flow induced vibration, transmission of vibration due to other mechanical sources like vibrating belts and pulleys can add significant amount of spurious signal to the measurements. The probe vibration can be analyzed using a spectrum analyzer at various frequencies. The spectral measurements did not indicate the existance of any spurious signal due to vibration.

Following Hartog (1947), the natural frequency of the probe and the probe support can be evaluated assuming that the probe acts like a concentrated mass at the end of the support. The natural frequency in bending mode is given by,

$$\omega_n^2 = (\omega_n^2)_{\Omega=o} + a\Omega^2$$

where:

$(\omega_n)_{\Omega=o} = 3.03\ EI/\ell_o^3\ (M + 0.023\ m)$

E = elastic modulus = 30×10^6 psi

m = mass per unit length of the probe = $0.0018\ \ell_o$

M = mass of the probe = 0.0041 lbm

I = moment of area = $\frac{1}{2} M(r_o^2 - r_i^2) = 2.65 \times 10^{-4}$

r_o and r_i are outer and inner radius of the probe support, respectively.

a = constant (according to Hartog = 1.5)

The natural frequencies at lower and mid-radii were found to be greater than the cut-off frequency and so did not affect the measurements. Spectral measurements at higher radii did not exhibit the existance of spurious signal, so the error arising due to probe support vibration, if any, is neglected.

2. Gear slack in the traverse mechanism. This problem, if present during rotation, can present a major source of error in the tangential distance moved by the probe. This source of error can be visualized using a strobeflash and was found to be neglegible. The gear slack, when the rotor was stationary was found to be around 1/8" at the tip radius. To eliminate this slack, the traverse gear shaft was pre-torsioned by a spring.

3. Spurious and stray electrical noise from line frequency, impure mercury in the slip-ring unit, or ground loops in the electronic circuitry can introduce a major source of error in the data. Spectrum analysis of the signal would show up these signals. It was found that it made no significant contribution to the data.

4. Errors due to improper sensor angle measurement as well as misalignment of the probe could make a significant contribution to the error in the data. The anticipated errors were of the same order as that given by Anand (1976) and hence are not given here.

Appendix A4

PROGRAM FOR FOURIER DECOMPOSITION OF ROTOR-WAKE

The program listed below was employed in the present investigation for the Fourier analysis of rotor-wake data. The problem description and method of analysis is given in Section 4.5. Reference is made to Ralston (1960) for description of FORIT and program variables.

The input to the main program is velocity, turbulent intensity, or any such parameter whose Fourier decomposition is desired. The data points can be either at regular or irregular intervals. The program executes a linear interpolation between the points and generates data points at equal intervals. Subsequent to this the program starts to normalize the given velocity and tangential locations such that it modifies an asymmetrical wake into a symmetrical wake. The mathematical implications for such normalizations are discussed in Section 4.5 The program FORIT evaluates the hormonic content in the wake up to the desired number of coefficients. Given below is a list of input variables. Refer to Figure 134 for some of the notations used below.

V(I,L)	velocity for the parameter whose Fourier decomposition is desired) at the ith point; L refers to the component of velocity to be considered
UMAX1	maximum free-stream velocity on one side of the blade surface
UMAX2	maximum free-stream velocity on the other side of the blade surface
UMIN	minimum velocity in the wake
N1	tangential location where UMAX1 occurs
N2	tangential location where UMAX2 occurs

NM tangential location where UMIN occurs

For the Fourier analysis the tangential locations are subscripted such that N2 (where UMAX2 occurs, UMAX2 > UMAX1) assumes a value of $\theta = 0$ and N1 takes a value of $\theta = 2\pi$. The value of θ at NM is π.

The data input for this program is in the form of punched cards which is obtained from the program given in Appendix A1. The output can either be in the form of printed output or punched cards of the Fourier coefficients. Listed on the next page is the combined MAIN and FORIT program along with a sample listing of the data input format.

```
      IMPLICIT REAL*8(A-H,O-Z)
C X/C=0.083,R/RT=0.860,I=10                                                    MANA  10
C  FOURIR ANALYSIS OF ROTOR WAKE
C     MAIN PROGRAM
      DIMENSION U(391),UD(391),T(391),TD(391),M(20),A(20),B(20),V(391,4)MANA  40
      DIMENSION VEL(391),FNT(391),TN(391),UN(391)                              MANA  50
      N=27
      DO 100 I=1,N
  555 FORMAT(20X,'AVGV1S      AVGV2S       AVGV3S       AVG123'/11X,4(' IN
     -TENSITY')//)
      READ(5,10) (V(I,L),L=1,4)
      READ (5,10) VV1                                                          MANA  80
 5555 FORMAT(' ',10X,4F10.5)                                                   MANA 100
  100 CONTINUE
   10 FORMAT(5E15.8)
      DO 1000 L=1,1
      READ(5,20) UMAX1,UMAX2,UMIN,N1,N2,NM                                     MANA 130
                                                                               MANA 140
   20 FORMAT(3F10.6,3I5)                                                       MANA 150
C UPDATING VELOCITY SUBSCRIPTS                                                 MANA 160
      DO 200 I=N1,N2                                                           MANA 170
      J=I-N1+1                                                                 MANA 180
      U(J)=V  (I,L)                                                            MANA 190
  200 CONTINUE                                                                 MANA 200
      NN=N2-N1+1                                                               MANA 210
      N=(NN-1)/2                                                               MANA 220
      T(1)=0.0                                                                 MANA 230
      T(NN)=360.0                                                              MANA 240
      K=NM-N1+1                                                                MANA 250
      T(K)=180.0                                                               MANA 260
      AA=K-1                                                                   MANA 270
      DT=180.0/AA                                                              MANA 280
      DO 60 I=2,K                                                              MANA 290
   60 T(I)=T(I-1)+DT                                                           MANA 300
      K1=K+1                                                                   MANA 310
      AA=NN-K                                                                  MANA 320
      DT=180.0/AA
```

```
      DO 70 I=K1,NN                                                    MANA 330
 70   T(I)=T(I-1)+DT                                                   MANA 340
      AA=K-1                                                           MANA 350
      DT=180.0/AA                                                      MANA 360
      NK=2*K-1                                                         MANA 370
      TN(K)=180.0                                                      MANA 380
      DO 71 I=K1,NK                                                    MANA 390
 71   TN(I)=TN(I-1)+DT                                                 MANA 400
C FINDING U-DEFECT                                                     MANA 410
      UDC=UMAX1-UMIN                                                   MANA 420
      DO 300 I=1,K                                                     MANA 430
      UD(I)=(UMAX1-U(I))/UDC
      UD(I)=(UMAX1-U(I))/UDC                                           MANA 440
 300  CONTINUE                                                         MANA 450
      UDC=UMAX2-UMIN                                                   MANA 460
      DO 400 I=K1,NN                                                   MANA 470
      UD(I)=(UMAX2-U(I))/UDC                                           MANA 480
 400  CONTINUE                                                         MANA 490
      DO 410 I=K1,NK                                                   MANA 500
      DO 420 K=K1,NN                                                   MANA 510
      IF(TN(I).GT.T(K)) GO TO 420                                      MANA 520
      GO TO 430                                                        MANA 530
 420  CONTINUE                                                         MANA 540
      K=NN                                                             MANA 550
 430  KS=K-1                                                           MANA 560
      UN(I)=UD(KS)+(UD(K)-UD(KS))*(TN(I)-T(KS))/(T(K)-T(KS))           MANA 570
 410  CONTINUE                                                         MANA 580
      DO 440 I=K1,NK                                                   MANA 630
      T(I)=TN(I)                                                       MANA 640
 440  UD(I)=UN(I)                                                      MANA 650
      NN=NK                                                            MANA 660
C FINDING THETA'S AND THETA-P'S                                        MANA 670
      VH=0.5                                                           MANA 680
      DO 500 I=1,K                                                     MANA 690
      IF(UD (I).GT.VH) GO TO 510                                       MANA 700
      GO TO 500                                                        MANA 710
```

```
  510  IS=I-1                                                                  MANA 720
       II=I                                                                    MANA 730
       GO TO 520                                                               MANA 740
  500  CONTINUE                                                                MANA 750
       II=K                                                                    MANA 760
   520 I=II                                                                    MANA 770
       IF(I.EQ.1) GO TO 1000                                                   MANA 780
       TS=T(IS)+(UD(I)-VH)/(UD(I)-UD(IS))*(T(I)-T(IS))                         MANA 790
       DO 600 I=K1,NN                                                          MANA 800
       IF(VH.GT.UD (I)) GO TO 610                                              MANA 810
       GO TO 600                                                               MANA 820
  610  IS=I-1                                                                  MANA 830
       II=I                                                                    MANA 840
       GO TO 620                                                               MANA 850
  600  CONTINUE                                                                MANA 860
       II=NN                                                                   MANA 870
   620 I=II                                                                    MANA 880
       TP=T(IS)+(UD(I)-VH)/(UD(I)-UD(IS))*(T(I)-T(IS))                         MANA 890
C NORMALISING THETA'S                                                          MANA 910
       DO 700 I=1,K                                                            MANA 920
   700 TD(I)=(180.0-T(I))/(180.0-TS)                                           MANA 930
       DO 800 I=K1,NN                                                          MANA 940
   800 TD(I)=(T(I)-180.0)/(TP-180.0)                                           MANA 950
    15 FORMAT(3X,'THETA',4X,'FOURIER  MEASURED    DIFFERENCE'/12X,2(' UDCMANA1010
      +NORM')/)                                                                MANA1020
       MA=9                                                                    MANA1030
       N=(NK-1)/2
       CALL FORIT(UD,N,MA,A,B,IER)                                             MANA1040
       PRINT,126,IER
   126 FORMAT(' FORIT ERROR=',I4)
       IF(L.EQ.1) WRITE(6,103)                                                 MANA1050
       IF(L.EQ.2) WRITE(6,104)                                                 MANA1060
       IF(L.EQ.3) WRITE(6,105)                                                 MANA1070
       IF(L.EQ.4) WRITE(6,106)                                                 MANA1080
  103  FORMAT(10X,'AVGV1S'//)                                                  MANA1090
  104  FORMAT(10X,'AVGV2S'//)
```

```
  105  FORMAT(10X,'AVGV3S'//)                                                MANA1110
  106  FORMAT(10X,'AVG123'//)                                                MANA1200
       PRINT 101,(A(I),I,I=1,MA)                                             MANA1130
   101 FORMAT(' A0=',8(F10.7,' A',I1,'='),F10.7/(8(' A',I2,'=',F11.8)))      MANA1140
       PRINT 102,(B(I),I,I=1,MA)                                             MANA1150
   102 FORMAT(' B0=',8(F10.7,' B',I1,'='),F10.7/(8(' B',I2,'=',F11.8)))      MANA1160
       WRITE(7,1112)(A(I),I=1,7)
       WRITE(7,1112)(B(I),I=2,7)
  1112 FORMAT(7F10.4,F9.4)
       DO 1111 I=1,NN                                                        MANA1180
       U(I)=A(1)                                                             MANA1190
       DO 810 J=2,MA                                                         MANA1200
       AJ=J-1                                                                MANA1210
       THETA=AJ*T(I)*22.0/7.0/180.0                                          MANA1220
       U(I)=U (I)+A(J)*DCOS(THETA)+B(J)*DSIN(THETA)                          MANA1230
   810 CONTINUE                                                              MANA1240
       TD(I)=UD(I)-U(I)                                                      MANA1250
  1111 CONTINUE                                                              MANA1270
  1000 CONTINUE                                                              MANA1280
       STOP                                                                  MANA1290
       END                                                                   MANA1300
       SUBROUTINE FORIT(FNT,N,M,A,B,IER)                                     FRIT 490
C                                                                            FRIT  10
C      .....................................................................FRIT  20
C                                                                            FRIT  30
C         SUBROUTINE FORIT                                                   FRIT  40
C                                                                            FRIT  50
C         PURPOSE                                                            FRIT  60
C            FOURIER ANALYSIS OF A PERIODICALLY TABULATED FUNCTION.          FRIT  70
C            COMPUTES THE COEFFICIENTS OF THE DESIRED NUMBER OF TERMS        FRIT  80
C            IN THE FOURIER SERIES F(X)=A(0)+SUM(A(K)COS KX+B(K)SIN KX)      FRIT  90
C            WHERE K=1,2,...,M TO APPROXIMATE A GIVEN SET OF                 FRIT 100
C            PERIODICALLY TABULATED VALUES OF A FUNCTION.                    FRIT 110
C                                                                            FRIT 120
C         USAGE                                                              FRIT 130
C            CALL FORIT(FNT,N,M,A,B,IER)                                     FRIT 140
```

```
C                                                                       FRIT 150
C                                                                       FRIT 160
C       DESCRIPTION OF PARAMETERS                                       FRIT 170
C          FNT-VECTOR OF TABULATED FUNCTION VALUES OF LENGTH 2N+1       FRIT 180
C          N  -DEFINES THE INTERVAL SUCH THAT 2N+1 POINTS ARE TAKEN     FRIT 190
C              OVER THE INTERVAL (0,2PI). THE SPACING IS THUS 2PI/2N+1  FRIT 200
C          M  -MAXIMUM ORDER OF HARMONICS TO BE FITTED                  FRIT 210
C          A  -RESULTANT VECTOR OF FOURIER COSINE COEFFICIENTS OF       FRIT 220
C              LENGTH M+1                                               FRIT 230
C              A SUB 0, A SUB 1,..., A SUB M                            FRIT 240
C          B  -RESULTANT VECTOR OF FOURIER SINE COEFFICIENTS OF         FRIT 250
C              LENGTH M+1                                               FRIT 260
C              B SUB 0, B SUB 1,..., B SUB M                            FRIT 270
C          IER-RESULTANT ERROR CODE WHERE                               FRIT 280
C              IER=0  NO ERROR                                          FRIT 290
C              IER=1  N NOT GREATER OR EQUAL TO M                       FRIT 300
C              IER=2  M LESS THAN 0                                     FRIT 310
C                                                                       FRIT 320
C       REMARKS                                                         FRIT 330
C          M MUST BE GREATER THAN OR EQUAL TO ZERO                      FRIT 340
C          N MUST BE GREATER THAN OR EQUAL TO M                         FRIT 350
C          THE FIRST ELEMENT OF VECTOR B IS ZERO IN ALL CASES           FRIT 360
C                                                                       FRIT 370
C       SUBROUTINES AND FUNCTION SUBPROGRAMS REQUIRED                   FRIT 380
C          NONE                                                         FRIT 390
C                                                                       FRIT 400
C       METHOD                                                          FRIT 410
C          USES RECURSIVE TECHNIQUE DESCRIBED IN A. RALSTON, H. WILF,   FRIT 420
C          'MATHEMATICAL METHODS FOR DIGITAL COMPUTERS', JOHN WILEY     FRIT 430
C          AND SONS, NEW YORK, 1960, CHAPTER 24. THE METHOD OF INDEXING FRIT 440
C          THROUGH THE PROCEDURE HAS BEEN MODIFIED TO SIMPLIFY THE      FRIT 450
C          COMPUTATION.                                                 FRIT 460
C                                                                       FRIT 470
C     ..................................................................FRIT 480
C
      IMPLICIT REAL*8(A-H,O-Z)                                          FRIT 500
      DIMENSION A(20),B(20),FNT(391)
```

```
C                                                                       FRIT 510
C         CHECK FOR PARAMETER ERRORS                                    FRIT 520
C                                                                       FRIT 530
      IER=0                                                             FRIT 540
   20 IF(M) 30,40,40                                                    FRIT 550
   30 IER=2                                                             FRIT 560
      RETURN                                                            FRIT 570
   40 IF(M-N) 60,60,50                                                  FRIT 580
   50 IER=1                                                             FRIT 590
      RETURN                                                            FRIT 600
C                                                                       FRIT 610
C         COMPUTE AND PRESET CONSTANTS                                  FRIT 620
C                                                                       FRIT 630
   60 AN=N                                                              FRIT 640
      COEF=2.0/(2.0*AN+1.0)                                             FRIT 650
      CONST=3.141593*COEF                                               FRIT 660
      S1=DSIN(CONST)                                                    FRIT 670
      C1=DCOS(CONST)                                                    FRIT 680
      C=1.0                                                             FRIT 690
      S=0.0                                                             FRIT 700
      J=1                                                               FRIT 710
      FNTZ=FNT(1)                                                       FRIT 720
   70 U2=0.0                                                            FRIT 730
      U1=0.0                                                            FRIT 740
      I=2*N+1                                                           FRIT 750
C                                                                       FRIT 760
C         FORM FOURIER COEFFICIENTS RECURSIVELY                         FRIT 770
C                                                                       FRIT 780
   75 U0=FNT(I)+2.0*C*U1-U2                                             FRIT 790
      U2=U1                                                             FRIT 800
      U1=U0                                                             FRIT 810
      I=I-1                                                             FRIT 820
      IF(I-1) 80,80,75                                                  FRIT 830
   80 A(J)=COEF*(FNTZ+C*U1-U2)                                          FRIT 840
      B(J)=COEF*S*U1                                                    FRIT 850
      IF(J-(M+1)) 90,100,100                                            FRIT 860
```

```
 90 Q=C1*C-S1*S                                                    FRIT 870
    S=C1*S+S1*C                                                    FRIT 880
    C=Q                                                            FRIT 890
    J=J+1                                                          FRIT 900
    GO TO 70                                                       FRIT 910
100 A(1)=A(1)*0.5                                                  FRIT 920
    RETURN                                                         FRIT 930
    END                                                            FRIT 940
```

1. Report No.	2. Government Accession No.	3. Recipient's Catalog No.
NASA CR-159518		

4. Title and Subtitle	5. Report Date
THREE DIMENSIONAL MEAN FLOW AND TURBULENCE CHARACTERISTICS OF THE NEAR WAKE OF A COMPRESSOR ROTOR BLADE	June 1980
	6. Performing Organization Code
7. Author(s)	8. Performing Organization Report No.
A. Ravindranath and B. Lakshminarayana	PSU/TURBO 80-4
	10. Work Unit No.
9. Performing Organization Name and Address	
The Pennsylvania State University 233 Hammond Building University Park, Pennsylvania 16802	11. Contract or Grant No. NSG-3012
	13. Type of Report and Period Covered
12. Sponsoring Agency Name and Address	Contractor Report
National Aeronautics and Space Administration Washington, D.C. 20546	14. Sponsoring Agency Code

15. Supplementary Notes

Final report. Project Managers, Marcus F. Heidman (1974-1980) and Loretta Shaw (1980-present), Fluid Mechanics and Acoustics Division, NASA Lewis Research Center, Cleveland, Ohio 44135.

16. Abstract

Three-dimensional characteristics of the mean velocity and turbulence structure in the near-wake of a moderately loaded compressor rotor is reported in this report. The experimental investigation was carried out using the rotating hot-wire technique. To discern the effect of annulus- and hub-wall boundary layer, secondary flow and tip-leakage on the wake structure, measurements were also taken inside the end-wall boundary layer. Static pressure gradients across the wake were measured using a static-stagnation pressure probe insensitive to flow direction changes. The set of wake data presented in this thesis is probably the first set of comprehensive measurements taken in the trailing-edge and near-wake regions and reflects the highly complex and three-dimensional nature of the rotor-wake. The axial and the tangential velocity defects, the radial component of velocity and turbulence intensities were found to be very large as compared to the near- and far-wake regions. The radial velocities in the trailing-edge region exhibited characteristics prevalent in a trailing vortex system. Flow near the blade tips was found to be highly complex due to interaction of the end-wall boundary layers, secondary flows, and tip-leakage-flow with the wake. The streamwise curvature was found to be appreciable near the blade trailing-edge. This investigation did reveal that flow properties in the trailing-edge region are quite different compared to that in the near- and far-wake regions with respect to their decay characteristics, similarity, etc. Fourier decomposition of the rotor-wake revealed that for a normalized wake only the first three coefficients are dominant. The derived results of the measurements indicated the inability of the cascade analysis to accurately predict the deviation angles for the rotor. Many useful correlations are attempted and reported in this investigation.

17. Key Words (Suggested by Author(s))	18. Distribution Statement
Turbomachinery Rotating blade wakes Axial flow compressor	Unclassified - unlimited STAR Category 02

19. Security Classif. (of this report)	20. Security Classif. (of this page)	21. No. of Pages	22. Price*
Unclassified	Unclassified	297	A13

* For sale by the National Technical Information Service, Springfield, Virginia 22161

NASA

DO NOT REMOVE SLIP FROM MATERIAL

Delete your name from this slip when returning material to the library.

If Undeliverable (Section 158 Postal Manual) Do Not Return

NAME	MS
~~Etiang F.~~	~~149~~
R. Thomas	460

NASA Langley (Rev. May 1988) RIAD N-75